Imperial College
London

Single-Molecule DNA Detection in Nanopipettes Using High-Speed Measurements and Surface Modifications

Raquel Leh-na Fraccari

A thesis submitted in partial fulfilment of the requirement for the degree of

Doctor of Philosophy

Department of Chemistry
Imperial College London
November 2016

Abstract

Inspired by transmembrane pores found in cell membranes and the operating principle of the Coulter counter used for cell counting, nanopore biosensors have emerged as a tool for single-molecule detection. This thesis describes single-molecule DNA detection through resistive pulse sensing using nanopipettes, a novel subclass of solid-state nanopores.

In the first part of this thesis, double-stranded (ds) DNA-nanopipette surface interactions were probed in 1 M KCl electrolyte using DNA molecules with lengths ranging from 48.5 to 4 kilobase pair (kbp). A custom-built current amplifier was employed for low-noise and high-bandwidth measurements. Results from these experiments were used to theoretically rationalise DNA-surface interactions and suggest that dsDNA adsorption to the nanopipette surface prior to translocation through the pore is likely to be an important factor in the process. Subsequently, initial investigations to probe DNA-surface interactions were carried out by modifying the surface charge of nanopipettes using silanes. Additionally, experiments were performed to detect shorter dsDNA lengths. In 1 M KCl electrolyte, 200 base pair (bp) long dsDNA was successfully detected using the low-noise and high-bandwidth current amplifier. However detection of 100 bp long dsDNA required the use of 2 or 4 M LiCl electrolyte.

Attention was finally shifted to the detection of 100 bp dsDNA in 1 M KCl electrolyte using functionalised lipid bilayer coated nanopipettes. Additional techniques were employed to prepare and characterise the lipid bilayers, including atomic force microscopy (AFM) and dynamic light scattering (DLS). The promising preliminary results provide a framework for further experiments using functionalised lipid bilayers to coat nanopipettes.

Overall, results of the aforementioned research presented in this thesis demonstrate high-speed single-molecule detection of DNA and provide novel insights into the translocation dynamics of DNA molecules in nanopipettes and the sensing capabilities of nanopipettes.

Declarations

I, the author, hereby declare that the work presented in the following thesis is original and performed by myself; otherwise it is clearly cited and acknowledged.
This work has not previously been submitted in any form to satisfy any degree requirement at this or any other university.

Raquel Leh-na Fraccari

2/11/2016

Copyright notice

Acknowledgements

I wish to thank first and foremost, my PhD supervisor Dr. Tim Albrecht for giving me the opportunity to undertake my PhD. I wish to express my sincere gratitude for your continued support, guidance and most of all patience. Thank you also Tim for organising the Albrecht group trip to the Cairngorms in Scotland. It was a very memorable trip and one I shall certainly not forget (for many different reasons)!

To all the Albrecht group both past and present, thank you for making it an enjoyable place to work these last three years. To Azadeh and Pippa, thank you for teaching me so many things, my first year would not have been possible without you. Best of all from that first year of my PhD I found not only mentors but friends. To Billy, sitting next to you in the office was a pleasure, you brightened up my days. Mike, thank you, you are the coolest geek I've met thus far. To Alex A, I hope we will be friends for many years to come. Good luck to Lucy, Mario and Silvia. I'm glad to have shared this PhD journey with you. Finally, thank you Eva. I will be eternally indebted to you for your constant help and support and for putting up with me! I am privileged to have you as a friend.

Thank you to everyone at the Politecnico di Milano, for making me feel welcome when I visited. Giorgio, Marco, Pietro and Giacomo, thank you all for your patience and for teaching me so much.

I would also like to express my gratitude to those outside of the Albrecht group who have helped me over the last three years. In particular thank you to Arwen, Yuval, Tom M and Beth, your time and generosity is much appreciated. I am also indebted to the Membrane Biophysics group. Thank you for all your help and sorry I realise I ask a lot of questions!

I have also met many wonderful people throughout my time at Imperial. Thank you Jasmine for all the wonderful times together, from Budapest to Washington DC to 30 hours in Italy. I hope we will share many more dinners together. Thank you to Binoy for all your help. I don't think I have ever met anyone with as much patience as you. Robert, thank you for all the laughs and the many weird conversations that shall remain between us. Thank you Paul for making the BPS in LA such a memorable experience, I will definitely not forget our trip to Santa Monica beach anytime soon. Alex B, thank you for introducing me to DnD, definitely

not something I would have imagined learning about during my PhD.

I would also like to thank all my friends and family for your love and support and in particular (in height order) James, Stephen and Chris for always making me laugh over the silliest of things and for trying to take an interest in my work.

Finally, I would like to thank my parents. Thank you for giving me the opportunity to study and for always encouraging me to do whatever makes me happy in life. I am privileged to have you as my parents. None of this would have been possible without your unconditional love.

To my parents

List of Publications

1. Fraccari R.L.; Ciccarella P.; Bahrami A.; Carminati M.; Ferrari G.; Albrecht T. *Nanoscale* **2016**, 8, 7604-7611.
2. Fraccari, R.L.; Carminati M.; Piantanida G.; Leontidou T.; Ferrari G.; Albrecht T. *Faraday Discuss.* **2016**, Advance Article, DOI: 10.1039/C6FD00109B.
3. Ciccarella, P.; Carminati, M.; Ferrari, G.; Fraccari, R.; Bahrami, A. An Integrated Low-Noise Current Amplifier for Glass-Based Nanopore Sensing; 10th Conference on Ph.D. Research in Microelectronics and Electronics (PRIME 2014), Grenoble, France, June 29 - July 30, **2014**, 1– 4.

Table of Contents

List of Figures

List of Tables

Abbreviations

σ	sigma
σ_s	solution conductivity
λ	wavelength of light
λ-DNA	lambda DNA (48.5 kbp)
λ_D	Debye length
Φ	potential drop
Φ'	Coulomb potential
Φ_{ep}	electrostatic potential
θ	scattering angle
θ_c	contact angle
ε	dielectric constant
Γ	decay constant
ρ_N	distance between two bp
ΔI	peak amplitude
ΔI_{mp}	most probable peak amplitude
τ	dwell time
τ_{mp}	most probable dwell time
τ_{rise}	rise time
μ_{DNA}	DNA electrophoretic mobility
ζ	zeta potential
υ	speed
υ_F	Flory exponent
°C	degrees Celsius
2D	two-dimensional
α-HL	α-hemolysin
A	ampere
AFM	atomic force microscopy

ALD	atomic layer deposition
APTES	(3-aminopropyl) triethoxysilane
APTMS	(3-aminopropyl) trimethoxysilane
biotin-PE	biotinylated lipid
β	friction coefficient
bp	base pair
BSA	bovine serum albumin
c_{DNA}	bulk DNA concentration
cssDNA	complementary ssDNA
CV	cyclic voltammetry
D	diffusion coefficient
D_i	inner diameter at the base
d	hydrodynamic diameter
d_i	nanopore diameter
d_{DNA}	DNA diameter
DLS	Dynamic light scattering
DNA	Deoxyribonucleic acid
DPPE	1,2-dipalmitoyl-sn-glycero-3-phosphoethanolamine
DPPE-GA	1,2-dipalmitoyl-sn-glycero-3-phosphoethanolamine-N-(glutaryl) (sodium salt)
dsDNA	double stranded DNA
DSC	differential scanning calorimetry

$\mathbf{f}$	free energy barrier
$\mathbf{f_c}$	cut-off frequency
$\mathbf{F_{drag}}$	viscous drag force
$\mathbf{F_{driving}}$	driving force
$\mathbf{F_e}$	electrophoretic force
$\mathbf{F_v}$	viscous force
$\mathbf{F_R}$	friction force
$\mathbf{G_{pore}}$	pore conductance
$\mathbf{g(c)}$	electrolyte conductivity
$\mathbf{I(t)}$	current-time
$\mathbf{k_B}$	Boltzmann constant
kbp	kilobase pair
kHz	kilohertz
$\mathbf{l}$	taper length
$\mathbf{L_\alpha}$	liquid-crystalline
$\mathbf{L_\beta}$	ordered gel
$\mathbf{l_p}$	length of pore
$\mathbf{L_{DNA}}$	DNA length
$\mathbf{L_{pore}}$	length of cylindrical nanopore
M	molar
MD	molecular dynamics
MspA	Mycobacterium smegmatis porin A
$\mathbf{N}$	number of base pair
$\mathbf{N_{ads}}$	number of surface adsorbed bp
$\mathbf{N_{mt}}$	number of monomers
$\mathbf{Np}$	total number of monomers
$\boldsymbol{\eta_d}$	dynamic viscosity
$\boldsymbol{\eta_o}$	viscosity
$\mathbf{n}$	number of experiments
$\mathbf{n_{fe}}$	total number of folded events
$\mathbf{n_{le}}$	total number of linear events
$\mathbf{n_t}$	total number of events
nt	nucleotide(s)
MTB	Mycobacterium tuberculosis
$\mathbf{p}$	scaling factor ($\tau \propto (L_{DNA})^p$)
PAGE	polyacrylamide gel electrophoresis
PCR	polymerase chain reaction
POPC	1-palmitoyl-2-oleoyl-sn-glycero-3-phosphocholine
POPC/ 10-DPPE-GA	POPC doped with 10 mol% DPPE-GA
POPC/ 10-DPPE-GA/ ssDNA	POPC doped with 10 mol% DPPE-GA decorated with ssDNA
$\mathbf{q_{lDNA*}}$	effective DNA surface charge per unit length
$\mathbf{r}$	rectification ratio

r_c	capture radius
R_{diff}	diffusion-limited capture rate
r_g	radius of gyration
ref.	reference
rt	room temperature
RMS	root mean square
s	second(s)
SEM	scanning electron microscopy
SLB	supported lipid bilayer
SNR	signal-to-noise ratio
ssDNA	single-stranded DNA
TAE	40 mM tris (pH 7.6), 20 mM acetic acid, 1 mM EDTA
TBE	89 mM tris (pH 7.6), 89 mM boric acid, 2 mM
TB	tuberculosis
UV-Vis	ultraviolet-visible
V	volt(s)
v	translocation speed
V_{bias}	applied potential

Thesis Outline

This PhD thesis is divided into six chapters and describes the main research carried out. Nanopipettes, a subclass of solid-state nanopores were employed for single-molecule detection of DNA. In particular, the research undertaken was aimed at addressing two main challenges in the nanopore sensing field:

i) Ultrafast translocation of DNA and

ii) Identifying the molecular identity of DNA

Chapter 1 provides a brief introduction to the different types of nanopore sensing platforms and an overview of the relevant theory for resistive pulse sensing in solid-state nanopores.

The materials and methods used throughout the experiments presented in this thesis are described in **Chapter 2**.

Chapter 3 describes the investigation of the dwell time (τ) of dsDNA in nanopipettes as a function of DNA length in 1 M KCl electrolyte using a high-bandwidth and custom-built amplifier. Results in this chapter together with an analytical model suggested that DNA-surface interactions prior to translocation may play an important role in the translocation process. Initial experiments using surface modified nanopipettes to probe DNA-surface interactions are also detailed.

Chapter 4 presents experiments where short (<4 kbp) DNA was detected using nanopipettes. Double-stranded (ds) DNA that was 200 base pairs (bp) in length was detected in 1 M KCl. On the other hand, 2 or 4 M LiCl was necessary for the detection of 100 bp dsDNA. Detecting these short DNA fragments may have applications in disease diagnostics.

In **Chapter 5**, the design considerations for coating nanopipettes with a mobile lipid bilayer are outlined. In addition, a brief introduction to lipid molecules and their properties is given. Nanopipettes were coated with modified lipid bilayers in an attempt to identify the sequence of a 100 nt long ssDNA by complementary base pairing. Results from this chapter tentatively suggest the in-situ detection of DNA hybridisation using a lipid bilayer coated nanopipette.

Chapter 6 concludes this thesis by summarising the achievements of this thesis and by providing a brief outline of possible future work.

Chapter 1

Introduction

Synopsis: This chapter begins with a brief history of the origins of nanopore biosensors. Some of the key differences between biological and solid-state nanopore sensors are then highlighted and finally, key translocation principles governing resistive-pulse sensing in solid-state nanopores are introduced.

1.1 Single-molecule Detection Using Nanopore Sensors

Nanopore sensors have emerged as a single-molecule and often label-free detection method for biological (and non-biological) molecules such as DNA, RNA and proteins. Single-molecule detection can identify subtle differences between molecules which would otherwise appear identical when using bulk techniques that rely on ensemble averaging of results.[1]

The inception of nanopore sensors was inspired by the Coulter-counter and ion pores within membranes.[2,3] The holy grail of single-molecule and label-free DNA sequencing using nanopore sensors holds great promise for next-generation sequencing with much progress being made. In 2014 Oxford Nanopore Technologies Limited were the first company to commercialise a nanopore-based sequencing device, called MinION, for research purposes.[4,5] However, high DNA sequencing error rates have been reported using the MinION device,[6,7] which have partly limited the use of these devices as a portable nanopore biosensor for point-of-care diagnostics.[8]

The Coulter-counter was patented by Wallace H. Coulter in 1953 as a “means for counting particles suspended in a fluid”.[9] Originally told “You can’t patent a hole”, Coulter’s invention proved to be revolutionary in the field of haematology.[10] The Coulter Counter consists of a micrometre-sized aperture in an insulating membrane which separates two electrolyte-filled chambers, each containing an electrode. Passage of particles through the aperture, displaces electrolyte causing a decrease in conductivity and hence the so-called ‘resistive-pulse sensing’ term. The magnitude and frequency of these resistive current pulses provides information on the size and number of particles respectively.[2]

The cell membrane as well as the membrane of intracellular organelles contains ion channels that can actively or passively control the transport of ions and molecules across the membrane.[11] These ion channels are made up of multiple protein subunits and serve a diverse range of roles.[12,13] For example, voltage-gated Na^+, K^+ and Ca^{2+} channels are responsible for the generation of action potentials in neurons.[14] On the other hand, transport between the nucleus of a cell and the cytoplasm is through nuclear pores where for example, histones are imported from the cytoplasm to the nucleus whereas RNA is exported from the nucleus to the cytoplasm.[15]

In 1976, Neher and Sakmann reported for the first time on single-channel current recordings using the patch-clamp method.[16] Just over a decade later, a group of scientists rationalised that ion current measurements such as those described by Neher and Sakmann could be used to detect DNA molecules passing through a pore and thereby changing the current flow.[5,17]

This led to the emergence of two parallel nanopore sensing fields using biological nanopores and solid-state nanopores. In both cases a (bio-) molecule is typically electrophoretically driven through a nanometre-sized pore which separates two electrolyte-filled chambers. In the following sub-sections more details about nanopore sensing platforms, their properties and applications are described.

1.2 Biological Nanopores

Inspired by the Coulter counter, Bezrukov et al. in 1994 were the first to demonstrate that an ion pore embedded in a lipid bilayer could be used for single-molecule detection of polymers via resistive pulse sensing.[18] Then in 1996 Kasianowicz et al. extended this work to include the detection of DNA and RNA through the pore α-hemolysin (α-HL) reconstituted in a lipid bilayer.[19] The protein is secreted by the bacteria *Staphylococcus auereus* and forms pores in the membranes of red blood cells leading to cell death.[2,20,21]

The structure of α-HL is shown in Figure 1.1.[2] This toxic heptameric protein is mushroom-shaped and consists of a cap and a β-barrel that are connected via an inner constriction.[2,20,22] The external dimensions of the pore are 10 × 10 nm, while the inner diameter of the channel varies between 2.9 nm at the cis entrance, 4.1 nm in the vestibule of the cap and 2 nm at the trans entrance. The narrowest point of the pore is at the inner constriction where the diameter is 1.4 nm.[2,20]

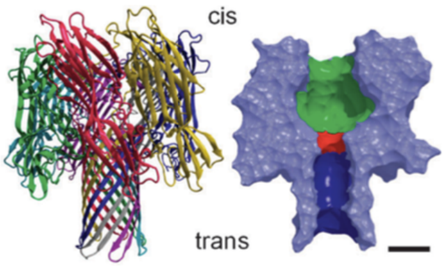

Figure 1.1. Ribbon representation of the heptameric pore α-hemolysin (left panel) and a cross-sectional view (right panel), showing the inner cavity of the vestibule (green), inner constriction (red) and the β-barrel (blue). Scale bar represents 2 nm. Figure reprinted with permission from ref. 2.

The α-HL pore is one of the most popular biological nanopores used as it has a number of attractive properties. The pore is robust being stable over a wide range of pH (2 – 12) and temperatures (up to 94 °C) and has no intrinsic ability to specifically bind analytes.[22,23]

Additionally, as the narrowest constriction of α-HL is 1.4 nm only single-stranded (ss) DNA can be detected with this pore.[19,22] Double-stranded (ds) DNA cannot be detected with this pore as it has a diameter of 2.2 nm.[22,24–26]

Another popular biological nanopore is the funnel-shaped *Mycobacterium smegmatis porin A* (MspA) which at its narrowest point is 1.2 nm in diameter.[5,22] One of its most attractive qualities compared to α-HL is its improved spatial resolution for sequencing due to its shorter sensing region. As shown schematically in Figure 1.2, the sensing region of MspA is 0.6 nm compared to 5 nm for α-HL. However, a disadvantage of MspA is that the wild-type form contains negatively charged residues which make translocation of negatively charged DNA unfavourable due to electrostatic interactions, which inhibit entry of the ssDNA into the pore.[5,27] Therefore, mutant forms of MspA where the negatively charged residues are mutated to neutral or positively charged residues are required.

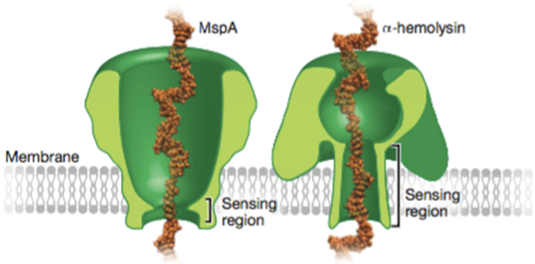

Figure 1.2. Schematic comparison of MspA (left) and α-HL (right). The sensing region of MspA is much shorter than α-HL. Figure reprinted with permission from ref. 5.

While α-HL and MspA are limited to the detection of ssDNA, the phi29 DNA packaging motor constitutes a channel varying in diameter from 3.6 – 6 nm.[22,28] This has allowed the detection of dsDNA.

Overall, biological nanopores share several favourable qualities such as reproducible pore size and shape while site-specific mutations can be used to introduce specificity for an analyte of interest.[2,3,22] However, there are also a number of challenges associated with biological nanopores. For example, the insertion of the pores into lipid bilayers is not always well controlled while the lipid bilayer itself is fragile and can rupture. Ideally the bilayer should be stable enough to allow for hours-long recordings.[2,22]

1.3 Solid-state Nanopores

Solid-state nanopores offer some advantages over biological nanopores such as tunable pore sizes, stability and robustness.[3,22] The ability to produce pore sizes of the desired diameter is particularly important as optimum single-molecule detection is achieved when the diameter of the nanopore is only slightly larger than the molecule of interest.[3] In addition, compared to biological nanopores, solid-state nanopores are more amenable to integration with microfluidic devices or fluorescence-based methods.[1,29]

Chip-based solid-state nanopores have been used to detect a range of analyte molecules including (but by no means limited to); ssDNA,[30] dsDNA,[31,32] proteins[33,34] and DNA-protein complexes.[35,36] In 2001 Li et al. were the first to show the detection of 500 base pair (bp) dsDNA fragments through solid-state nanopores.[37] In their method a focused Ar^+ ion beam was used to ion-sculpt pores with diameters as small as 1.8 nm in Si_3N_4 membranes. Since their report on solid-state nanopores, other materials have been used to fabricate solid-state nanopores including silicon oxide,[38] aluminum oxide (Al_2O_3),[39] molybdenum disulphide (MoS_2),[40,41] graphene and boron nitride.[42–44] Achieving single nucleotide (nt) resolution requires the membrane to be of a comparable thickness to a single nt (0.34 nm for dsDNA).[26,45,46] To this end, two-dimensional (2D) materials such as graphene, MoS_2 and boron nitride have attracted considerable interest (*vide infra*).[26]

Recently, MoS_2 nanopores have shown great promise for DNA sequencing. MoS_2 nanopores in combination with a viscosity gradient were used to distinguish between the four different DNA nt.[40,41] The membrane in these experiments was used to separate a compartment containing an ionic liquid and another containing 2M KCl electrolyte, thus producing a viscosity gradient which slowed down the translocation of λ-DNA (48.5 kbp) by two orders of magnitude relative to 2 M KCl.

1.4 Translocation principles

1.4.1 Electrophoresis in Nanopores

Figure 1.3, shows a representative chip-based, solid-state nanopore. An electrically insulating membrane separates a nanopore cell into two electrolyte-filled compartments. A nanometre-sized pore in this membrane forms the sole connection between these two compartments, each containing an electrode. When an electric field is applied between the electrodes, the transport of ions, solvent and analyte molecules across the nanopore occurs.

In such a nanopore system, the total electric field at a given point in the cell and at a given applied potential (V_{bias}) is made up of local electrostatics and a current-induced field.[47] However, the former only becomes important in close proximity to the charged walls of the nanopore (see section 1.4.2). Therefore, upon applying an electric field, the translocation of charged molecules, such as DNA through the nanopore is current-induced. The potential drop (Φ) in the nanopore cell can occur at i) the electrode/ solution interface ($\Delta\Phi_{electr}$), ii) across the electrolyte solution ($\Delta\Phi_{sol}$) and iii) across the nanopore($\Delta\Phi_{pore}$).

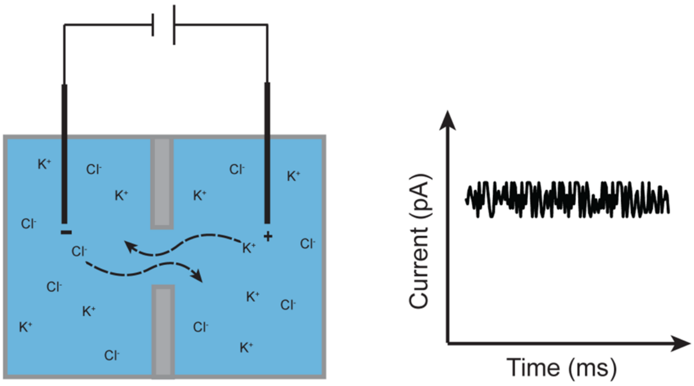

Figure 1.3. Schematic representation of chip-based nanopore set-up (left) and representative baseline I(t) trace in the absence of translocating molecules (right). The nanopore membrane separates two electrolyte-filled chambers. Each chamber contains an electrode.

Typically silver/silver chloride (Ag/AgCl) electrodes are used for nanopore experiments.[3] These are popular with the nanopore community as when immersed in an electrolyte solution containing Cl^- ions they are usually considered to be non-polarisable and Faradaic electrodes. Therefore, the $\Delta\Phi_{electr}$ at the electrode/solution interface is effectively zero.

Upon application of an electrochemical potential difference across the nanopore, at the positively charged anode, Ag is oxidised (equation (**1.1**). Ag reacts with Cl^- ions to form AgCl and an electron (e^-), which flows to the cathode via the measurement electronics.[48] At the negatively charged cathode, AgCl is reduced using an e^- from the measurement electronics while Cl^- ions are regenerated (equation (**1.2**)). The electrochemical potential difference between the two Ag/AgCl electrodes drives the redox reactions at the cathode and anode which in turn cause the flow of K^+ and Cl^- ions through the pore and thus establishes a baseline current (Figure 1.3, right panel). The ion mobilities of K^+ and Cl^- ions in aqueous electrolyte are closely matched therefore,[49] when an external electric field is applied, the two ions move in opposite directions at the same speed.

Anode: $Ag_{(s)} + Cl^{-}_{(aq)} \rightarrow AgCl_{(s)} + e^{-}$

(1.1)

Cathode: $AgCl_{(s)} + e^{-} \rightarrow Ag_{(s)} + Cl^{-}_{(aq)}$

(1.2)

In the case of chip-based nanopores, the nanopore is small and long compared to nanopores formed in 2D materials such as graphene. Therefore, when using chip-based nanopores, the pore resistance is significantly greater than the resistance of the bulk solution provided an electrolyte with a high solution conductivity (σ_s) is used.[49] Typically, pore resistance is in the MΩ – GΩ range. This means that most of the potential gradient occurs at the pore (or its vicinity) and that the Φ across the nanopore is approximately equal to V_{bias} when using non-polarisable electrodes as summarised by equation (1.3).[49] Therefore, if the voltage drop occurs almost entirely at the pore (and its vicinity), the local electric field inside the pore is the driving force for the electrophoretic transport of charged analytes through the pore.

$$V_{bias} = \Delta\Phi_{electr} + \Delta\Phi_{sol} + \Delta\Phi_{pore} \approx \Delta\Phi_{pore}$$

(1.3)

1.4.2 Conductance of the Nanopore

For nanopores that have a cylinder-like geometry, the conductance of the pore (G_{pore}) as a function of KCl concentration can be described by equation (1.4).[50] The two contributions to G_{pore} come from the ions in the bulk electrolyte solution and the counterions shielding the nanopore surface. The first term of equation (1.4) represents the bulk conductance of the KCl electrolyte while the second term represents the contributions of the surface charge of the nanopore.

$$G_{pore} = \frac{\pi {d_i}^2}{4\,L_{pore}}\left((\ _{k} + \ _{Cl})n_{KCl}e + \ _{K}\frac{4\sigma}{d_i}\right)$$

(1.4)

Where d_i and L_{pore} are the nanopore diameter and the length of the cylindrical nanopore respectively. σ is the surface charge density of the nanopore, e is the elementary charge and n_{KCl} is the number density of K^{+} and Cl^{-} ions. μ_K and μ_{Cl} are the electrophoretic mobilities of K^{+} and Cl^{-} ions, with values of 7.616×10^{-8} m^2/Vs and 7.909×10^{-8} m^2/Vs respectively.[50] At high KCl concentrations where $n_{KCl} \gg \sigma/d_i$ applies, the bulk conductance governs G_{pore} while in the opposite regime where $n_{KCl} \ll \sigma/d_i$ applies, then surface effects govern G_{pore}.

1.4.3 Charged Surfaces in Solution

The majority of surfaces immersed in a polar solvent carry at least some surface charge.[49] These surface charges may arise from ionisation of functional groups at the surface or protonation of surface groups. Therefore, when a surface is charged, mobile ions in solution carrying the opposite charge accumulate at the surface to compensate the charge and this is via electrostatic interactions.

An electric double layer forms at the surface/solution interface which can be described using the Gouy-Chapman model (Figure 1.4).[49] In this model, the solution side of the membrane/solution interface is composed of multiple layers. The innermost layer is immobile and consists of ions and solvent molecules that are specifically adsorbed to the charged surface. This layer is known as the Stern layer or the inner Helmholtz layer (IHL). The IHL is followed by the diffuse layer or outer Helmholtz layer (OHL). In this layer solvated ions are mobile and long-range electrostatic interactions exist between the solvated ions and the charged surface. The ions in the OHL are therefore described as being nonspecifically adsorbed. Due to thermal motion in the solution, nonspecifically adsorbed ions can be found in a region known as the diffuse double layer, the thickness of which is approximately equal to the Debye length (λ_D). This diffuse double layer extends from the OHL into the bulk solution and can be described by the Boltzmann distribution. The electrical potential of the diffuse double layer decreases exponentially away from the surface.[51]

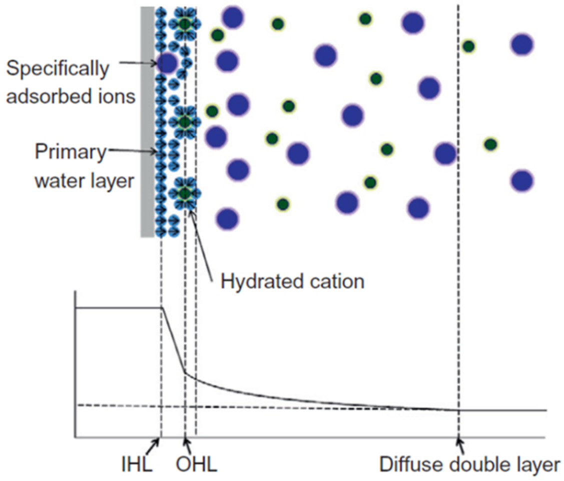

Figure 1.4. Schematic representation of a charged surface/solution interface according to the Gouy-Chapman model with the local potential distribution shown below. The electric double layer consists of the IHL and diffuse double layer. Figure adapted with permission from ref. 49.

While the Gouy-Chapman model is useful for understanding the surface/solution interface, it is only valid for low electrolyte concentrations as it makes a number of simplying assumptions. For example, it assumes that the surface charge at the molecular scale is homogenous and that charges are point ions in a continuum solvent.[52]

1.4.4 The Effect of Surface Charge in Nanopores

For nanopores with charged inner walls, the concentrations of ions at the inner walls of the pore will differ from the distribution of ions in the bulk solution where thermal motion distributes ions homogenously throughout the solution. For solid-state nanopores, where the membrane is commonly made from materials such as Si_3N_4 or SiO_2, when immersed in KCl electrolyte solution, the hydroxyl or oxide groups on the surface ionise. This creates a negative surface charge density where mobile K^+ ions in the electrolyte solution accumulate at the membrane via electrostatic interactions. Consequently, at the membrane/solution interface there is a local excess of K^+ ions and local depletion of Cl^- ions, resulting in an electric double layer which is electroneutral in the absence of an external electric field. Upon application of an external electric field, this electric double layer contributes to the current across the nanopore.[49]

In nanopore experiments, where typical KCl concentrations are between 0.1 and 1 M, the λ_D is approximately 1 and 0.3 nm, respectively.[49,51] Consequently, for nanopores with a small diameter or when using a low salt concentration, the λ_D is an important factor. In such cases the electric double layer of the nanopore walls can overlap and therefore electroneutral conditions are not maintained. If this occurs and the surface charge of the nanopore is greater than the charge of the DNA, then the DNA is unable to translocate through the nanopore.

1.4.5 Electroosmosis in Nanopores

Electroosmosis occurs when an electric field is applied parallel to the interface between the solution and charged surface, causing the motion of an electrically neutral liquid adjacent to this interface. In nanopores with charged walls, electroosmotic effects can be quite important, acting either with or against the direction of the applied electric field.

For example, in KCl electrolyte, the water molecules coordinate more strongly to K^+ ions than to Cl^- ions.[47] Assuming negatively charged nanopore walls where excess K^+ ions can be found at the surface; the result is a flow of K^+ ions which drag their solvation shells when an electric field is applied. If a negatively charged analyte such as DNA is added, the electrophoretic force will act to transport the DNA towards the anode (Figure 1.5, a). However, for negatively charged nanopore walls, electroosmosis will act in the opposite direction to the electrophoretic force and thus decrease the translocation speed of the DNA molecule. In the opposite scenario, in the case of a positively charged nanopore wall and negatively charged DNA molecule, electrophoresis and electroosmosis act in the same direction (Figure 1.5, b).

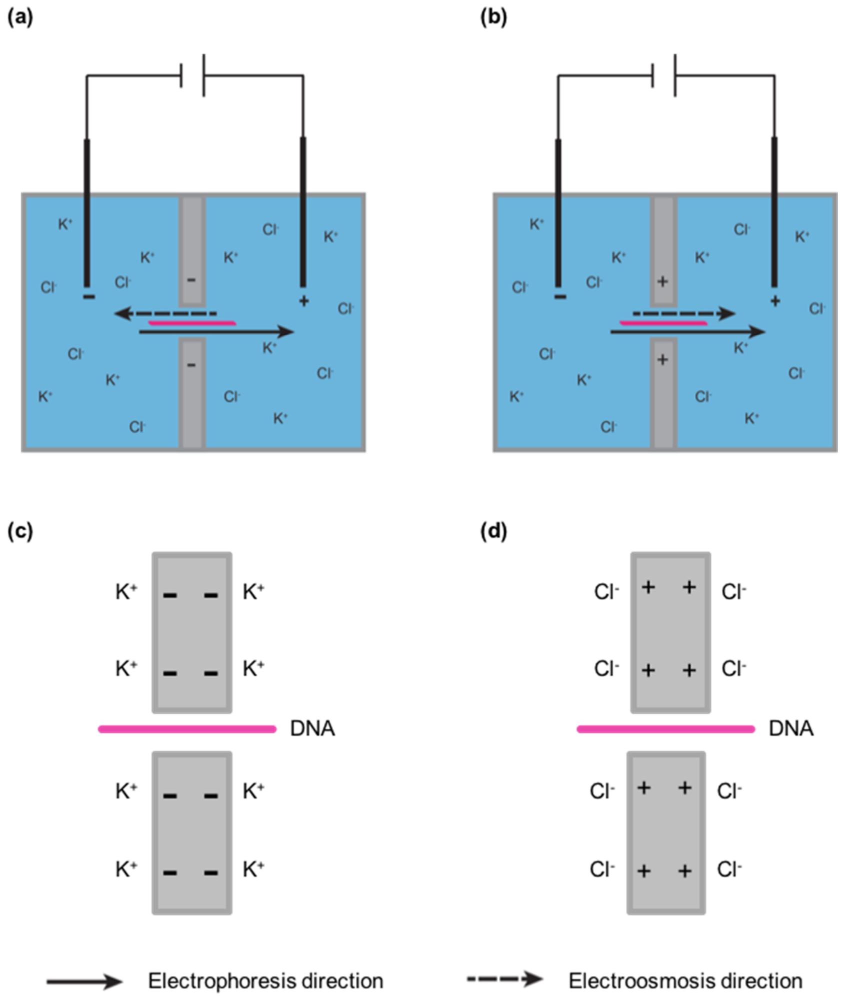

Figure 1.5. Schematic illustration of electrophoretic and electroosmotic effects for DNA translocation (pink) using nanopores that are **(a)** negatively and **(b)** positively charged. **(c)** and **(d)** show an enlarged view of the ion distribution around the nanopore surface for **(a)** and **(b)** respectively. Note: The magnitudes of the arrows are not to scale.

Electroosmostic effects can be an important parameter in nanopore sensing experiments. The magnitude of this depends on the surface properties from which the pore is made, the charge of the translocating analyte and the electrolyte solution. Electroosmotic effects have been reported to be prominent in (long, ca. > 275 nm) cylindrical shaped pores in a silicon nitride membrane.[53] The electroosmotic effects for the translocation of DNA are also less prominent than when translocating proteins. In the former case, DNA has a large fixed charge, while in the latter case, protein molecules have a lower effective charge. The charge density of proteins depends strongly on the properties of the solution, such as its pH and ionic strength and indeed the surface charge of the translocating protein and of the nanopore membrane have been found to dictate the interplay between electroosmotic and electrophoretic forces.[34] This resulted in variable translocation speeds and direction of transport through the nanopore.

1.4.6 DNA Capture Rate in Nanopores

The capture rate or frequency of DNA translocation, describes the fraction of DNA molecules that approach the nanopore and that are successful. There are a multitude of factors on which the capture rate depends, which include V_{bias}, DNA concentration, electrolyte concentration and its pH as well as the surface properties of the nanopore.[54]

The main steps involved in the successful translocation of a DNA molecule diffusing freely in the bulk electrolyte solution, far away from the surface of the nanopore are i) diffusion/ drift, ii) capture of a DNA molecule and iii) DNA translocation through the nanopore. This is shown schematically in Figure 1.6.[54–56]

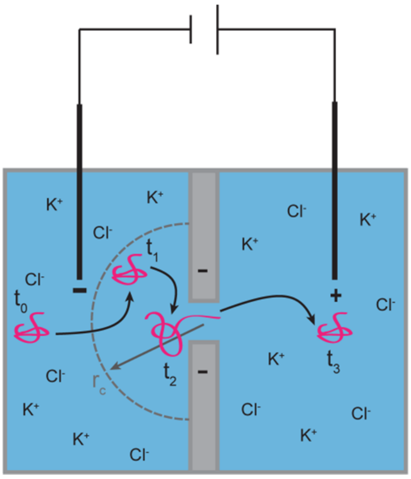

Figure 1.6. Schematic illustration of DNA capture and subsequent translocation through the nanopore when there is a potential drop, Φ across the nanopore.

Initially, at time t_0, the DNA molecule diffuses freely in the bulk electrolyte solution where at distances greater than the capture radius (r_c), the electric field is assumed to be zero.[54,55]

Once the DNA molecule is at a distance less than r_c at t_1, the motion of the DNA molecule is governed by drift. This drift is mainly due to interplay between electroosmotic and electrophoretic forces. These forces can act either to attract or repel the DNA molecules from the nanopore mouth. At t_2, the DNA molecule threads through the nanopore and this requires a conformational change from a coil in thermal equilibrium and at maximum entropy to an elongated state where one end of the DNA molecule can enter the pore. The uncoiling of the DNA strand requires overcoming a free energy barrier. Once this has been achieved, part of the DNA molecule can enter the nanopore with subsequent translocation of the rest of the DNA molecule into the opposite compartment, as shown at t_3.[54,56]

In the above model, there are three regimes for the capture and translocation of a DNA molecule; the diffusion-limited regime, the drift regime and the entropic barrier regime. The size of the pore relative to the DNA's r_g is important in determining the rate-limiting step.[57,58] When the r_g is smaller than the pore diameter, a barrier-free capture process occurs in which the capture rate is linearly related to V_{bias}.[55,57]

When the electric field is close to 0 and in the absence of an entropic barrier, the diffusion-limited regime is present at distances greater than r_c, and is defined as:[54,55]

$$r_c = \frac{d_i{}^2 \quad {}_{DNA}}{8lD} V_{bias} \tag{1.5}$$

Where μ_{DNA} the electrophoretic mobility of DNA and D is the diffusion coefficient of DNA.

In this regime, assuming that there are no interactions between the DNA molecules, the diffusion-limited capture rate (R_{diff}) is given by equation:[54,55]

$$R_{diff} = \frac{\pi d_i \quad {}_{DNA}}{4l_p} V_{bias} \tag{1.6}$$

where l_p is the length of the pore.

In such a case, the capture rate is limited by the time taken for the charged analyte to reach the pore opening and not by the final threading step. Equation (1.6) implies that, when the diffusion-limited regime dominates, the capture rate should be independent of the length of the DNA molecule. This at first may seem counterintuitive as the diffusion of a DNA molecule slows down as its length increases. However, r_c scales with D^{-1}, so that an increase in D is exactly compensated for by a decrease in r_c.

The drift-dominated regime is present at distances less than r_c, where the movement of the DNA is due to the applied V_{bias}, i.e DNA movement towards the nanopore is electrophoretic.

When the radius of gyration of the DNA molecule is larger than the pore diameter, the degrees of freedom of the DNA molecule are reduced and an entropic barrier exists for DNA translocation through the pore. Therefore, not all molecules in the proximity of the pore are immediately translocated and instead multiple threading attempts may be required.[55,59] When the entropic barrier regime dominates, the DNA molecule must first uncoil to expose a free end that can be localised at the pore mouth and second it must translocate through the pore as shown schematically in Figure 1.7.[56]

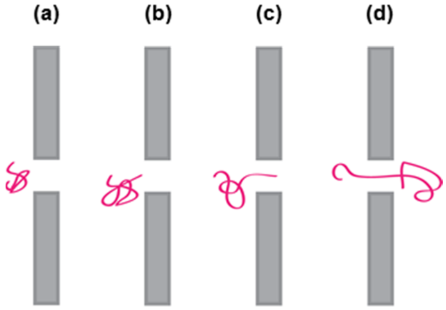

Figure 1.7. Schematic illustration of the DNA conformations in the entropic barrier regime, where **(a)** a coiled DNA molecule at the DNA mouth must uncoil to **(b)** expose a free DNA end that can **(c)** enter the pore followed by **(d)** translocation of the remainder of the DNA strand.[56]

Both of these steps have an associated free energy barrier. In the first step where the DNA molecule must partially uncoil to expose a free end, the associated free energy barrier (f_l) and is given by equation (1.7) for DNA lengths, L_{DNA} above a critical value.

$$f_l = \frac{1}{{L_{DNA}}^{\alpha}} \tag{1.7}$$

The entropic barrier, f_l scales inversely with the length of the DNA molecule, where α was found to be ≈ 0.2 ± 0.1.[56] This implies that long DNA molecules which have a looser coil in solution than shorter DNA molecules have a smaller value of f_l.[56,60]

A second energy barrier (f_t) is then associated with capturing this free DNA end and its translocation as given by equation (1.8), where the opposite trend is observed as f_t, scales linearly with the length of the DNA molecule.

$$f_t \approx L_{DNA} \tag{1.8}$$

The sum of these two entropic barriers makes up the total entropic barrier (F_{bar}) as shown in Equation (1.9).[55]

$$F_{bar} = f_l + f_t \approx \frac{1}{{L_{DNA}}^{\alpha}} + L_{DNA} \tag{1.9}$$

A complex F_{bar} relationship exists which is difficult to describe analytically. Parameters such as the pore geometry and the polymer affect F_{bar}.[54,56] However, for a nanopore embedded in a thin membrane, f_l dominates over f_t and thus $F_{bar} \approx f_l$.[56]

1.4.7 Conductance Modulation by Charged Analytes

Assuming that the Φ across the nanopore ≈ V_{bias}, then charged analytes in the proximity of the nanopore will be electrophoretically driven through the pore, provided that the nanopore diameter ≫ λ_D. In the case of negatively charged DNA molecules, these can be driven towards the anode.[34] As a DNA molecule translocates through the nanopore there is a change in the pore conductance. During this process, two competing effects are at play. On the one hand, the segment of the DNA molecule inside the nanopore excludes electrolyte volume from the nanopore and hence decreases G_{pore}. On the other hand, the segment of the negatively charged DNA molecule inside the nanopore introduces charge carriers as counterions shield the DNA backbone. This change in conductance (ΔG) upon DNA translocation through a nanopore with a cylinder-like geometry, can be approximated by equation (1.10):[50]

$$\Delta G = \frac{1}{L_{pore}}\left(-\frac{\pi}{4}{d_{DNA}}^{2}({}_{k} + {}_{Cl})n_{KCl}e + {}_{k}{}^{*}{q_{lDNA}}^{*}\right) \tag{1.10}$$

Where d_{DNA} is the diameter of the DNA molecule, ${}_{k}{}^{*}$ is the effective electrophoretic mobility of K^+ ions on the DNA surface and ${q_{lDNA}}^{*}$ is the effective DNA surface charge per unit length.

At high KCl concentrations, where the first term is greater than the second term, $\Delta G < 0$ and therefore translocation of DNA molecules through the nanopore causes current blockages. On the other hand, at low KCl concentrations, where the second term is greater than the first term, $\Delta G > 0$, the translocation of DNA molecules through the nanopore results in current enhancements. In the literature, current enhancements have been observed at KCl concentrations of ~100 mM and below using chip-based nanopores.[38,50]

Figure 1.8 schematically shows the translocation of a DNA molecule at a high salt concentration where bulk behavoiur dominates. In such a case, current blockages are observed and the resistive pulses, or events, can be analysed to extract information on the translocating molecules. Two important parameters can be extracted from translocation events; the dwell time (τ) and the peak amplitude (ΔI). These two parameters give information on the length of the translocating DNA molecule, its interactions with the pore walls and its cross-sectional area.[3,31,32,57,61]

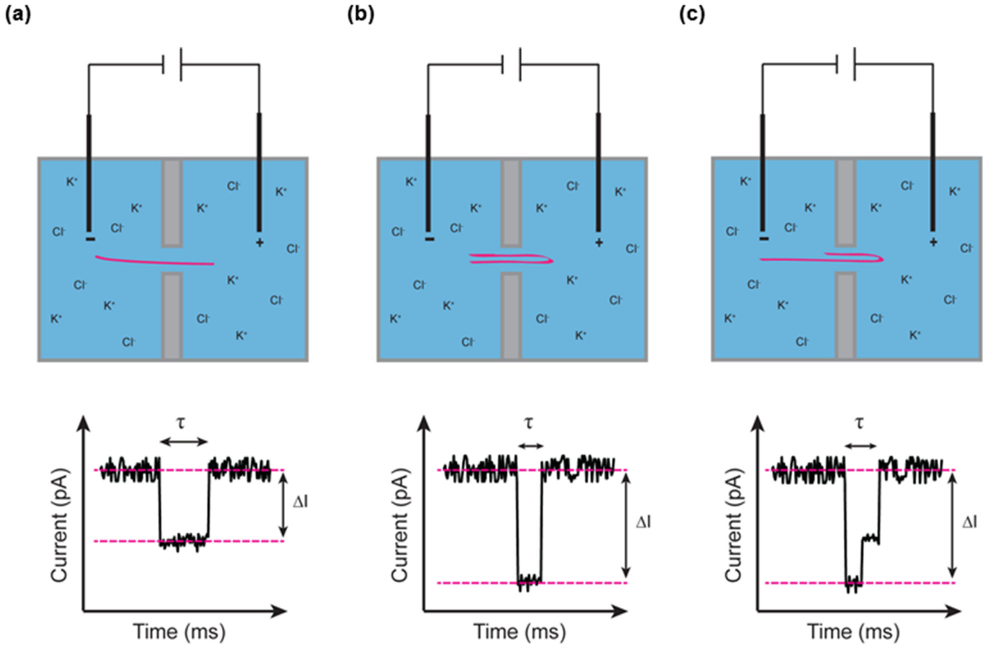

Figure 1.8. Schematic representation of a chip-based nanopore set-up when a DNA molecule translocates in a **(a)** linear, **(b)** folded and **(c)** partially folded conformation. Representative I(t) traces showing the τ and ΔI parameters of a translocation event are shown below each schematic.

When the DNA molecules translocates through the pore in a linear conformation (Figure 1.8, a), events are characterised by a longer τ and shorter ΔI than when the DNA molecules is in a (partially) folded configuration (Figure 1.8, b and c). In the latter case, two strands simultaneously enter the pore and hence double the electrolyte volume is excluded. This causes a greater change in G_{pore} and hence increases the ΔI relative to when one DNA strand occupies the pore. The ΔI can therefore be used to detect even the translocation of partially folded DNA molecules. As shown in Figure 1.8, c the event has two ΔI levels corresponding to the translocation of two DNA strands in the first part of the event and then one DNA strand in the second part of the event.

A third parameter of translocation events that can be studied is the event charge deficit (ecd) which describes the excluded charge from the nanopore during a translocation event. The ecd is defined as the integral of obstructed ionic current over the duration of a translocation event as given by:

$$\mathrm{ecd} = \int_{\mathrm{event}} \Delta \mathrm{I(t)}\, \mathrm{dt} \tag{1.11}$$

Figure 1.9 shows a schematic representation of the ecd of an event. Unlike the ΔI which is a measure of DNA folding states, the ecd gives information on the contour length of a DNA molecule and for a given DNA molecule is found to be constant.[62] This is because irrespective of DNA conformation, each DNA molecule will block equal amounts of ionic charge movement through the nanopore during the time it takes to translocate through the pore. The longer τ and smaller ΔI of linear translocation events is matched by the smaller τ and larger ΔI of folded translocation events.[62,63]

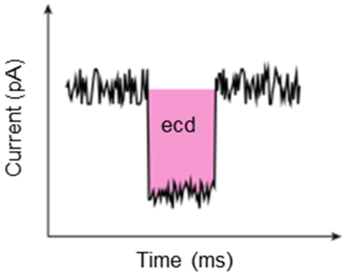

Figure 1.9. Schematic representation of the ecd of a translocation event.

1.5 Nanopipettes

Nanopipettes are a novel subclass of solid-state nanopores and in this thesis, were the only solid-state nanopore platform used. Nanopipettes have several advantages compared to classical chip-based solid-state nanopore platforms. These include; ease of fabrication outside of the cleanroom, lower fabrication cost and low device capacitance which facilitates high-bandwidth electric recording.[64–68] However, a drawback of nanopipettes is that pore diameters less than ~15 – 20 nm are difficult to achieve using laser-assisted pulling.

Nevertheless, smaller pore sizes can be achieved using surface modifications to further reduce their diameter.[66,69]

Figure 1.10 shows a schematic representation for the fabrication of nanopipettes from a quartz capillary, which is typically via a two-step programme.

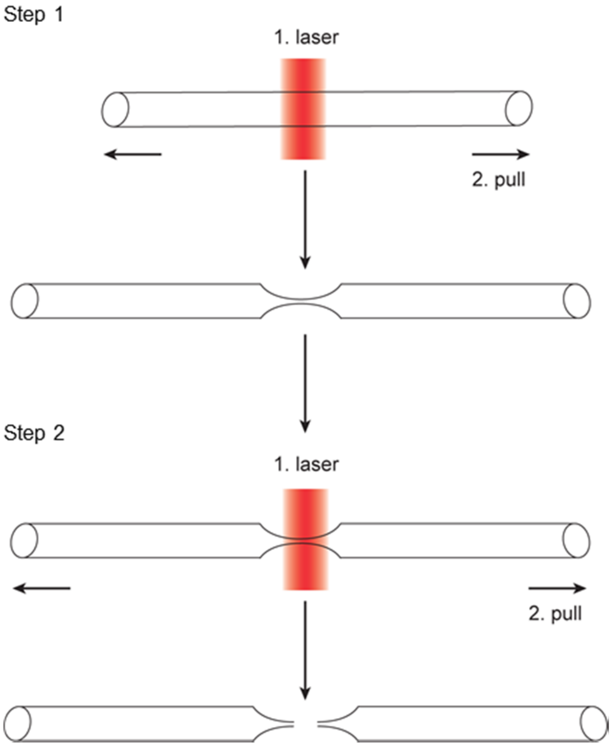

Figure 1.10. Schematic representation of nanopipette fabrication process using a laser-assisted puller. A CO_2 laser is used to heat the centre of the capillary, introducing a taper in the quartz capillary. In the second step, the laser heats the centre of the taper and a strong pull is applied in opposite direction to separate the two nanopipettes.

In the first step, the centre of a capillary is heated using a CO_2 laser to melt the glass and a pull in opposite directions applied. This introduces a taper in the capillary. In the second step, the taper region is heated and a hard pull in opposite directions is applied to pull the two nanopipettes apart. Each of the two nanopipettes has a nanometer-sized pore at the end of their taper.[70]

A typical nanopipette set-up is shown in Figure 1.11, which similar to the aforementioned nanopores, relies on resistive-pulse current sensing. Briefly, the electrolyte-filled nanopipette forms one compartment while the ‘bulk’ electrolyte solution surrounding the nanopipette forms a second compartment. The nanometre-sized pore at the tip of the nanopipette taper forms the sole connection between the two chambers. Two Ag/AgCl electrodes, one inserted inside the nanopipette and the other electrode placed in the bulk electrolyte solution are used for ionic current sensing in the same manner as with solid-state nanopores (see section 1.3 and 1.4).

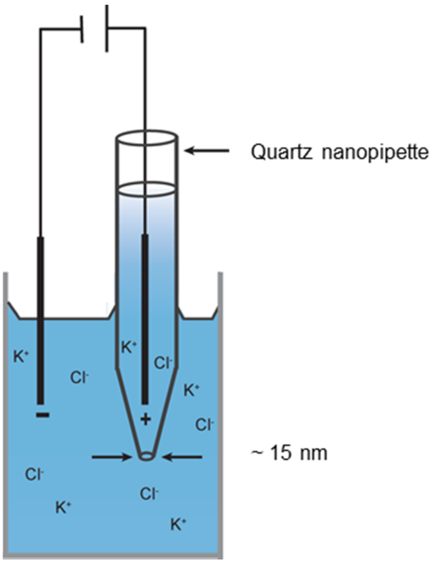

Figure 1.11. Schematic representation of a nanopipette set-up. The nanopipette separates the two electrolyte-filled chambers and each chamber contains a Ag/AgCl electrode.

Nanopipettes have been used to detect a range of analyte molecules including; ssDNA,[71] dsDNA,[64,72] proteins[68,73] and DNA-protein complexes.[74] Using an elegant DNA design Bell and Keyser,[75] were able to enrich the information available from experiments in nanopipettes. Their DNA structure contained a dsDNA backbone with a protruding zone consisting of two dumbbell structures that were separated by further dumbbell structures. The number and relative location of these acted as a ‘barcode’, so that each DNA structure now had a unique identity. Four of these unique strands were selected and functionalised, each with a different antigen, creating antibody capture probes. Simultaneous translocation of these four capture probes, then allowed the concomitant detection of four different antibodies.

1.6 Challenges and Limitations of Solid-State Nanopores

Nanopore sensors have many favourable qualities however, like all techniques there are also challenges and limitations associated with planar solid-state nanopores and nanopipettes. The speed at which the analyte translocates through the nanopore poses a significant challenge in the field.[30,76–78] In addition, resistive-pulse sensing using nanopore sensors does not give direct information on the molecular identity of the translocating species. Instead the molecular identity is inferred by comparing the different current signatures produced by different molecules.[3] There is also a need to find a technique that reproducibly fabricates nanopores to the desired dimensions (and geometry) that match the atomic precision and reproducibility of biological nanopores.[3,22]

1.7 Summary

This chapter has described some of the key differences between the two nanopore fields, namely biological pores and solid-state pores. Each of these have their advantages and disadvantages, as discussed in the relevant sections.

Moreover, some of the key theories behind the translocation of DNA molecules through a nanopore using the resistive-pulse sensing technique have been presented. These include; surface charge effects, electrophoresis and electroosmosis as well as the DNA capture rate regimes.

Recently, nanopipettes have emerged as a novel class of solid-state nanopores and the work presented in this thesis has been carried out using nanopipettes as the sole nanopore platform. Finally, this chapter highlighted the challenges and limitations of solid-state pores.

1.8 References

(1) Gibb, T. R.; Ivanov, A. P.; Edel, J. B.; Albrecht, T. *Anal. Chem.* **2014**, *86*, 1864–1871.

(2) Howorka, S.; Siwy, Z. *Chem. Soc. Rev.* **2009**, *38* (8), 2360–2384.

(3) Wanunu, M. *Phys. Life Rev.* **2012**, *9*, 125–158.

(4) https://nanoporetech.com. Accessed on 1/11/2016.

(5) Deamer, D.; Akeson, M.; Branton, D. *Nat. Biotechnol.* **2016**, *34* (5), 518–524.

(6) Feng, Y.; Zhang, Y.; Ying, C.; Wang, D.; Du, C. *Genomics, Proteomics Bioinforma.* **2015**, *13* (1), 4–16.

(7) Mikheyev, A. S.; Tin, M. M. Y. *Mol. Ecol. Resour.* **2014**, *14* (6), 1097–1102.

(8) Kilianski, A.; Haas, J. L.; Corriveau, E. J.; Liem, A. T.; Willis, K. L.; Kadavy, D. R.; Rosenzweig, C. N.; Minot, S. S. *Lancet Infect. Dis.* **2015**, *14* (11), 1123–1135.

(9) Coulter, W. H. Means for counting particles suspended in a fluid, 1953.

(10) Graham, M. D. *JALA - J. Assoc. Lab. Autom.* **2003**, *8* (6), 72–81.

(11) Dekker, C. *Nat. Nanotechnol.* **2007**, *2* (4), 209–216.

(12) Green, W. N.; Millar, N. S. *Trends Neurosci.* **1995**, *18* (6), 280–287.

(13) Bahrami, A.; Dogan, F.; Japrung, D.; Albrecht, T. *Biochem. Soc. Trans.* **2012**, *40* (4), 624–628.

(14) Catterall, A. W. *Annu. Rev. Biochem.* **1995**, *64* (1), 493–531.

(15) Dirk, G.; Kutay, U. *Annu. Rev. Cell Dev. Biol.* **1999**, *15*, 607–660.

(16) Neher, E.; Sakmann, B. *Nature* **1976**, *260* (5554), 799–802.

(17) Pennisi, E. *Science (80-.).* **2012**, *336* (6081), 534–537.

(18) Bezrukov, S. M.; Vodyanoy, I.; Parsegia, V. A. *Nature* **1994**, *370* (6487), 279–281.

(19) Kasianowicz, J. J.; Brandin, E.; Branton, D.; Deamer, D. W. *Proc. Natl. Acad. Sci. U. S. A.* **1996**, *93* (24), 13770–13773.

(20) Song, L.; Hobaugh, M. R.; Shustak, C.; Cheley, S.; Bayley, H.; Gouaux, J. E. *Science* **1996**, *274* (5294), 1859–1866.

(21) Bhakdil, S. *Microbiol. Rev.* **1991**, *55* (4), 733–751.

(22) Haque, F.; Li, J.; Wu, H.-C.; Liang, X.-J.; Guo, P. *Nano Today* **2014**, *8* (1), 56–74.

(23) Kang, X.; Gu, L.-Q.; Cheley, S.; Bayley, H. *Angew. Chemie* **2005**, *117* (10), 1519–1523.

(24) Anderson, B. N.; Muthukumar, M.; Meller, A. *ACS Nano* **2013**, *7* (2), 1408–1414.

(25) Wanunu, M.; Sutin, J.; McNally, B.; Chow, A.; Meller, A. *Biophys. J.* **2008**, *95* (10), 4716–4725.

(26) Li, J.; Yu, D.; Zhao, Q. *Microchim. Acta* **2016**, *183* (3), 941–953.

(27) Butler, T. Z.; Pavlenok, M.; Derrington, I. M.; Niederweis, M.; Gundlach, J. H. *Proc. Natl. Acad. Sci. U. S. A.* **2008**, *105* (52), 20647–20652.

(28) Wendell, D.; Jing, P.; Geng, J.; Subramaniam, V.; Lee, T. J.; Montemagno, C.; Guo, P. *Nat. Nanotechnol.* **2009**, *4* (11), 765–772.

(29) Pitchford, W. H.; Kim, H.; Ivanov, A. P.; Kim, H.; Yu, J.; Leatherbarrow, R. J.; Albrecht, T.; Kim, K.; Edel, J. B. *ACS Nano* **2015**, *9* (2), 1740–1748.

(30) Akahori, R.; Haga, T.; Hatano, T.; Yanagi, I.; Ohura, T.; Hamamura, H.; Iwasaki, T.; Yokoi, T.; Anazawa, T. *Nanotechnology* **2014**, *25* (27), 275501.

(31) Storm, a. J.; Chen, J. H.; Zandbergen, H. W.; Dekker, C. *Phys. Rev. E - Stat. Nonlinear, Soft Matter Phys.* **2005**, *71* (5), 1–10.

(32) Fologea, D.; Brandin, E.; Uplinger, J.; Branton, D.; Li, J. *Electrophoresis* **2007**, *28* (18), 3186–3192.

(33) Larkin, J.; Henley, R. Y.; Muthukumar, M.; Rosenstein, J. K.; Wanunu, M. *Biophys. J.* **2014**, *106* (3), 696–704.

(34) Firnkes, M.; Pedone, D.; Knezevic, J.; Döblinger, M.; Rant, U. *Nano Lett.* **2010**, *10*, 2162–2167.

(35) Nuttall, P.; Lee, K.; Ciccarella, P.; Carminati, M.; Ferrari, G.; Kim, K.; Albrecht, T. *J. Phys. Chem. B* **2016**, *120* (9), 2106–2114.

(36) Japrung, D.; Bahrami, A.; Nadzeyka, A.; Peto, L.; Bauerdick, S.; Edel, J. B.; Albrecht, T. *J. Phys. Chem. B* **2014**, *118* (40), 11605–11612.

(37) Li, J.; Stein, D.; McMullan, C.; Branton, D.; Aziz, M. J.; Golovchenko, J. a. *Nature* **2001**, *412* (6843), 166–169.

(38) Chang, H.; Kosari, F.; Andreadakis, G.; Alam, M. A.; Vasmatzis, G.; Bashir, R. *Nano Lett.* **2004**, *4* (8), 1551–1556.

(39) Venkatesan, B. M.; Shah, A. B.; Zuo, J. M.; Bashir, R. *Adv. Funct. Mater.* **2010**, *20* (8), 1266–1275.

(40) Feng, J.; Liu, K.; Bulushev, R. D.; Khlybov, S.; Dumcenco, D.; Kis, A.; Radenovic, A. *Nat. Nanotechnol.* **2015**, *10* (12), 1070–1076.

(41) Liu, K.; Feng, J.; Kis, A.; Radenovic, A. *ACS Nano* **2014**, *8* (3), 2504–2511.

(42) Schneider, G. F.; Kowalczyk, S. W.; Calado, V. E.; Pandraud, G.; Zandbergen, H. W.; Vandersypen, L. M. K.; Dekker, C. *Nano Lett.* **2010**, *10* (8), 3163–3167.

(43) Zhou, Z.; Hu, Y.; Wang, H.; Xu, Z.; Wang, W.; Bai, X.; Shan, X.; Lu, X. *Sci. ReportsScientific reports* **2013**, *3*, 3287.

(44) Liu, S.; Lu, B.; Zhao, Q.; Li, J.; Gao, T.; Chen, Y.; Zhang, Y.; Liu, Z.; Fan, Z.; Yang, F.; You, L.; Yu, D. *Adv. Mater.* **2013**, *25* (33), 4549–4554.

(45) Grosberg, A. Y.; Rabin, Y. *J. Chem. Phys.* **2010**, *133* (16), Article Number: 165102.

(46) Storm, A. J.; Storm, C.; Chen, J.; Zandbergen, H.; Joanny, J. F.; Dekker, C. *Nano Lett.* **2005**, *5* (7), 1193–1197.

(47) Albrecht, T.; Carminati, M.; Ferrari, G.; Nuttall, P.; Pitchford, W.; Rutkowska, A. J. *Electrochemistry: Nanosystems Electrochemistry*; Jay D., W., G. Compton, R., Eds.; RSC Publishing, 2014.

(48) Tabart-Cossa, V. *Engineered Nanopores for Bioanalytical Applications*; Edel, J. B., Albrecht, T., Eds.; Elsevier, 2013.

(49) Edel, J.; Albrecht, T. *Engineered Nanopores for Bioanalytical Applications*; Elsevier, 2013.

(50) Smeets, R. M. M.; Keyser, U. F.; Krapf, D.; Wu, M.; Dekker, N. H.; Dekker, C. *Nano Lett.* **2006**.

(51) Bard, A. J.; Faulkner, L. R. *ELECTROCHEMICAL METHODS Fundamentals and Applications*; 2001.

(52) Torrie, G. M.; Valleau, J. P. *J. Phys. Chem.* **1982**, *86* (16), 3251–3257.

(53) Yusko, E. C.; An, R.; Mayer, M. *ACS Nano* **2010**, *4* (1), 477–487.

(54) Otto, O.; Keyser, U. F. *Engineered Nanopores for Bioanalytical Applications*; Edel, J. B., Albrecht, T., Eds.; Elsevier, 2013.

(55) Wanunu, M.; Morrison, W.; Rabin, Y.; Grosberg, A. Y.; Meller, A. *Nat. Nanotechnol.*

2010, *5* (2), 160–165.

(56) Muthukumar, M. *J. Chem. Phys.* **2010**, *132* (19), 1–10.

(57) Liu, Q.; Wu, H.; Wu, L.; Xie, X.; Kong, J.; Ye, X.; Liu, L. *PLoS One* **2012**, *7* (9), e46014.

(58) Salieb-Beugelaar, G.; Dorfman, K. D.; Berg, A. Van Den; Eijkel, J. C. T. *Lab Chip* **2009**, *9* (17), 2508–2523.

(59) Muthukumar, M. *Annu. Rev. Biophys. Biomol. Struct.* **2007**, *36*, 435–450.

(60) He, Y.; Tsutsui, M.; Taniguchi, M.; Kawai, T. *J. Mater. Chem.* **2012**, *22* (27), 13423–13427.

(61) Li, J.; Gershow, M.; Stein, D.; Brandin, E.; Golovchenko, J. A. *Nat. Mater.* **2003**, *2* (9), 611–615.

(62) Fologea, D.; Brandin, E.; Uplinger, J.; Branton, D.; Li, J. *Electrophoresis* **2007**, *28*, 3186–3192.

(63) Garaj, S.; Hubbard, W.; Reina, A.; Kong, J.; Branton, D.; Golovchenko, J. A. *Nature* **2010**, *467* (7312), 190–193.

(64) Fraccari, R. L.; Ciccarella, P.; Bahrami, A.; Carminati, M.; Ferrari, G.; Albrecht, T. *Nanoscale* **2016**, *8* (14), 1–20.

(65) Fraccari, R. L.; Carminati, M.; Piantanida, G.; Leontidou, T.; Ferrari, G.; Albrecht, T. *Faraday Discuss.* **2016**, 1–15.

(66) Sze, J. Y. Y.; Kumar, S.; Ivanov, A. P.; Oh, S.; Edel, J. B. *Analyst* **2015**, *140*, 4828–4834.

(67) Hernández-Ainsa, S.; Muus, C.; Bell, N. a W.; Steinbock, L. J.; Thacker, V. V; Keyser, U. F. *Analyst* **2013**, *138* (1), 104–106.

(68) L. J. Steinbock, S. Krishnan, R. D. Bulushev, L. Fellety, a R. *in Prepration* **2014**, 14380–14387.

(69) Steinbock, L. J.; Steinbock, J. F.; Radenovic, A. *Nano Lett.* **2013**, *13* (4), 1717–1723.

(70) Gong, X.; Patil, A. V; Ivanov, A. P.; Kong, Q.; Gibb, T.; Dogan, F.; deMello, A. J.; Edel, J. B. *Anal. Chem.* **2014**, *86*, 835–841.

(71) Ying, L.; Bruckbauer, A.; Rothery, A. M.; Korchev, Y. E.; Klenerman, D. *Anal. Chem.* **2002**, *74* (6), 1380–1385.

(72) Steinbock, L. J.; Otto, O.; Chimerel, C.; Gornall, J.; Keyser, U. F. *Nano Lett.* **2010**, *10* (7), 2493–2497.

(73) Li, W.; Bell, N. a W.; Hernández-Ainsa, S.; Thacker, V. V.; Thackray, A. M.; Bujdoso, R.; Keyser, U. F. *ACS Nano* **2013**, *7* (5), 4129–4134.

(74) Bell, N. A. W.; Keyser, U. F. *J. Am. Chem. Soc.* **2015**, *137* (5), 2035–2041.

(75) Bell, N. A. W.; Keyser, U. F. *Nat. Nanotechnol.* **2016**, No. April.

(76) Bell, N. A. W.; Muthukumar, M.; Keyser, U. F. *Phys. Rev.* **2016**, *93* (2), 1–10.

(77) Venkatesan, B. M.; Bashir, R. *Nat. Nanotechnol.* **2001**, *6* (10), 615–624.

(78) Fologea, D.; Uplinger, J.; Thomas, B.; Mcnabb, D. S.; Li, J. *Nano Lett.* **2005**, *5* (9), 1734–1737.

Chapter 2

Materials and Methods

Synopsis: This chapter outlines the materials and methods used for the experiments presented in this thesis.

The methods have been split into four main sections. Firstly, the fabrication of quartz nanopipettes, cell set-up and the required electrical instrumentation for current measurements are described. The preparation of DNA samples is then presented followed by the materials and methods used to achieve silanization of nanopipettes. Finally, the preparation of unilamellar vesicles, their characterisation and rupture onto nanopipettes to form a supported lipid bilayer are discussed.

2.1 Nanopore Set-up

2.1.1 Nanopipette Fabrication

Nanopipettes were made from filamented quartz capillaries which had an outer diameter of 1 mm, an inner diameter of 0.5 mm and length of 7.5 cm (Sutter Instruments, Novato, USA). The filament refers to the ~160 μm rod of glass annealed to the internal wall of the capillaries which helps to fill the nanopipettes with electrolyte solution by capillary action.[1]

The capillaries were plasma cleaned for 5 – 10 minutes prior to being pulled using a laser pipette puller (P2000, Sutter Instruments®, Novato, USA). Quartz capillaries were loaded onto the pipette puller by placing the capillary in the grooves of the puller bar and tightening the clamping knobs. The nanopipettes were pulled using one of two programmes. Both programmes use two steps, the parameters for which are shown in Table 2.1. The first cycle pulls a taper in the region where the quartz capillary is heated while in the second cycle the quartz is heated further and pulled to form the two nanopipettes.[2] It should be noted that pulling programmes are highly instrument specific and sensitive to very small changes in the optical pathway of the carbon dioxide (CO_2) laser that may arise during routine cleaning of the instrument's mirror as well as changes in the temperature and humidity of the room.[3–5] Pulling conditions were chosen on the basis of which gave the most reproducible pore size. The pore size of each nanopipette was estimated from the pore conductance, which was estimated using cyclic voltammetry (CV) measurements (see chapter 3).

Each programme had five parameters that could be adjusted; heat, filament, velocity, delay and pull.[6] 'Heat' determines the power of the laser and hence the amount of energy supplied to the quartz while the 'filament' parameter determines the longitudinal length of the quartz capillary that is heated by the laser. The 'velocity' parameter specifies the velocity at which the quartz capillary is extended prior to the hard pull; 'delay' specifies the onset time between the laser being switched off and the execution of the hard pull and finally the 'pull' parameter determines the force of the hard pull.

Table 2.1. Laser-assisted pipette puller parameters for the two programs used to pull nanopipettes.

Program number	**Step 1**					**Step 2**				
	Heat	**Filament**	**Velocity**	**Delay**	**Pull**	**Heat**	**Filament**	**Velocity**	**Delay**	**Pull**
57	575	3	35	145	75	900	0	15	128	200
99	700	5	35	150	75	700	0	15	128	200

2.1.2 Imaging of Fabricated Nanopipettes

Scanning electron microscopy (SEM) images were acquired by Dr Thomas Gibb, a former PhD candidate in the Albrecht group. Optical imaging was performed by Thomas Mickleburgh, a PhD candidate in the Klug group, Imperial College London.

SEM was performed on a Leo Gemini 1525 field emission gun SEM (Carl Zeiss AG, Germany) while optical images were acquired using a Nikon TI-E (Nikon, Japan) microscope, 10 x magnifications and with a numerical aperture (NA) of 0.25.

2.1.3 Silver/ Silver Chloride Electrode Preparation

For all experiments, as is common with nanopore experiments, silver/silver chloride (Ag/AgCl) electrodes were used as these are non-polarisable. This means that the potential difference that occurs at the interface between the electrode surface and the electrolyte is negligible.[7] A silver (Ag) wire (10 cm in length, 0.25 mm diameter, Goodfellow Cambridge Ltd, Cambridgeshire, UK) was cleaned by immersion in 50% nitric acid (HNO_3, VWR International, Pennsylvania, USA) for 30 s to remove its oxide layer from the surface. The cleaned Ag wire was electroplated in 1 M potassium chloride (KCl, VWR International) using chronopotentiometry with a current of 0.5 mA for 15 min and an Ag wire as the reference electrode at room temperature (rt) on a Reference 600 potentiostat (Gamry Instruments, Warminster, USA). The redox reactions for the electroplating are shown in equations 2.1 and 2.2.

$$\text{Anode: } Ag_{(s)} + Cl^{-}_{(aq)} \rightleftharpoons AgCl_{(s)} + e^{-} \qquad (2.1)$$

$$\text{Cathode: } 2H^{+}_{(aq)} + 2e^{-} \rightleftharpoons H_{2(g)} \qquad (2.2)$$

All Ag/AgCl electrodes were either used the same day or stored at rt and used within one week. Before use, the Ag/AgCl electrodes were soldered to gold pins to allow connection with either the potentiostat or nanopore set-up.

2.1.4 Electrolyte Solutions

For nanopore experiments electrolyte solutions of either 1 M KCl, 2 or 4 M lithium chloride (LiCl, Fisher Scientific Ltd, Hampshire, UK), each with 10 mM tris-hydrochloride (tris-HCl, Amresco®, Ohio, USA) were used. The desired KCl or LiCl and tris-HCl were dissolved in deionised (DI) ultrapure water (H_2O) and their pH measured (S20 pH meter, Mettler-Toledo International Inc., Leicester, UK) and buffered to pH 8 using 1 M potassium hydroxide (KOH, VWR International) solution. The electrolyte solutions were filtered using a 0.2 µm syringe filter (Millex syringe filter, EMD Millipore, Hertfordshire, UK) to remove large particle contamination then autoclaved for sterilisation. Electrolyte solutions were stored at 4 ± 1 °C until use. The conductivity of electrolyte solutions was measured with a conductivity meter (SG78, Mettler-Toledo Internation Inc., Leicester, UK) at rt. Conductivity measurements have an error of ± 0.5 % of the measured value.[8]

2.1.5 Nanopipette Translocation Set-up

Fabricated nanopipettes were filled with electrolyte solution using a MicroFil syringe needle (World Precision Instruments, Florida, USA) attached to a 1 millilitre (mL) Norm-Ject® Luer syringe (Henke Sass Wolf, Germany). Air bubbles that remained in the tip of the nanopipette were removed by rasping with corrugated tweezers.

A glass vial was washed with 70 % ethanol (EtOH, VWR International) then rinsed with autoclaved ultrapure DI H_2O and the electrolyte solution to be used. The vial was filled with electrolyte solution forming the 'bulk' solution, as shown schematically in Figure 2.1. The vial was then sealed using a plastic screw cap lid with septa. The electrolyte–filled nanopipette and the electrode exposed to the bulk solution were fixed to the lid while a second electrode was inserted inside the nanopipette.

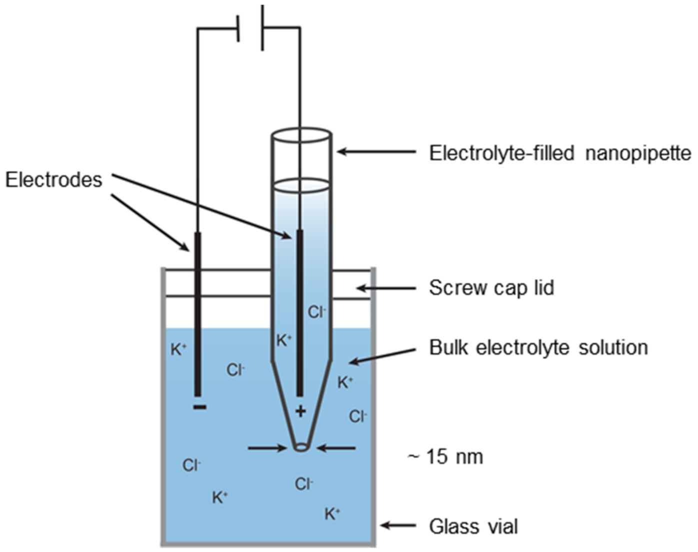

Figure 2.1. Schematic of nanopipette cell set-up used for ionic current measurements. Electrolyte-filled vial contains 'bulk' solution while the electrolyte-filled nanopipette and a Ag/AgCl electrode are fixed to the vial cap. A second Ag/AgCl electrode is placed inside the nanopipette. *Note: figure not drawn to scale.*

DNA samples were added to the bulk electrolyte solution with final DNA concentrations of i) 100 - 300 pM for experiments described in chapter 3, ii) 420 nM for ssDNA experiments described in chapter 4 and iii) 3 - 6 nM for dsDNA experiments described in chapter 4.

2.1.6 Electrochemical Measurements

A Gamry Reference 600 potentiostat (Gamry Instruments, Warminster, USA) was used to estimate the conductance of fabricated nanopipettes using CV measurements. Using the set-up described in section 2.1.5, a bias of +0.5 to -0.5 V (unless otherwise stated), was applied across the working electrode (WE) and the counter electrode (CE)/ reference electrode (RE) with a scan rate between 50 – 100 mV/s and a step size between 1 – 2 mV.

2.1.7 Custom-built amplifier and peripheral electronics

The amplifier was designed and built by Pietro Ciccarella, Marco Carminati and Giorgio Ferrari from the electrical engineering department at the Politecnico di Milano, Italy.

Current-time (I(t)) measurements were made with a low-noise, wide-bandwidth current amplifier, ‘Polimi’.[9,10]

Figure 2.2, shows an image of the internal architecture of the Polimi amplifier. This CMOS technology based amplifier splits the current into an alternating current (AC) and a direct current (DC) channel which show fast and slow modulations in the ionic current respectively. The AC channel detects current blockages (or enhancements) and is baseline adjusted to 0 A while the DC channel reports on the open pore current of the pore.

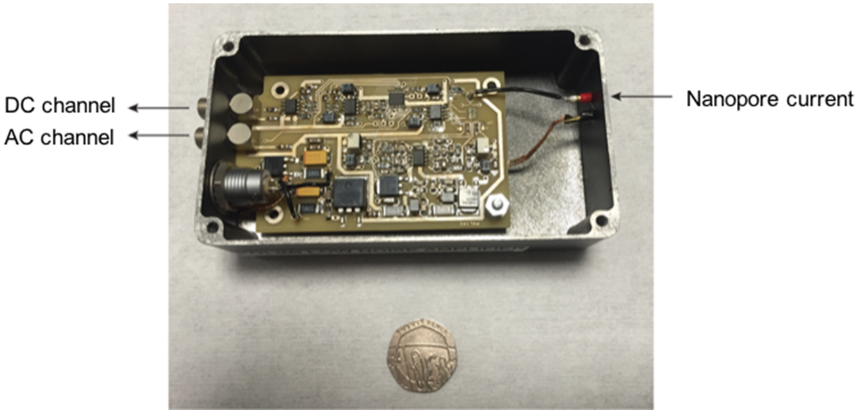

Figure 2.2. Image of the internal architecture of the Polimi amplifier, showing the input from the nanopore set-up and the DC and AC channel outputs.

Amplified current is converted to a voltage by a transimpedance amplifier (TIA), then low-pass Bessel filtered (8 poles, 3382 or 3940 Krohn-Hite filter, Krohn-Hite Corporation, Massachusetts, USA) and finally the signal can be viewed in real-time using the Picoscope 4262 (Pico Technology, Cambridgeshire, UK) oscilloscope. A more detailed description of the Polimi amplifier is given in chapter 3. The nanopipette set-up is placed inside a small Faraday cage containing a low-pass filter to reduce 50 Hz noise which is due to the frequency of the AC coming from the mains power supply. This small Faraday cage is in turn placed inside a larger Faraday cage alongside the Polimi amplifier. The two Faraday cages help to shield the set-up from electromagnetic radiation.

2.1.8 Data acquisition and data analysis

The I(t) traces were sampled at 1 MHz, unless otherwise stated and the filter frequency varied between 10 and 200 kHz, as specified.

Custom-written MATLAB codes[*] were used to collect the data alongside a log file which contained the root-mean-square (RMS) noise, mean and standard deviation, σ of the I(t) traces for both the AC and DC channel. Each file contained ten-million data points and where applicable, the average RMS noise of multiple files at a given voltage was taken and the standard error of the mean calculated.

Analysis of the raw AC channel I(t) traces was performed using a separate custom-written MATLAB code.[*] Translocation events were defined as current modulations with a peak amplitude (ΔI) greater than a 5 σ cut-off except for the detection of 200 bp DNA where a 4 σ cut-off was used due to the low signal-to-noise (SNR) ratio. The standard deviation was defined by plotting the current histogram of the AC channel and determining the σ of the distribution from a Gaussian fit. The dwell time (τ) for each event was defined as the data points where the current crossed a 1 σ cut-off (Figure 2.3). The event charge deficit (ecd) was calculated as the integral of the I(t) trace for an event defined using a 1 σ cut-off. A 1 σ cut-off was chosen to capture a significant part of the event while accounting for small baseline fluctuations. Output data from the MATLAB code was plotted in Origin 9.0 (OriginLab Corporation, Massachusetts, USA).

---

[*] Written by Dr Tim Albrecht, Imperial College London.

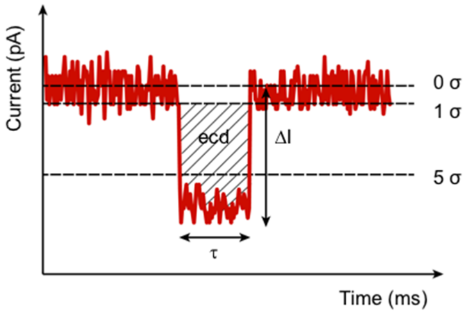

Figure 2.3. I(t) trace showing a translocation event that crosses a 5 σ cut-off. The peak amplitude, ΔI is defined using a 0 σ cut-off while the dwell time, τ and the integrated event area, ecd are defined using a 1 σ cut-off.

2.2 DNA Samples

The following dsDNA samples were commercially available; 48.502 kbp (Promega Ltd., Southampton, UK), 10 kbp (Promega), pET-24a-d(+) plasmid (Merck Chemicals Ltd., Nottingham, UK), 4 kbp (ThermoFisher Scientific, Hampshire UK) and 200 bp (ThermoFisher Scientific).

Two ssDNA fragments with complementary sequence, 100 nt long were purchased from Integrated DNA Technologies (Leuven, Belgium). One of the two ssDNA fragments was purchased with an amino group modification at the 5’ end attached via a C6 carbon chain spacer (5AmMC6). The sequences were:

5’-/ 5AmMC6/
GCCCGGTCGGTTGCCGAGACCATGGGCAACTACCACCCGCACGGCGACGCGTCG
ATCTACGACAGCCTGGTGCGCATGGCCCAGCCCTGGTCGCTGCGCT – 3’

and

5’- AGCGCAGCGACCAGGGCTGGGCCATGCGCACCAGGCTGTCGTAGATCGACG

CGTCGCCGTGCGGGTGGTAGT TGCCCATGGTCTCGGCAACCGACCGGGC – 3’

The manufacturer’s concentration was confirmed by ultraviolet-visible (UV-Vis) spectroscopy and their purity confirmed by agarose gel electrophoresis. All DNA samples were stored at -20 °C until use and aliquots of the DNA samples were stored where necessary to avoid repeated freeze-thaw cycles.

2.2.1 Ultraviolet-Visible (UV-Vis) Spectroscopy

Prior to use in DNA translocation experiments, the concentration and purity of DNA samples was measured using a NanoDrop^{TM} 2000 Spectrophotometer (ThermoFisher Scientific). Sample purity was evaluated using the 260/280 as a primary and 260/230 absorbance ratio as a secondary measure of purity. According to the manufacturer's manual for a pure DNA sample a 260/280 ratio of ~1.8 and 260/230 ratio in the range of 1.8 – 2.2 is to be expected.[11] Briefly, sample buffer was loaded onto the pedestal and a blank measurement recorded. The sample buffer was gently removed from the pedestal using a lint-free laboratory wipe, 1 μL of the sample loaded onto the pedestal and the UV-Vis measurement recorded.

2.2.2 Gel Electrophoresis

A 0.5 %, 1 % or 2 % agarose gel (Sigma-Aldrich Company Ltd., Dorset, UK) pre-stained with 2 μL of GelRed (Biotium Inc., California, USA) dye was moulded in a 7 × 10 cm casting tray then loaded with approximately 25 ng of DNA sample per well alongside DNA ladders. Depending on the DNA sample, a '1 kb extend DNA ladder' (New England Biolabs (NEB), Hertfordshire, UK), '1 kb DNA ladder' (NEB, Hertfordshire, UK) or '50 bp DNA ladder' (ThermoFisher Scientific) was used as appropriate.

As a running buffer 40 mM tris (pH 7.6), 20 mM acetic acid, 1 mM EDTA (TAE, Bio-Rad Laboratories Inc., California, USA) or 89 mM tris (pH 7.6), 89 mM boric acid, 2 mM (TBE, Bio-Rad Laboratories Inc.) was used with an applied potential of approximately 5 V/cm at rt. Photographs of the gel were taken using a GelDoc XR+ system (BioRad Laboratories) and analysed using Image Lab^{TM} software (BioRad Laboratories).

2.2.3 Plasmid Digestion

The 5.31 kb DNA sample was obtained by digestion of the pET-24a-d(+) plasmid using the restriction enzyme *Bam*H1(Sigma-Aldrich). This restriction enzyme has the recognition sequence 5' -GGATCC- 3' and cleaves at this target site.

For the digestion reaction 15 μL of circular pET-24a-d(+) (0.5 μg/μL) was added to 2 μL of 100 mM tris-HCl, 50 mM magnesium chloride ($MgCl_2$), 1000 mM NaCl, 10 mM 2-mercaptoethanol (buffer SB, Sigma-Aldrich) pH 8.0, 1 μL of restriction enzyme *Bam*H1 (Sigma-Aldrich) and 2 μL of bovine serum albumin (BSA, Promega) to give a final digestion mixture of 20 μL. The BSA protein is added to the reaction mixture to minimise adhesion of the *Bam*H1 enzyme to the Eppendorf tubes® (Hertfordshire, UK) and plastic pipette tips.

The digestion mixture was incubated at 37 °C for 3 h and purified using the Qiagen polymerase chain reaction (PCR) purification kit (Hilden, Germany). Agarose gel electrophoresis was used to confirm the linearisation of pET-24a-d(+) henceforth referred to as 'pET24aD'.

2.2.4 Long range polymerase chain reaction (PCR)

For experiments in Chapter 3, the 4 kbp dsDNA sample was obtained as outlined below from Dr Azadeh Bahrami, a former research associate in the Albrecht group.

DNA was extracted from the MCF-7 human breast carcinoma cell line (Cell Culture Service, Cancer Research UK, London, UK), according to the manufacturer's instructions using a Qiagen DNeasy kit. The FOXA promoter from the extracted DNA was amplified by long range PCR using a Qiagen LongRange PCR kit and the DNA purified using a Qiagen PCR purification kit. The sample concentration was measured by UV-Vis spectroscopy and purity confirmed by agarose gel electrophoresis.

2.2.5 DNA Hybridisation

For the hybridisation reaction, 1 µL of each of the ssDNA fragments at a concentration of 100 µM was added to 5 µL of PerfectHyb^{TM} Plus Hybridization buffer (Sigma-Aldrich) and 43 µL of UltraPure^{TM} DNase/RNase-free distilled H_2O (ThermoFisher Scientific), to give a final reaction volume of 50 µL.[12] The reaction mixture was heated at 95 °C for five min in a dry bath, the temperature reduced to 37 °C and the reaction mixture left for five h then incubated at 4 °C for 20 min. The final product was stored at -20 °C. The concentration of the DNA was measured by UV–Vis spectroscopy and successful hybridisation of the two single strands tested using 2% agarose gel electrophoresis.

Alternatively, 1 µL of each of the ssDNA at a concentration of 100 µM was added to 1 mL of 1 M KCl, 10 mM trisHCl, pH 8 and left to incubate for 1 h at rt. The concentration was measured by UV-Vis spectroscopy and the degree of hybridisation assessed using 2 % agarose gel electrophoresis.

2.3 Surface Silanization of Nanopipettes

2.3.1 Contact angle (θc) measurements

Contact angle measurements were performed and analysed by Tina Leontidou, an MSci student in the Albrecht group.

Contact angle (θ_c) measurements were determined using the sessile drop method. A quartz microscope slide (GPE Scientific Ltd, Bedfordshire, UK) was plasma cleaned for five min. The plasma cleaned slide was placed inside a desiccator alongside a vial containing 120 µL of (3-aminopropyl)trimethoxysilane (APTMS, Sigma-Aldrich) and evacuated for 15 min. The desiccator was then left under vacuum for 45 min.

A droplet (100 µL) of DI ultrapure H_2O was placed either on the plasma cleaned quartz slide or the APTMS coated quartz slide and an image of the droplet captured using a camera connected to a Raspberry Pi. The image was analysed using ImageJ software with the contact angle plug-in to determine the θ_c, as shown schematically Figure 2.4.

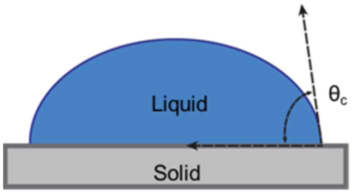

Figure 2.4. Schematic representation of the contact angle (θ_c) of a droplet on a solid surface.

2.3.2 Nanopipette Surface Silanization

Prior to surface silanization, the nanopipettes were plasma cleaned for 5 - 10 min after pulling to ensure that free hydroxyl groups were exposed. These nanopipettes were placed in a desiccator with a vial containing 120 µL of APTMS (Sigma-Aldrich) and evacuated for 15 min. The desiccator was left under vacuum for a minimum of 45 min or overnight if used the following day. Silanised nanopipettes were then assembled as described in section 2.1.5 for DNA translocation experiments.

2.4 Coating of Nanopipettes Using Modified Lipid Bilayers

1-palmitoyl-2-oleoyl-sn-glycero-3-phosphocholine (POPC), 1,2-dipalmitoyl-sn-glycero-3-phosphoethanolamine (DPPE) and 1,2-dipalmitoyl-sn-glycero-3-phosphoethanolamine-N-

(glutaryl) (sodium salt) (DPPE-GA) were purchased from Avanti® Polar Lipids Inc., (Alabama, USA) either in powder form or dissolved in chloroform ($CHCl_3$). When lipids were purchased in powder form, the lipids were dissolved in $CHCl_3$ (Sigma-Aldrich) to make stock solutions.

2.4.1 Preparation of Small Unilamellar Vesicles (SUV)

The desired lipid or lipid mixture was dissolved in $CHCl_3$, vortexed to ensure homogenous mixing and the solvent evaporated under nitrogen (N_2), then dried in a desiccator under vacuum for 12 – 24 hours.[13,14] The dried lipid film was stored at -20 ℃ until further use. Vesicles formed consisted of either pure POPC or POPC 'doped' with DPPE or DPPE-GA. The final concentration of POPC was kept constant at 2 mM.

Dried lipid films were hydrated in 1 mL of UltraPure™ DNase/RNase-free distilled H_2O (ThermoFisher Scientific), to form a cloudy solution of multilamellar vesicles (MLV). Disruption of the MLV to form small unilamellar vesicles (SUV) was achieved by sonicating the lipid suspension for 20 – 40 min in an Elmasonic P 30 H ultrasonic bath (Elma Electronic Ltd., Bedfordshire, UK) using an ultrasonic frequency of 37 kHz and a bath temperature of 50 – 60 ℃. Formation of SUV was confirmed by a colour change from cloudy to clear due to a reduction in light scattering when disrupting the MLV to form SUV.[14] Vesicles were used on the day or stored at -4 ℃ for a maximum of 5 days.

2.4.2 Dynamic Light Scattering (DLS) measurements of vesicles

Dynamic light scattering (DLS) sizing measurements were acquired with a Beckman Coulter, Inc. Delsa™ Nano C (California, USA) instrument at 22 ℃.[15] Measurements were made using a 3 mL quartz cell (Agilent Technologies, California, USA) or 1.5 mL disposable cuvettes (VWR International). The cuvette was rinsed with copious amounts of DI ultrapure H_20 before use and in-between sample measurements when using the quartz cell.

The DLS has a 658 nm laser with dual 30 mW laser diodes and detects scattered light at 165° ($q^2 = 6.34 \times 10^{14}$ Å^{-1}, q is the scattering vector). Each sample run was obtained from 100 accumulations of the intensity autocorrelation function (ACF), where the scattering intensity was quantified from the number of photons per 1 s (i.e sampling rate). The ACF for each run was calculated over 75 seconds and the 100 accumulations acquired from a single run were summed together to reduce noise. Three sample runs were collected for each sample.

The DelsaNano software fits the ACF with an exponential to determine the decay constant (Γ). Using equations 2.3 and the Stokes-Einstein equation 2.4 the diffusion coefficient (D) and the hydrodynamic diameter (d) respectively can be calculated.

$$\Gamma = Dq \tag{2.3}$$

Where q is the scattering vector.[†]

$$D = \frac{k_B T}{3\pi\eta_o d} \tag{2.4}$$

Where k_B is the Boltzmann's constant, T the absolute temperature, η_o the viscosity and d the hydrodynamic diameter.

The Delsa Nano 2.31 software contains a 'dust' filter that rejects accumulations when the intensity of the scattered light is above a specific threshold, set at 25% above the mean scattering intensity. The mean scattering intensity was determined at the beginning of each experiment; however, accumulations were very rarely rejected. In order to minimise contamination all vesicle solutions were hydrated in UltraPure^{TM} DNase/RNase-free distilled H_2O (ThermoFisher Scientific) which is filtered with a 0.1 μm membrane.

2.4.3 Modification of Unilamellar Vesicles Using ssDNA

Attachment of ssDNA to vesicles was attempted using POPC vesicles doped with 9 mol% DPPE-GA, henceforth deferred to as POPC/9-DPPE-GA. Following formation of vesicles as described in section 2.4.1, 10 μL of 0.86 mg/μL freshly prepared stock *N*-(3-Dimethylaminopropyl)-*N′*-ethylcarbodiimide hydrochloride (EDCI, Sigma-Aldrich) solution was added and the mixture shaken for 15 min. Another 10 μL of the stock EDCI solution and 3 μL of 100 μM ssDNA with a 5'NH_2 group was added and the mixture shaken for 90 min. The modified lipids were then added to the bulk electrolyte solution of the nanopipette set-up described in section 2.1.5. These ssDNA decorated vesicles are referred to as POPC/9-DPPE-GA/ssDNA.

[†] $q = \frac{4\pi n \sin\theta/2}{\lambda}$ where n is the refractive index of water, λ is the wavelength of the incident light (658 nm) and θ is the scattering angle (165°).

2.4.4 Atomic Force Microscopy (AFM) of Supported Lipid Bilayers (SLB)

All AFM images of lipid bilayers were obtained at rt in liquid with an Agilent 5500 AFM/SPM microscope (Keysight Technologies, California, USA) and using the liquid cell holder mounted onto the sample plate. All images of mica were obtained at rt in air. For both air and in liquid, the AFM was operating in contact mode.

Commercial pyrex–nitride triangular cantilevers (PNP–TR, Windsor Scientific Ltd., Berkshire, UK) with the following parameters were used; force constant, 0.08 N/m, length, 200 μm, mean width 28 μm and thickness 0.5 μm. Image scan areas of 1 × 1 μm, 5 × 5 μm and 10 × 10 μm with scan rates of 1 line/s or 0.5 lines/s and a resolution of 512 points/ line were employed. All the raw images were processed with a first–order 'flatten filter' using WS×M 5.0 Develop 6.5 (Nanotec Electronica S.L., Spain) to remove a linear background.[16,17] For images of POPC doped with varying amounts of DPPE a 'flooding' process was used in the WS×M software where a cut-off height is used to determine the percentage coverage of light areas compared to dark areas.

A mica disk (15 mm diameter, Agar Scientific Ltd., Stansted, UK) was glued to a metal specimen disk (15 mm diameter, Agar Scientific) and secured to the sample plate's magnetic core. To ensure anatomically flat and uniform surfaces, the mica was cleaved using adehesive tape (VWR International) prior to imaging.

Supported lipid bilayer (SLB) formation on mica was achieved by the vesicle fusion method. Although the process by which SUVs form a bilayer on the solid support is not fully understood, the main steps consist of vesicle adsorption to the mica, deformation, flattening and then rupturing to form a SLB, as depicted Figure 2.5.[13]

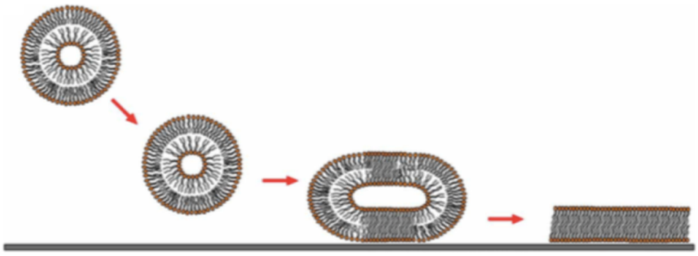

Figure 2.5. A simplified schematic of the vesicle adsorption method used to prepare a SLB on mica. SUV adsorb to the mica, deform, flatten and finally rupture. Figures reprinted with permission from ref. 13.

A stock solution of 10 mM calcium chloride ($CaCl_2$, VWR International) solution was added to freshly cleaved mica so that the final $CaCl_2$ concentration upon addition of the vesicle solution would be 2 - 3 mM. Addition of $CaCl_2$ has been reported to encourage the formation of a SLB by forming a ‘bridge’ between the negatively charged mica and negatively charged phosphate groups of the phospholipids.[13,18] The $CaCl_2$ solution was covered and left to incubate for 10 - 15 min. After the incubation period 200 - 300 μL of the desired liposomes were added, left to incubate for 30 - 45 min then excess liposomes were washed away using copious amounts of UltraPure^{TM} DNase/RNase-free DI H_2O (ThermoFisher Scientific) and the sample imaged.

2.4.5 Differential Scanning Calorimetry (DSC)

DSC measurement and scan analysis was performed by Dr Arwen Tyler, a research associate in the Membrane Biophysics group Imperial College London.

A dried lipid film, prepared as described in section 2.4.1 of POPC with 10 mol% DPPE-GA was hydrated with UltraPure^{TM} DNase/RNase-free distilled H_2O (ThermoFisher Scientific) in a glass vial to give a final concentration of 0.43 mg/μL. The lipid suspension was frozen by suspending the vial in liquid nitrogen then heated (i.e. a freeze-thaw cycle). Four further freeze-thaw cycles were repeated to obtain a thick paste that was transferred to a DSC pan (TA Instruments, Delaware, USA) and sealed using a second DSC pan. DSC measurements were performed on a Diamond DSC (PerkinElmer, Buckinghamshire, UK), using an empty DSC pan as a reference. A heating and cooling rate of 5 °C/min was used throughout. The temperature was held at -5 °C for 5 min, ramped from -5 °C to 70 °C, held at 70 °C for 1 min then cooled from 70 °C to -5 °C. The onset of the peak in the DSC scan is the phase transition temperature of the lipid mixture. This onset was defined as the point where the tangent to the peak at its maximum gradient meets the tangent to the baseline.[19,20]

2.4.6 Experimental set-up for nanopipette coating with a lipid bilayer

Figure 2.6 shows the experimental set-up used when coating nanopipettes with a lipid bilayer. To allow for exchange of liposomes, 1 M KCl electrolyte and $CaCl_2$ solution, 1 mL Norm-Ject® Luer syringes (Henke Sass Wolf, Germany) and two Microlance^{TM} needles (Becton, Dickinson and Company, New Jersey, USA) were fixed to the plastic screw cap lid with septa. These needles were in turn connected to polythene tubing (Harvard Apparatus Ltd., Kent, UK) with an inner diameter of 0.38 mm and an outer diameter of 1.09 mm. The tubing served as an extension, so that solution exchange would occur at the bottom of the vial away from the nanopipette tip and hence disturb the coating process as little as possible.

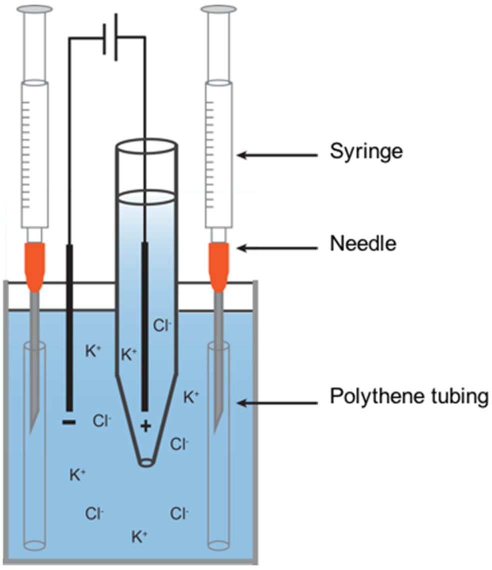

Figure 2.6. Schematic representation of set-up for coating of nanopipettes using liposomes. *Note: diagram not to scale.*

2.4.7 Experimental Procedure for Nanopipette Coating with a Lipid Bilayer

CV measurements and I(t) traces were recorded as described in sections 2.1.6 - 2.1.8 to follow the progression of the nanopipette coating experiments.

For the coating procedure, 600 µL of KCl bulk electrolyte solution was removed and replaced with 600 µL of 10 mM $CaCl_2$ (2 mM final $CaCl_2$ concentration in the bulk solution), left for approximately 10 min, followed by the addition of 200 - 300 µL of the desired vesicles. After 30 - 45 min the bulk solution was exchanged for fresh KCl electrolyte by removing electrolyte while injecting the equivalent volume of electrolyte. Care was taken not to expose the nanopipette tip to air as lipid bilayers can re-arrange when exposed to air.

As a control, CV measurements were taken for a bare nanopipette then 600 µL of KCl electrolyte removed and replaced with 600 µL of 10 mM $CaCl_2$, followed by the addition of 300 µL of UltraPure^{TM} DNase/RNase-free DI H_2O (ThermoFisher Scientific), the hydrating medium of dried lipid films and another CV measurement recorded after 20 min. The change in electrolyte conductivity with the addition of 2 mM $CaCl_2$ was measured with a conductivity meter (SG78, Mettler-Toledo) at rt.

When the nanopipette was coated with a lipid bilayer decorated with ssDNA, 3 µL of the complementary 100 µM ssDNA was added to the bulk solution and left to incubate for one h before recording I(t) traces.

2.5 References

(1) http://www.sutter.com/MICROPIPETTE/glass.html. Accessed on 2/11/2016.

(2) Steinbock, L. J.; Otto, O.; Chimerel, C.; Gornall, J.; Keyser, U. F. *Nano Lett.* **2010**, *10*, 2493–2497.

(3) Gong, X.; Patil, A. V; Ivanov, A. P.; Kong, Q.; Gibb, T.; Dogan, F.; DeMello, A. J.; Edel, J. B. *Anal. Chem.* **2014**, *86*, 835–841.

(4) Sze, J. Y. Y.; Kumar, S.; Ivanov, A. P.; Oh, S.; Edel, J. B. *Analyst* **2015**, *140*, 4828–4834.

(5) Wang, Y.; Velmurugan, J.; Mirkin, M. V.; Rodgers, P. J.; Kim, J.; Amemiya, S. *Anal. Chem.* **2010**, *82*, 77–83.

(6) http://www.sutter.com/manuals/P-2000_OpMan.pdf. Accessed on 2/11/2016.

(7) Wanunu, M. *Phys. Life Rev.* **2012**, *9*, 125–158.

(8) Israelachvili, J. N. http://www.mt.com/dam/Analytical/pH-LabMeters/me-pdf/30208950_ph_SevenGoDuo_Broch_EN_16.10.2014_LOW.pdf. Accessed on 2/11/2016.

(9) Fraccari R.L.; Ciccarella P.; Bahrami A.; Carminati M.; Ferrari G, Albrecht T. *Nanoscale* **2016**, 8, 7604-7611.

(10) Ciccarella, P.; Carminati, M.; Ferrari, G.; Fraccari, R.; Bahrami, A. An Integrated Low-Noise Current Amplifier for Glass-Based Nanopore Sensing; 10th Conference on Ph.D. Research in Microelectronics and Electronics (PRIME 2014), Grenoble, France, June 29 - July 30, **2014**, 1– 4.

(11) http://www.nanodrop.com/Library/NanoDrop%202000%20User%20Manual.pdf. Accessed on 2/11/2016.

(12) http://www.sigmaaldrich.com/technical-documents/protocols/biology/annealing-oligos.html. Accessed on 2/11/2016.

(13) Mingeot-Leclercq, M.-P.; Deleu, M.; Brasseur, R.; Dufrene, Y. F. *Nat. Protoc.* **2008**, *3*, 1654–1659.

(14) https://avantilipids.com/tech-support/liposome-preparation/. Accessed on 1/11/2016.

(15) https://www.beckmancoulter.com/wsrportal/techdocs?docname=B08631AA.pdf. Accessed on 1/11/2016.

(16) Horcas, I.; Fernández, R.; Gómez-Rodríguez, J. M.; Colchero, J.; Gómez-Herrero, J.; Baro, A. M. *Rev. Sci. Instrum.* **2007**, *78,* 013705.

(17) Hansma, H. G.; Revenko, I.; Kim, K.; Laney, D. E. *Nucleic Acids Res.* **1996**, *24*, 713–720.

(18) Richter, R.; Mukhopadhyay, A.; Brisson, A. *Biophys. J.* **2003**, *85*, 3035–3047.

(19) Ferreira, E. B.; Lima, M. L.; Zanotto, E. D. *J. Am. Ceram. Soc.* **2010**, *93*, 3757–3763.

(20) Garidel, P.; Johann, C.; Blume, A. *J. Therm. Anal. Calorim.* **2005**, *82*, 447–455.

Chapter 3

Translocation of Long DNA in Nanopipettes

Synopsis: This chapter describes the investigation of DNA/surface interactions in nanopipettes in 1 M KCl electrolyte. To enable the translocation events to be fully resolved in this electrolyte, custom-built and high-speed detection electronics were used. The scaling factor, p between the DNA length (L_{DNA}) and the translocation time, i.e. $\tau \propto (L_{DNA})^{p}$, was found to be different from previous translocation studies in nanopipettes but similar to results from chip-based nanopore sensors. The observed variation in the scaling factor can be rationalised based on DNA/surface interactions (friction), as illustrated with a suitable analytical model ("Ghosal+"). This extended model suggested that such friction is indeed an important part of the translocation process. Experimentally this was investigated further by comparing DNA translocation events in silane modified and unmodified nanopipettes.

Part of this chapter has been published as Fraccari R.L.; Ciccarella P.; Bahrami A.; Carminati M.; Ferrari G, Albrecht T. *Nanoscale* **2016**, 8, 7604-7611.

3.1 Introduction

Over the years, quartz nanopipettes have emerged as a novel sub-class of solid-state nanopores.[1] However, compared to classical planar devices there are subtle differences between their sensing regions. In the former case, due to the high aspect ratio of the nanopipette, the electric field drops relatively rapidly on the outside of the nanopipette compared to the inside. Moreover, the capture volume on the outside of the nanopipette is relatively larger than on the inside where there is a more confined environment. On the other hand, for planar chip-based devices, the electric field is (approximately) symmetrically distributed on both sides of the nanopore while likewise the capture radius of the analyte occurs in an approximately hemispherical volume around the entrance of the nanopore.[2] It is speculated that these subtle differences give rise to different DNA translocation dynamics in these two types of nanopore platforms. For chip-based devices and nanopipettes, the relationship between the translocation time, τ and DNA length, L_{DNA} is given by $\tau \propto (L_{DNA})^p$, where p is the scaling factor. In the literature, the value of p has found to vary depending on the different experimental conditions used.[3–6]

3.1.1 Translocation of Different DNA Lengths in Chip-Based Nanopores

Ghosal proposed a hydrodynamic model to determine the electrophoretic speed of a DNA molecule translocating through a chip-based nanopore.[7,8] In this model, a cylindrical-shaped pore is assumed, with radius R through which a polyelectrolyte such as DNA translocates in the axial direction. The part of the polyelectrolyte inside the pore, which is translocating at a velocity υ, is modeled as a rigid cylindrical rod, with radius a, as shown in Figure 3.1.[8]

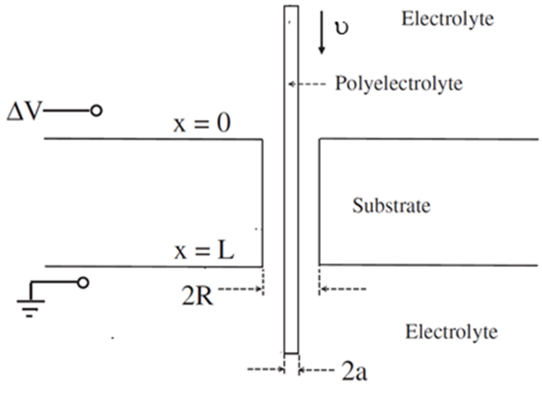

Figure 3.1 Geometry of pore assumed in the Ghosal model, where R is the radius of the pore and a is the radius of the polyelectrolyte. Both are modeled as cylinders. Figure reprinted with permission from ref. 8.

The υ of the DNA segment inside the pore was determined using the condition set out in equation (3.1). The total force acting on the DNA segment inside the pore is equal to zero and is made up of an electrophoretic (F_e) and viscous (F_v) force per unit length of the polyelectrolyte.[8]

$$\mathrm{F_e} + \mathrm{F_v} = 0 \tag{3.1}$$

This gave equation (3.2) for the υ of the polyelectrolyte, assuming there is no pressure difference between the compartments on either side of the pore and within the limit of a thin Debye layer around the polyelectrolyte.[8] The first part of equation (3.2) represents the electrophoretic speed of the polyelectrolyte, while the second part of the equation represents electroosmotic flow through the pore which is generated by an V_{bias}.

$$\upsilon = \frac{\varepsilon \cdot \mathrm{E_0} \cdot \zeta_\mathrm{p}}{\eta_d} + \frac{\varepsilon \cdot \mathrm{E_0} \cdot \zeta_\omega}{\eta_d} \tag{3.2}$$

Where ε is the dielectric constant of the electrolyte, E_0 the applied electric field in the pore, η_d the dynamic viscosity of the electrolyte and respectively, ζ_p and ζ_ω the zeta (ζ) potentials at the surface of the polyelectrolyte and wall.

For chip-based nanopore platforms operating in 1 M KCl electrolyte, p varied from ~1.26 – 2.28.[3,4,6] The τ therefore has a dependence on L_{DNA} which could not be explained by the Ghosal model in which all of the resistive force for polymer translocation are located at the pore region. The authors conclude that the dependence of the τ on L_{DNA} must arise from additional effects not considered in the Ghosal model.[7]

Wanunu et al. used SiN pores with diameters between 5.0 and 2.7 nm to detect L_{DNA} between 150 bp and 20 kbp.[6] The authors report two different p values; for short L_{DNA} in the range of 150 bp to 3.5 kbp, $p = 1.40 \pm 0.05$ and for long L_{DNA} above 3.5 kbp, $p = 2.28 \pm 0.05$. They also reported on unsuccessful threading attempts or 'collisions' with the pore which increased with decreasing pore size. Additionally, the effects of pore size and temperature were also investigated. Decreasing the pore size from 5.0 to 2.7 nm led to a 13-fold increase in τ which was thought to be incommensurate with the increased viscous drag inside the pore. On the other hand, decreasing the temperature of the nanopore system from 30 to 0 °C resulted in a seven-fold increase in τ which was again thought to be disproportionate with the increased electrolyte viscosity. Their experiments which examined translocation dynamics as a function of pore size, length and temperature led the authors to suggest that DNA/surface interactions are an important part of the translocation process however no quantitative model was developed.

On the other hand, for solid-state SiO_2 planar devices, Storm et al. reported a p value of ~1.26 – 1.27 for linear translocation events.[3,4] Additionally, they theoretically modeled the threading of DNA through a nanopore where they assume that the potential drop, Φ occurs exclusively inside the pore. In their model, they included a driving force ($F_{driving}$) acting on the DNA molecule due to the difference in V_{bias} across the membrane. Opposing this force is a viscous drag force (F_{drag}) acting on the untranslocated part of the DNA molecule which is described as being in a 'blob-like' configuration, as shown in Figure 3.2.[4] The DNA in the blob-like configuration becomes smaller as the DNA translocates through the pore, yielding a τ that scales with the square of the DNA radius of gyration i.e. $\tau \sim R_g^2$, where R_g scales with the Flory exponent, $\upsilon_F = 0.6$.[4,9] Using this model the value of p was estimated to be 1.22, in good agreement with their experimental data.

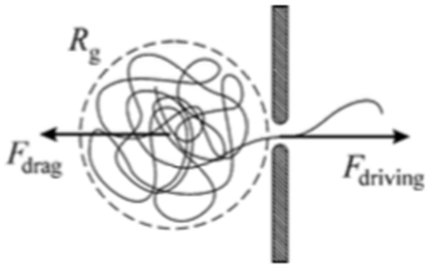

Figure 3.2. Schematic showing the balance between $F_{driving}$ and F_{drag} in a solid-state nanopore. Figure reprinted with permission from ref. 5.

3.1.2 Translocation of Different DNA Lengths in Nanopipettes

The detection of the translocating DNA molecule can be limited by the time resolution of the electronics used to measure the current. The fast μs timescales for DNA and protein translocations pose a significant challenge in the nanopore field.[10–14] To this end, Kowalczyk et al. have shown that using LiCl electrolyte slows down the translocation of DNA compared to KCl electrolyte (see Chapter 4).[15] Therefore, in his L_{DNA} dependence study in nanopipettes Bell used 4 M LiCl electrolyte to allow dsDNA lengths as short as 500 bp to be detected.[5] For translocation experiments with L_{DNA} between 500 bp and 48.5 kbp, two different p regimes were found; one for short L_{DNA} in the 500 bp to 4 kbp region and another for the 5 to 48.5 kbp region. For the short and long L_{DNA}, p values of ~0.86 and ~1.01 respectively were found when analysing the DNA translocation events of linear (not folded) conformations only (*vide infra*). On average, p ~ 1 is line with the Ghosal model which takes into account the structure of the electrical double layer as well as hydrodynamic drag inside the pore to determine τ.[7,8] Bell notes that the p value determined was significantly lower than that reported for planar solid-state pores and hypothesises that this may be due to little surface interaction between the DNA and the outside of the nanopipette, however no quantitative model was developed to assess this.

The variations in reported values of p using different solid-state nanopore platforms and electrolytes suggested that DNA/surface interactions play an important role in the translocation process, however to date there has been no L_{DNA} translocation study reported using nanopipettes and KCl electrolyte (which is the electrolyte used for all planar solid-state nanopore experiments to determine p). This has been in part due to limitations in the fast DNA translocation speed.

3.1.3 Surface Modifications of Nanopores

DNA/surface interactions appear to be an important consideration in nanopore experiments and indeed experiments that have aimed to tailor the surface properties of nanopores are well documented in the literature.[16–20]

Examples of surface modifications in chip-based solid-state nanopores include coating with organosilanes,[16,17] nitriloacetic acid (NTA) receptors[21] and addition of homocysteines for the detection of insulin.[22]

Meller and co-workers coated SiN pores that were 5 - 6 nm in diameter with APTMS, (Figure 3.3, a), making them sensitive to pH changes.[17] Decreasing the pH of the electrolyte solution, increased the τ of 1, 4 and 10 kbp dsDNA translocations which was explained as a stronger DNA/surface interactions being present in acidic conditions. On the other hand, Wei and co-workers modified the surface of SiN nanopores with a layer of gold (Au) that was then chemically modified using a mixed self-assembled monolayer (SAM) of alkane-thiols (Figure 3.3, b).[21] Some of these alkane-thiols were functionalised with a nitrilotriacetic acid (NTA) receptor which was used to specifically bind histidine-tagged proteins using a nickel (Ni) ion as a bridge inside the pore.

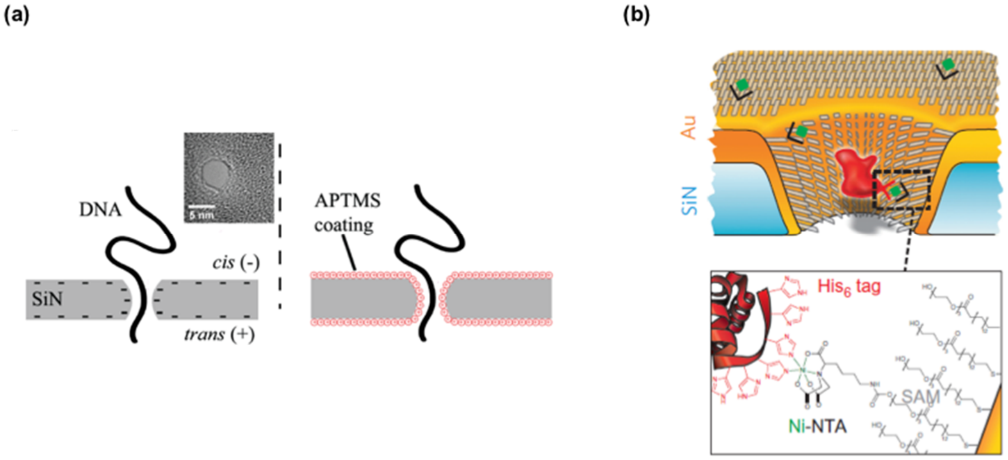

Figure 3.3. (a) Schematic representation of DNA translocation through a solid-state nanopore before and after coating with the organosilane APTMS and **(b)** schematic showing Au-coated solid-state nanopore functionalised with NTA receptors (black) which specifically binds to histidine tagged proteins (red) using a Ni ion as a bridge (green). Figures reprinted with permission from ref. 16 and 21.

On the other hand, Rutkowska et al. used a metalized planar nanopore containing an embedded Au layer to which homocysteines were covalently attached via thiol-Au bonds, leaving free carboxyl and amino groups (Figure 3.4).[22] Using 100 mM KCl, 40 mM HCl, pH 1.6 they were able to able to detect translocation events caused by the electrophoretic transport of insulin through the pore. However, no translocation events were detected in control experiments using metallic nanopores with no layer of homocysteines or SiN-based nanopores. It was suggested that specific interactions between the homocysteins and insulin caused a decrease in τ which allowed the protein to be detected. Moreover, under the conditions used, both the homocysteine layer and insulin were positively charged. The authors suggest that an attractive interaction existed between the two that could have been hydrophobic or van der Waals interactions.[22]

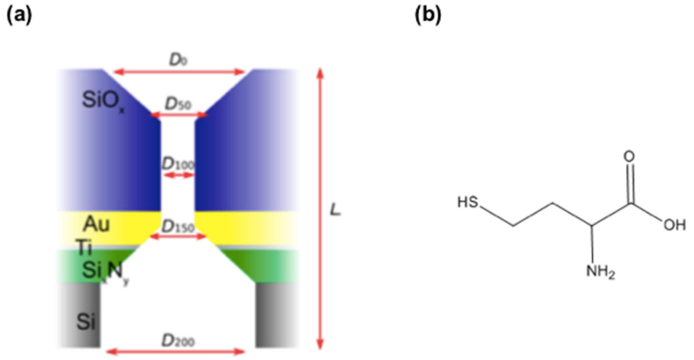

Figure 3.4. (a) Schematic of metalized nanopore platform and **(b)** structure of homocysteine. Panel (a) figure reprinted with permission from ref. 22.

Examples of surface modifications in nanopipettes have included using organosilanes[20] and dendrimers.[19] Sa et al. used silane chemistry to chemically attach dihydroimidazole (DHI) to the inside surface of nanopipettes.[20] The DHI moiety contains two amine groups, which when deprotonated acted as binding sites for Co^{2+} ions (Figure 3.5, a). Decreasing the electrolyte pH caused protonation of the amine groups and displacement of the bound Co^{2+} ions, then increasing the electrolyte pH, deprotonated the amine groups and regenerated the Co^{2+} ion binding sites. In this way, the nanopipette surface was made to reversibly respond to Co^{2+} ions by changing the pH of the electrolyte solution. In another study, silane chemistry was used to introduce aldehyde groups to the nanopipette surface that could be reacted with amine groups on dendrimers; highly branched molecules containing 64 primary amine groups (Figure 3.5, b).[19] The amine groups on the dendrimers were used to detect ssDNA through electrostatic complex formation between the amine groups and the ssDNA.

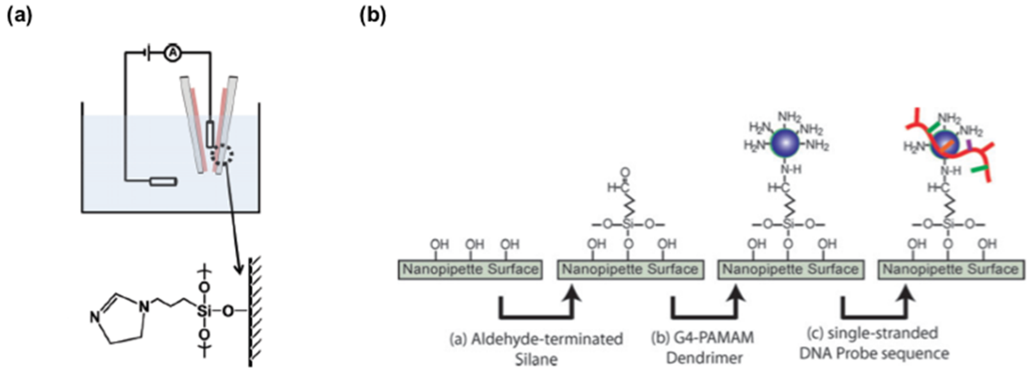

Figure 3.5. **(a)** Schematic representation of DHI bound to the inside of the nanopipette surface using silane chemistry. **(b)** Schematic showing the attachment of an aldehyde-terminated silane layer that is reacted with the primary amine of dendrimers. Free primary amines can then form electrostatic complexes with ssDNA. Figures reprinted with permission from ref. 20 and 19.

3.2 Experimental Objectives

The first aim of this chapter was to study the p using nanopipettes and KCl electrolyte as opposed to that reported by Bell using LiCl electrolyte. The Ghosal model was then extended in an attempt to shed light on the various p values observed in the literature using planar solid-state devices and KCl electrolyte or nanopipettes and LiCl electrolyte.

The second aim was to experimentally probe DNA-surface interactions by performing DNA translocations in nanopipettes modified using silane chemistry.

3.3 Results and Discussion

3.2.1 Electrochemical Characterisation of Nanopipettes

Figure 3.6 shows representative current-voltage (I-V) curves for two nanopipettes in 1 M KCl electrolyte. As expected, Ohmic behaviour was observed for this high electrolyte concentration where bulk electrolyte conditions dominated G_{pore} (see chapter 1). On the rare occasions where this was not the case the nanopipettes were discarded.[23]

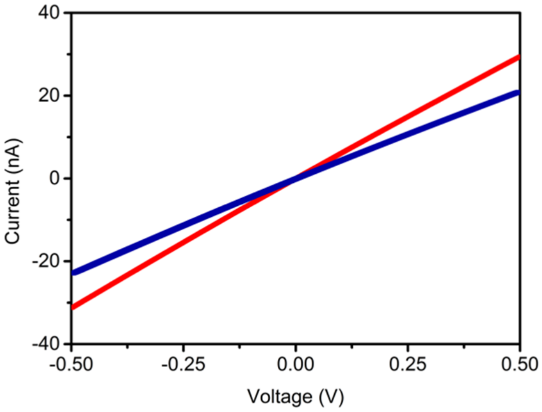

Figure 3.6. Representative CV measurements for two nanopipettes with estimated diameters of 21 nm (red, G_{pore} = 61 nS) and 15 nm (blue, G_{pore} = 44 ns).

The slope of the I-V curve gives the pore conductance, G_{pore} which was used to estimate the nanopore diameter (d_i) using the following equation:[23]

$$d_i = \frac{4G_{pore}l + {}^{\pi}/_{2}\, G_{pore}D_i}{D_i\pi g(c) - {}^{\pi}/_{2}G_{pore}} \tag{3.3}$$

Where d_i is the estimated nanopore size, g(c) the KCl conductivity, D_i the inner diameter at the base of the nanopipette and l the nanopipette taper length.

The conductivity of the KCl electrolyte was measured as 10.2 S/m, which is in good agreement with the value reported in the literature of 11 S/m at ~22 °C.[24] The value of 0.5 mm was used for $D_{i,}$ as defined by the manufacturer. For nanopipettes fabricated using programme 57, the value l was obtained by SEM imagang by Thomas Gibb, a former PhD student in the Albrecht group.[25] This gave a value l of ~1.2 mm. On the other hand, for nanopipettes fabricated using programme 99, the value l was determined using optical micrograph images (see appendix I) taken by Thomas Mickleburg, a PhD student in the Klugg group, Imperial College London. The value of l for these nanopipettes was ~2.7 mm.

Equation 3.1 is a very simplified model where the tip of the nanopipette is modeled as a conical cylinder; nevertheless, the equation proved sufficient for relating measured pore conductances to pore size in 1 M KCl. Good agreement was found between pore diameters determined by SEM imaging and those estimated using conductance measurements.[25] Equation 3.1 makes the assumption that at high KCl concentrations, salt dependent surface charge effects can be neglected. At these high salt concentrations (> 0.1 M) the surface contribution to the ionic current is expected to be small and instead the G_{pore} is largely determined by the conductivity of the bulk electrolyte (and the channel geometry).[23] It should also be noted that small changes in l associated with device-to-device variation can have a significant effect on the estimated d_i. However, due to the sample preparation required for SEM imaging it was impractical and time-consuming to determine l for each individual nanopipette used.

3.2.2 Custom-built Amplifier

Custom-designed electronics used herein were built by Dr. Ferrari's group at the Politecnico di Milano in Italy. As aforementioned, a common problem in the field is that the τ for small analytes, such as short DNA fragments or proteins, is shorter than the minimum temporal resolution of the detection electronics used to record the I(t) traces. This results in events that are not fully resolved.[1,14] Towards this end, the 'Polimi' amplifier was designed to improve the temporal resolution of the measurements and RMS noise compared to the commonly used commercial Axopatch 200B. The Polimi amplifier enabled translocation events to be fully resolved in 1 M KCl electrolyte using nanopipettes.

Figure 3.7 shows the nanopore set-up using the Polimi amplifier, with components inside the red box making up the benchtop amplifier. Two pathways consisting of the 'AC channel' and the 'DC channel' make up the amplifier, each of which shall be discussed briefly in turn.

The amplifier overcomes the traditional gain-bandwidth trade-off of transimpedance amplifiers (TIA) by using a 0.35 μm CMOS current amplifier which pre-amplifies the current by a factor of 990 without the use of noisy resistors. Instead of resistors, two pairs of matched transistors and capacitors on a single chip are used.[26–28] The input current from the nanopore set-up is converted into a voltage then reconverted into current. This current is amplified with respect to the input current and is again converted to a voltage then back to a current, providing further amplification. Amplified current from the current pre-amplifier is then converted to a voltage again by an off-chip TIA. This makes up the AC channel of the Polimi amplifier. In the absence of this current pre-amplifier, the noise performance of the amplifier would have been determined by a noisy resistor in the TIA.

On the other hand, the DC channel consists of the low frequency DC feedback network, which handles the large DC current coming from the nanopore and which flows through the resistor, R_1. The value of the current flowing through the pore is obtained by measuring the voltage drop across R_1.

The voltage from the TIA is then low-pass Bessel filtered by the Krohn-Hite filter and the resultant analog signal is converted to a digital signal by the Picoscope oscilloscope and viewed using a standard computer. Similarly, the DC current coming from the DC feedback network is converted to a digital signal by the Picoscope oscilloscope and viewed using a computer.

Overall, the AC channel responds quickly to current changes and is used to detect current blockages (or enhancements) while also being baseline adjusted to 0 pA. On the other hand, the DC channel responds slowly to current changes and reports on the open pore current (I_o).

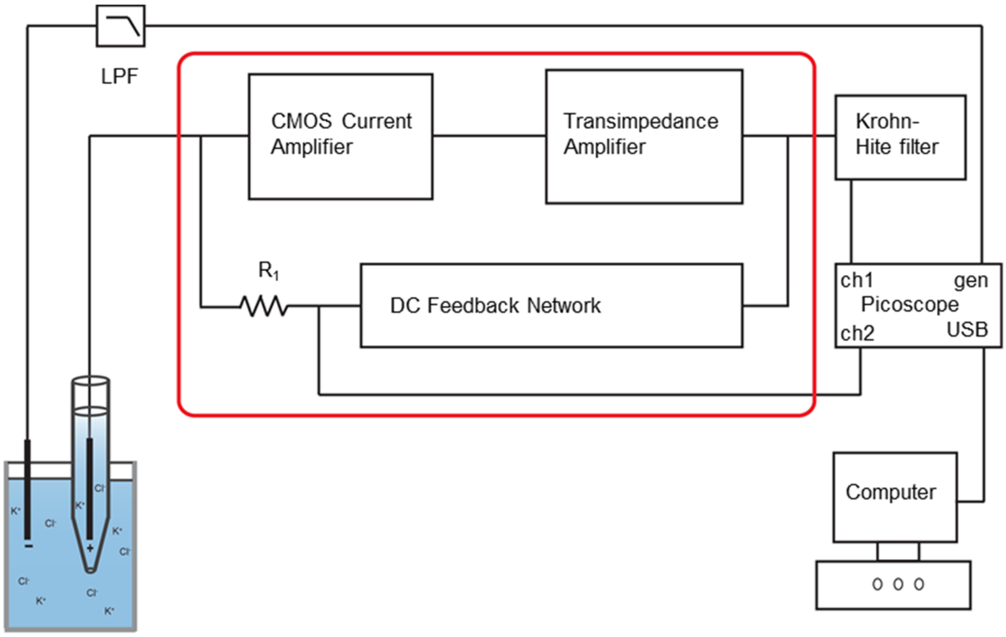

Figure 3.7. Schematic representation of the Polimi amplifier and peripheral hardware. A voltage is applied to the nanopore set-up by the Picoscope oscilloscope and the measured current response is amplified by the bench-top Polimi amplifier, consisting of the components inside the red box. The output voltage (see main text) is low-pass Bessel filtered (8 poles) and converted to a digital signal by the Picoscope then viewed on a computer.

3.2.3 Signal and Noise

For a translocation event, its ΔI and τ will dictate the necessary noise level of the measurement and temporal resolution required respectively. Statistical analysis of translocation events is only possible if these events can be distinguished from the baseline noise. High-frequency noise contributes to the RMS of the measured I(t) signal and increases as the bandwidth of the measurement increases.[11,29] Therefore, a low-pass filter can be used to attenuate the high-frequency components of the ionic current signal being measured.[11,29,30] Some of the filter terminology associated with a low-pass filter are shown in Figure 3.8, where the -3 dB or cut-off frequency (f_c) defines the cut-off between the pass band and the stop band. The pass-band represents the frequency region in which there is no attenuation of the signal, while the stop band represents the region in which the frequency of the signal decreases from the f_c frequency to the maximum frequency of the filter.[30]

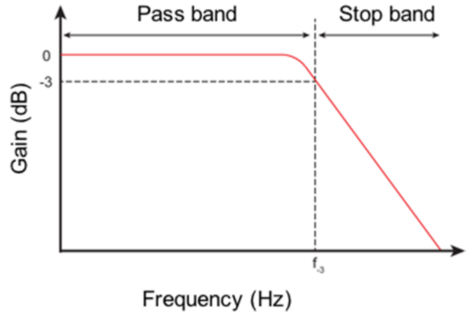

Figure 3.8. Illustration of a low-pass filter and the -3dB (f_c) frequency.[30]

However, applying a low-pass filter to attenuate high-frequency components has the unwanted effect of reducing the temporal resolution of the ionic current modulations, i.e distorting the τ of events as well as distorting the shape of the signal.[11,29] This can therefore, lead to a loss of information on the translocating analyte.

Moreover, the signal is affected by the type of filter used and the number of poles. Typically, for nanopore experiments, a Bessel filter is chosen when investigating current signals in the time domain as the distortion to the shape of the signal in the pass band region is minimal.[29,30] Additionally, the higher the number of poles, the smaller the attenuation between the pass band and stop band of the filter (Figure 3.9).[30]

A further consideration is choosing the correct f_c for the signal's expected duration and minimum acceptable SNR. The rise time (τ_{rise}) of a signal is defined as the time it takes the signal to rise from 10 to 90% of its final value which will affect the ΔI of translocation events.[30] For example, the ΔI of the translocation event will be attenuated if its τ is ≤ 2 the τ_{rise}.[29]

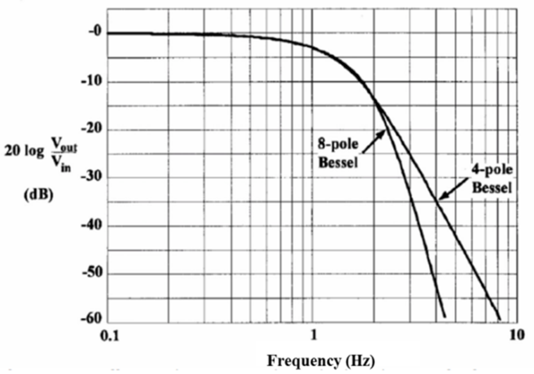

Figure 3.9. Illustration showing the difference between an 8-pole and 4-pole Bessel filter. Figure adapted, with permission from ref. 30.

Figure 3.10 illustrates I(t) traces acquired using the commercial Axopatch 200B (Figure 3.10, a) and Polimi amplifier (Figure 3.10, b) in parallel for the translocation of 4 kbp dsDNA. Two traces were recorded simultaneously for the Polimi amplifier corresponding to the AC channel (Figure 3.10, b left panel) and the DC channel (Figure 3.10, b right panel). The RMS noise of the AC channel, where translocation events are detected is 14 pA which is more than two-fold lower than the Axopatch 200B which had an RMS noise of 34 pA. This decreased RMS noise for the AC channel compared to the Axopatch is important for achieving a high SNR and hence detection of the translocation events.

Figure 3.10, b shows three events that had a ΔI greater than 5 σ cut-off, however due to the larger RMS noise for the Axopatch I(t) trace only events one and two were detected, whereas event three which is indicated by a hollow pink circle is lost in the baseline noise of the trace (Figure 3.10, a). Therefore, low-noise ionic current measurements are needed to achieve a high SNR at a given filter frequency.

Additionally, the two amplifiers differ in their operating bandwidths, the Axopatch 200B has a maximum recording bandwidth of 100 kHz while the Polimi amplifier has a bandwidth in excess of 1 MHz.[28] With the applied filter frequency determining the temporal resolution of events, provided that the sampling rate is greater than this minimum time resolution, at 100 kHz the time resolution is ~0.01 ms while for 1 MHz this value is ~0.001 ms. Therefore, for events with a high enough SNR to be detected, temporal changes that occur on a timescale faster than 0.01 and 0.001 ms for a 100 kHz and 1 MHz bandwidth respectively, will be incompletely resolved and their shape distorted.

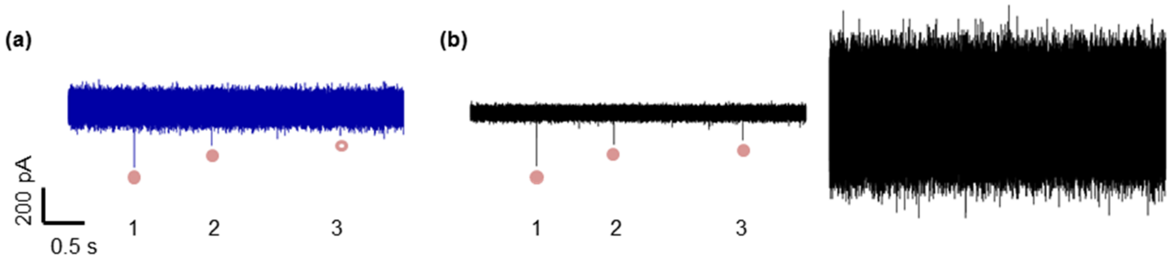

Figure 3.10. Comparison if I(t) traces recorded simultaneously by **(a)** the Axopatch 200B set-up and **(b)** the Polimi 'AC channel' (left panel) and 'DC channel' (right panel). Events that have a ΔI greater than a 5 σ cut-off are indicated by filled in pink circles whereas the event that has a ΔI less than a 5 σ cut-off in (a) is denoted by a hollow pink circle. I(t) traces were recorded for 4 kbp dsDNA in 1 M KCl, 10 mM tris-HCl, 1 mM EDTA, pH 8 with V_{bias} of -500 mV, filter frequency of 60 kHz and a sampling rate of 4 μs.

The advantages of a higher applied filter frequency, assuming a high enough SNR, using the low noise Polimi amplifier are illustrated in Figure 3.11. Two translocations events for 5 kbp dsDNA, recorded in 1 M KCl electrolyte are shown. The event on the left was recorded using an applied filter frequency of 100 kHz while the better resolved event on the right was recorded using an applied filter frequency of 200 kHz, the highest applied filter frequency used for I(t) measurements with the Polimi amplifier in this chapter.

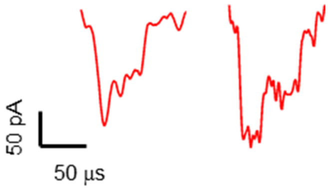

Figure 3.11. Two representative events for 5 kb dsDNA events recorded using a bandwidth of 100 kHz (left) and 200 kHz (right) in 1 M KCl, V_{bias} of -600 mV.

3.2.4 Agarose Gel Electrophoresis of Different DNA Lengths

Prior to nanopore experiments, the purity of the four L_{DNA}; 48.5, 10, 5.31 and 4 kbp used in this study were confirmed by using agarose gel electrophoresis. The 5.31 kbp dsDNA linear sample was obtained by digestion of pET-24a-d(+) plasmid using the restriction enzyme *Bam*H1 which cleaves the plasmid when the sequence 5'-GGATCC- 3' is present. Successful linearisation was confirmed by agarose gel electrophoresis as shown in Figure 3.12, where lanes 1 and 4 show the DNA ladder standard, lane 2 the plasmid and lane 3 the linearised DNA following digestion. Two DNA bands were visible in lane 2 corresponding to the different coiling states of the plasmid; wherein the more intense band is attributed to supercoiled DNA that migrates faster through the gel than the fainter band corresponding to a relaxed species.[31]

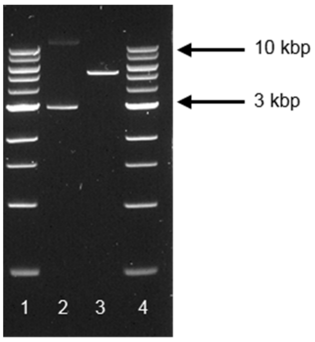

Figure 3.12. Agarose gel electrophoresis image (1%, 4.3 V/cm, 90 min, 1x TAE) confirming linearisation of a pET-24a-d(+) plasmid. **(a)** Lane 1 and 4: '1 kb DNA ladder' (NEB), Lane 2: pET-24a-d(+) and Lane 3: linearised pET-24a-d(+).

The other three L_{DNA} samples were obtained in a linearised conformation as shown in Figure 3.13 together with the linearised 5.31 kbp sample[*] Figure 3.13, a shows a 0.5% agarose gel where lanes 1 and 3 show the DNA ladder standard while lane 2 contains a band that matches the 48.5 kbp of the DNA ladder standard. The other three lengths were confirmed using a 1 % agarose gel as shown in Figure 3.13, b where lanes 1 and 5 show the DNA ladder standard. Lanes 2, 3 and 4 show bands at the correct locations relative to the standard for 10, 5.31 and 4 kbp DNA respectively.

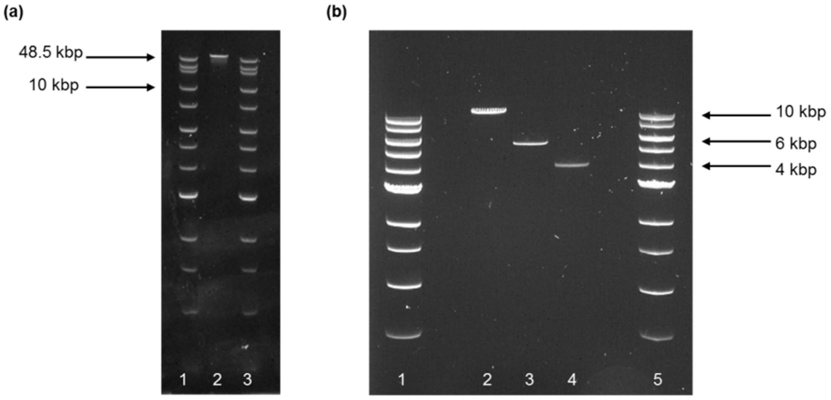

Figure 3.13. Agarose gel electrophoresis image confirming purity of DNA samples. **(a)** Lane 1 and 3: '1 kb extend DNA ladder' (NEB), Lane 2: 48.5 kbp (0.5%, 4.3 V/cm, 175 min, 1x TBE). **(b)** Lane 1 and 5: '1 kb DNA ladder' (NEB), Lane 2: 10 kbp, Lane 3: 5.31 kbp and Lane 4: 4 kbp (1%, 3.8 V/cm, 80 min, 1x TAE).

---

[*] The 4 kbp dsDNA sample used for L_{DNA} experiments was obtained from Dr Azadeh Bahrami, a former research associate in the Albrecht group.

3.2.5 Translocation of Different DNA lengths

Translocation experiments of the four L_{DNA} samples were performed in 1 M KCl, 10 mM trisHCl, pH 8 with nanopipettes that had estimated d_i between 10 – 22 nm. After the addition of DNA to the bulk electrolyte solution to give final DNA concentrations of 100 – 300 pM and applying a negative bias voltage, V_{bias} to the electrode in the external compartment, the negatively charged DNA translocated though the pore causing current blockages or events which were not seen prior to the addition of DNA. Figure 3.14 shows representative I(t) traces before the addition and after the addition of each of the four L_{DNA} at V_{bias} of -300, -500 and -800 mV.

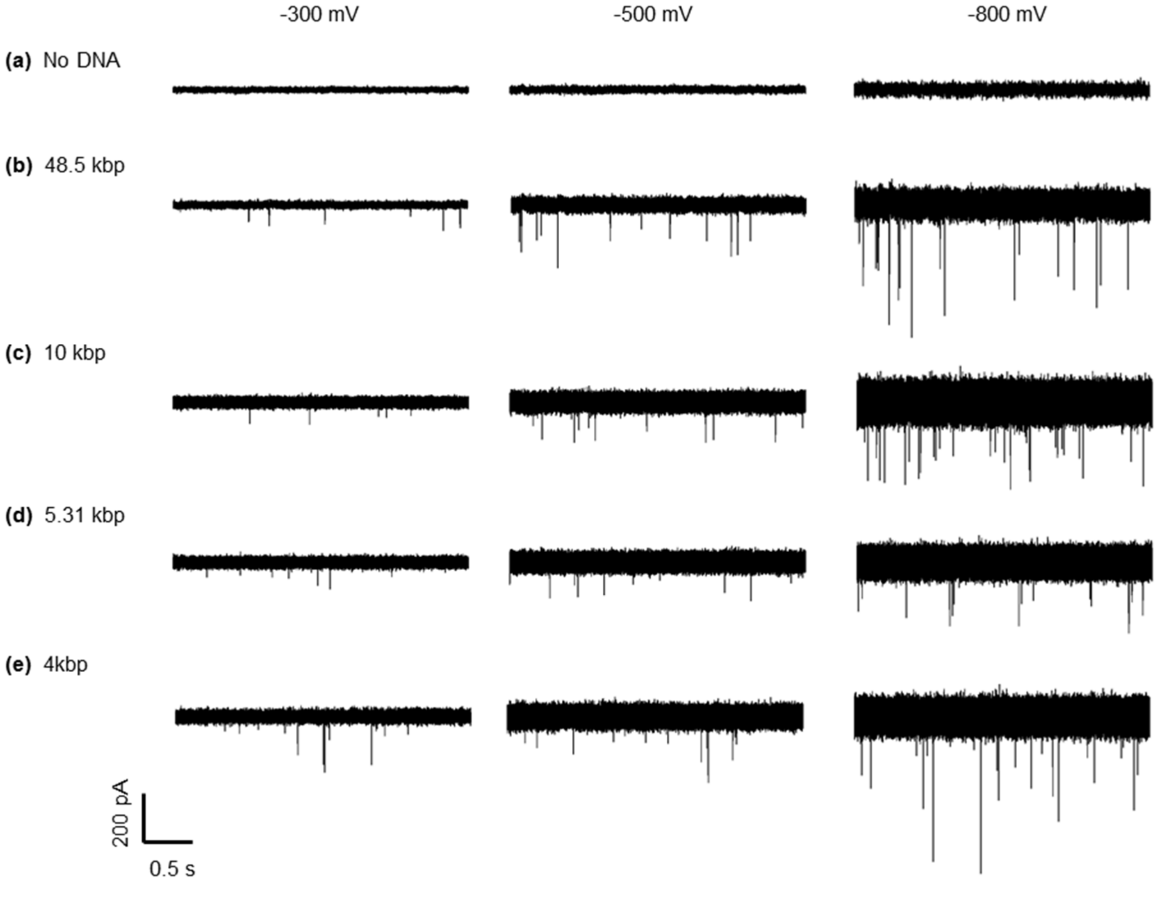

Figure 3.14. Representative I(t) traces with **(a)** no DNA (control), **(b)** 48.5, **(c)** 10, **(d)** 5.31 and **(e)** 4 kbp dsDNA with V_{bias} of -300 mV (left panel), -500 mV (middle panel) and -800 mV (right panel). All I(t) traces with no DNA were filtered at 10 kHz. At V_{bias} of -300 mV a filter frequency of 20 kHz was used for the 48.5 kbp DNA sample, 50 kHz for the 10 kbp DNA sample and 60 kHz was for the 5.31 and 4 kbp DNA sample. At V_{bias} of -500 mV a filter frequency of 50 kHz was used for the 48.5 kbp DNA sample, 100 kHz for the 10 and 5.31 kbp sample and 150 kHz for the 4 kbp DNA sample. At V_{bias} of -800 mV filter frequencies of 100 kHz for the 48.5 kbp DNA sample and 200 kHz for the 10, 5.31 and 4 kbp DNA samples were used.

3.2.5.1. Clustering of DNA Translocation Events

The scatter plots shown in Figure 3.15 for the four L_{DNA} samples each showed two prominent populations. In each case one population had longer τ and smaller ΔI values than the other population. Additionally, in some cases a third population was found which was characterised by short τ and small ΔI.

The two main populations were assigned to translocation of the DNA in either a linear or folded DNA conformation. This has been well documented in the literature,[3,32–35] where the DNA population with a smaller ΔI and longer τ consists of translocation events where the DNA is predominantly in a linear conformation. Conversely, the DNA population with a longer ΔI and shorter τ is assigned to translocation events where the DNA is predominantly in a folded configuration. Wanunu et al,[6] also reported on 'collision' events which they describe as unsuccessful DNA translocation events that are characterised by a small τ.

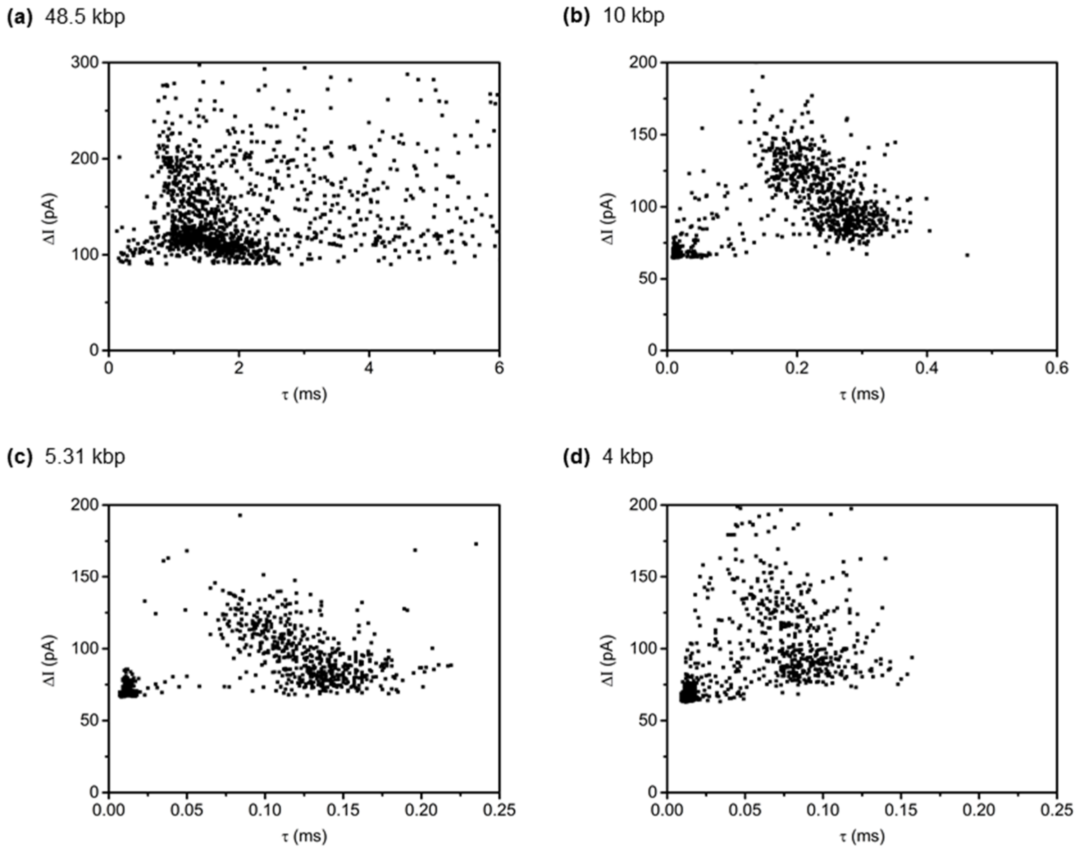

Figure 3.15 Representative scatter plots of τ vs. ΔI for L_{DNA} of **(a)** 48.5, **(b)** 10, **(c)** 5.31 and **(d)** 4 kbp dsDNA at an V_{bias} of -400 mV.

Clustering of the DNA translocation events was achieved by defining a cut-off in the ΔI histogram or using a Gaussian mixture model (GMM) in MATLAB. Figure 3.16, a shows events for 48.5 kbp DNA that were clustered using a ΔI cut-off as populations were not as well defined compared to the 5.31 kbp DNA dataset shown in b where events were clustered using the GMM model. The total number of events (n_t) clustered in Figure 3.16 a and b were 1842 and 834 respectively. When using the GMM, the population of events with a short τ (black) were excluded from the analysis as these were assigned to either collision events or noise. In Figure 3.16, b the I(t) trace was filtered at 100 kHz giving a minimum time resolution on the order of ~0.01 ms which is comparable to the τ of the fast events assigned here to collision events or noise. The shape of these events is likely to be incompletely resolved due to convolution with the filter frequency used.

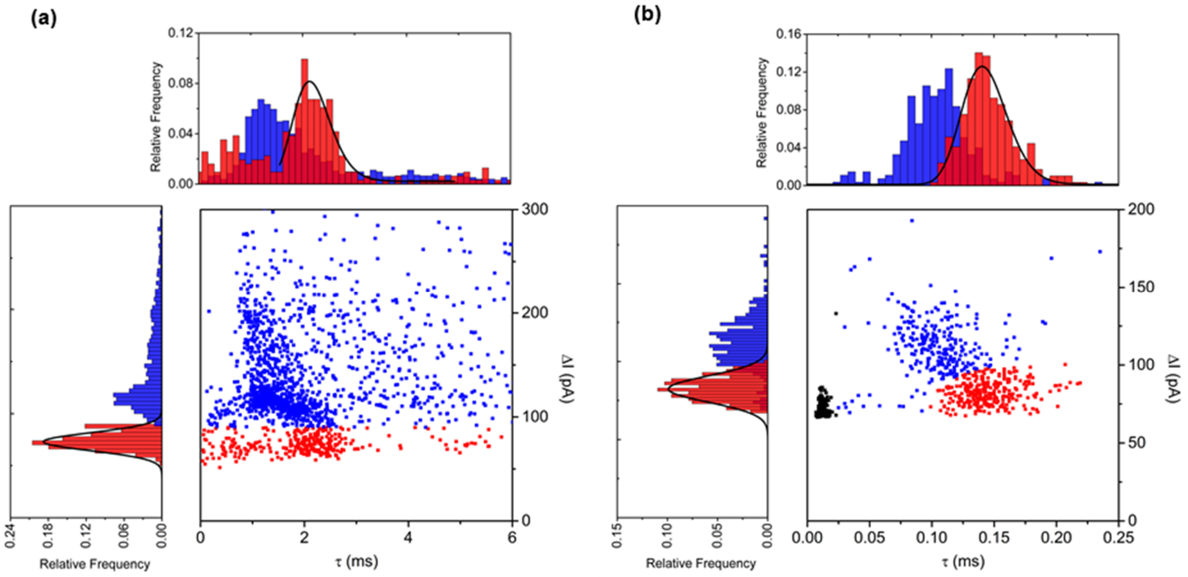

Figure 3.16. Event scatter plot of ΔI vs. τ with V_{bias} of -400 mV for **(a)** 48.5 kbp dsDNA translocations using a ΔI cut-off (n = 1842) and **(b)** 5.31 kbp dsDNA translocations clustered using a GMM model (n = 834). Linear DNA translocations are shown in red while folded DNA translocations are shown in blue. Events in black are attributed to noise or 'collision' events and were not included in the clustering analysis. The corresponding ΔI and τ histograms are shown to the left and above respectively. Events corresponding to linear translocations were fitted with a Gaussian distribution in the ΔI histogram and with a log-normal distribution in the τ histogram. I(t) traces were filtered at 30 and 100 kHz for the 48.5 and 5.31 kbp datasets respectively.

Furthermore, analysis of the event shapes was used to confirm the results obtained using either the ΔI cut-off method or using the GMM to cluster events. As shown in Figure 3.17 and as expected, folded DNA translocations (blue) had a greater ΔI and smaller τ than linear DNA translocations (red). Folded DNA translocations also showed more sub-levels, indicative of non-uniform folding of the DNA molecule as it translocated through the pore. Once translocation events had been clustered, analysis was focused on the better defined linear population of events and for comparison to previous work in the literature (*vide infra*).[5,6]

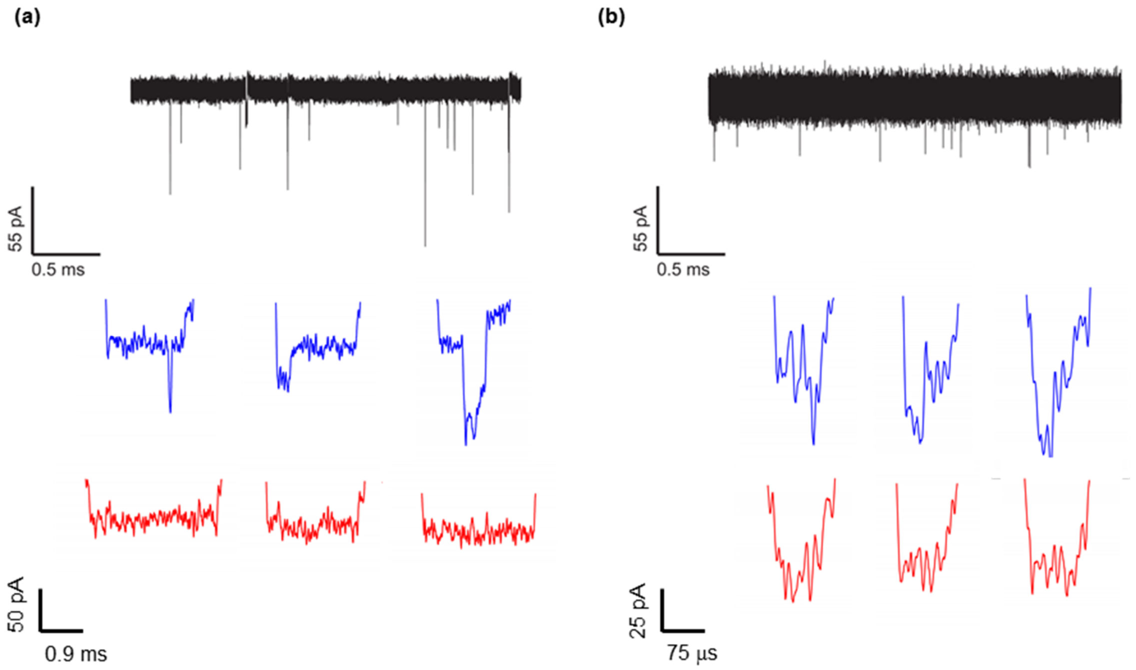

Figure 3.17. Typical I(t) traces with V_{bias} of -400 mV for **(a)** 48.5 kbp DNA, filtered at 30 kHz and **(b)** 5.31 kbp DNA, filtered at 100 kHz. Representative examples of folded (blue) and linear (red) events are shown below each I(t) trace.

3.2.5.2. DNA Capture Rate

The DNA capture rate or the frequency of DNA translocations was analysed to obtain information on the predominant regimes for transport of DNA molecules from the bulk electrolyte solution to the pore's mouth for translocation (see chapter 1). In general, for diffusion-dominated DNA capture rate, a linear relationship between V_{bias} and capture rate is expected.[2,36] In addition, in this regime, the capture rate is independent of L_{DNA}. On the other hand, for an entropic barrier-dominated capture rate, a nonlinear relationship is expected between V_{bias} and capture rate.

Using chip-based solid-state pores in 1 M KCl electrolyte, Wanunu et al. investigated the capture rate as a function of L_{DNA}.[2] The capture rate was found to change from an entropic barrier-dominated regime to a diffusion-dominated regime, at ~8 kbp. Contrary to this finding,[36] using nanopipettes in 1 M KCl electrolyte, a diffusion-limited regime was found for L_{DNA} of 5, 10 and 20 kbp dsDNA. In addition, no significant difference in the capture rate as a function of L_{DNA} was found.

The translocation frequency for the linear population of events was calculated and is defined here as the number of events per second per unit concentration of DNA. Figure 3.18 shows the translocation frequency for the four different L_{DNA}. Due to the large errors calculated here as standard errors of the mean, extracting meaningful information for the 48.5, 10 and 5.31 DNA samples was difficult. For these three L_{DNA}, it is unclear whether the translocation frequency increases linearly with V_{bias} or exponentially with V_{bias}. In contrast to the other three L_{DNA}, for the 4 kbp DNA sample a linear relationship is observed, and the gradient found to be 0.012 ± 0.002 $s^{-1} \cdot pM^{-1} \cdot V^{-1}$. Such a linear relationship indicates diffusion-dominated behavior under these experimental conditions.

(a) 48.5 kbp **(b)** 10 kbp

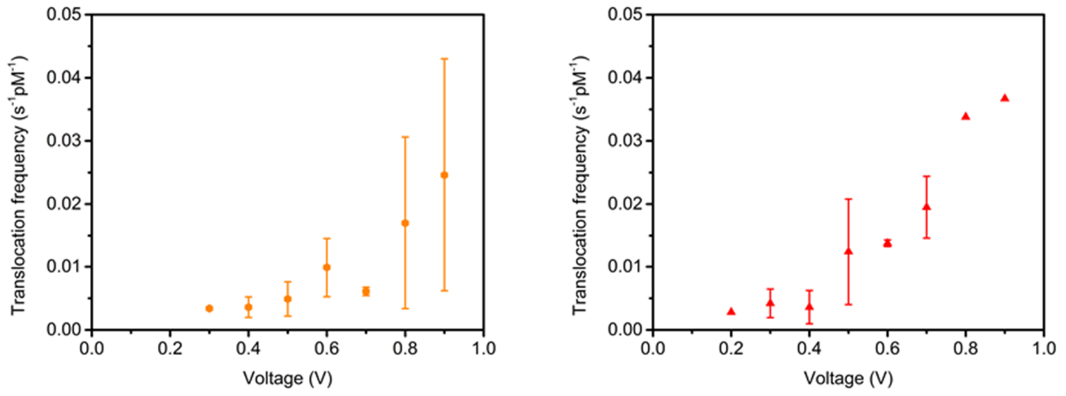

(c) 5.31 kbp **(d)** 4 kbp

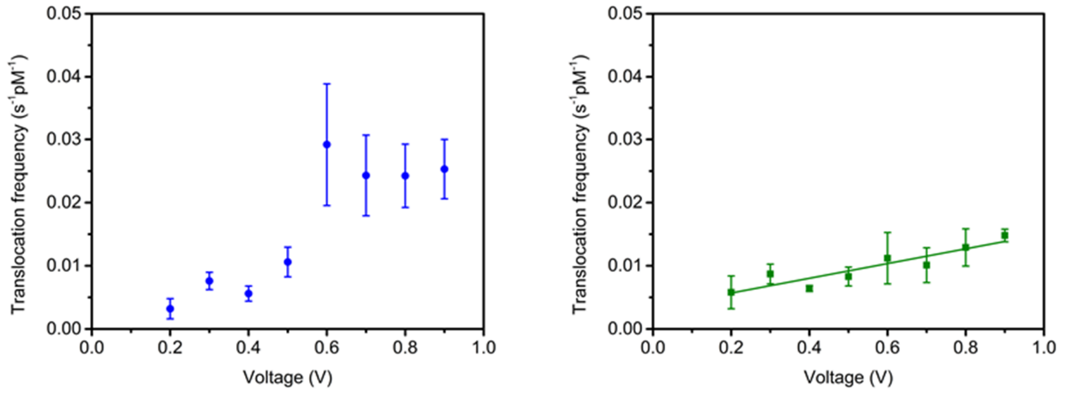

Figure 3.18. Plot of translocation frequency as a function of V_{bias} for **(a)** 48.5, **(b)** 10, **(c)** 5.31 and **(d)** 4 kbp, solid line is a linear fit with slope $m = 0.012 \pm 0.002$ $s^{-1} \cdot pM^{-1} \cdot V^{-1}$, where the error is denoted as the standard error of the fit.

In light of Bell et al. a diffusion-dominated regime was expected in this work using nanopipettes with no significant difference between the capture rate of the four L_{DNA},[36] however this was not the case for three out of the L_{DNA}. The origin of these large error bars for L_{DNA} of 48.5, 10 and 5.31 kbp DNA is unclear although it is speculated that subtle differences in the pore geometries and diameters of the nanopipettes used may contribute to the large error bars.[13,36,37]

3.2.5.3. Dwell Time (τ)

Figure 3.19 shows representative relative τ histograms for V_{bias} of -500 and -700 mV, where the linear population of events was fitted with a log-normal distribution and the maxima used to determine τ_{mp}. The errors denote the standard error of the mean.

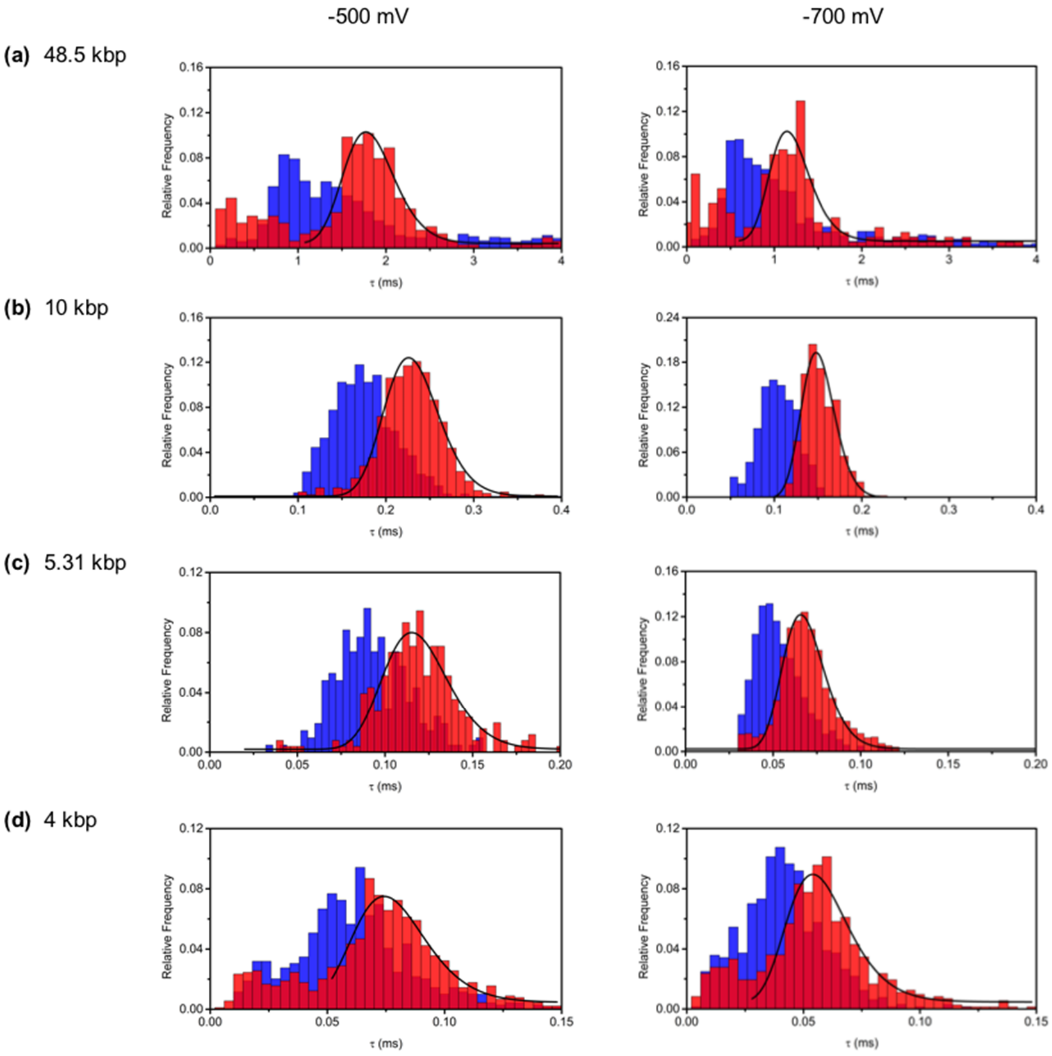

Figure 3.19. Histogram analysis of event τ with V_{bias} of -500 mV (left panel) and -700 mV (right panel) for translocation of **(a)** 48.5, **(b)** 10, **(c)** 5.31, and **(d)** 4 kbp dsDNA. For V_{bias} of -500 mV, I(t) traces were filtered at 50 kHz for the 48.5 kbp sample (n_{le} 315, n_{fe} 1848), 100 kHz for the 10 kbp (n_{le} 821, n_{fe} 968) and 5.31 kbp sample (n_{le} 254, n_{fe} 208) and 150 kHz for the 4 kbp sample (n_{le} 898 n_{fe} 690). For V_{bias} of -700 mV, I(t) traces were filtered at 100 kHz for the 48.5 kbp sample (n_{le} 232, n_{fe} 1019) and 200 kHz was used for the 10 kbp (n_{le} 548, n_{fe} 557), 5.31kbp (n_{le} 1573, n_{fe} 1034) and 4 kbp sample (n_{le} 721 n_{fe} 642).

For the histograms shown in Figure 3.19, the total number of linear events, n_{le} varied between 315 and 915 events while the total number of folded events, n_{fe} varied between 690 and 1848 events for an V_{bias} of -500mV. Likewise, n_{le} varied between 232 and 1573 events while n_{fe} varied between 557 and 1034 events for an V_{bias} of -700 mV. Average τ_{mp} values of 1.59 ± 0.20 (n = 2), 0.25 ± 0.03 (n = 3), 0.11 ± 0.01 (n = 4) and 0.06 ± 0.01 ms (n = 3) for the 48.5, 10, 5.31 and 4 kbp DNA samples respectively, were found at an V_{bias} of -500 mV. On the other hand, for V_{bias} of -700 mV, τ_{mp} values of 1.06 ± 0.05 (n = 3), 0.15 ± 0.01 (n = 2), 0.07 ± 0.01 (n = 2) and 0.05 ± 0.01 ms (n = 3) for the 48.5, 10, 5.31 and 4 kbp DNA samples respectively, were found. As expected a faster τ_{mp} is observed at higher V_{bias} consistent with a stronger electrophoretic driving force acting on the DNA molecules.[18] The full set of τ_{mp} values obtained for seven different V_{bias} are shown in appendix II.

Finally, τ_{mp} was found to be linearly dependent on V_{bias}^{-1} as shown in Figure 3.20, a. The slope, m of each L_{DNA} from Figure 3.20, a was found to be linearly dependent on L_{DNA} (Figure 3.20, b) where m = 0.015 ± 0.001 $ms \cdot V \cdot kbp^{-1}$. This is in line with previous work in the literature by Kowalczyk et al. but differs from Wanunu et al. where τ_{mp} was found to decrease exponentially with increasing V_{bias}.[6,15,38] Smaller τ_{mp} values at higher values of V_{bias} are in line with a greater electrophoretic force acting on the DNA molecules with increasing V_{bias} and hence a shorter τ.

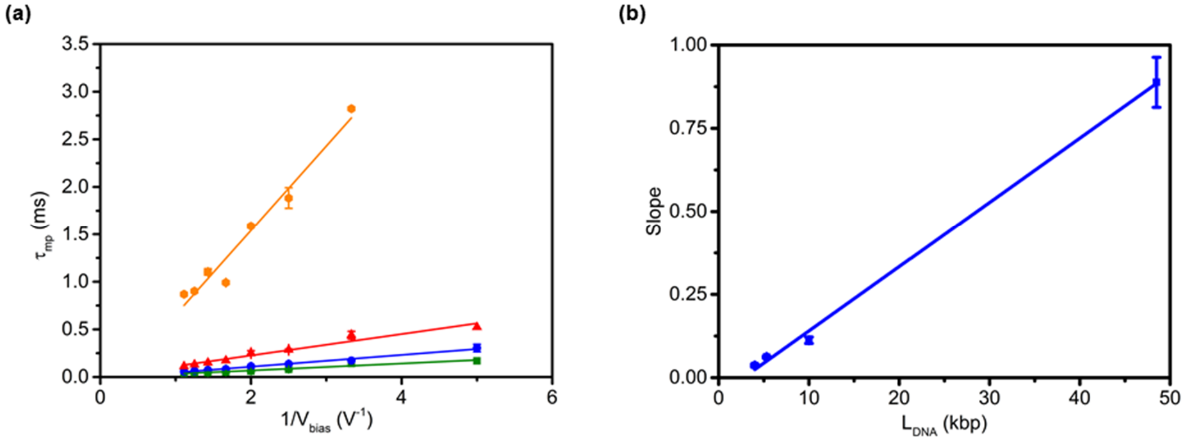

Figure 3.20. **(a)** Scatter plot of τ_{mp} vs. V_{bias}^{-1} for 48.5 (orange hexagons), 10 (red triangles), 5.31 (blue circles) and 4 kbp (green squares) dsDNA. Solid lines are linear fits for each of the four L_{DNA}. The slopes m were obtained as 0.888 ± 0.075, 0.112 ± 0.009, 0.062 ± 0.003 and 0.037 ± 0.003 ms·V for 48.5, 10, 5.31 and 4 kbp respectively. **(b)** Plot of the slope m vs. $L_{DNA,}$ showing a linear relationship, m = 0.0153 ± 0.0003 $ms \cdot V \cdot kbp^{-1}$ and intercept = -0.027 ± 0.008.

3.2.5.4. Peak Amplitude (ΔI)

Next, the ΔI histograms of the four L_{DNA} samples were analysed. Figure 3.21, shows representative relative ΔI histograms for V_{bias} of -500 and -700 mV where the linear population of events was fitted with a Gaussian distribution and the mean used to determine the most probable peak amplitude ΔI_{mp}. Errors denote the standard error of the mean ΔI_{mp}.

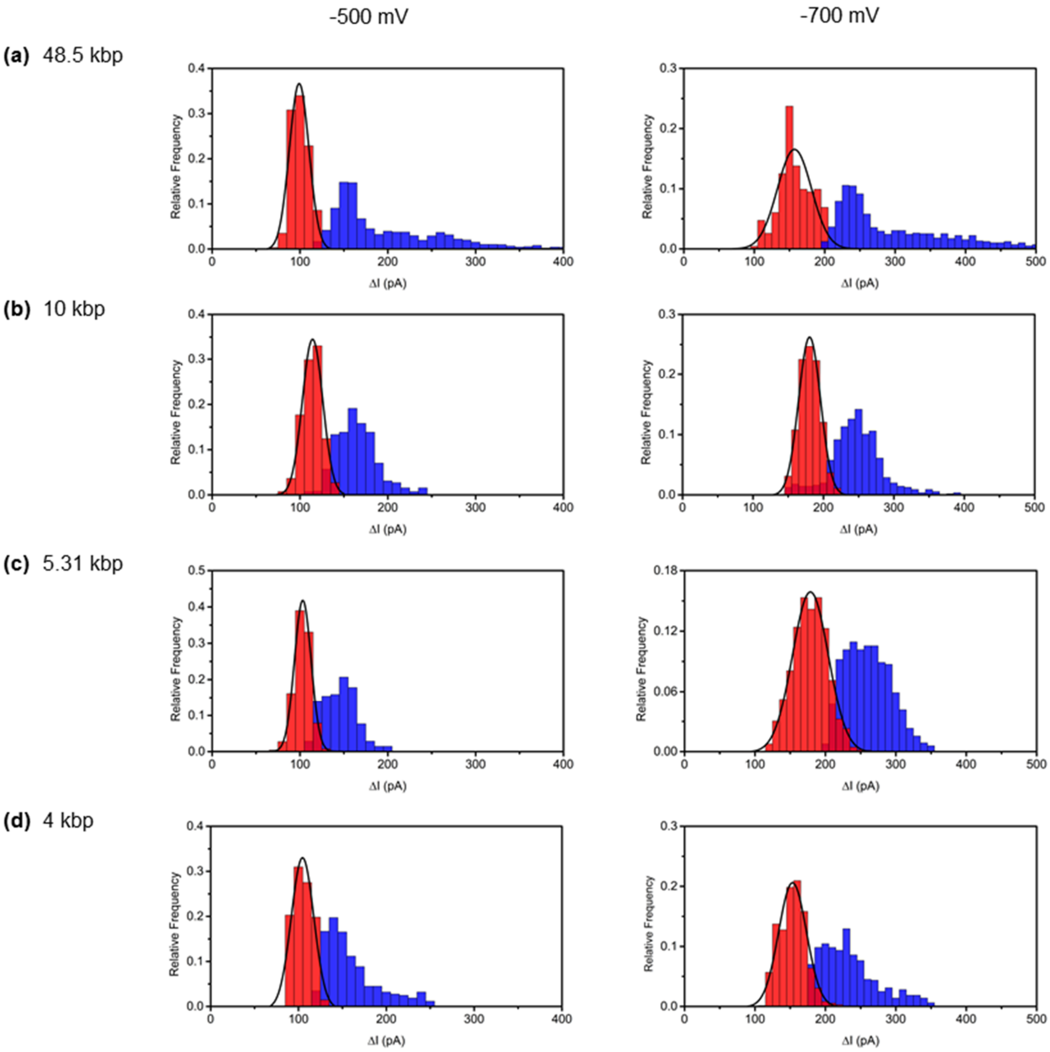

Figure 3.21. Histogram analysis of event ΔI with an V_{bias} of -500 (left panel) and -700 mV (right panel) for translocation of **(a)** 48.5, **(b)** 10, **(c)** 5.31 and **(d)** 4 kbp dsDNA. For an V_{bias} of -500 mV the I(t) traces were filtered at 50 kHz, for the 48.5 kbp sample (n_{le} 315, n_{fe} 1848), 100 kHz for the 10 (n_{le} 821, n_{fe} 968) and 5.31 kbp sample (n_{le} 254, n_{fe} 208) and 150 kHz for the 4 kbp DNA sample (n_{le} 898 n_{fe} 690). For an V_{bias} of -700 mV, the I(t) traces were filtered at 100 kHz for the 48.5 DNA sample (n_{le} 232, n_{fe} 1019) and 200 kHz for the 10 (n_{le} 548, n_{fe} 557), 5.31 (n_{le} 1573, n_{fe} 1034) and 4 kbp sample (n_{le} 721 n_{fe} 642).

For an V_{bias} of -500 mV average ΔI_{mp} values of 99 ± 1 (n = 2), 106 ± 4 (n = 3), 101 ± 6 (n = 4) and 104 ± 4 pA (n = 3) for the 48.5, 10, 5.31 and 4 kbp DNA samples respectively, were obtained. On the other hand, for an V_{bias} of -700 mV average ΔI_{mp} values of 161 ± 4 (n = 3), 180 ± 1 (n = 2), 168 ± 12 (n = 2) and 149 ± 85 pA (n = 3) for the 48.5, 10, 5.31 and 4 kbp DNA samples respectively, were obtained. This is in line with previous reports in the literature which also found ΔI_{mp} values to increase with increasing V_{bias}.[35] The full set of ΔI_{mp} values is shown in appendix III.

Plotting ΔI_{mp} for the linear population of events as a function of V_{bias}, as shown in Figure 3.22 gave a linear relationship, consistent with previous work in the literature using solid-state nanopores in KCl electrolyte.[10,35,39] Linear fits gave gradients of 337 ± 46, 252 ± 21, 273 ± 19 and 275 ± 30 pA·V for the 48.5, 10, 5.31 and 4 kbp DNA sample respectively. Overall, at a given V_{bias}, the ΔI_{mp} was found to be approximately constant. This result can be rationalised by assuming a simple volume-exclusion model where for each L_{DNA} translocating in a linear conformation through the pore, the diameter of the DNA is constant at 2.2 nm and hence the volume of electrolyte volume excluded in each case is also constant.[6]

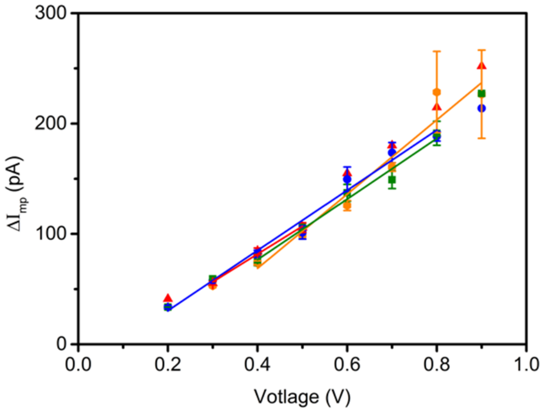

Figure 3.22. Plot of ΔI_{mp} vs. V_{bias} for linear translocation events of 48.5 (orange hexagons), 10 (red triangles), 5.31 (blue circles) and 4 kbp (green squares) dsDNA. Solid lines are linear fits for each the four L_{DNA}. The slopes, m = 337 ± 46, 252 ± 21, 273 ± 19 and 275 ± 30 for 48.5, 10, 5.31 and 4 kbp respectively.

3.2.5.5. Event Charge Deficit (ecd)

The ecd, which is the integral of the ionic current modulation over the duration of a translocation event was analysed for linear translocation events. The ecd reports on the excluded electrolyte charge during the translocation of the DNA molecule through the pore.[33,35]

Figure 3.23 shows the ecd histograms for the linear population of events for each of the four L_{DNA} investigated for V_{bias} of -500 and -700 mV. The ecd distributions were fitted with a

Gaussian distribution and as expected the distributions of the two V_{bias} overlap.[33,35] As for τ_{mp} and ΔI_{mp}, the errors are denoted as standard errors of the ecd mean. The average ecd values for 48.5 kbp dsDNA were identical, with values of 0.103 ± 0.010 (n = 2) and 0.103 ± 0.006 (n = 3) pA·s obtained for V_{bias} of -500 and -700 mV respectively. Similarly, for 10 kbp DNA the average ecd values with an V_{bias} of -500 and -700 mV were very similar to each other at 0.161 ± 0.001 (n = 3) and 0.170 ± 0.001 (n = 2) pA·s respectively. For the 5 kbp DNA sample the average ecd values were 0.007 ± 0.001 (n = 4) and 0.008 ± 0.007 (n = 2) pA·s for V_{bias} of -500 and -700 mV respectively, while finally for the 4 kbp DNA sample the average ecd values were 0.004 ± 0.001 (n = 3) and 0.005 ± 0.001 (n = 3) pA·s for V_{bias} of -500 and -700 mV respectively. With increasing V_{bias} the τ decreases while ΔI decreases so that overall the net effect is that the ecd does not change, as documented previously in the literature.[33,40]

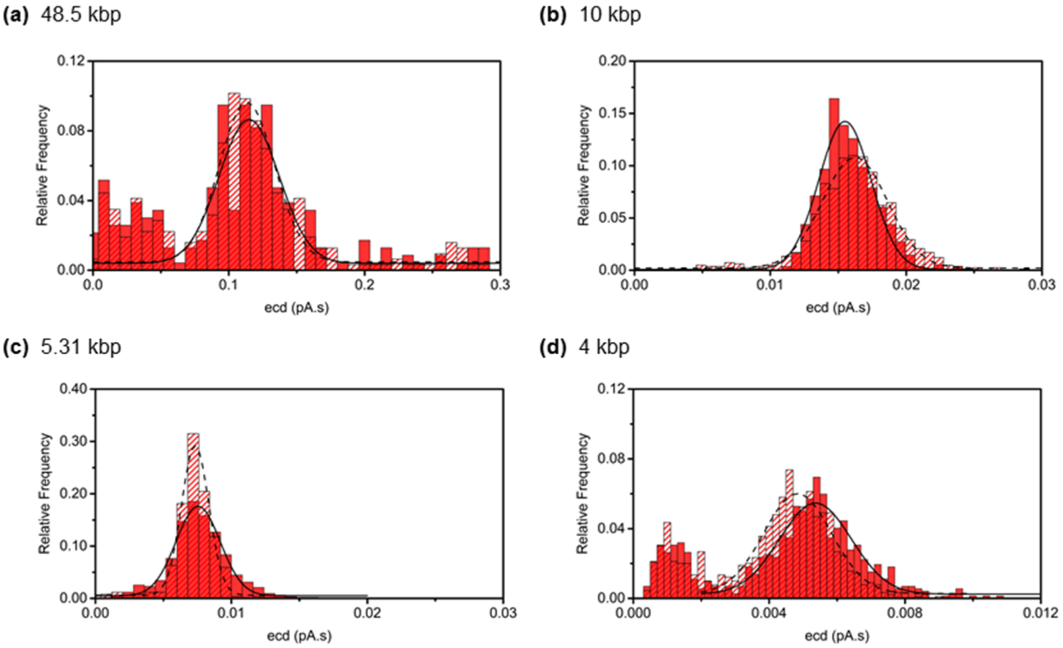

Figure 3.23. Histograms of the ecd for the linear population of translocation events with an V_{bias} of -500 (striped red) and -700 (solid red) mV. For an V_{bias} of -500 mV; (a) n_{le} 315, (b) n_{le} 821, (c) n_{le} 254 and (d) n_{le} 898.For an V_{bias} of -700 mV; (a) n_{le} 232, (b) n_{le} 548, (c) n_{le} 1573and (d) n_{le} 721.

3.2.6 The DNA Length Dependence of the Translocation Time - the Scaling Factor

Finally, τ_{mp} as a function of L_{DNA} for linear translocation events was investigated using nanopipettes operating in 1 M KCl electrolyte, which is the electrolyte commonly used in chip-based nanopore experiments. As aforementioned different scaling factors, p between

DNA length, L_{DNA} and translocation time, τ have been reported in the literature (*vide infra*). Reported values range from $p \approx 1.3$ for solid-state nanopores in 1 M KCl to $p \approx 1$ for nanopipettes in 4 M LiCl.[3–6] It was unclear whether the observed p values could reflect the different properties of the polymer, the electrolyte solution the polymer is in or instead other features of the translocation process, such as DNA/surface adsorption. Bell hypothesised,[5] that the observed p values in chip-based pores may arise due to interactions between the DNA outside of the pore and the membrane. In nanopipettes however, when translocating DNA molecules from the outside to the inside, their high aspect ratio makes DNA adsorption prior to translocation less likely than in chip-based pores where a larger surface is available and hence his observed $p \approx 1$. On the other hand, Wanunu et al.,[6] argue that for their long DNA lengths (~3.5 – 20 kbp), the higher scaling factor observed compared to their short DNA lengths (~150 bp – 3.5 kbp) may be due to interactions between DNA outside the pore region and the nanopore membrane. This argument is reminiscent of Bell's argument, however in both cases no quantitative model was developed.[5,6] Here, p was therefore investigated to shed light on these different reported values and an analytical model to rationalise observed results based on DNA/surface interactions developed.

Figure 3.24 shows on a double logarithmic plot, the relationship of τ_{mp} versus L_{DNA} for the eight V_{bias} measured and where p is equal to the gradient. On average, a scaling factor, $p = 1.22 \pm 0.01$ was found for the eight V_{bias} measured and this was independent of V_{bias}. The p values for each of the eight V_{bias} measured are shown in Table 3.1.

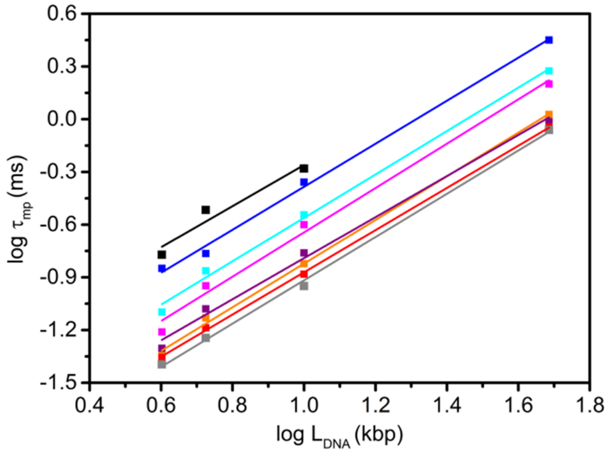

Figure 3.24. Log-log plot of L_{DNA} vs. τ_{mp} with an V_{bias} of -200 (black), -300 (blue), -400 (cyan), -500 (magenta), -600 (purple), -700 (orange), -800 (red) and -900 mV (grey). The scaling factor, $p = 1.22 \pm 0.01$ (average of all V_{bias} measured) and is independent of V_{bias} within experimental error.

Table 3.1. Scaling factors p for different V_{bias}

V_{bias}	*p*	Δp (std. err.)
-900	1.232	0.032
-800	1.201	0.016
-700	1.243	0.037
-600	1.169	0.056
-500	1.262	0.077
-400	1.235	0.052
-300	1.224	0.048
-200	1.170	0.285

The p value determined here is in line with the theoretical value predict by Storm et al. for solid-state nanopores but significantly greater than the p value reported by Bell in nanopipettes using LiCl electrolyte.[3–6] It is also slightly lower than other reported values in the literature for solid-state pores in 1 M KCl.[3,4,6] It was hypothesised that DNA/surface interactions could explain some of the wide range of p values observed in the literature, as discussed in the next section.

3.2.7 The Potential Role of Surface Friction

A range of p values had been reported in the literature for solid-state planar devices in KCl electrolyte and nanopipettes in LiCl electrolyte. For the first time, the scaling factor was determined in nanopipettes using KCl electrolyte, giving p = 1.22 ± 0.01. To rationalise this and other results theoretically, DNA adsorption to the surface of the pore prior to its translocation was considered by extending the Ghosal model.[7,8,†] In this extended model, "Ghosal+" the DNA initially adsorbs to the surface of the nanopore on the 'cis' side (*vide infra*), one end of the DNA molecule then enters the pore and finally the strand is pulled through the nanopore one bp at a time to the 'trans' side.

In this Ghosal+ model, again the pore is modeled as cylindrical-shaped where the part of the polyelectrolyte inside the pore is a rigid cylindrical rod (see Figure 3.1). At a given moment in time, the number of monomers adsorbed to the pore wall before translocations,

---

[†] Extended Ghosal+ model derived by Dr Tim Albrecht.

N_{ads} (i.e. the cis side) is equal to the total number of monomers (N_p) in the polymer minus the number of monomers that have translocated (N_{mt}) as expressed in equation (3.4).

$$N_{ads} = \left(N_p - N_{mt}\right)^{\alpha} \tag{3.4}$$

Where α is an exponent that scales with the number of monomers on the 'cis' side of the pore and the assumption that α does not change during the translocation process is made. Two possible values of α are considered schematically in Figure 3.25, where during translocation the monomers pass from the arbitrarily defined 'cis' chamber to the 'trans' chambers.

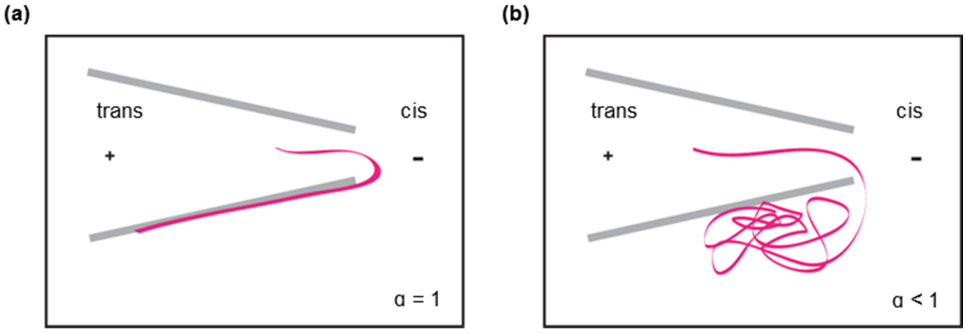

Figure 3.25. Schematic representation of DNA/surface interactions when **(a)** all DNA monomers on the 'cis' side of the pore are adsorbed to the pore surface, α = 1 and **(b)** when the DNA on the cis side is in a globular conformation and only a few bp are adsorped to the pore wall, α < 1.

When α is equal to 1 all the DNA monomers on the cis side of the pore are adsorbed to the pore surface, while when α is less than one the monomers on the cis side of the pore are in a more globular conformation which is more akin to the state in solution.[4] The friction force (F_R) is defined by equation (3.5).

$$F_R = N_{ads} \cdot \beta \cdot v = \left(N_p - N_{mt}\right)^{\alpha} \cdot \beta \cdot v \tag{3.5}$$

Where β is the friction coefficient and v the translocation speed.

During the translocation process, for an infinitely small amount of time, the assumption that the electrophoretic, viscous and friction force acting on the DNA equals zero is made as expressed in equation (3.6). This expression is an extension of the Ghosal model (*vide infra*), in which only the electrophoretic and viscous forces are considered.[8]

$$\mathrm{F_e + F_v + F_R = 0}$$

(3.6)

Where F_e, F_v and F_R are the electrophoretic, viscous and friction force respectively. F_e and F_v are given by equation (3.7) and (3.8) respectively, and can be found in ref. 8.

$$\mathrm{F_e} = -2\pi \cdot \varepsilon \cdot \mathrm{E_0} \cdot \mathrm{a} \cdot \Phi'(\mathrm{a})$$

(3.7)

$$\mathrm{F_v} = 2\pi \cdot \varepsilon \cdot \mathrm{E_0} \cdot \mathrm{a} \cdot \Phi'(\mathrm{a}) + \frac{2\pi \cdot \quad {}_{\mathrm{d}}}{\ln\left(\frac{\mathrm{a}}{\mathrm{R}}\right)} \cdot \mathrm{v} + \frac{2\pi \cdot \varepsilon \cdot \mathrm{E_0}}{\ln\left(\frac{\mathrm{a}}{\mathrm{R}}\right)} \cdot \left(\zeta_{\mathrm{w}} - \zeta_{\mathrm{p}}\right)$$

(3.8)

Where ε is the dielectric constant of the electrolyte, Φ' the Coulomb potential, a the cross-sectional radius of the polymer, R the radius of the cylindrical-shaped pore, η_d the dynamic viscosity of the electrolyte, v the translocation speed of the polymer, E_0 the electric field inside the pore and finally ζ_w and ζ_p, the ζ-potentials at the surface of the pore wall and the polymer, respectively.

Substituting equations (3.5), (3.7) and (3.8) into equation (3.6) and rearranging for v gives:

$$\mathrm{v} = -\frac{\frac{2\pi \cdot \varepsilon \cdot \mathrm{E_0}}{\ln\left(\frac{\mathrm{a}}{\mathrm{R}}\right)}\left(\zeta_{\mathrm{w}} - \zeta_{\mathrm{p}}\right)}{\frac{2\pi \cdot \mu_{\mathrm{d}}}{\ln\left(\frac{\mathrm{a}}{\mathrm{R}}\right)} + \left(\mathrm{N_p} - \mathrm{N_{mt}}\right)^{\alpha}\beta}$$

(3.9)

However, the translocation speed, v may also be written as:

$$\mathrm{v} = \rho_{\mathrm{N}} \cdot \frac{\mathrm{dN_{mt}}}{\mathrm{dt}} \approx \rho_{\mathrm{N}} \cdot \frac{\Delta \mathrm{N_{mt}}}{\Delta \mathrm{t}}$$

(3.10)

Where ρ_N is the distance between two bp (0.34 nm/ bp for dsDNA)[17,41] and Δt is the time required to pass ΔN_{mt} through the pore. When one monomer passes through the pore, i.e. $\Delta N_{mt} = 1$, then Δt is given by:

$$\Delta \mathrm{t}\ (\mathrm{N_{mt}}) = \rho_{\mathrm{N}} \cdot \frac{1}{\mathrm{v}(\mathrm{N_{mt}})}$$

(3.11)

Then, substituting equation (3.9) into equation (3.11), gives:

$$\Delta t\,(N_{mt}) = -\frac{\rho_N\ d}{\varepsilon \cdot E_0 \cdot \left(\zeta_w - \zeta_p\right)} - \frac{\left(N_p - N_{mt}\right)^{\alpha} \rho_N \cdot \beta \cdot \ln\left(\frac{a}{R}\right)}{2\pi \cdot \varepsilon \cdot E_0 \cdot \left(\zeta_w - \zeta_p\right)}$$

(3.12)

Thus, the increment in time, Δt required for each monomer from $N_{mt} = 1$ to N_p to pass through the pore can be summed over all N_p, giving the translocation time, τ as expressed in equation (3.13).

$$\tau = \sum_{N_{mt}=1}^{N_p} \Delta t(N_{mt})$$

(3.13)

This can then be expressed as shown in equation (3.14).

$$\tau = -\frac{\rho_N \cdot\ d}{\varepsilon \cdot E_0\left(\zeta_w - \zeta_p\right)} \cdot N_p - \left(\frac{\ln\left(\frac{a}{R}\right)}{2\pi \cdot \varepsilon \cdot E_0 \cdot \left(\zeta_w - \zeta_p\right)} \cdot \rho_N \cdot \beta \cdot \sum_{1}^{N_p} \left(N_p - N_{mt}\right)^{\alpha}\right)$$

(3.14)

The summation, on the right hand side can be solved analytically by Euler-Maclaurin summation or when Np is large enough, approximated by an integral, which gives:

$$\sum_{N_{mt}=1}^{N_p} \left(N_p - N_{mt}\right)^{\alpha} \approx \frac{{N_p}^{\alpha+1}}{\alpha + 1}$$

(3.15)

The τ, in equation (3.14) can then be expressed by equation (3.16), where $\left(\zeta_w - \zeta_p\right) < 0$.

$$\tau \approx -\frac{\rho_N \cdot\ d}{\varepsilon \cdot E_0\left(\zeta_w - \zeta_p\right)} \cdot N_p - \frac{\ln\left(\frac{a}{R}\right)}{2\pi \cdot \varepsilon \cdot E_0 \cdot \left(\zeta_w - \zeta_p\right)} \cdot \rho_N \cdot \beta \cdot \frac{{N_p}^{\alpha+1}}{\alpha + 1}$$

(3.16)

Therefore, if the friction coefficient, β is negligible or for small values of N_p, then:

$$\tau \approx -\frac{\rho_N \cdot\ d}{\varepsilon \cdot E_0\left(\zeta_w - \zeta_p\right)} \cdot N_p \ \text{or} \log(\tau) \propto \log(N_p)$$

On the other hand, in the limit of large N_p, τ is approximately given by:

$$\tau \approx -\frac{\ln\left(\frac{a}{R}\right)}{2\pi \cdot \epsilon \cdot E_0 \cdot \left(\zeta_w - \zeta_p\right)} \cdot \beta \cdot \rho_N \cdot \frac{{N_p}^{\alpha+1}}{\alpha+1} \text{ or } \log(\tau) \propto (\alpha+1) \cdot \log(N_p) \tag{3.17}$$

The transition from the two limits (small N_p and large N_p) thus depends on the friction coefficient, β. In the limit of small N_p, the scaling factor is $p = 1$ while in the opposite limit for large N_p, $p = \alpha+1$. Moreover, for large N_p, the expression $\log(\tau) \propto (\alpha + 1) \cdot \log(N_p)$ is in the form of $y = mx$, where $m = \alpha+1$. This can be related to the log-log plot of τ_{mp} versus L_{DNA}, shown in Figure 3.24, where the gradient m is equal $\alpha+1$. It therefore follows that p is equal to $\alpha+1$ and referring back to Figure 3.25, when α is equal to one, p is equal to two while when α is less than one, this gives a p value that is less than two.

Experimentally, p here was found to be 1.22 ± 0.01 which suggests that DNA/surface interactions prior to translocation may be an important factor to consider. This value differs from previous work in the literature using nanopipettes in 4 M LiCl where $p \approx 1$.[5] However, the value reported here is close to $p \approx 1.3$ which has been observed for chip-based solid-state nanopores.[3,4,6] Subtle differences between the various nanopore platforms and electrolyte solutions give different p values, which is difficult to reconcile in a model where the p value results from the hydrodynamic drag acting on the DNA blob at the entrance of the pore.[4] Thus, other effects, such as DNA adsorption to the surface prior to translocation may contribute to the observed values of p. The Ghosal+ model, described here suggests that DNA/surface interactions prior to DNA translocation through the pore may be an important part of the translocation process and approximately covers the range of experimentally observed p values.

3.2.8 Modification of Nanopipette Surface Charge via Silane Deposition

Investigation of τ_{mp} as a function of V_{bias} together with the extended Ghosal model suggested that surface adsorption of DNA molecules prior to translocation may be an important factor contributing to the translocation process. To probe this experimentally, the negative charge of the quartz nanopipette at pH 8 (pKa 2-3) was made positive using silane chemistry.[42] This was expected to change the level of surface interactions between the (negatively charged) DNA and the nanopipette surface.

Vapour phase deposition was used to chemically couple the organosilane, APTMS to the quartz surface of nanopipettes. The structure of APTMS is shown in Figure 3.26. At pH 8, which is the same pH used to study the different L_{DNA} above, the amino group is expected to be positively charged as its pKa value is ~9.[16,43‡] It was expected that the negatively charged DNA would adsorb more strongly to a positively charged surface compared to the negatively charged quartz nanopipette surface at pH 8.

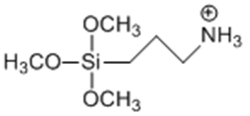

Figure 3.26. Chemical structure of APTMS.

Nanopipettes were oxygen plasma cleaned after pulling to remove any organic surface contaminants and to expose the free hydroxyl groups for reaction with APTMS.[44,45] The reaction involved four steps, as shown in Figure 3.27. Initially, the methoxy groups of APTMS are hydrolysed followed by condensation of these hydrolysed products. The resulting oligomer hydrogen bonds to the surface hydroxyl groups then in the final stage, covalent bonds are formed with loss of water.[45–47]

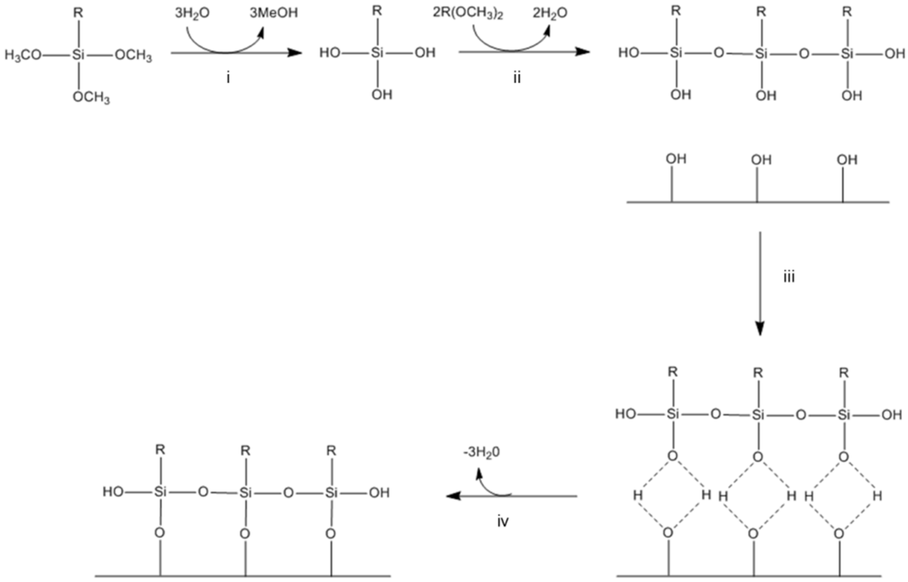

Figure 3.27. Reaction scheme for APTMS deposition on quartz, where R = $(CH_2)_3NH_2$. Mechanism involves step (i) hydrolysis of methoxy groups; (ii) condensation; (iii) hydrogen bonding to surface and (iv) formation of covalent linkages.

[‡] Surface pKa values are lower than solution pKa values, however determination of surface pKa value depends on conditions and techniques used.[16,54–56]

3.2.9 Contact Angle (θ_c) Measurements

Coating of the negatively charged quartz with APTMS was expected to make the surface more hydrophobic.[48] Figure 3.28 shows images of water droplets on (a) uncoated and (b) APTMS coated quartz slides. These images were analysed using 'ImageJ' software to determine the θ_c.[§] Contact angles of 18 ± 4° (n = 2) and 38 ± 1° (n=4) were determined for the uncoated and coated respectively. An increased contact angle upon coating of the quartz slide is consistent with a more hydrophobic surface.

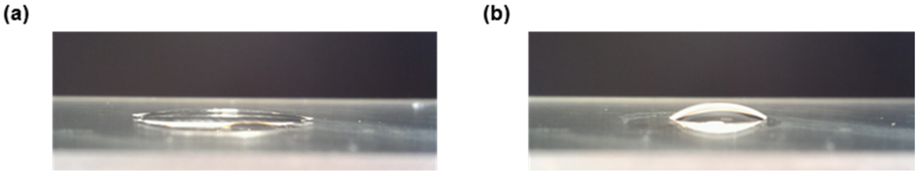

Figure 3.28. Contact angle (θ_c) measurements of water drops on **(a)** plasma cleaned quartz slide and **(b)** APTMS-coated quartz slide.[49]

3.2.10 Electrochemical Characterisation of APTMS-Coated Nanopipettes

Initially, the APTMS coated nanopipette was characterised using CV measurements (Figure 3.29). In 1 M KCl, the pore conductance was expected to depend solely on the bulk KCl electrolyte conductance (Ohmic behaviour, *vide infra*).[16,23] However, the I-V curve for the APTMS modified nanopipette, showed ion current rectification (non-Ohmic behaviour).

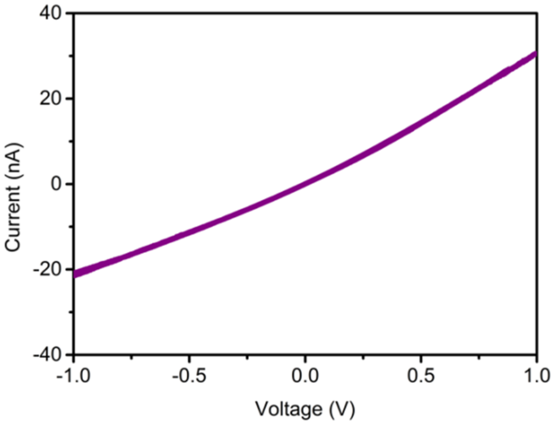

Figure 3.29. CV measurements for an APTMS-coated nanopipette with an estimated d_i of 10 nm (G_{pore} = 30 nS, r = 0.8).[**]

[§] Contact angle measurements and analysis performed by Tina Leontidou, MSci student in the Albrecht group.[49]

[**] G_{pore} was calculated using a V_{bias} range of -100 to +100 mV range while r was calculated at V_{bias} of -500 mV.

Ion current rectification has been reported in nanopipettes with charged surface walls and an asymmetric tip geometry.[52,53] This ion current rectification can be quantified using the rectification ratio, r defined by equation (3.18).[50]

$$r = \left|\frac{i_{-1}}{i_{+1}}\right| \tag{3.18}$$

Where i_{-1} is the ion current at a given negative V_{bias} and i_{+1} is the ion current at the same positive V_{bias}.

In the present case, r = 0.8, indicating an increased current at positive V_{bias} compared to negative V_{bias}. One possible explanation for this ion current rectification is that the surface charge density for the APTMS modified nanopipettes is greater than that of an unmodified nanopipette. Ion current rectification in 1 M KCl electrolyte has been reported previously by Kim et al., using (3-aminopropyl)triethoxysilane (APTES) coated chip-based solid-state nanopores.[51]

In the present case the positively charged nanopipette surface is balanced by Cl^- ions. The changing geometry of the conical nanopipette tip results in different electrostatic potentials (Φ_{ep}) experienced by the Cl^- ions. Ion current rectification was observed by Siwy et al.,[52,53] in negatively charged conical nanotubes with diameters less than ~15 nm and their results were rationalised on a model based on an uneven electrostatic potential profile due to the conical shape. Such a model could also explain the ion current rectification observed for the APTMS modified nanopipette as discussed herein.

In the absence of a V_{bias}, the Cl^- ions experience a non-constant Φ_{ep} that changes as a function of the x distance (Figure 3.30). In the narrowest pore region which is in contact with the electrolyte solution, Φ_{ep} is constant (i to ii). Then in the portion of the charged conical nanopipette where the diameter is comparable to the thickness of the electrical double-layer, the potential of the Cl^- ions is lowered due to electrostatic interactions with the positively charged surface (ii to iii). The potential of the Cl^- ions then increases as the diameter of the conical nanopipette increases in the x direction, as shown by the increasing slope. Finally, section iii to iv shows the Φ_{ep} when the diameter of the nanopipette becomes much greater than the electrical double-layer thickness.

When a negative V_{bias} is applied to the electrode inside the nanopipette (Figure 3.20, b), the solution voltage drop for Cl^- ions increases linearly with increasing x direction while the opposite case occurs when a positive V_{bias} is applied (Figure 3.20, c). When applying a V_{bias}, the electrostatic potentials combine to give two regimes (Figure 3.20 b and c, right panels). In the case of a negative V_{bias}, the resulting electrostatic potential profile effectively turns counterclockwise creating a Cl^- electrostatic trap. In the opposite case of a positive V_{bias}, the resulting electrostatic potential profile effectively turns clockwise and therefore there is no Cl^- electrostatic trap. In such a case there in an increase in current compared to that expected by Ohmic behaviour as the Cl^- ions shielding the charged surface also contribute to the current. Overall, different ion current magnitudes are possible due to the different electrostatic profiles for negative and positive V_{bias}.

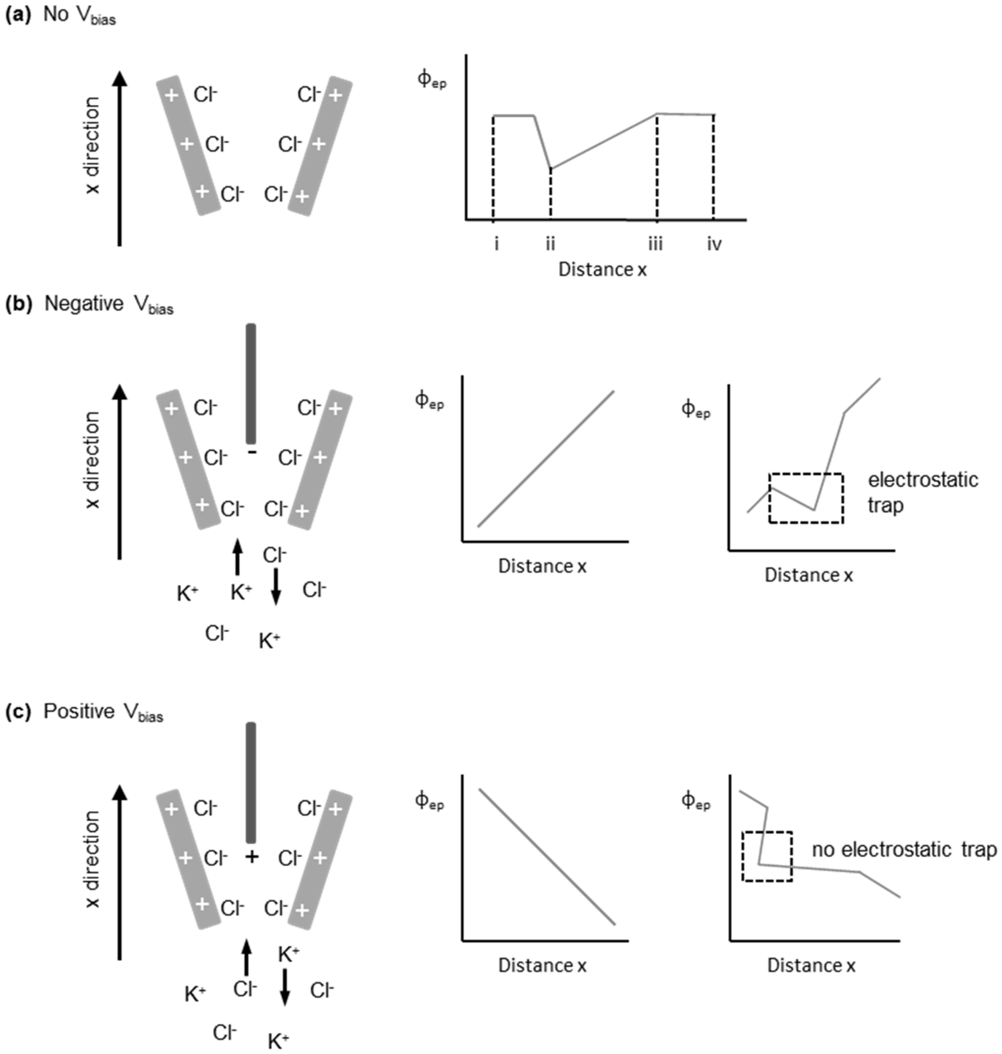

Figure 3.30. (a) Positively charged nanopipette and the electrostatic potential (Φ_{ep}) profile for Cl^- ions with no V_{bias}. Schematic representation of positively charged nanopipette and surrounding ions for a **(b)** negative and **(c)** positive V_{bias} (left) shown together with the solution voltage drop profile experienced by Cl^- ions (middle) and the overall nanopipette Φ_{ep} profile (right).[53]

3.2.11 DNA Translocation Using a Silane Modified Nanopipette

For comparison with previous data in this chapter, the translocation of 100 pM of 4 kbp dsDNA was performed in 1 M KCl, 10 mM trisHCl, pH 8. Figure 3.31 shows representative I(t) traces for 4 kbp DNA translocations using an APTMS-coated nanopipette at three different V_{bias}.

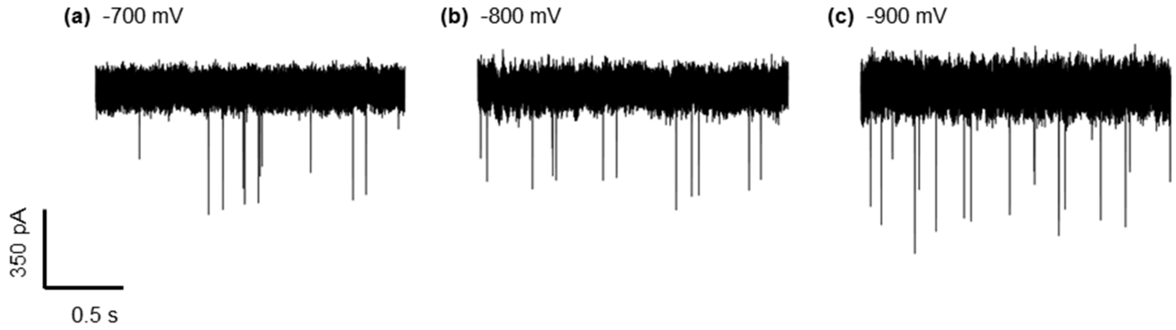

Figure 3.31. Representative I(t) traces for **(a)** -700 **(b)** -800 and **(c)** -900 mV for the APTMS-coated nanopipette (G_{pore} = 30 nS, r = 0.8). All I(t) traces were filtered at 200 kHz.

The scatter plots of τ versus ΔI for all translocation events detected with the APTMS-coated nanopipette are shown in Figure 3.32. As expected, increasing V_{bias} from -700 to -900 mV, decreased the τ while increasing ΔI. This is consistent with a greater electrophoretic force acting on the DNA molecules at a higher V_{bias}. The ecd remains constant for a given L_{DNA}, therefore as the τ decreases with increasing V_{bias}, the opposite trend is observed for ΔI which increases with increasing V_{bias}.[33] For each V_{bias}, two populations of events were observed similar to translocations in unmodified nanopipettes. These were clustered, as discussed in sections 3.2.11.1.

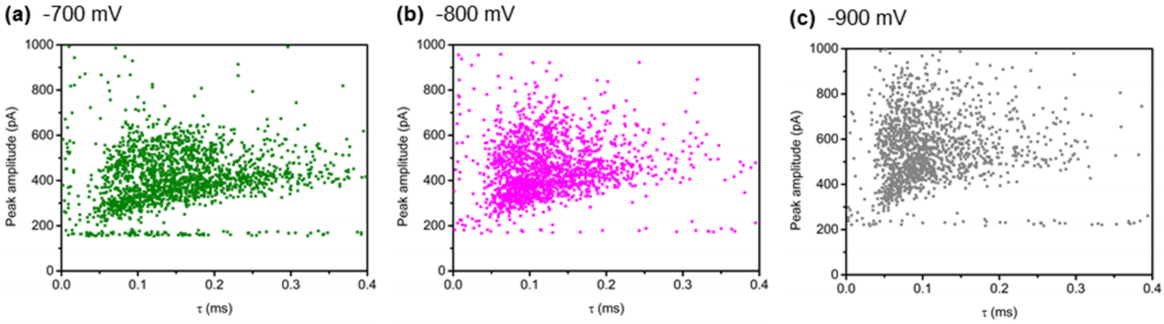

Figure 3.32. Scatter plot of τ vs. ΔI for APTMS-coated nanopipette (G_{pore} = 30 nS) with an V_{bias} of **(a)** -700, **(b)** -800 and **(c)** -900 mV. All I(t) traces were filtered at 200 kHz.

The translocation events for 4 kbp DNA in the APTMS-coated nanopipette (purple) were then compared to the unmodified nanopipettes (black) used in the L_{DNA} study as shown in the scatter plots in Figure 3.33.[††] Coating of nanopipettes with APTMS increased the τ and ΔI, consistent with a greater DNA/surface interaction.

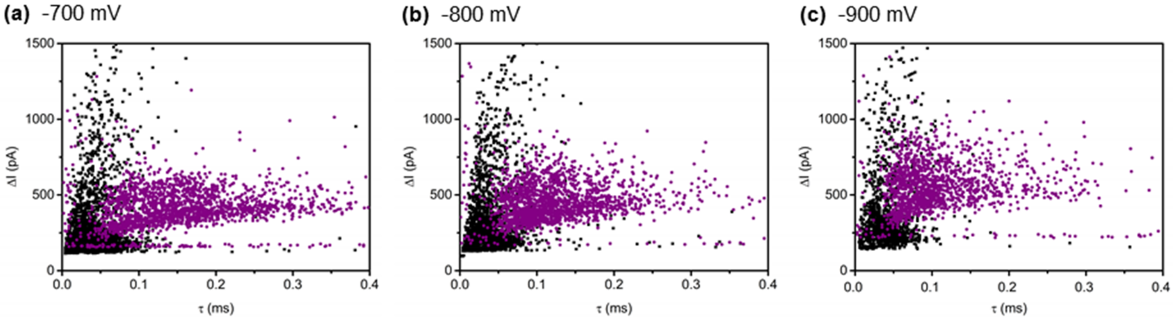

Figure 3.33. Scatter plot of τ vs. ΔI for unmodified (black) and APTMS coated (purple) nanopipette with V_{bias} of **(a)** -700, **(b)** -800 and **(c)** -900 mV. For the unmodified nanopipettes with V_{bias}; -900 mV (n = 2), G_{pore} = 37 and 35 nS, -800 mV (n = 2), G_{pore} = 37 and 35 nS and -700 mV (n = 2), G_{pore} = 37, 35 and 29 nS.

3.2.11.1. Clustering of DNA Translocation Events in APTMS Coated Nanopipettes

Figure 3.34, shows scatter plots of τ versus ΔI, for the clustering of translocation events in APTMS modified nanopipettes with representative translocation events at V_{bias} of -800 mV for linear and folded DNA translocations. As with some of the L_{DNA} data presented earlier in this chapter, clustering was achieved using the GMM model. The population of events with a short τ (black events) were excluded from the analysis as these were assigned to either collision events or noise. The cluster with a smaller ΔI than the other cluster was attributed to primarily DNA translocations in a linear conformation while the cluster with a larger ΔI was attributed to mainly DNA translocations in a folded conformation. As seen with unmodified nanopipettes, folded DNA translocations (blue) overall showed more sub-levels than those of linear DNA translocations. This is indicative of non-uniform folding of the DNA molecule during translocation through the pore. For comparison with previous work presented in this chapter, analysis was focused on the better defined linear population of events.

[††] Different nanopipettes were used, however the G_{pore} values of the nanopipette were similar making comparisons between unmodified and APTMS modified nanopipettes reasonable.

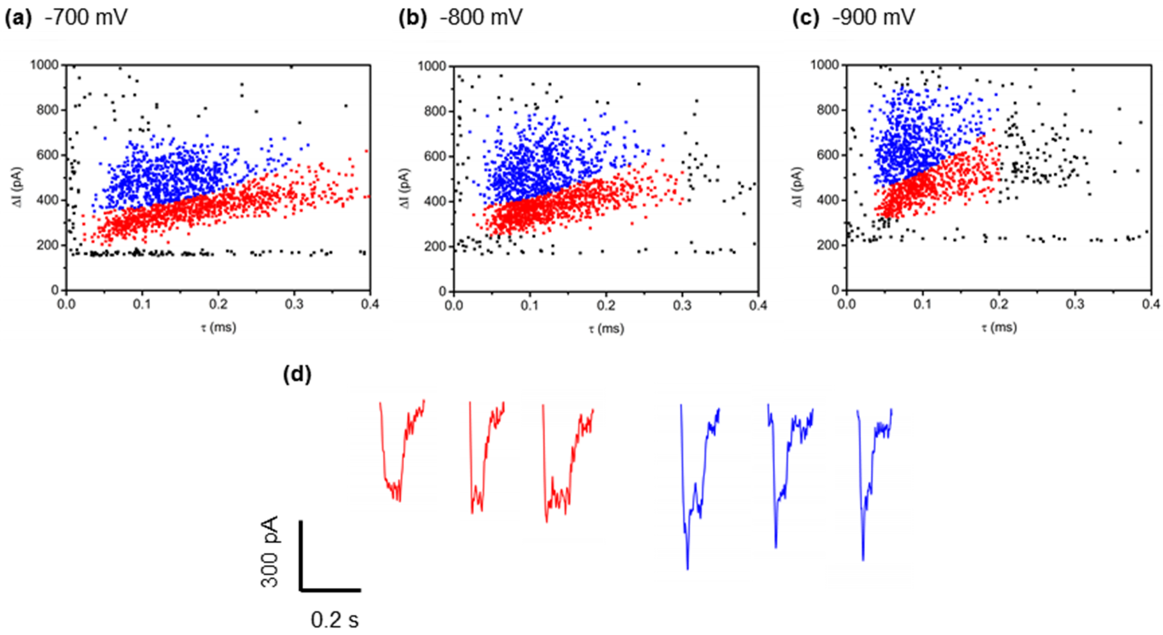

Figure 3.34. Scatter plot of τ vs. ΔI for the APTMS-coated nanopipette (G_{pore} = 30 nS) showing the translocation of linear (red) and folded (blue) events with V_{bias} of **(a)** -700, **(b)** -800 and **(c)** -900 mV. **(d)** Examples of linear (red) and folded (blue) translocation events with V_{bias} of -800 mV. All I(t) traces were filtered at 200 kHz.

3.2.11.2. Translocation Event Analysis in APTMS Coated Nanopipettes

As above with the L_{DNA} study, the τ and ΔI of the 4 kbp DNA translocation events were analysed using histograms. As shown in Figure 3.35, for the linear population of events, the τ (left panel) and ΔI (right panel) histograms were fitted with a log-normal distribution in both cases. The ΔI histograms were well-represented with a single log-normal distribution. As a $\Delta I \sim \tau^{-1}$ relationship is found for nanopore experiments, fitting both parameters with a log-normal distribution did not seem unreasonable. The τ_{mp} value decreased from 0.125 to 0.097 and 0.083 ms for V_{bias} of -700, -800 and -900 mV respectively. On the other hand, ΔI_{mp} increased from 351 to 368 and 450 pA for V_{bias} of -700, -800 and -900 mV respectively. However, as no repeats of this experiment were conducted, calculation of standard errors of the mean was not possible.

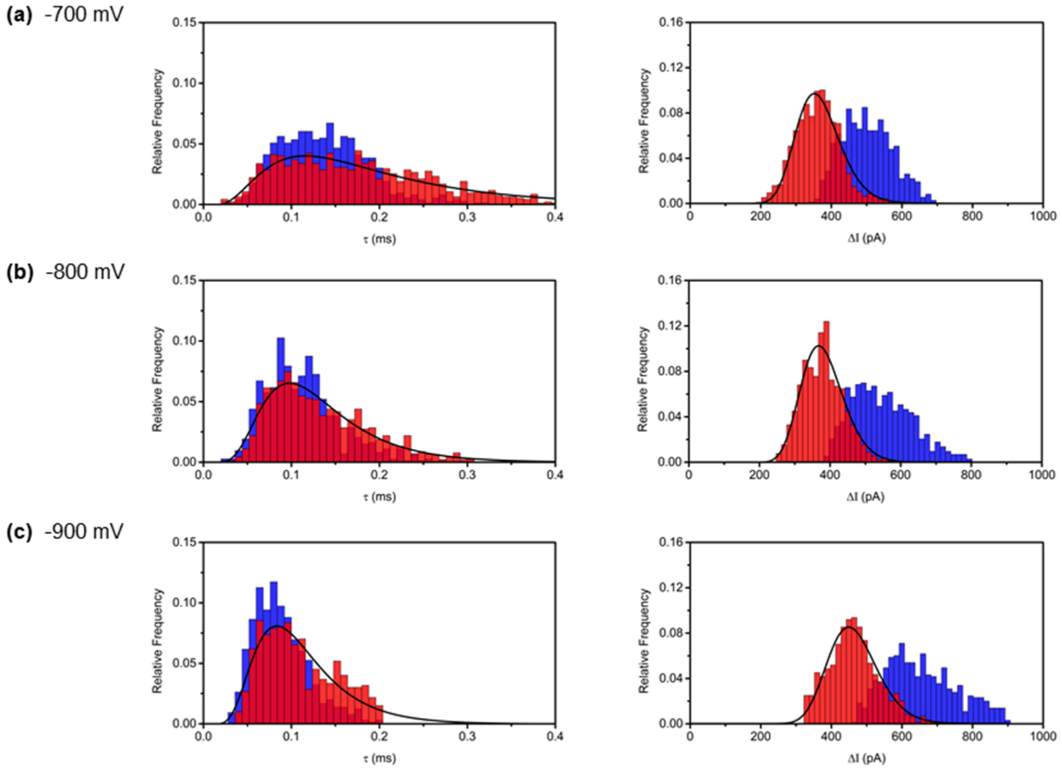

Figure 3.35. Histogram analysis of linear (red) and folded (blue) translocation event *τ* (left panel) and *ΔI* (right panel) with V_{bias} of **(a)** -700 mV (n = 1911), **(b)** -800 (n = 1879) and **(c)** -900 (n = 1520), for an APTMS coated nanopipette. A filter frequency of 200 kHz was used to acquire all data and a sampling rate of 1 µs.

The τ_{mp} for the APTMS-coated nanopipette was compared to the data acquired with unmodified nanopipettes and presented earlier on in this chapter, as shown in Figure 3.36. The APTMS-coated nanopipette increased the τ_{mp} relative to the unmodified nanopipettes. In the former case a gradient, m of 0.10 ± 0.001 ms·V was found while in the latter case m = 0.037 ± 0.004 ms·V. This is consistent with the prediction that interactions between the surface and DNA molecules prior to translocation are important. The increase in τ_{mp} is tentatively hypothesised to be due to an increased electrostatic interaction between the positively charged APTMS-coated nanopipette at pH 8 and the negatively charged DNA relative to the negatively charged unmodified nanopipette at the same pH.[42] Such an interaction in the positively charged nanopipette could explain the observed increase in τ_{mp} for a given V_{bias}. However, the increase in τ_{mp} for the APTMS modified nanopipette relative to the unmodified nanopipette is not constant, as seen with the different values of m.

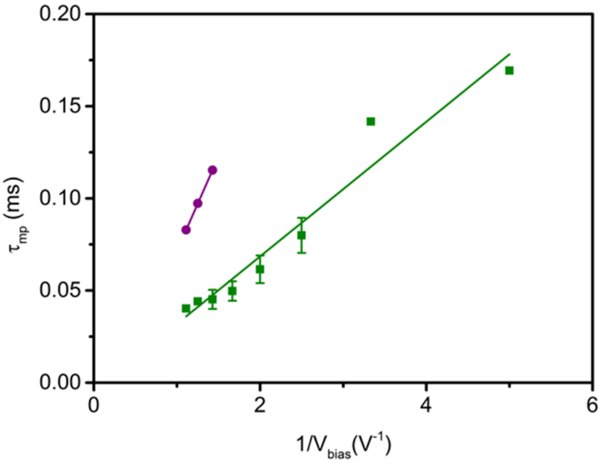

Figure 3.36. Comparison of τ_{mp} vs. V_{bias}^{-1} for 4 kbp dsDNA for an unmodified (green) and APTMS modified (purple), showing a linear relationship, m = 0.037 ± 0.003 and 0.10 ± 0.001 ms·V for the unmodified and APTMS modified nanopipette respectively.

Finally, the ecd of linear translocation events for the APTMS modified nanopipette was analysed as shown in Figure 3.37. Consistent with expectations, the ecd of events at different V_{bias} overlapped; as the τ decreases, the ΔI increases with increasing V_{bias} so that the net effect is a constant ecd at all V_{bias}.[33,40]

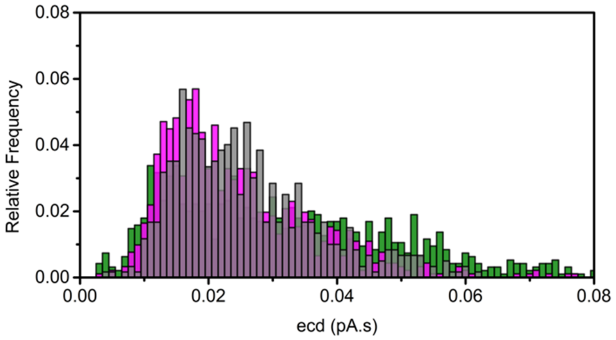

Figure 3.37. Histograms of the ecd for the linear population of translocation events using the APTMS modified nanopipette with an V_{bias} of -700 (green), -800 (magenta) and -900 (grey).

3.4 Conclusion

In this chapter, a DNA length dependence study using nanopipettes in 1 M KCl electrolyte has been described for the first time. This was achieved using custom-built, high-bandwidth detection electronics to fully capture DNA translocations occurring on the μs timescale.

Using a double logarithmic plot of τ_{mp} versus L_{DNA} a scaling factor, p = 1.22 ± 0.01 was found which differs from previous work in the literature using different platforms and in the case of nanopipettes, electrolyte solution.[3–6] An extension of the Ghosal model was then derived to account for friction between the DNA molecule and the surface of the membrane (or nanopipette surface) before translocation. In this extended Ghosal model when $p = 2$ strong DNA/surface interactions prior to DNA translocation are present whereas when $p = 1$ negligible DNA/surface interactions are expected. The value found in this work of $p = 1.22 \pm 0.01$ indicates that DNA adsorption to the nanopipette surface may be an important part of the translocation process.

Finally, attention was shifted to initial experiments probing DNA/surface interactions using an APTMS-coated nanopipette so that at pH 8 the nanopipette would be positively charged. The decreased τ_{mp} values observed for 4 kbp dsDNA translocation in an APTMS-coated nanopipette compared to the unmodified nanopipettes, is hypothesised to be because the negatively charged DNA interacts with the surface to a greater extent in the former case compared to the latter.

Future work could include a DNA length dependence study using APTMS-coated nanopipettes at pH 8 in 1 M KCl electrolyte to determine p. If DNA/surface interaction prior to translocation are indeed an important parameter as predicted by the extended Ghosal model, the value of p is expected to increase in such a case.

3.5 References

(1) Karhanek, M.; Kemp, J. T.; Pourmand, N.; Davis, R. W.; Webb, C. D. *Nano Lett.* **2005**, *5*, 403–407

(2) Wanunu, M.; Morrison, W.; Rabin, Y.; Grosberg, A. Y.; Meller, A. *Nat. Nanotechnol.* **2010**, *5*, 160–165.

(3) Storm, a. J.; Chen, J. H.; Zandbergen, H. W.; Dekker, C. *Phys. Rev. E - Stat. Nonlinear, Soft Matter Phys.* **2005**, *71*, 1–10.

(4) Storm, A. J.; Chen, J. H.; Zandbergen, H. W.; Dekker, C. *Phys. Rev. E: Stat., Nonlinear, Soft Matter Phys.* **2005**, *71*, 1–10.

(5) Bell, N. A. DNA Origami Nanopores and Single Molecule Transport through Nanocapillaries, University of Cambridge, 2013.

(6) Wanunu, M.; Sutin, J.; McNally, B.; Chow, A.; Meller, A. *Biophys. J.* **2008**, *95*, 4716–4725.

(7) Ghosal, S. *Phys. Rev.* **2006**, *74*, 41901.

(8) Ghosal, S. *Phys. Rev. Lett.* **2007**, *98*, 238104.

(9) Smith, D. E.; Perkins, T. T.; Chu, S. *Macromolecules* **1996**, *29*, 1372–1373.

(10) Fologea, D.; Uplinger, J.; Thomas, B.; Mcnabb, D. S.; Li, J. *Nano Lett.* **2005**, *5*, 1734–1737.

(11) Wanunu, M. *Phys. Life Rev.* **2012**, *9*, 125–158.

(12) Bell, N. A. W.; Keyser, U. F. *J. Am. Chem. Soc.* **2015**, *137*, 2035–2041.

(13) Plesa, C.; Kowalczyk, S. W.; Zinsmeester, R.; Grosberg, A. Y.; Rabin, Y.; Dekker, C. *Nano Lett.* **2013**, *13*, 658–663.

(14) Liang, Z.; Tang, Z.; Li, J.; Hu, R.; Yu, D.; Zhao, Q. *Nanoscale* **2015**, *7*, 10752–10759.

(15) Kowalczyk, S. W.; Wells, D. B.; Aksimentiev, A.; Dekker, C. *Nano Lett.* **2012**, *12*, 1038–1044.

(16) Wanunu, M.; Meller, A. *Nano Lett.* **2007**, *7*, 1580–1585.

(17) Anderson, B. N.; Muthukumar, M.; Meller, A. *ACS Nano* **2013**, *7*, 1408–1414.

(18) Sze, J. Y. Y.; Kumar, S.; Ivanov, A. P.; Oh, S.; Edel, J. B. *Analyst* **2015**, *140*, 4828–4834.

(19) Fu, Y.; Tokuhisa, H.; Baker, L. A. *Chem. Commun. (Camb).* **2009**, 4877–4879.

(20) Sa, N.; Fu, Y.; Baker, L. A. *Anal. Chem.* **2010**, *82*, 9963–9966.

(21) Wei, R.; Gatterdam, V.; Wieneke, R.; Tampé, R.; Rant, U. *Nat. Nanotechnol.* **2012**, *7*, 257–263.

(22) Rutkowska, A.; Freedman, K.; Skalkowska, J.; Kim, M. J.; Edel, J. B.; Albrecht, T. *Anal. Chem.* **2015**, *87*, 2337–2344.

(23) Steinbock, L. J.; Lucas, A.; Otto, O.; Keyser, U. F. *Electrophoresis* **2012**, *33*, 3480–3487.

(24) Nicoli, F.; Verschueren, D.; Klein, M.; Dekker, C.; Jonsson, M. P. *Nano Lett.* **2014**, *14*, 6917–6925.

(25) Gibb, T. R.; Ivanov, A. P.; Edel, J. B.; Albrecht, T. *Anal. Biochem.* **2014**, *86*, 1864–1871.

(26) Ferrari, G.; Farina, M.; Guagliardo, F.; Carminati, M.; Sampietro, M. *Electron. Lett.* **2009**, *45*, 1278–1280.

(27) Ciccarella, P.; Carminati, M.; Ferrari, G.; Fraccari, R.; Bahrami, A. An Integrated Low-

Noise Current Amplifier for Glass-Based Nanopore Sensing; 10th Conference on Ph.D. Research in Microelectronics and Electronics (PRIME 2014), Grenoble, France, June 29 - July 30, **2014**, 1– 4.

(28) Fraccari, R. L.; Ciccarella, P.; Bahrami, A.; Carminati, M.; Ferrari, G.; Albrecht, T. *Nanoscale* **2016**, *8*, 7604–7611.

(29) Tabart-Cossa, V. *Engineered Nanopores for Bioanalytical Applications*; Edel, J. B.; Albrecht, T., Eds.; Elsevier, 2013.

(30) http://mdc.custhelp.com/euf/assets/content/Axon%20Guide%203rd%20edition.pdf. Accessed on 2/11/2016.

(31) Viovy, J.-L. *Rev. Mod. Phys.* **2000**, *72*, 813–872.

(32) Steinbock, L. J.; Otto, O.; Chimerel, C.; Gornall, J.; Keyser, U. F. *Nano Lett.* **2010**, *10*, 2493–2497.

(33) Fologea, D.; Brandin, E.; Uplinger, J.; Branton, D.; Li, J. *Electrophoresis* **2007**, *28*, 3186–3192.

(34) Li, J.; Gershow, M.; Stein, D.; Brandin, E.; Golovchenko, J. A. *Nat. Mater.* **2003**, *2*, 611–615.

(35) Liu, Q.; Wu, H.; Wu, L.; Xie, X.; Kong, J.; Ye, X.; Liu, L. *PLoS One* **2012**, *7*, e46014.

(36) Bell, N. A. W.; Muthukumar, M.; Keyser, U. F. *Phys. Rev.* **2016**, *93*, 1–10.

(37) Squires, A.; Meller, A. *Biophys. J.* **2013**, *105*, 543–544.

(38) Kowalczyk, S. W.; Hall, A. R.; Dekker, C. *Nano Lett.* **2010**, *10*, 324–328.

(39) Yu, J.; Lim, M.; Duyen, T. N. H.; Kim, H.; Kim, H.; Kim, Y.; Kim, K. *ACS Nano* **2015**, *9*, 5289–5298.

(40) Garaj, S.; Hubbard, W.; Reina, A.; Kong, J.; Branton, D.; Golovchenko, J. A. *Nature* **2010**, *467*, 190–193.

(41) Nuttall, P.; Lee, K.; Ciccarella, P.; Carminati, M.; Ferrari, G.; Kim, K.; Albrecht, T. *J. Phys. Chem. B* **2016**, *120*, 2106–2114.

(42) Wang, Y.; Ferrari, M. *J. Mater. Sci.* **2000**, *35*, 4923–4930.

(43) Chauhan, A. K.; Aswal, D. K.; Koiry, S. P.; Gupta, S. K.; Yakhmi, J. V.; Sürgers, C.; Guerin, D.; Lenfant, S.; Vuillaume, D. *Appl. Phys. A Mater. Sci. Process.* **2008**, *90*, 581–589.

(44) Yang, C. Y.; Huang, L. Y.; Shen, T. L.; Andrew Yeh, J. *Eur. Cells Mater.* **2010**, *20*, 415–430.

(45) Glass, N. R.; Tjeung, R.; Chan, P.; Yeo, L. Y.; Friend, J. R. *Biomicrofluidics* **2011**, *5*, 1–7.

(46) Arkles, B. *Chemtech* **1977**, *7*, 766.

(47) Mussi, V.; Fanzio, P.; Firpo, G.; Repetto, L.; Valbusa, U. *Nanotechnology* **2012**, *23*, 435301.

(48) Wang, Y.; Velmurugan, J.; Mirkin, M. V.; Rodgers, P. J.; Kim, J.; Amemiya, S. *Anal. Chem.* **2010**, *82*, 77–83.

(49) Leontidou, T. DNA translocation studies using functionalised nanopipettes, MSci Thesis, Imperial College London, 2016.

(50) Actis, P.; Mak, A. C.; Pourmand, N. *Bioanal. Rev.* **2010**, *1*, 177–185.

(51) Kim, Y. R.; Min, J.; Lee, I. H.; Kim, S.; Kim, A. G.; Kim, K.; Namkoong, K.; Ko, C. *Biosens. Bioelectron.* **2007**, *22*, 2926–2931.

(52) Wei, C.; Bard, A. J.; *Anal. Chem.* **1997**, 69,4627-4633.

(53) Siwy, Z.; Heins, E.; Harrell, C. C.; Kohli, P.; Martin, C. R. *J . Am. Chem. Soc.* **2004**, *126*, 10850–10851.

(54) Reijenga, J.; van Hoof, A.; van Loon, A.; Teunissen, B. *Anal. Chem. Insights* **2013**, *8*, 53–71.

(55) Kakiuchi, T.; Iida, M.; Imabayashi, S.; Niki, K. *Langmuir* **2000**, *6*, 5397–5401.

(56) Fears, K. P.; Creager, S. E.; Latour, R. A. *Langmuir* **2008**, *24*, 837–843.

Chapter 4

Detection of Short DNA

Synopsis: This chapter describes work undertaken to detect a 100 nt sequence and its complement, the sequence of which is biologically relevant. Initially, the shortest DNA length detectable in 1 M KCl using the custom-built and high-bandwidth ‘Polimi’ amplifier was estimated. With an applied potential of -100 mV it was estimated that ~150 bp would be the smallest length detectable. Experimentally the translocation of 200 bp dsDNA in 1 M KCl was achieved, in good agreement with predictions. Instrumental limitations meant that 100 bp ssDNA was incompletely detected in 2 M LiCl. However, 100 bp dsDNA was successfully detected in 2 and 4 M LiCl.

Part of this chapter has been published as Fraccari, R.L.; Carminati M.; Piantanida G.; Leontidou T.; Ferrari G.; Albrecht T. *Faraday Discuss.* **2016**, Advance Article, DOI: 10.1039/C6FD00109B.

4.1 Introduction

Detection of short DNA fragments using nanopore biosensors could be relevant to disease diagnostics.[1] With this in mind, the detection of a 100 nt sequence and its complement which is known to cause resistance to fluoroquinolones,[i] a class of antibiotics was investigated using nanopipettes and the custom-built and high-bandwidth Polimi amplifier. Fluoroquinolones are used to treat the infectious disease tuberculosis (TB) caused by *Mycobacterium tuberculosis* (MTB).[2] According to a report published in 2015 by the World Health Organization (WHO), TB caused 1.5 million deaths worldwide in 2014 and of these deaths, 190 000 were caused by multi-drug resistant TB. Therefore, antibiotic resistance is a major concern in the fight against TB.[3]

Different translocation dynamics are expected for 'short' (~4 kbp and below) and 'long' dsDNA (~4 kbp and above). The persistence length of dsDNA is on the order of 35 nm and higher (depending on the electrolyte conditions),[4,5] while the geometric length of 100 bp dsDNA is ~34 nm. Therefore, for short dsDNA where the persistence length is comparable to the geometric length, the dsDNA is more akin to a rigid rod than a flexible polymer. Contrary to this, for long dsDNA the geometric length (~1360 nm for 4kbp dsDNA) is much longer than the persistence length and thus the DNA is more akin to a flexible polymer.

The difficulties encountered in achieving sub-10 nm pores in quartz nanopipettes compared to planar solid-state devices has so far limited detection to DNA lengths of ~500 bp and above in nanopipettes.[6] However, using planar, chip-based solid-state pores, much shorter DNA lengths have been detected in 1 M KCl electrolyte. For example, Wanunu et al. were able to detect 150 bp dsDNA using SiN pores with a 4 nm diameter. They also found that decreasing the pore diameter from 5 to 2.7 nm resulted in an order of magnitude increase in τ.[7] On the other hand, Thangaraj et al. detected 10 bp long ssDNA and dsDNA in 1 M KCl using planar solid-state pores coated with Al_2O_3 to achieve pores diameters of ~2.2 nm.[8]

While smaller pores have been successful in increasing the τ of translocation events and thereby allowing for the detection of short DNA another approach to increasing the τ of events is to change the electrolyte. Using a combination of experiments in solid-state nanopores and molecular dynamic (MD) simulations, Kowalczyk et al. showed that changing the electrolyte from KCl to either NaCl or LiCl slowed down the translocation of DNA.[9]

---

[i] Sequence provided by the Breuer laboratory, University College London.

Experiments were performed using pore diameters between 15 and 20 nm to detect 48.5 kbp dsDNA and 7200 nt long ssDNA in the different electrolytes. Figure 4.1 shows translocation events for λ-DNA in the three different electrolytes with 1 M NaCl and 1 M LiCl increasing the τ by 1.7 and 4.8 times respectively, relative to 1M KCl electrolyte. The ΔI of events did not however change significantly. Furthermore, increasing the concentration of LiCl from 1 to 2 and 4 M increased the τ of events by 1.5-fold and two-fold respectively. The ΔI of events also increased as the concentration of LiCl increased. A similar trend was also observed for the translocation of ssDNA where changing the electrolyte from 1 M KCl to 1 M NaCl increased the τ by 1.4-fold while 1 M LiCl increased the τ by 10.2-fold. The ΔI of events was similar between the different electrolyte solutions.

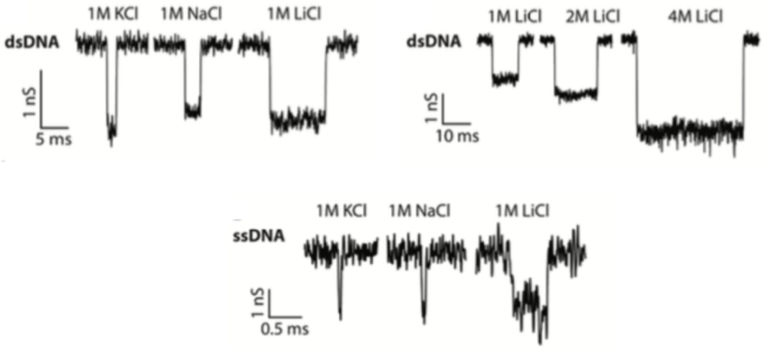

Figure 4.1. Example events for dsDNA (top panel) translocation in 1 M KCl, NaCl and LiCl (left) and 1, 2 and 4 M LiCl (right). Examples events for ssDNA (bottom panel) translocation events in 1 M KCl, NaCl and LiCl. Figure reprinted with permission from ref. 9.

MD simulations were used to explain how the different counterions that differ only in size with $K^+ > Na^+ > Li^+$ caused the observed τ trends. The increase in τ when changing from KCl to NaCl to LiCl electrolyte was explained as follows. The bonds formed between Li^+ ions to the dsDNA last longer than those of Na^+ ions which in turn last longer than K^+ ions. Therefore, as the size of the counterion decreases and the bonds to the DNA last longer, the negative charge of the DNA is neutralised to a greater extent. A decrease in the overall negative charge of DNA causes a decrease in velocity because of a decrease in the electrophoretic force acting on the molecule.[9]

Uplinger et al. also reported an increase in τ when changing from 1 M KCl to 1 M NaCl electrolyte to translocate 3 kb dsDNA (Figure 4.2).[10] Using a chip-based solid-state pore with a ~12 nm pore size, they found the most probable τ to increase by a factor of 1.5. This is in agreement Kowalczyk et al. who found the translocation of λ-DNA to increase by a factor of 1.7 in 1 M NaCl electrolyte compared to 1 M KCl electrolyte.[9,10]

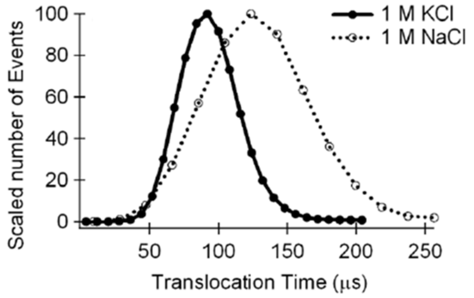

Figure 4.2. Histogram analysis of τ for 3 kbp dsDNA in NaCl and KCl electrolyte. Figure reprinted with permission from ref. 10.

This slowing down of the translocation process has also been shown in nanopipettes by Bell and co-workers who have used 4 M LiCl electrolyte to detect dsDNA as short as 500 bp.[6,11]

4.2 Experimental Objectives

The aim of this chapter was to detect the 100 nt sequence of interest and its complement using nanopipettes and the Polimi amplifier. The sequence investigated is relevant to antibiotic resistance in TB and therefore its detection using nanopipettes could be of diagnostic relevance.

Given that nanopore sensors are unable to detect the molecular entity of the DNA directly, the aim was to detect the 100 nt sequence by using complementary base pairing to its complement. It was envisioned that at a given V_{bias}, the ssDNA would produce a different current signature to its dsDNA counterpart. Analysis of I(t) traces could therefore be used to detect whether ssDNA had hybridised to its complement (when present) and even the ratio of ssDNA to dsDNA by comparing the relative ratio of the different current signatures.

4.3 Results and Discussion

4.3.1 Predicting the Shortest Detectable dsDNA Length

In chapter 3 a DNA length dependence study in nanopipettes was described using dsDNA with lengths between 4 and 48.5 kbp. Data from this study was used to predict the shortest detectable DNA length using nanopipettes in 1 M KCl electrolyte and the Polimi amplifier while using a 1 µs sampling rate.

To begin with the SNR was calculated for each of the four different L_{DNA} at four different V_{bias} by dividing the ΔI_{mp} by the RMS noise of the AC channel (I_{rms}^{AC}, see appendix IV for full dataset). On average the SNR was 7.4 and appeared to be roughly independent of V_{bias} and DNA sample, although it should be noted that different filter frequencies were used at a given V_{bias} for the different L_{DNA}. In light of this, the assumption that the SNR was constant irrespective of DNA sample and V_{bias} was made. In addition, another assumption made was that the scaling law log (τ_{mp}) ~ log $(L_{DNA})^{1.22}$ is valid for lengths of dsDNA outside of the 4 to 48.5 kbp range. The short L_{DNA} investigated here were more akin to rigid rods than long flexible polymers (*vide infra*). It is not unreasonable therefore to expect the scaling law to be (somewhat) different for short L_{DNA} compared to long L_{DNA}. This is a rather crude approximation given that different p regimes have been reported for DNA lengths less than ~ 4 kbp.[7,11] Nevertheless, the predicted values proved to be a useful guideline.

From a double logarithmic plot of τ_{mp} versus L_{DNA}, individual p values of 1.17, 1.22, 1.24 and 1.20 were found for V_{bias} of -200, -300, -400 and -800 mV respectively (see chapter 3), as shown in Figure 4.3. Assuming a maximum time resolution of 10 µs which corresponds to a 100 kHz filter frequency, the minimum L_{DNA}, $L_{DNA,m}$ detectable at each of the four V_{bias} was calculated using the linear fits obtained (Figure 4.3). Predicted $L_{DNA,m}$ values of 326, 480, 684 and 1152 bp were obtained for V_{bias} of -200, -300, -400 and -800 mV respectively.

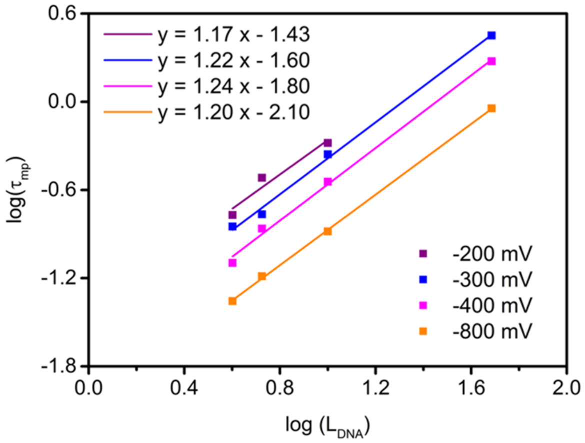

Figure 4.3. Log-log plot of L_{DNA} vs. τ_{mp} for V_{bias} of -200, -300, 400 and -800 mV. The linear fits at each V_{bias} are indicated (solid lines) and the equations shown.

The predicted $L_{DNA,m}$ values were approximately linearly dependent on V_{bias} (Figure 4.4) and this allowed for extrapolation of $L_{DNA,m}$ at V_{bias} of -50, -100 and -200 mV giving values of 152, 220 and 355 bp respectively.

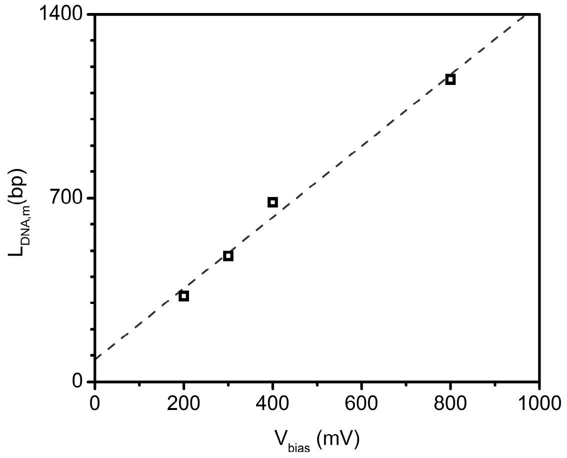

Figure 4.4. Estimated $L_{DNA,m}$ vs. V_{bias} with linear fit (dashed line), m = -1.4 ± 0.1 bp·mV^{-1}, intercept = 83.83 bp.

4.3.2 Translocation of short dsDNA in KCl Electrolyte

The theoretical predictions in section 4.3.1 were confirmed experimentally using 1 M KCl to translocate 200 bp dsDNA.[j] The I(t) traces were acquired using filter frequencies between 50 – 70 kHz and are shown together with example translocation events in Figure 4.5. The data was acquired using a nanopipette with an estimated diameter of 12 nm (n = 1).

To differentiate between noise and translocation events the I(t) traces were analysed for events with a negative and positive polarity. It was expected that current blockages (negative polarity, green squares) or enhancements (positive polarity, pink squares) caused by random noise would be equally distributed around the mean. At each V_{bias}, a greater number of events with a negative polarity were found than with a positive polarity. This indicated that some of the current blockages were due to the translocation of the 200 bp dsDNA sample.

---

[j] DNA sample commercially bought, see appendix V for results from agarose gel electrophoresis.

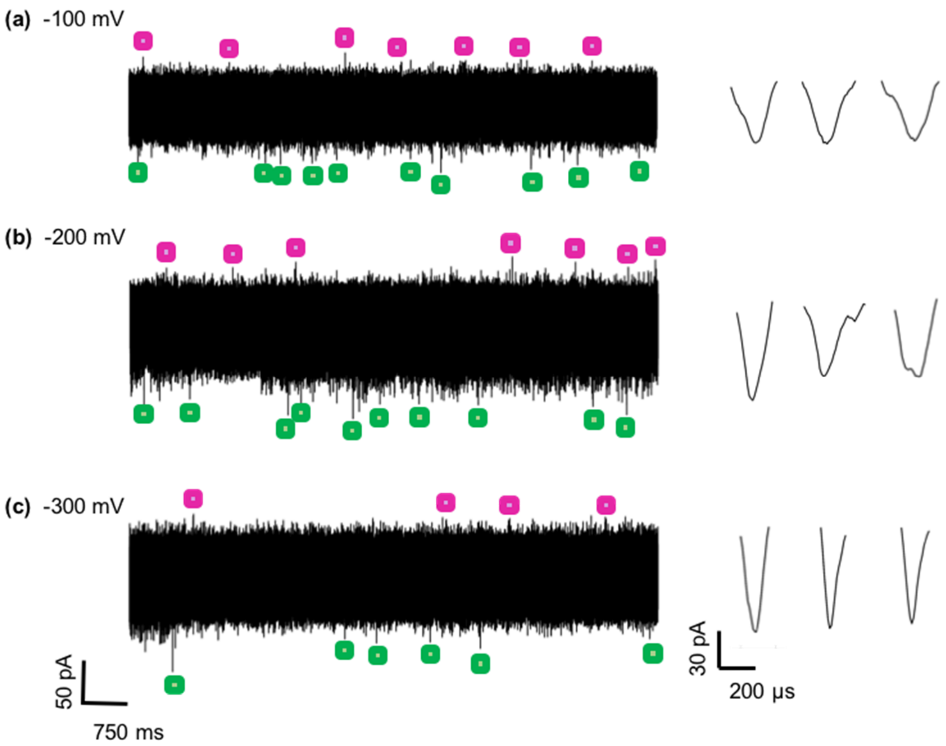

Figure 4.5. I(t) traces for the translocation of 200 bp long dsDNA in 1 M KCl electrolyte (left panel) at V_{bias} of **(a)** -100, **(b)** -200 and **(c)** -300 mV with representative events (right panel). Examples of events detected using the MATLAB code (see chapter 2) with a 4 σ cut-off using negative (green squares) and a positive (pink squares) event polarity are shown. I(t) traces filtered at 50, 60 and 70 kHz for V_{bias} of -100, -200 and -300 respectively. (G_{pore} = 34 nS, estimated d_i = 12 nm)

Figure 4.6 shows the contours plots for events with a positive polarity (pink) overlaid on the events with a negative polarity (green). Unlike the translocation of long DNA lengths (> 4 kbp), different folding conformations were not detected as the short DNA is more akin to a rigid rod than a long flexible polymer.

If only random noise were detected the contour plots for negative and positive polarity events would be expected to overlap exactly which was not the case here. At each V_{bias} the τ distribution of events with a negative and positive polarity were approximately equal. However, events with a negative polarity showed a larger ΔI distribution than events with a positive polarity. Negative and positive polarity events that were equal in τ and ΔI (i.e. areas of overlap) were interpreted as random noise. The remaining negative polarity events were assigned to DNA translocation events.

With V_{bias} of -300 mV, the ΔI of translocation events was well-defined compared to events assigned to random noise. On the other hand, this differentiation between events and random noise was less clear with V_{bias} of -100 and -200 mV. Attention was therefore focused on the analysis of translocation events with V_{bias} of -300 mV.

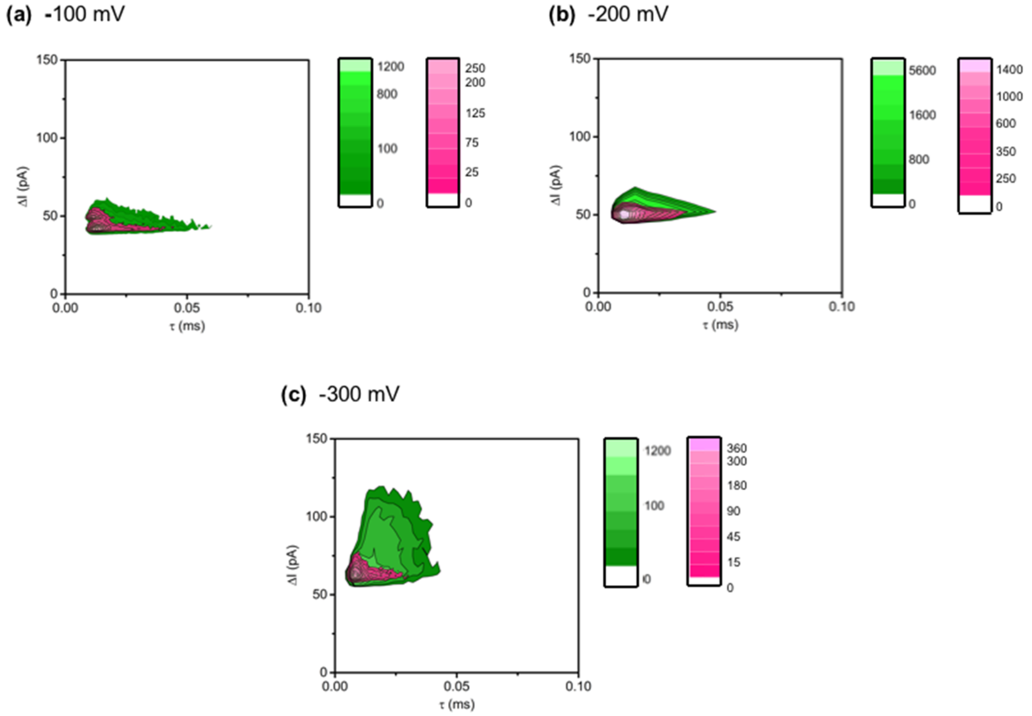

Figure 4.6. Contour plots for τ_{mp} vs. ΔI for the translocation of 200 bp dsDNA in 1 M KCl electrolyte with V_{bias} of **(a)** -100, **(b)** -200 mV and **(c)** -300 mV. Events with negative (green) and positive (pink) polarity are overlaid. Filter frequencies of 50, 60 and 70 kHz were used for V_{bias} of -100, -200 and -300 mV respectively.

Histogram analysis of the τ and ΔI for events with a negative and positive polarity with an V_{bias} of -300 mV is shown in Figure 4.7. For events with a negative polarity, two populations were visible while for events with a positive polarity, primarily one population of events was visible. Events with a positive polarity overlapped well with the first of the two populations seen for negative polarity events and these events were assigned to random noise. On the other hand, the second population of events which had a longer τ and larger ΔI than events in the first population were assigned to translocation events. These corresponded to 7061 events at an V_{bias} of -300 mV.

The τ histogram for events with a negative polarity was well-represented by a double log-normal fit and the mode of each population was used to determine the most probable τ, defined as τ_{mp1} and τ_{mp2}, for random noise and translocation events respectively. This gave values of 9 and 19 µs (n = 1) for τ_{mp1} and τ_{mp2} respectively. The ΔI histogram showed a surprisingly wide distribution. For V_{bias} of -300 mV, the ΔI_{mp} of events assigned to DNA translocations was 80 – 90 pA. This is speculated to be related to the orientation of the short DNA molecules as they translocate through the pore.[12]

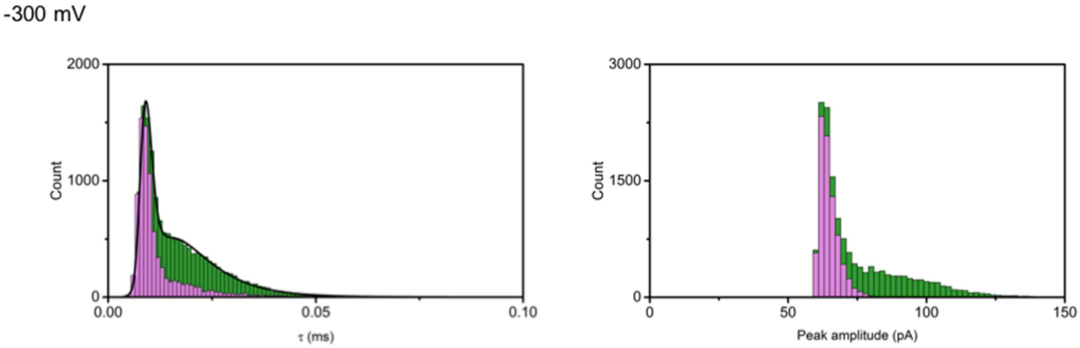

Figure 4.7. Histogram analysis of τ (left) and ΔI (right) for events with a negative (green) and positive (pink) polarity for V_{bias} of -300 mV. Events with a negative polarity are fitted with a double log-normal. A filter frequency of 70 kHz was used.

Overall, using the Polimi amplifier, 200 bp dsDNA in 1 M KCl electrolyte was detected, however the SNR ratio was a limitation as a 4 σ cut-off was needed to differentiate events from the baseline noise due to their small ΔI. Nevertheless, the translocation of 200 bp dsDNA in 1 M KCl electrolyte was achieved albeit at the limit of detection. The minimum time resolution at an V_{bias} of -300 mV, set by the filter frequency used was ~ 0.014 ms. This is close to the τ_{mp2} of 0.019 ms assigned to translocation events at this V_{bias}. Unsurprisingly, attempts to translocate 100 bp dsDNA were unsuccessful (data not shown). In an effort to detect shorter DNA lengths, 2 and 4 M LiCl electrolyte were used as discussed in the following sections.

4.3.3 Translocation of short ssDNA in 2 M LiCl Electrolyte

As aforementioned, Kowalczyk et al. and Uplinger et al. showed that using NaCl and LiCl electrolyte instead of KCl electrolyte slowed down the translocation process.[9,10] Using a nanopipette with an estimated diameter of 20 nm (n = 1), 2 M LiCl electrolyte was used to translocate the 100 nt sequence of interest.

Figure 4.8 shows typical I(t) traces for the translocation of 100 nt ssDNA in 2 M LiCl with an V_{bias} of -800 and -900 mV as well as example translocation events detected with a 5 σ cut-off. The total number of events (n_t) detected were 432 and 531 with V_{bias} of -800 and -900 mV respectively. Moreover, the translocation frequency decreased from 1.1 to 0.6 events·s^{-1}

with V_{bias} of -800 and -900 mV respectively. This is consistent with a decreased capture probability with lower V_{bias} which decreases the translocation frequency.[13] However, given that data was available for only two V_{bias}, determining whether a diffusion-limited or entropic barrier-limited regime dominated was not possible.

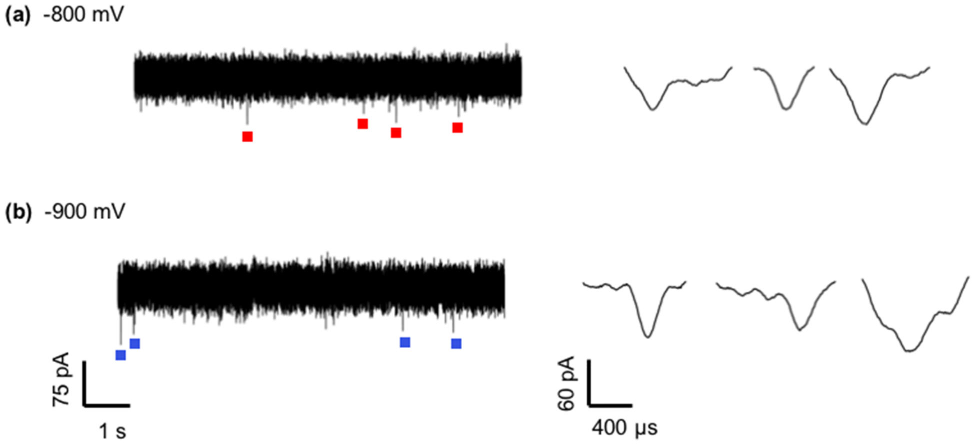

Figure 4.8. I(t) traces for the translocation of 100 nt long ssDNA in 2 M LiCl electrolyte (left panel) at V_{bias} of **(a)** -800 and **(b)** -900 mV. Some of the translocation events detected using the MATLAB code (see chapter 2) are indicated by red and blue squares for (a) and (b) respectively. Typical translocation events are shown on right. I(t) traces were filtered at 50 kHz. (G_{pore} = 27 nS, estimated d_i = 20 nm)

The scatter plot of τ versus ΔI for the translocation events is shown in Figure 4.9. Unlike the scatter plots for longer dsDNA lengths, distinct populations for each of the two V_{bias} were not observed.

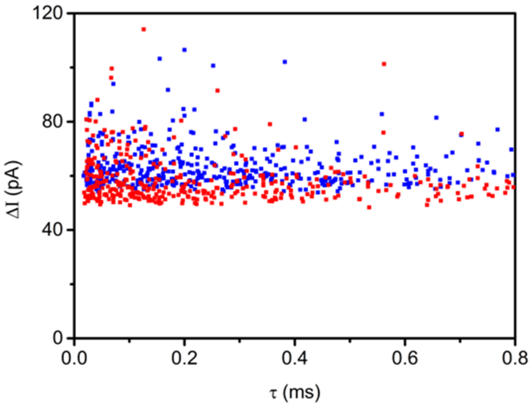

Figure 4.9. Scatter plot of τ vs. ΔI for the translocation events of ssDNA in 2 M LiCl with an V_{bias} of -800 (red) and -900 mV (blue). I(t) traces were filtered at 50 kHz.

Figure 4.10 shows the τ and ΔI event histograms. The τ histogram shows that the time resolution of the set-up was insufficient to fully resolve the translocation events as the τ did not decrease with increasing V_{bias}. A filter frequency of 50 kHz was used giving a minimum time resolution of ~0.02 ms. However, many of the events had a τ faster than 0.02 ms and were therefore incompletely resolved. Nevertheless, the ΔI increased at a higher V_{bias}, encouragingly confirming the detection of the ssDNA (as opposed to noise) albeit with insufficient temporal resolution.

(a) -800 mV

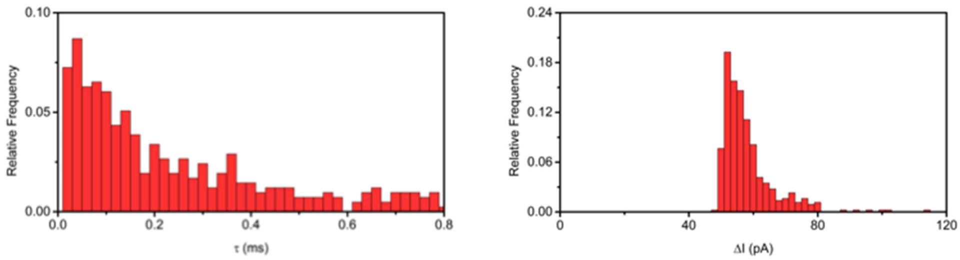

(b) -900 mV

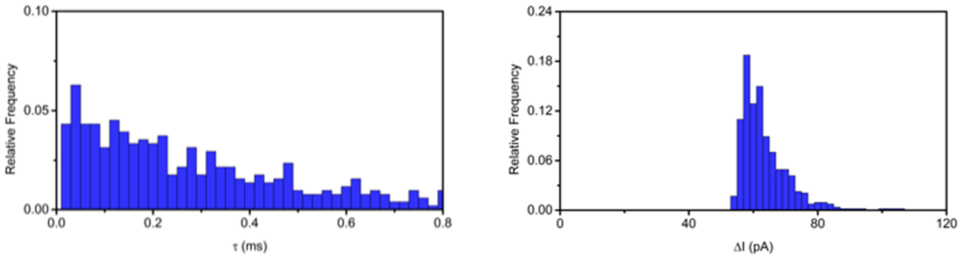

Figure 4.10. Histogram analysis of τ (left) and ΔI (right) for translocation events of 100 nt ssDNA in 2 M LiCl with an V_{bias} of **(a)** -800 mV ($n_t = 432$) and **(b)** -900 mV ($n_t = 531$). I(t) traces were filtered at 50 kHz.

A higher time resolution can be achieved by using a higher filter frequency or alternatively the τ can be increased by applying a lower V_{bias}. For a given DNA sample and V_{bias}, increasing the filter frequency reduces the SNR because of an increase in the peak-to-peak noise of the I(t) trace. On the other hand, ΔI scales linearly with V_{bias}, therefore a lower V_{bias} decreases the ΔI of translocation events.[14–16] This would again decrease the SNR. In both cases, translocation events would be difficult to distinguish from the baseline noise. Other methods such as using smaller pore diameters or surface modifications are likely to be needed to fully resolve the translocation of 100 nt long ssDNA in nanopipettes.

4.3.4 Hybridisation of the 100 nt Sequence to its Complement

Following the partially successful detection of the 100 nt ssDNA, the translocation of its dsDNA counterpart was attempted. The 100 nt sequences was hybridised to its complementary ssDNA (cssDNA) sequence by adding the two strands in equal amounts and heating at 95 °C for five min. This temperature is above the melting temperature of the DNA and ensures that no secondary structures are present. The mixture was then incubated at 37 °C for five h to allow the cssDNA strands to hybridise.

Hybridisation was confirmed using agarose gel electrophoresis as shown in Figure 4.11. Lane one and five show the DNA ladder standards while lane two and three show the 100 nt sequence and the 100 nt cssDNA with a 5' NH_2 group which was necessary for downstream applications (see chapter 5). As expected, the ssDNA migrates faster through the gel than the corresponding dsDNA due to the lower molecular weight.[17] The presence of two smeared bands in lane three for the cssDNA with 5'NH_2 group indicates the presence of impurities,[k] however this was not of great concern as the dsDNA showed a well-defined band. Finally, lane four shows the hybridisation of the ssDNA to form 100 bp dsDNA, with a band that matches the 100 bp band of the DNA ladder standard.

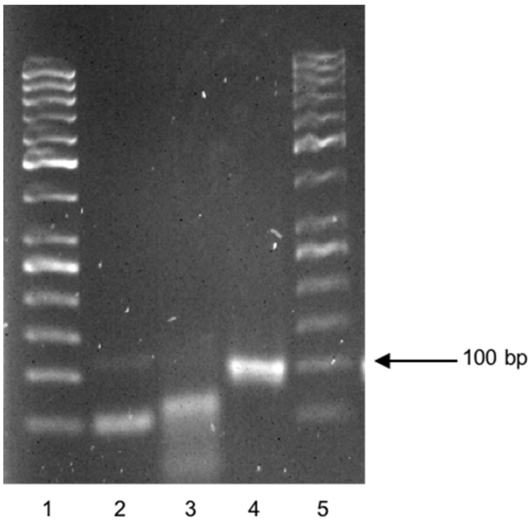

Figure 4.11. Agarose gel electrophoresis image (2%, 5 V/cm, 70 min, 1x TBE) confirming hybridisation of the 100 nt sequence to its complement. Lane 1 and 5: '50 bp ladder' (ThermoFisher), Lane 2: 100 nt ssDNA sequence, Lane 3: 100 nt cssDNA sequence with 5' NH_2 group, Lane 4: 100 bp dsDNA.

4.3.5 Translocation of short dsDNA in 2 M LiCl Electrolyte

Following the hybridisation of the ssDNA, the 100 bp dsDNA was translocated with V_{bias} of -100 and -200 mV. Figure 4.12 shows typical I(t) traces and translocation events. Data was acquired using two different nanopipettes with estimated diameters of 11 and 20 nm and the n_t recorded were 5009 for an V_{bias} of -100 mV and 9362 for an V_{bias} of -200 mV. At an V_{bias}

---

[k] The 100 nt ssDNA was PAGE purified while the cssDNA with 5' NH_2 group was purified using HPLC due to the modification.[19] A greater DNA sample purity is achieved with PAGE than with HPLC.

of -100 and -200 mV, there was a translocation frequency of 8 ± 1 and 26 ± 2 events·s^{-1} respectively. As expected, a lower frequency of translocation events was observed for smaller V_{bias} despite using nanopipettes with different pore sizes. The capture rate and hence translocation frequency has previously been shown to decrease with decreasing pore size.[7]

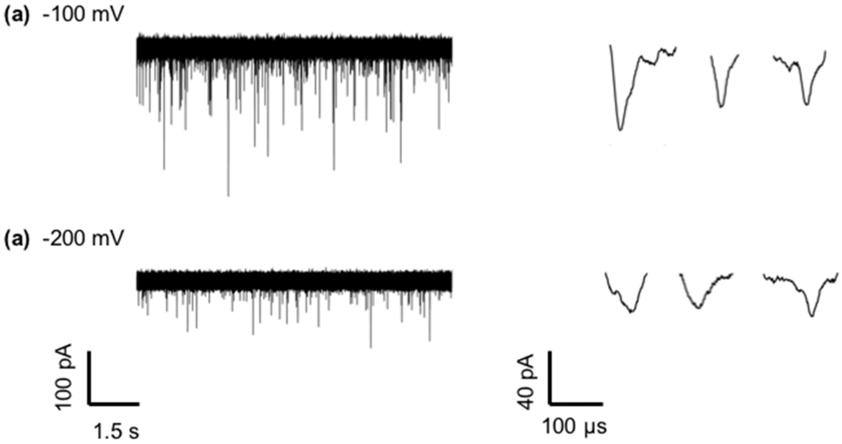

Figure 4.12. Typical I(t) traces for the translocation of 100 bp dsDNA in 2 M LiCl electrolyte (left panel) at an V_{bias} **(a)** -100 and **(b)** -200 mV with representative events (right panel). I(t) traces were filtered at 50 kHz. (G_{pore} = 27 nS, estimated d_i = 20 nm).

Representative contour plots for the translocation events are shown in Figure 4.13 for V_{bias} of -100 and -200 mV where again different folding states were not detected. The τ and ΔI histogram analysis are also shown alongside the contour plots (Figure 4.13) where an increase in τ and decrease ΔI with V_{bias} was observed.

The τ histograms were well-represented by a single log-normal fit, the mode of which was used to determine τ_{mp}. This gave average τ_{mp} values of 117.3 ± 4.5 and 73.6 ± 3.6 µs (n = 2) for V_{bias} of -100 and -200 mV respectively. Moreover, as observed for translocation events in 1 M KCl, the ΔI histograms had a broad distribution which nevertheless were fitted with a single log-normal and the mode used to determine ΔI_{mp}. For the two nanopipettes used, the individual ΔI_{mp} values were 33 and 56 pA at an V_{bias} of -100 mV and 46 and 88 pA at an V_{bias} of -200 mV. The average of these gives ΔI_{mp} values of 44 ± 9 pA for an V_{bias} of -100 mV and 67 ± 17 pA for an V_{bias} of -200 mV. The relatively large errors reflect the broad distributions in the ΔI histograms and different pore sizes (~11 - 20 nm) used. There errors were calculated as standard errors of the mean.

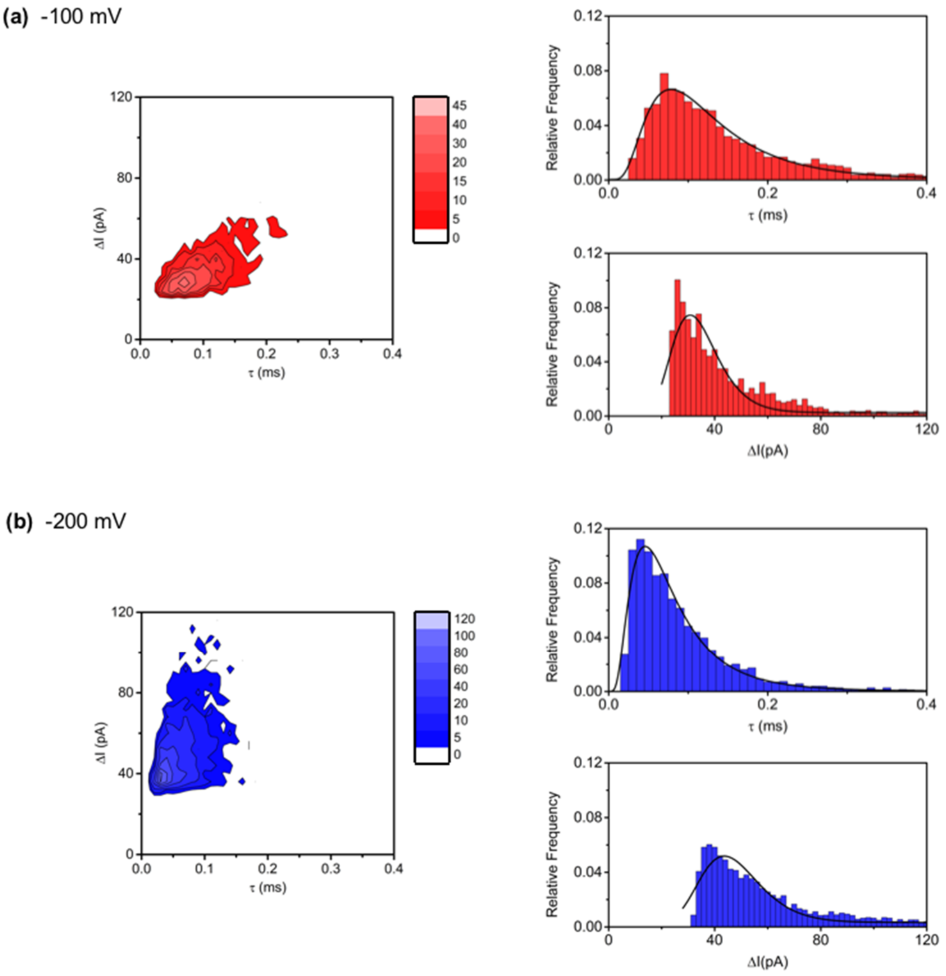

Figure 4.13. Translocation experiment with 100 bp dsDNA in 2 M LiCl electrolyte at an V_{bias} of **(a)** -100 mV (n_t = 2150) and **(b)** -200 mV (n_t = 4012). I(t) traces were filtered at 40 and 50 kHz for V_{bias} of -100 and -200 mV respectively. All histograms are fitted with a log-normal distribution. (G_{pore} = 27 nS, estimated d_i = 20 nm).

The predicted τ_{mp} values for the translocation of 200 bp dsDNA in 1 M KCl electrolyte are 15 and 11 μs for V_{bias} of -100 and -200 mV, respectively.[9] These values are close to the time resolution set by a 100 kHz filter frequency and would to some extent explain why 100 bp dsDNA was not detected in 1 M KCl. Finally, analysis of the ecd histogram (Figure 4.14) showed that as expected the ecd of events with V_{bias} of -100 and -200 mV remained constant for each of the two nanopipettes used to translocate 100 bp dsDNA in 2 M LiCl electrolyte. This is consistent with the decrease in τ with decreasing V_{bias} being matched with an increase in the ΔI of translocation events.

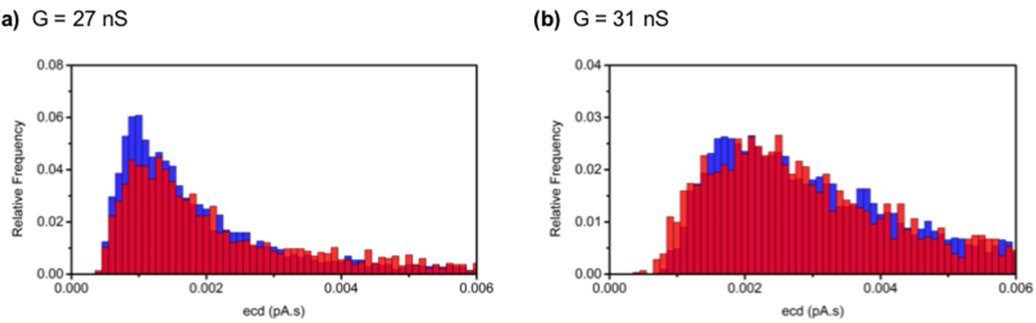

Figure 4.14. Histogram analysis of the ecd of translocation events for 100 bp dsDNA in 2 M LiCl with an V_{bias} of -200 (blue) and -100 mV (red) using two different nanopipettes. **(a)** G_{pore} = 27 nS, estimated d_i = 20 nm, nt = 4012 (V_{bias} = -200 mV) and n_t = 2150 (V_{bias} = -100 mV). **(b)** G_{pore} = 31 nS, estimated d_i = 11 nm, n_t = 5350 (V_{bias} = -200 mV) and n_t = 2859 (V_{bias} = -100 mV).

4.3.6 Translocation of short dsDNA in 4 M LiCl Electrolyte

In an attempt to further increase the τ of 100 bp dsDNA translocation events the electrolyte was changed from 2 to 4 M LiCl electrolyte. Typical I(t) traces and translocation events are shown in Figure 4.15 where an increase in V_{bias} from -100 to -200 mV resulted in an increase in translocation frequency from 6 ± 2 to 14 ± 4 events·s^{-1}, respectively. Events were detected using a 5 σ cut-off and three different nanopipettes with estimated diameters between 15 and 19 nm. A total of 3999 and 6810 events were detected with V_{bias} of -100 and -200 mV respectively, using the three nanopipettes.

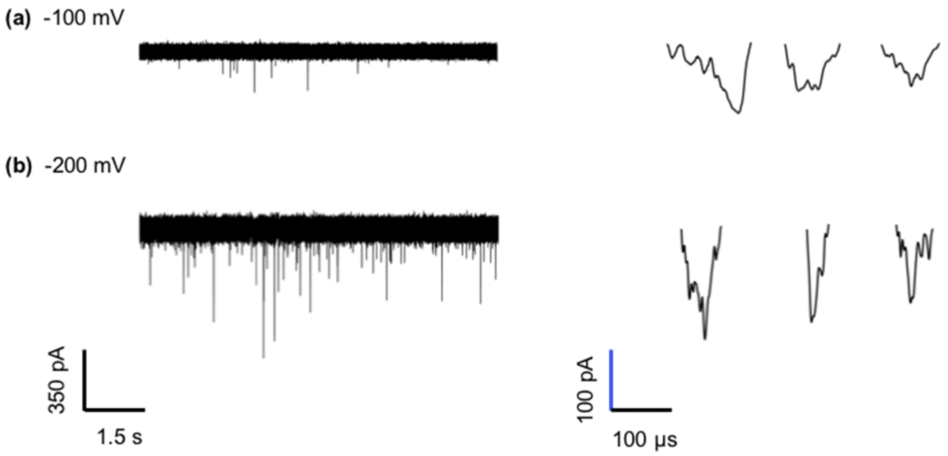

Figure 4.15. Typical I(t) traces for the translocation of 100 bp dsDNA in 4 M LiCl electrolyte (left panel) at an V_{bias} of **(a)** -100 and **(b)** -200 mV with representative translocation events (right panel). I(t) traces were filtered at 50 and 100 kHz for V_{bias} of -100 and -200 mV respectively. (G_{pore} = 43 nS, estimated d_i = 15 nm).

Figure 4.16 shows the contour plots of translocation events for V_{bias} of -200 and -100 mV, where similar to 2 M LiCl different folding states were not detected. The τ and ΔI histogram analysis are also shown alongside the contour plots (Figure 4.16) where a decrease in the τ and an increase in the ΔI is observed with increasing V_{bias}.

(a) -100 mV

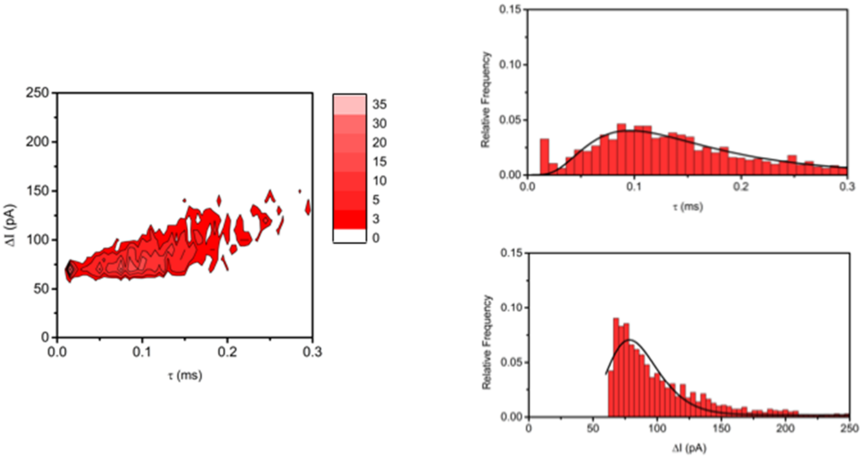

(b) -200 mV

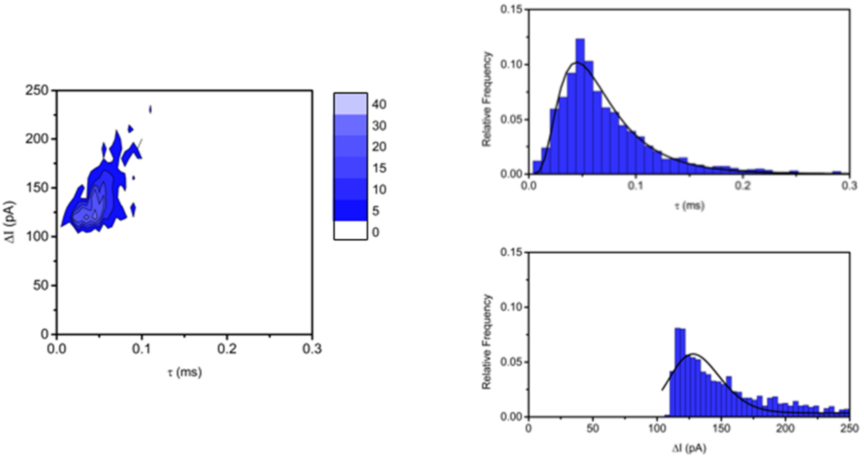

Figure 4.16. Translocation experiment with 100 bp dsDNA in 4 M LiCl electrolyte at an V_{bias} of **(a)** -100 mV (n_t = 1650) and **(b)** -200 mV (n_t = 1682). I(t) traces were filtered at 50 and 100 kHz for V_{bias} of -100 and -200 mV respectively. All histograms are fitted with a log-normal distribution. (G_{pore} = 43 nS, estimated d_i = 15 nm).

The τ histograms were fitted with a log-normal distribution and the mode was used to determine τ_{mp}. Average τ_{mp} values of 124.3 ± 15.2 and 63.5 ± 1.5 μs (n = 3) for V_{bias} of -100 and -200 mV respectively were found. Similar to the results obtained using 2 M LiCl, the ΔI histograms had a broad distribution which were fitted with a single log-normal and the mode used to determine ΔI_{mp}. For an V_{bias} of -200 mV this gave ΔI_{mp} values between 96 and 143 pA while for an V_{bias} of -100 mV, the ΔI_{mp} was between 52 and 94 pA. On average there was a decrease in ΔI_{mp} from 123 ± 14 to 76 ± 12 pA for V_{bias} of -200 and -100 mV respectively.

Despite this wide variation in ΔI_{mp} values, a decrease in ΔI_{mp} with V_{bias} was observed as expected for DNA translocations.

Finally, analysis of the ecd histograms for V_{bias} of -100 and -200 mV remained unchanged (Figure 4.17) for each of the three nanopipettes used. This means that for each nanopipette, an increase in the V_{bias}, resulted in a decrease in the τ with a corresponding increase in the ΔI.

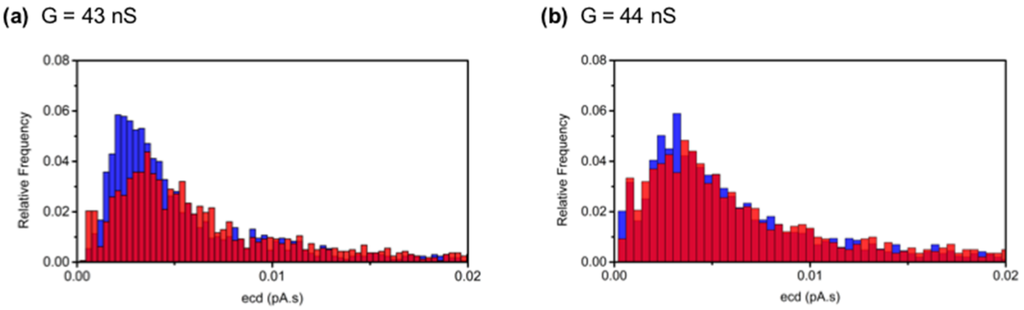
(a) G = 43 nS

(b) G = 44 nS

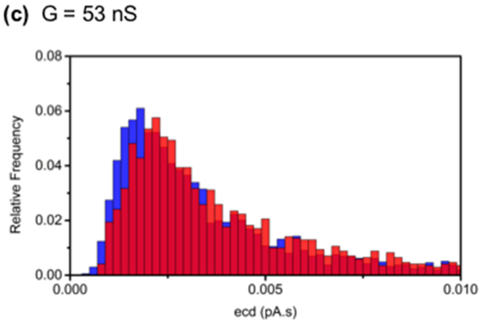
(c) G = 53 nS

Figure 4.17. Histogram analysis of the ecd of translocation events for 100 bp dsDNA in 4 M LiCl with an V_{bias} of -200 (blue) and -100 mV (red). **(a)** G_{pore} = 43 nS, estimated d_i = 15 nm, nt = 1682 (V_{bias} = -200 mV) and n_t = 1650 (V_{bias} = -100 mV). **(b)** G_{pore} = 44 nS, estimated d_i = 15 nm, nt = 1407 (V_{bias} = -200 mV) and n_t = 555 (V_{bias} = -100 mV). **(c)** G_{pore} = 53 nS, estimated d_i = 19 nm, nt = 3721 (V_{bias} = -200 mV) and n_t = 1794 (V_{bias} = -100 mV).

It was expected that changing the electrolyte from 2 to 4 M LiCl would slow down the translocation process and thus increase the τ_{mp} value. For the translocation of 200 bp dsDNA, changing the electrolyte from 2 to 4 M KCl resulted in a ~1.1-fold increase in τ_{mp} with an V_{bias} of -100 mV. The opposite trend, however, was observed with an V_{bias} of -200 mV, where a ~1.2-fold decrease in τ was seen.

In the literature,[7,18] it has been reported that a decrease in the pore size slows down the translocation of ssDNA and dsDNA. The two nanopipettes used in 2 M LiCl electrolyte had pore diameters of 11 and 20 nm, giving τ_{mp} values of ~78 and 69 μs, respectively. This large variation in pore size skews the average τ_{mp} calculated from the two nanopipettes. Therefore, the increase in τ_{mp} when changing the electrolyte from 2 to 4 M LiCl is likely to be masked by τ_{mp} variations arising from the different pore sizes used. Moreover, in 4 M LiCl electrolyte, where the pore diameters used were more similar to each other (15 - 19 nm), τ_{mp} values of ~60.6, 64.5 and 65.3 μs were obtained. Using nanopipettes with a more uniform pore size is expected to increase τ_{mp} when changing the electrolyte from 2 to 4 M LiCl.

Kowalcyzk et al. observed an increase in ΔI when changing from 2 to 4 M LiCl, however, no reasons were given to explain this observation.[9] For the data presented here, with an V_{bias} of -200 mV, a ~1.8-fold increase in ΔI was seen and for -100 mV, the increase was ~1.7-fold, when changing the electrolyte from 2 to 4 M LiCl. It is speculated that the observed increase in ΔI at higher LiCl concentrations may in part be due to greater DNA-surface adsorption.

4.4 Conclusion

In conclusion, using results from the L_{DNA} study it was predicted that with an V_{bias} of -100 and -200 mV, 152 and 220 bp respectively could be detected using nanopipettes in 1 M KCl and the Polimi amplifier. Experimentally, 200 bp dsDNA was detected which is in good agreement with the predictions made. However, the sequence of interest was 100 nt long, therefore LiCl electrolyte was used instead of KCl electrolyte in an effort to slow down the translocation process. Using 2 M LiCl the 100 nt sequence was detected with V_{bias} of -800 and -900 mV, however the temporal resolution was insufficient to fully resolve translocation events. Detection of the 100 bp dsDNA sequence was however possible. A further increase in τ was observed by using 4 M LiCl electrolyte with an V_{bias} of -100 mV however, unexpectedly a decrease in τ was observed with an V_{bias} of -200 mV. This is most likely due to the large variation in the pore sizes of nanopipettes. The ~1.1-fold increase in τ for the translocation of dsDNA in 4 M LiCl compared to 2 M LiCl was not deemed sufficient to fully resolve the translocation of the ssDNA at comparable V_{bias}.

Challenges were encountered in the detection of the 100 nt sequence of interest however, its dsDNA counterpart was successfully detected in 4 M LiCl electrolyte. This shows promise for use in sensing devices for disease diagnostics. In such a sensing device, at a given V_{bias} the 100 nt ssDNA fragment would not be detectable. However, if the cssDNA is added the resulting 100 bp dsDNA would produce detectable translocation events in the I(t) traces. If on the other hand, ssDNA that is non-complementary in sequence is added, there would be no detectable change in the measured I(t) traces.

4.5 References

(1) LeProust, E. M.; Peck, B. J.; Spirin, K.; McCuen, H. B.; Moore, B.; Namsaraev, E.; Caruthers, M. H. *Nucleic Acids Res.* **2010**, *38*, 2522–2540.

(2) Ginsburg, A. S.; Grosset, J. H.; Bishai, W. R. *Lancet Infect. Dis.* **2003**, *3*, 432–442.

(3) *Global Tuberculosis Report* 2015; World Health Organization, WHO Press: Geneva, Switzerland, 2015.

(4) Brinkers, S.; Dietrich, H. R. C.; De Groote, F. H.; Young, I. T.; Rieger, B. *J. Chem. Phys.* **2009**, *130*, 1–9.

(5) Hagerman, P. J. *Annu. Rev. Biophys. Biophys. Chem.* **1988**, *17*, 265–286.

(6) Bell, N. A. W.; Muthukumar, M.; Keyser, U. F. *Phys. Rev.* **2016**, *93*, 1–10.

(7) Wanunu, M.; Sutin, J.; McNally, B.; Chow, A.; Meller, A. *Biophys. J.* **2008**, *95*, 4716–4725.

(8) Thangaraj, V.; Lepoitevin, M.; Smietana, M.; Balanzat, E.; Bechelany, M.; Janot, J. M.; Vasseur, J. J.; Subramanian, S.; Balme, S. *Microchim. Acta* **2016**, *183*, 1011–1017.

(9) Kowalczyk, S. W.; Wells, D. B.; Aksimentiev, A.; Dekker, C. *Nano Lett.* **2012**, *12*, 1038–1044.

(10) Uplinger, J.; Thomas, B.; Rollings, R.; Fologea, D.; Mcnabb, D.; Li, J. *Electrophoresis* **2012**, *33*, 3448–3457.

(11) Bell, N. A. DNA Origami Nanopores and Single Molecule Transport through Nanocapillaries, University of Cambridge, 2013.

(12) Qiu, Y.; Hinkle, P.; Yang, C.; Bakker, H. E.; Schiel, M.; Wang, H.; Melnikov, D.;

Gracheva, M.; Toimil-molares, M. E.; Imhof, A.; Siwy, Z. S. *ACS Nano* **2015**, *9*, 4390–4397.

(13) Wanunu, M.; Morrison, W.; Rabin, Y.; Grosberg, A. Y.; Meller, A. *Nat. Nanotechnol.* **2010**, *5*, 160–165.

(14) Fologea, D.; Uplinger, J.; Thomas, B.; Mcnabb, D. S.; Li, J. *Nano Lett.* **2005**, *5*, 1734–1737.

(15) Liu, Q.; Wu, H.; Wu, L.; Xie, X.; Kong, J.; Ye, X.; Liu, L. *PLoS One* **2012**, *7*, e46014.

(16) Yu, J.; Lim, M.; Thi, D.; Huynh, N.; Kim, H.; Kim, H.; Kim, Y. *ACS Nano* **2015**, *9*, 5289–5298.

(17) Citartan, M.; Tang, T. H.; Tan, S. C.; Gopinath, S. C. B. *World J. Microbiol. Biotechnol.* **2011**, *27* (5), 1167–1173.

(18) Akahori, R.; Haga, T.; Hatano, T.; Yanagi, I.; Ohura, T.; Hamamura, H.; Iwasaki, T.; Yokoi, T.; Anazawa, T. *Nanotechnology* **2014**, *25* (27), 275501.

(19) https://www.idtdna.com/pages/products/dna-rna/hplc-page. Accessed on 2/11/2016.

Chapter 5

Coating of Nanopipettes Using a Functionalised Lipid Bilayer

Synopsis: This chapter begins with a brief introduction to the structure and behaviour of phospholipids. Initially, the preparation and characterisation of vesicles used as supported lipid bilayers (SLB) is described followed by experiments evaluating the coating of nanopipettes with a POPC lipid bilayer in 1 M KCl. Next, binary lipid mixtures were examined with the aim of introducing functionalisation to the lipid bilayer coating. In the final sections of this chapter, initial experiments to coat nanopipettes with a functionalised lipid bilayer are presented. A range of techniques were employed to characterise vesicles including DLS, AFM and DSC that were complimentary to the electrochemical measurements used to detect changes in pore diameter and DNA translocations through modified pores.

5.1 Introduction

Nanopipettes have numerous advantages including ease of fabrication, easy wettability with electrolyte and low manufacturing costs.[1] However, one of their main disadvantages is that pore sizes below ~15 nm are hard to achieve by changing the laser-assisted pulling parameters alone.[2–4] This is in contrast to classical chip-based devices that have been made with sub-5 nm diameters.[5,6] Having a pore size that closely matches the size of the analyte is paramount for achieving a high SNR.[1,3,4]

In light of this, SEM and atomic layer deposition (ALD) are two methods that have been employed to fine tune the size of quartz nanopipettes fabricated using laser-assisted pulling.[3,4] Steinbock et al.,[4] used the beam of electrons of a SEM to shrink the pore diameter of nanopipettes from 42 nm down to 11 nm and were able to control the rate of shrinking by changing the beam potential and beam current. The main advantage of their approach is that SEM imaging could be used to monitor the shrinking in real-time. On the other hand, ALD was used to control the deposition of aluminum oxide (Al_2O_3) layers onto nanopipettes with starting diameters of 25 ± 3 nm to achieve pore sizes a small as 7.5 nm.[3] One of the advantages of ALD deposition is that the technique is amenable to batch deposition on multiple nanopipettes at the same time. However, unlike the method used by Steinbock et al. the reduction in pore size of nanopipettes used for DNA translocations is inferred from conductance measurements. [3,4]

Alternatively, the 'fluid-wall technology' has been utilised to reduce the diameter of nanopores and also has a number of other advantages as shall be discussed.[7] In this approach, lipid bilayers are used to create hybrid biological solid-state nanopore sensors. Initial work in the literature showed coating of planar silicon nitride (Si_3N_4) nanopores and later of nanopipettes.[8,9] Mayer and co-workers were inspired by the olfactory system of insects that have nanopores in their exoskeletons.[8] These nanopores are coated with a fluid lipid bilayer containing receptors specific to odorant molecules. Once bound, the odorant molecules are translocated to specific receptors on the olfactory neurons in the antennae of the insect. Similarly, Mayer et al. used lipid bilayers to coat planar solid-state nanopores. Firstly, they were able to fine-tune the pore size by using different lipids with thicker bilayers resulting in a greater reduction in pore size. Additionally, by changing the temperature, lipids undergo a phase transition resulting in a change in bilayer thickness. In this way the pore size can be changed in-situ (*vide infra*). The fluid lipid bilayer coating also prevented the nanopore from clogging and thus allowed the translocation of the amyloid-beta (Aβ) peptide which is a hallmark of Alzheimer's disease. In the absence of the mobile lipid bilayer coating, within a few min of Aβ peptide addition the pore was clogged. Secondly, as shown schematically in Figure 5.1 they coated their solid-state pores with a POPC bilayer containing a biotinylated lipid (biotin-PE). These biotin groups form a strong non-covalent interaction with streptavidin and pre-concentrate streptavidin added to the bulk solution to the mobile lipid bilayer. This induces a much higher streptavidin translocation frequency compared to when antibodies, which have a much lower affinity to biotin are added to the bulk solution.

Work from Keyser's laboratory then applied the technique to nanopipettes, coating quartz nanopipettes with a mobile lipid bilayer (Figure 5.1).[9] Using a KCl concentration of 0.5 M, they were able to detect different folding states when translocating λ-DNA with an V_{bias} of +500 mV. Additionally, they reported a higher DNA detection success rate when using their lipid coated nanopipettes compared to uncoated nanopipettes.

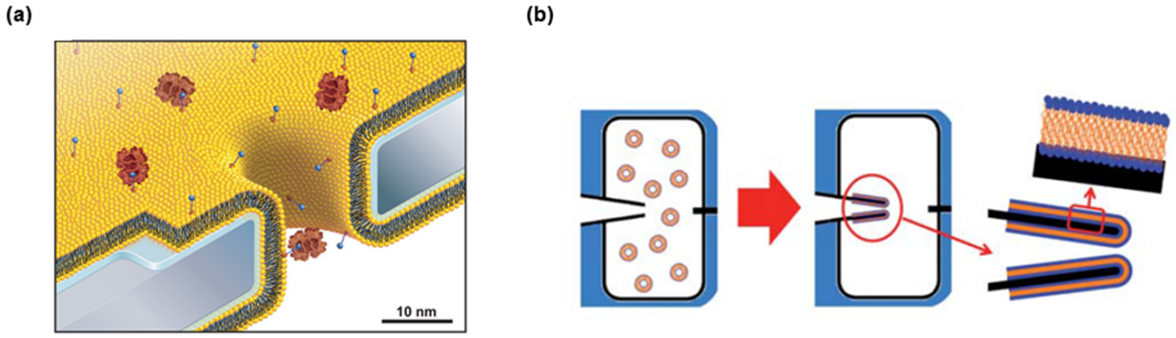

Figure 5.1. Schematic representation of a hybrid biological solid-state nanopore systems **(a)** Si_3N_4 planar chip coated with a POPC lipid bilayer containing biotin-PE groups (blue circles). The high affinity of biotin to streptavidin (red) pre-concentrates streptavidin close to the pore with subsequent translocation through the nanopore of the biotin-streptavidin complex. **(b)** Exposure of the nanopipette tip to vesicle solution results in their rupturing and spreading onto the walls of the nanopipette tip to form a lipid bilayer. Figures reprinted with permission from ref. 8 and ref. 9.

Advantages of this 'fluid-wall technology' include a reduction in pore size that can be controlled by careful choice of lipids, little to no pore clogging as well as real-time control of the pore-size using temperature. Furthermore, molecular specificity can be introduced by incorporating mobile receptors within the lipid bilayer to pre-concentrate the desired analyte close to the pore.[8] This is particularly desirable as more information can be extracted by using these receptors relative to an unmodified nanopore. In addition, by incorporating a range of different receptors that are specific to different target molecules, a new level of molecular specificity can be introduced to the platform.

5.1.1 Introduction to Phospholipids

Biological membranes, typically ~3-5 nm in height (depending on lipid composition), are crucial to life, forming a semi-permeable barrier which delimits a cell from its environment.[10–13] In eukaryotes, membranes compartmentalise intracellular structures (or organelles) such as the nucleus and mitochondria from the cytoplasm. In 1972, Singer and Nicolson,[14] proposed the fluid mosaic model to describe the gross architecture of a membrane. In this model, proteins are embedded within a fluid two-dimensional lipid matrix.

A huge variety of lipids exist within biological membranes, however, only two classes of phospholipids will be introduced here as these are most relevant to the research discussed in this chapter. Phospholipids are amphiphilic molecules consisting of a phosphate-based, hydrophilic head group and a hydrophobic fatty acid region, with the different head groups being used to define phospholipid classes.[15] Two such classes are the phosphatidylcholine (PC) and phosphatidylethanolamine (PE), the former has a tertiary amine while the later has a primary amine. In this study POPC and DPPE, the structure of which are shown in Figure 5.2, were the two major phospholipids used. POPC has two asymmetric acyl chains, an 18 carbon saturated acyl chain and a 16 carbon unsaturated acyl chain while DPPE has two saturated 16 carbon long acyl chains.

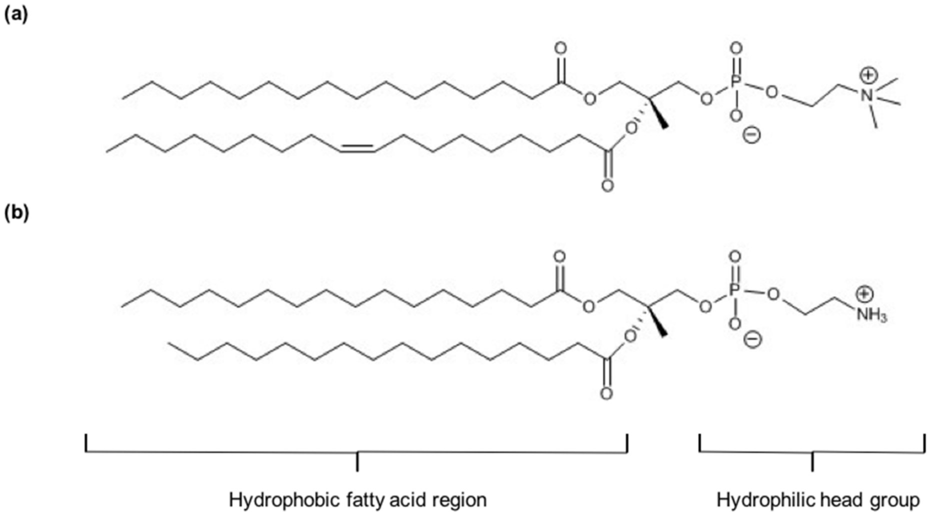

Figure 5.2. Structure of **(a)** POPC and **(b)** DPPE showing the hydrophobic fatty acid region and the hydrophilic head group.

A further difference between PC and PE is in their shape. PC lipids have a cylinder shape (type 0) while PE lipids have an inverse cone shape (type II), as shown schematically in Figure 5.3.[10,15,16] PC lipids have a head group cross sectional area comparable to their tail region while PE lipids have a smaller head group than PC lipids and a head group cross sectional area that is smaller than its tails.[17,18]

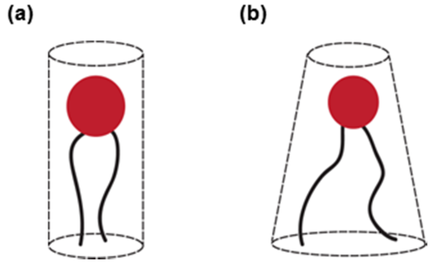

Figure 5.3. Schematic representation of lipid shapes, **(a)** type 0 and **(b)** type II.

In an aqueous environment the hydrophobic effect drives the lipids to arrange themselves so that exposure of the hydrophobic region with water is minimized.[19] Depending on the lipid structure different phases exist. For example, pure type 0 lipids like POPC will form a lamellar or bilayer phase such as the ordered gel (L_β) or liquid-crystalline (L_α) phase, shown schematically in Figure 5.4, where monolayers arrange themselves with their hydrophobic fatty acid region facing each other.[10,15,20,21] Pure type II lipids on the other hand, such as DPPE will form an inverted hexagonal phase (H_{II}, Figure 5.4). Mixing type 0 and type II lipids, as is common in eukaryotic membranes will however result in a bilayer formation.[22]

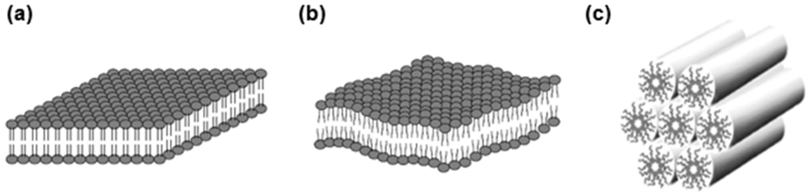

Figure 5.4. Schematic representation of **(a)** L_β state, **(b)** L_α state, **(c)** H_{II} phase. Figures reprinted with permission from ref. 20 (a and b) and ref. 21 (c).

The most common phase in cells is the bilayer phase, with the transition temperature (T_m) of the lipids determining whether the bilayer is in a L_β or L_α state. Each lipid has its own characteristic T_m, below which the lipid is in a rigid L_β state and above which it is in a mobile L_α state as shown schematically in Figure 5.5.[20,21] In the L_β state lipids have fully extended hydrocarbon chains then when heated above their T_m the hydrocarbon chains melt and become more disordered.[23] This process is cooperative, reversible and thermotropic.

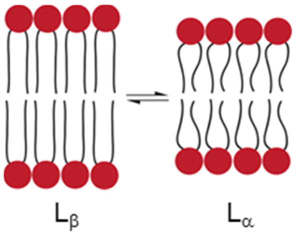

Figure 5.5. Schematic representation of the **(a)** L_β and **(b)** the L_α state.[23]

The T_m of a lipid or lipid mixture depends on their structure. The T_m will increase with acyl chain length, as van der Waals interactions increase with chain length and thus more energy is required to disrupt the L_β state. On the other hand, the T_m decreases in the presence of one or more double bonds as these introduce kinks in the acyl chain which disrupts the close packing of lipids.[23–25] Additionally, the T_m is affected by the lipid head group due to the different electrostatic interactions.[25,26]

In this work SLB, a type of artificial model membrane formed on a solid support, have been employed to add functionality to nanopipettes. One way to form an SLB is using vesicles[I] which are classified according to the number of bilayers and size as; multilamellar vesicles (MLV), large unilamellar vesicles (LUV) and small unilamellar vesicles (SUV). These are shown schematically in Figure 5.6. In each case these spherical structures have an internal and external aqueous environment.

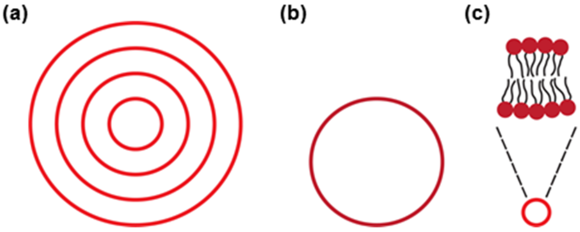

Figure 5.6. Schematic representation of a **(a)** MLV, **(b)** LUV and **(c)** SUV. *Note: diagram not drawn to scale.*

MLV consist of multiple lamellar phases separated by water, forming a structure resembling the layers of an onion and with a diameter of ~100 - 5000 nm.[24,27–29] On the other hand, LUV and SUV consist of a single lamellar with the former being ~100 - 1000 nm in diameter and the latter ~10 - 100 nm.

[I] Liposomes are artificially made lipid vesicles. The two terms are often used interchangeably.

5.2 Experimental Objectives

Previous work presented in this thesis was aimed at the detection of a 100 nt sequence relevant to drug resistance in MTB. Detection of the 100 nt ssDNA was limited by the electronic detection system while detection of the 100 bp dsDNA sequence required the electrolyte to be changed from KCl to 2 or 4 M LiCl.

The aim of this chapter was to coat the tip of nanopipettes with a mobile lipid bilayer attached to the ssDNA of interest, as shown schematically in Figure 5.7. This surface immobilised ssDNA acts as a 'capture probe' for its cssDNA. Addition of cssDNA and non-cssDNA to the bulk electrolyte solution should result in hybridisation of only the cssDNA to the capture probe forming dsDNA. In this manner, the desired ssDNA is pre-concentrated close to the pore and will translocate preferentially. Such a platform was envisioned to be able to detect a ssDNA sequence of interest from a mixture of sequences. Additionally, simply by changing the sequence of the capture probe, a different ssDNA sequence could be detected.

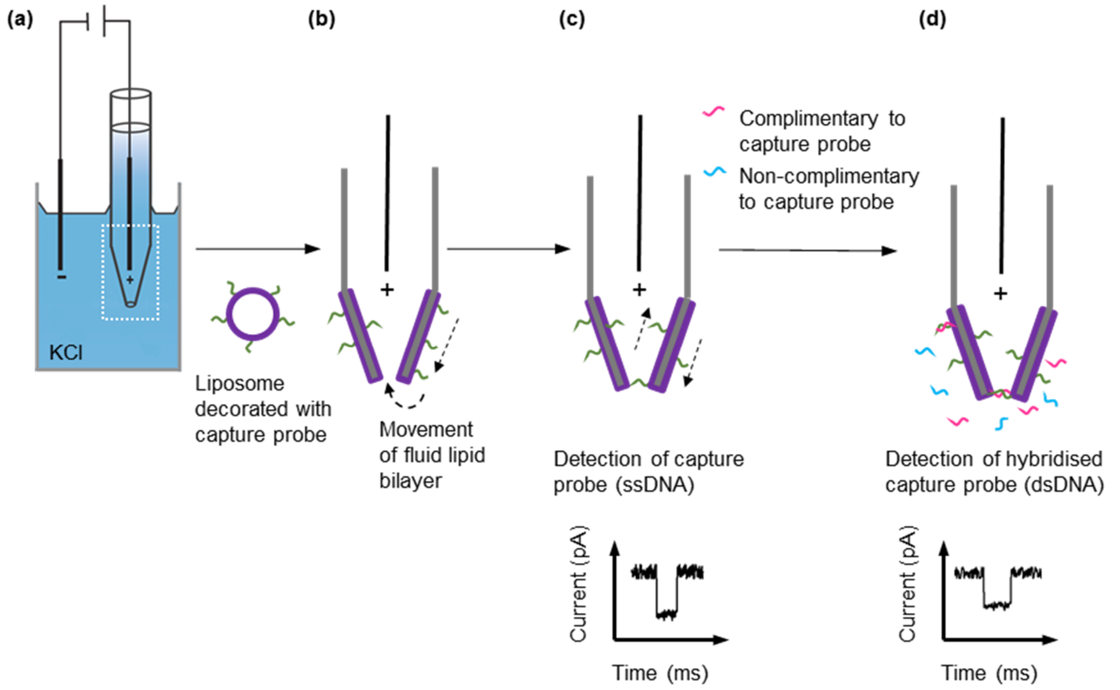

Figure 5.7. Schematic representation of **(a)** a nanopipette exposed to capture probe decorated liposomes, to form **(b)** a SLB attached to the capture probe. **(c)** The negatively charged and surface-bound ssDNA can translocate through the pore, giving a detectable current signature**.** **(d)** In the presence of cssDNA and non-cssDNA, only cssDNA hybridises to the capture probe forming dsDNA, the current signature of which upon translocation is different to that produced by ssDNA translocation. *Note: diagram not to scale.*

Moreover, it was also envisioned that similar chemistry could be used to link a range of proteins instead of ssDNA to the mobile lipid bilayer. For example, anti-5-methylcytosine (anti-5mC) antibodies could be attached to the fluid lipid bilayer to detect DNA cytosine methylation. This epigenetic modification has been extensively studied due to its relevance as a cancer biomarker.[30,31]

5.3 Results and Discussion

5.3.1 Characterisation of POPC Vesicles

POPC is one of the most abundant types of lipid in mammalian cells and was chosen as a model system as it is zwitterionic so has no overall charge and has a phase transition temperature of -2 °C.[10,12,13,32,33] Therefore, at rt the POPC bilayer is in a fluid L_α state.

Initially, DLS was used to estimate the hydrodynamic diameter of three SUV samples prepared by bath sonication (Table 5.1) and assess their hydrodynamic diameter over a five-day period. The hydrodynamic diameter for samples one and two did not change significantly over the five-day measurement period. For sample one the hydrodynamic diameter varied between 66 - 68 nm while for sample two it varied between 107 - 110 nm. Conversely, for sample three the diameter did not remain stable over the five-days and instead vesicle aggregation was seen.

Table 5.1. Hydrodynamic diameter in nm for POPC vesicles measured by DLS over a five day period.[m]

Sample	**Day**				
	1	**2**	**3**	**4**	**5**
1	66.13 ± 0.3	66.4 ± 0.2	65.7 ± 0.3	66.8 ± 0.2	68.2 ± 0.2
2	107.3 ± 0.3	106.8 ± 0.6	111.0 ± 0.7	106.6 ± 0.1	110.4 ± 0.5
3	59.9 ± 0.5	68.6 ± 3.7	-	-	-

In Figure 5.8, the intensity histograms for sample three are plotted. From day three onwards the emergence of two populations was visible. It should be noted, that particle sizing measurements using DLS are highly sensitive to sample aggregation as the intensity of scattered light is proportional to particle diameter to the sixth power.[34] Therefore, given the

---

[m] Mean diameter is the average of three measurements, quoted with the standard errors of the mean.

sensitivity of DLS to particle size, the amount of unilamellar vesicle aggregation is likely to be small.

While samples one and two showed no sign of aggregation, using DLS the appearance of a second population was observed for sample three from the third day onwards. All vesicles were therefore used within three days of being made to ensure consistency between experiments.

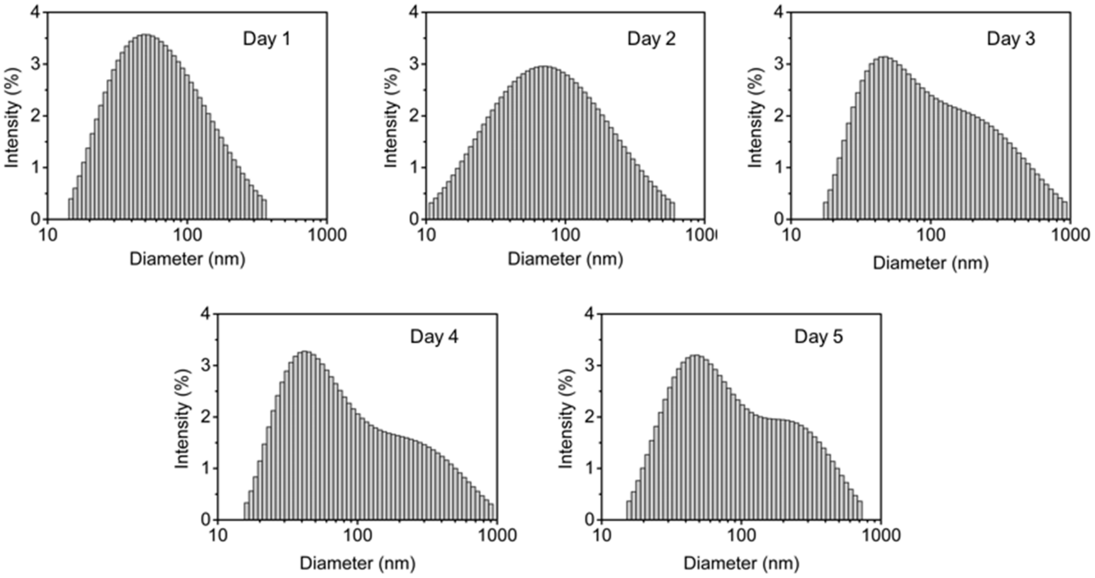

Figure 5.8. DLS measurements of sample three over a five-day period for 2 mM POPC vesicles in H_2O.

SUV with a more uniform size distribution can be achieved by disruption of MLV by membrane extrusion instead of bath sonication. In this method the lipid suspension is forced through a polycarbonate membrane that has well-defined pore sizes, producing unilamellar vesicles that have a diameter closely matching the pore size of the polycarbonate membrane. While the unilamellar vesicles produced have a more uniform size compared to those produced by sonication, the process is more time consuming and was therefore not deemed necessary for these experiments.[35] The aim here was to rupture vesicles on the surface of nanopipettes, so size homogeneity was not of great concern.

5.3.2 Cyclic Voltammetry (CV) Measurements of POPC Coated Nanopipettes

Figure 5.9, shows CV measurements for a nanopipette before and after exposure to 2 mM POPC vesicles in H_2O. For consistency between experiments, conductance measurements throughout this chapter were determined by fitting the ±200 mV range of the CV graphs.[n]

For the nanopipette shown in Figure 5.9, a 27% decrease in G_{pore} was observed between the bare and coated nanopipette. This 9 nS decrease corresponded to an estimated 9 nm reduction in pore size. The height of a POPC bilayer and water layer between the bilayer and quartz are 3.7 ± 0.1 nm[o] and 1 ± 0.1 nm respectively,[8,13,36,37] so formation of a uniform lipid bilayer coating around the nanopore was expected to decrease the pore size by 9.4 ± 0.1 nm which is in good agreement with the observed decrease in pore diameter.[p] Moreover, a similar change in conductance was found when coating other nanopipettes, the average decrease in conductance was 25 ± 2% (n = 4).

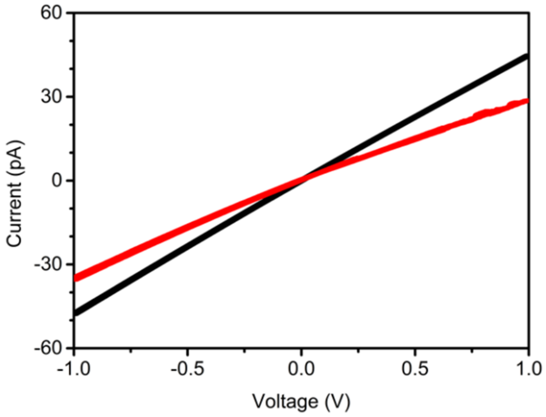

Figure 5.9. Representative CV measurement for a bare nanopipette (black, G_{pore} = 35 nS) and after exposure to POPC vesicle (red, G_{pore} = 25 nS).

To assess whether the decrease in conductance could be attributed to other effects such as electrolyte evaporation, firstly the conductance of a bare nanopipette was monitored over the time frame of the experiment and was found to be negligible (Figure 5.10, a). Over a six h period the change in conductance was on average 100 ± 3% (n = 3) when comparing the initial and final CV measurements of nanopipettes in 1 M KCl. During the coating procedure, changes in the KCl electrolyte concentration occur by the addition of $CaCl_2$ solution and vesicles. As another control, the coating procedure was modified so that following the

---

[n] Slight current rectification was observed for the coated nanopipette. r = 1.2 and was calculated using V_{bias} values at ±900 mV (see chapter 3 for equation). This small current rectification was observed for this instance only and not in the three repeat experiments.

[o] Mayer et al. and Keyser et al. assume a POPC bilayer height of 3.7 ± 0.1 nm based on data for the closely related 16:0 PC lipid. For consistency and comparison this value has also been assumed, although work by Kučerka et al. found a POPC bilayer height of 3.91 nm (refer also to section 5.3.6).[8,9,12,37]

[p] Estimation of pore diameter based on conductance measurements is highly dependent on the taper length parameter which was not accurately determined for each nanopipette used.

exchange of 600 µL of 1 M KCl electrolyte with 10 mM $CaCl_2$ solution, the addition of 200–300 µL of POPC vesicles was replaced by 300 µL of the vesicle hydration medium (Figure 5.10, b). The current-voltage response was then measured after 20 min to allow the system to equilibrate. On average there was an 18 ± 4% (n = 3) decrease in conductance which is smaller than the 25 ± 2% decrease in conductance observed when adding POPC vesicles. This is in agreement with the measured decrease in 1 M KCl conductivity by the addition of $CaCl_2$ which was found to be 17 ± 0.6%.[q]

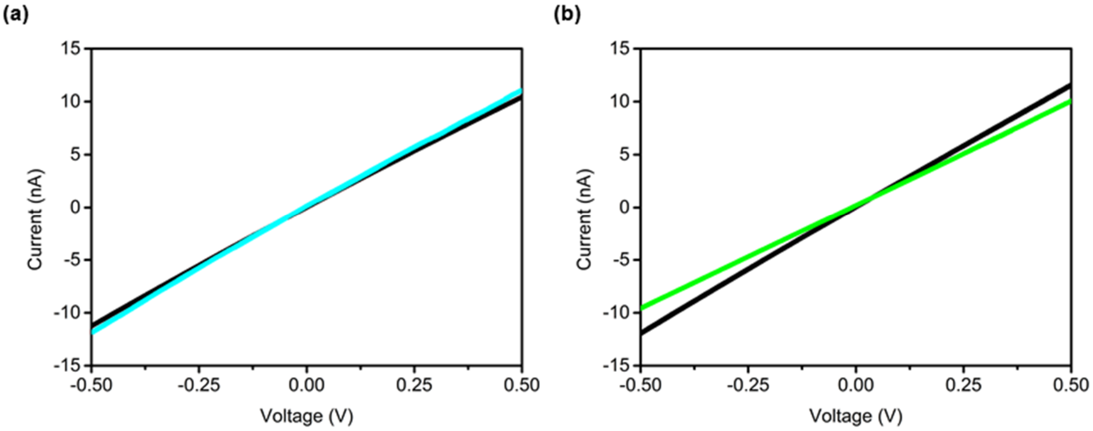

Figure 5.10. Representative CV measurements for **(a)** a bare nanopipette (t = 0 hr, black, G_{pore} = 22 nS) which was measured again six h later (t = 6 h, cyan, G_{pore} = 23) and **(b)** a bare nanopipette (black, G_{pore} = 23 nS) was subjected to a control KCl dilution procedure and the CV measured (green, G_{pore} = 20 nS).

Together these two control experiments suggest that the decrease in conductance observed when adding POPC vesicles were attributable to a lipid bilayer coating the nanopipette tip or at least partial coating of the tip. The decrease in conductance when adding vesicles to the system is greater than the reduction in conductance due to electrolyte evaporation over a six h period or a change in electrolyte conductivity by $CaCl_2$ addition.

5.3.3 Current-Time (I(t)) Measurements of POPC-Coated Nanopipettes and RMS Noise

Next the I(t) response of the POPC-coated nanopipettes was recorded and given that POPC has no overall charge and that DNA is negatively charged, a negative V_{bias} to the electrode in the external bulk solution was of particular interest. Notably, 1 M KCl electrolyte was chosen in an attempt to increase the SNR. Previous work in the literature using lipid-coated solid-

---

[q] Error propagation used when calculating relative conductivity decrease.[46]

state nanopores used KCl concentrations between 0.15 – 2 M KCl while for nanopipettes KCl concentrations between 0.15 – 0.5 M KCl have been used.[8,9]

Figure 5.11 shows representative I(t) traces for a nanopipette with an initial G_{pore} of 35 nS and an V_{bias} of -100 mV, before and after coating with a POPC bilayer. A modest increase in RMS noise is seen following coating of the pore; the RMS noise for the traces shown increased by 34% from 8.4 to 11.3 pA for the bare and coated nanopipette respectively.

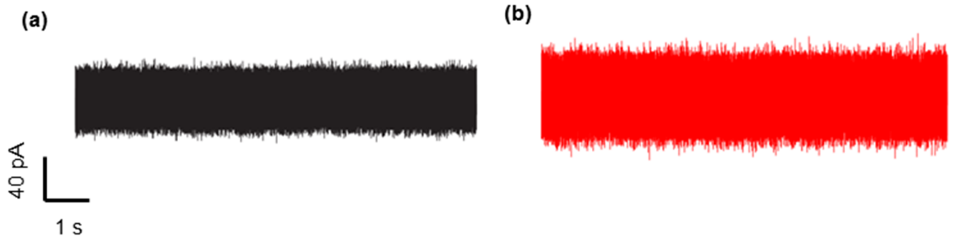

Figure 5.11. I(t) traces with an V_{bias} of -100 mV for a bare (black) and POPC-coated (red) nanopipette. Initial G_{pore} = 35 nS. I(t) traces were filtered at 20 kHz.

At higher V_{bias} there was a greater difference in the I(t) traces of the bare and coated nanopipette (Figure 5.12). The RMS noise for the nanopipette with an V_{bias} of -500 mV increased more than fourfold from 11.0 to 48.9 pA (Figure 5.12, a). On the other hand, with an V_{bias} of -900 mV current blockages were observed for the coated nanopipette that were not present in the I(t) traces prior to coating (Figure 5.12, b). Current blockages were also observed with V_{bias} of -600, -700 and -800 mV (appendix VI).

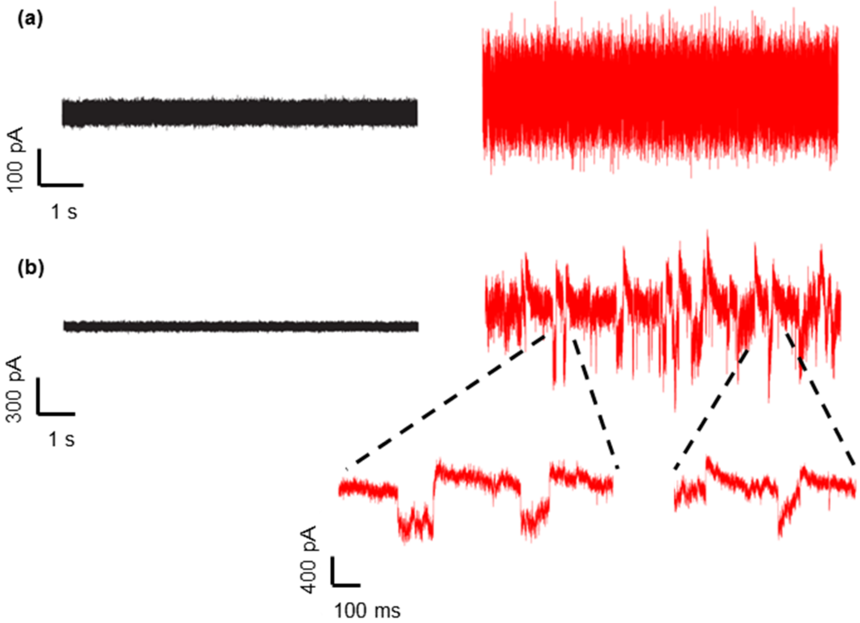

Figure 5.12. Comparison of I(t) traces for a nanopipette at an V_{bias} of **(a)** -500 and **(b)** -900 mV before (black) and after coating with a POPC bilayer (red). Initial G_{pore} = 35 nS. I(t) traces were filtered at 20 kHz.

RMS noise was calculated from at least 18 million data points of recorded I(t) traces for two uncoatead nanopipettes and upon coating with a POPC bilayer, as shown in Figure 5.13. The two nanopipettes had an initial conductance of 35 and 45 nS (Figure 5.13, a and b respectively) and for both nanopipettes there was an increase in RMS noise upon coating, especially above -500 mV. As shown in Figure 5.12 however, current decreases attributed to translocation of lipid fragments were observed, therefore in these cases, calculation of the RMS noise by taking the data points of the entire I(t) traces results in an overestimate of RMS noise compared to calculating the RMS noise for portions of the trace without current decreases. For example, calculation of the RMS noise with an V_{bias} of -900 mV for portions of the I(t) trace where no translocation events were visible gave a value of 89.3 ± 7 pA[r] compared to the higher value of 129.3 ± 14 pA when including these translocation events. Nevertheless, it was decided to include these events in the RMS noise calculations plotted in Figure 5.13 as the overall increase in noise for a coated nanopipette was of interest.

For positive V_{bias} the two coated nanopipettes showed different behaviour. Little increase in RMS noise was seen for the nanopipette with an initial conductance of 35 nS while the nanopipette with an initial conductance of 45 nS (Figure 5.13, a and b, respectively) showed a greater increase in RMS noise at positive V_{bias}, especially above +200 mV compared to negative potentials.

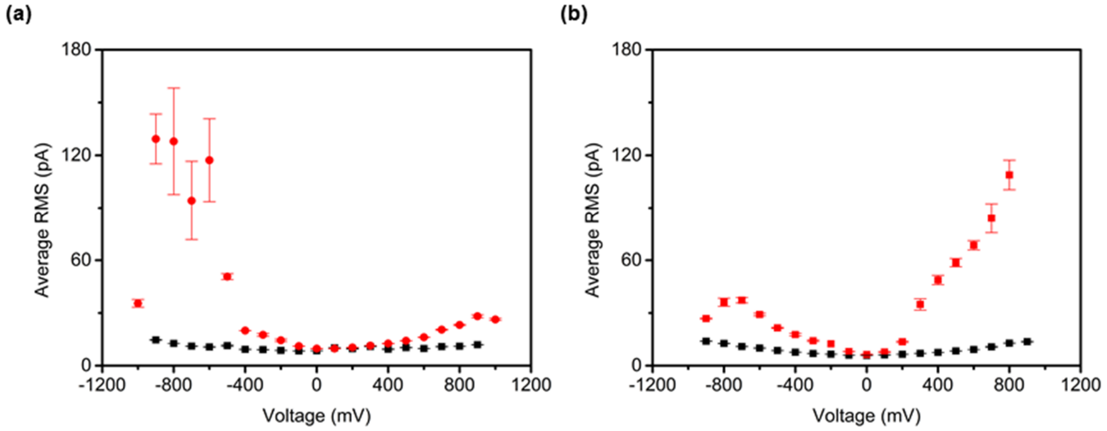

Figure 5.13. RMS noise for a bare (black squares) and coated (red circles) nanopipette. **(a)** bare nanopipette (G_{pore} = 35 nS) and after coating (G_{pore} = 25 nS) and **(b)** bare nanopipette (G_{pore} = 45 nS) and after coating (G_{pore} = 33 nS). Errors denote the standard error of the mean from multiple I(t) files.

The RMS values shown here indicated that the lipid bilayer is especially unstable at biases above -500 mV and depending on the device also at positive potentials; therefore, for

---

[r] Over four million data points used to calculate this RMS value.

subsequent coating experiments a smaller bias range was applied in an attempt to minimse damage to the bilayer.

5.3.4 Device-to-device Variation for POPC-Coated Nanopipettes

Differences in the RMS noise behaviour of two coated platforms were noted in section 5.3.3 at positive V_{bias} however, a high device-to-device variation was also present at negative V_{bias} for other platforms examined. Current blockages were observed at much lower V_{bias} for nanopipettes with a larger initial G_{pore} than the nanopipette data shown in section 5.3.3. Figure 5.14, shows the I(t) traces for V_{bias} at -100 and -200 mV for nanopipettes with an initial G of 47 and 45 nS respectively. For the coated traces shown in red, the square denotes some of the events that were greater than a 5 σ cut-off, determined using the MATLAB analysis script (see chapter 2 for more details on analysis code).

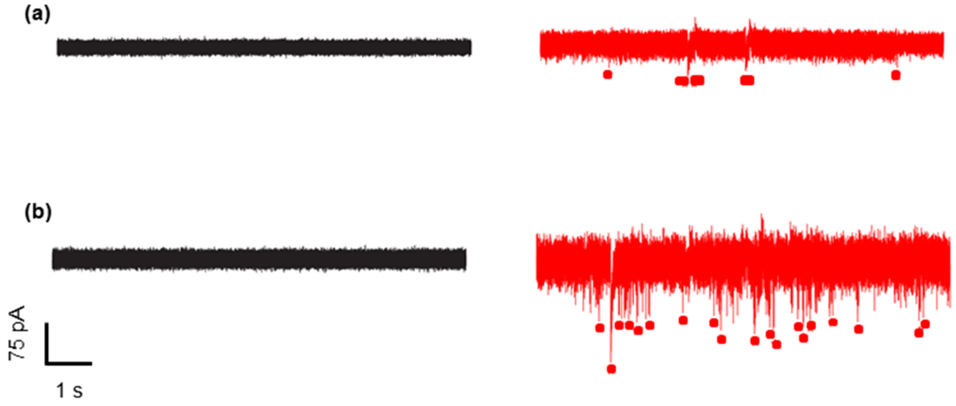

Figure 5.14. Representative I(t) traces for nanopipettes with an V_{bias} of **(a)** -100 mV, initial G_{pore} = 47 nS and **(b)** -200 mV, initial G_{pore} = 45 nS. I(t) traces were filtered at 20 kHz.

An increase in RMS noise upon POPC-coating together with the detection of current blockages indicated the formation of an unstable mobile lipid bilayer in 1 M KCl. It is not clear though, whether a uniform lipid bilayer was formed on the nanopipette tip which was damaged when a potential was applied or instead lipid 'islands' formed on the nanopipette tip. Alternatively, it is also speculated that despite exchanging the vesicle solution with fresh electrolyte not all vesicles were removed and therefore these may in part be responsible for the observed events. However, by DLS measurements the hydrodynamic diameter of the POPC vesicles in 2 mM solution was found to be ~60 - 110 nm, which is much greater than the diameter of the nanopores (~13 - 33 nm). Therefore, translocation of intact vesicles seems unlikely.

5.3.5 Choice of Lipids for Capture Probe Attachment

Having characterised the coating of nanopipettes with POPC, the next step was the incorporation of a modified lipid for attachment to the capture probe. DPPE-GA (Figure 5.15) was chosen, as this lipid is readily available commercially and has a carboxylic acid group for reaction with the capture probe. DPPE (Figure 5.2) on the other hand which is the unmodified version of DPPE-GA was used for control experiments.

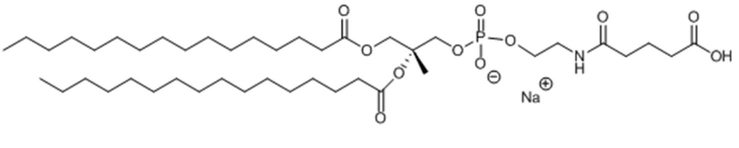

Figure 5.15. Structure of DPPE-GA.

Figure 5.16 shows the reaction scheme for the covalent attachment of the desired ssDNA with 5’ NH_2 group (i.e the capture probe) to DPPE-GA via an amide coupling reaction in the presence of EDCI, an activating agent for the carboxylic acid.

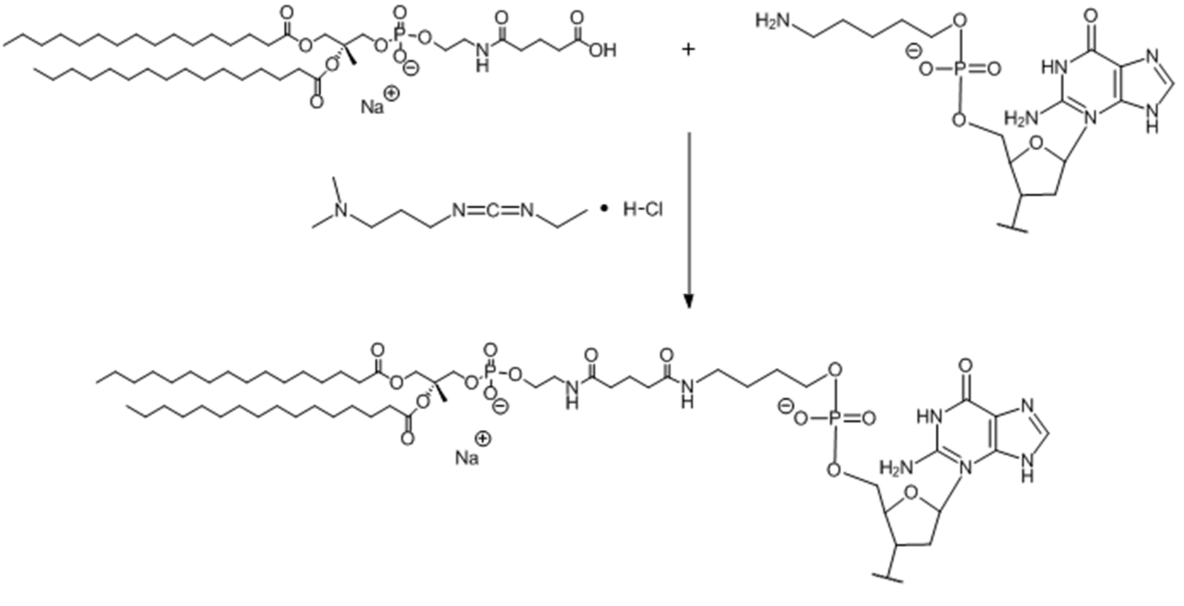

Figure 5.16. Reaction mechanism for amide bond formation between DPPE-GA and ssDNA with a 5’NH_2 group, using EDCI. *Note: for clarity only the first DNA nucleotide out of the 100 nucleotides is shown.*

5.3.6 Atomic Force Microscopy (AFM) Studies of POPC/DPPE Ratios

Prior to coating the nanopipettes, AFM was used to choose the amount of DPPE, the control for the modified lipid, to add to the binary lipid mixture. Given that in subsequent steps DPPE-GA would provide the sites available for the amide coupling reaction with the capture probe it was desirable to have 1) homogenous mixing and 2) sufficient number of sites available for coupling. The former was important to ensure uniform ssDNA coverage and the latter to ensure high coverage of ssDNA but also avoid overcrowding which could potentially hinder DNA hybridisation or cause clogging of the pore.

Initially POPC doped with 1 mol% DPPE was examined. A difference was observed in comparison to freshly cleaved mica, as shown in Figure 5.17, indicating the presence of a SLB. The lighter regions were attributed to DPPE while the darker 'background' to POPC. A height difference of ~1.1 nm was observed for the difference between POPC and DPPE, in reasonable agreement with the literature where a height of 0.65 - 1 nm has been reported for binary SLB.[38–40] However, POPC doped with 1 mol% DPPE showed an island of DPPE which would be unfavourable for the addition of ssDNA. Next, POPC doped with 9 and 17 mol% was assessed. In both cases a homogenous distribution of the two lipids was observed with height differences of ~0.4 and ~1.1 nm respectively. All images were acquired in contact mode, therefore it is speculated that the smaller than expected height difference for the 9 mol% sample could be due to excessive force on the sample by the AFM tip.

Moreover, although a rather crude comparison due to the different experimental techniques employed; Kučerka et al. found a POPC bilayer height at 30 °C of 3.91 – 4.51 nm while Stidder et al. report a thicker bilayer height for DPPE of 5.4 nm in the 25.2 – 65.5 °C range.[11–13] This supports the experimental data presented here where DPPE regions were taller than POPC regions.

In addition, reassuringly, an increase in the mol fraction of DPPE translated into an increase in the higher regions seen in the AFM images which were attributed to DPPE. Intuitively, one would expect that for an SLB of POPC doped with 9 and 17 mol% DPPE, that the DPPE would constitute approximately 9 and 17% respectively, of the image which is not the case in Figure 5.17. Using the flooding process in the WSxM software (see chapter 2) to estimate the percentage coverage of DPPE relative to POPC, values of 0.95%, 12.7% and 27% were found for the 1, 9 and 17 mol% doped samples respectively. While the 1 mol% sample is in good agreement with the flooding process analysis, an overestimate was found for the 9 and 17 mol% samples. Such a difference between the actual doped mol fraction and flooding result is likely to be due to tip-sample convolution and the contact mode imaging employed. Using contact mode imaging large lateral forces exist between the AFM tip and the sample,[41] which is hypothesised to exaggerate the lateral area of DPPE. This effect is likely to be more pronounced with the 9 and 17 mol% sample where there were more POPC/DPPE boundaries.

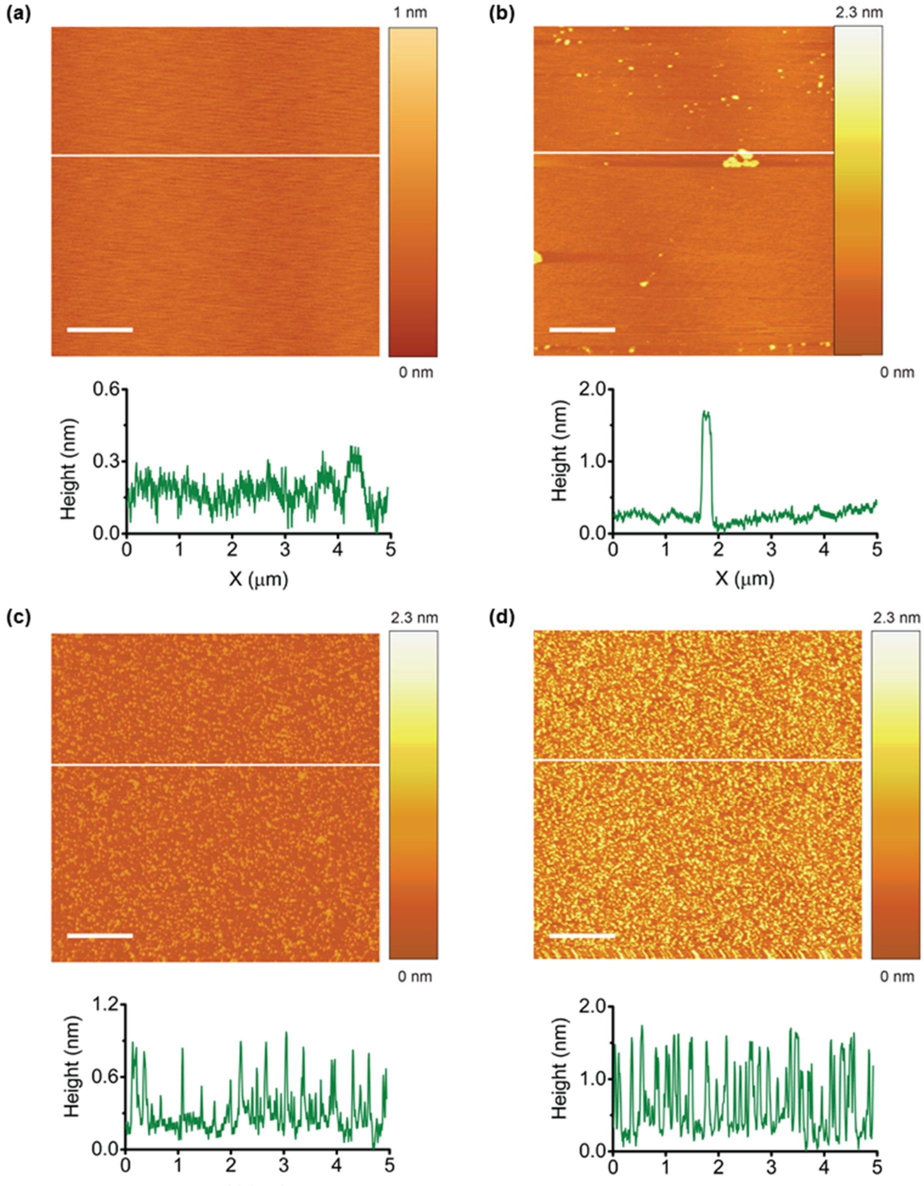

Figure 5.17. AFM images of **(a)** bare mica in air, POPC doped with **(b)** 1 mol%, **(c)** 9 mol% and **(d)** 17 mol% DPPE. Below each image the height profiles at the position indicated by the white line are shown. All scale bars are 1 μm.

However, it is also interesting to note that as aforementioned; PE lipids have a smaller head group than PC lipids. Incorporation of PE lipids into a PC bilayer therefore results in a decrease in the area occupied by each PC lipid as the PE lipids form intermolecular hydrogen bonds with neighbouring PC lipids while decreasing electrostatic repulsion between PC headgroups.[17,38] However, given the sub-nm^2 area per lipid, such difference are not detectable via AFM using nm sized probes.

Overall, the DPPE coverage observed in the AFM images scaled approximately with the expected values. The 1 mol% sample exhibited an island of DPPE although this may be an imaging artefact. A greater number of AFM images doped with 1 mol% DPPE are required to confirm whether the observed island is inherent to the sample or simply an imaging artefact. On the other hand, the 9 and 17 mol% samples showed no DPPE islands and homogenous POPC/DPPE mixing. In light of these AFM images, 9 mol% DPPE doping appeared to satisfy the two aforementioned criteria; homogenous mixing and sufficient sites for capture probe attachment. It was therefore decided to form POPC liposomes doped with 9 mol% DPPE-GA (POPC/9-DPPE-GA) for the attachment of capture probes.

5.3.7 Determination of Phase Transition Temperature by DSC

DSC[5] was used to examine the T_m of POPC/9-DPPE-GA. Figure 5.18 shows a selected region of the DSC scan with the peak used to determine the T_m. POPC and DPPE have a phase T_m of -2 and 64 °C respectively.[12,42,43] It was expected that the T_m would be in-between the T_m of POPC and DPPE-GA but closer to that of POPC as this lipid made up a greater proportion of the binary mixture and this was confirmed experimentally.[44] A T_m of 16.4 °C was found for this binary lipid mixture. Therefore, at rt a POPC/9-DPPE-GA bilayer is in a fluid L_α state.

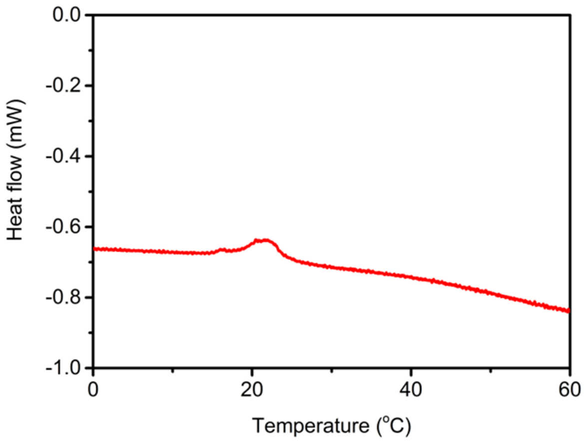

Figure 5.18. Selected DSC scan of POPC/9-DPPE-GA.

---

[5] DSC experiments were performed and analysed by Dr Arwen Tyler, research associate in the Membrane Biophysics group, Imperial College London.

5.3.8 Hybridisation of ssDNA

In chapter 4 agarose gel electrophoresis confirmed successful hybridisation of the two ssDNA sequences to form dsDNA. The established protocol however required the presence of buffers and heating to 95 °C then cooling of the DNA to 37 °C.[45] This protocol was not optimal for the envisioned nanopore sensor where hybridisation occurs between the capture probes attached to the lipid bilayer and cssDNA in the bulk KCl electrolyte. As heating the nanopore set-up to 95 °C was undesirable, hybridisation of the two ssDNA strands in KCl electrolyte incubated for one h at rt was tested. Surprisingly, using these conditions hybridisation did occur. The agarose gel electrophoresis image in Figure 5.19 shows the 100 nt sequence with no modification in lane 2 and the 100 nt sequence with the 5’ NH_2 group in lane 3. The presence of 100 bp dsDNA for samples hybridised using the established protocol and using KCl electrolyte at rt are shown in lanes 4 and 5 respectively. A very faint band, corresponding to unhybridised ssDNA is visible in lane 5 for the hybridisation at rt. However, given that the hybridised product was observed and the downstream application, incomplete hybridisation was not of great concern.

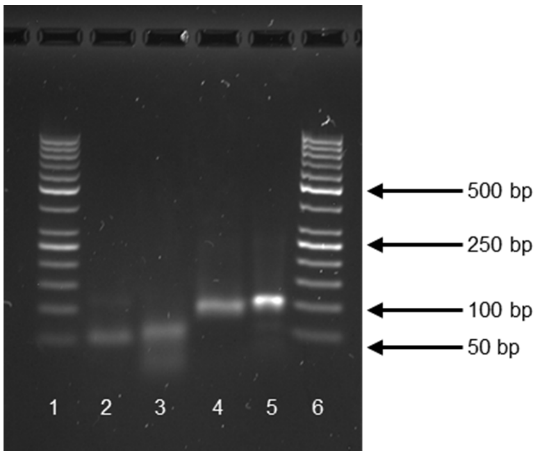

Figure 5.19. Agarose gel electrophoresis image (2%, 5 V/cm, 70 min, 1x TBE) comparing dsDNA hybridisation using an established protocol and at rt. Lane 1 and 6: ‘50 bp ladder’ (ThermoFisher), Lane 2: 100 nt ssDNA sequence, Lane 3: 100 nt cssDNA sequence with 5’ NH_2 group, Lane 4: ds100 bp DNA hybridised using standard protocol and Lane 5: 100 bp dsDNA hybridised in 1 M KCl electrolyte at rt for 1 h.

5.3.9 CV Measurements of Nanopipettes exposed to Modified Vesicles

Having confirmed the hybridisation of ssDNA in 1 M KCl electrolyte at rt and decided on the amount of modified lipid with which to dope the POPC bilayer, preliminary experiments were carried out towards achieving the experimental objective set out in section 5.2.

POPC/9-DPPE-GA vesicles were incubated with EDCI, to activate the free carboxylic acid groups then the ssDNA with 5' NH_2 group was added and left for 1 h 30 min to form vesicles decorated with ssDNA, henceforth referred to as POPC/9-DPPE-GA/ssDNA vesicles. The lipid composition of these vesicles is shown schematically in Figure 5.20 for clarity.

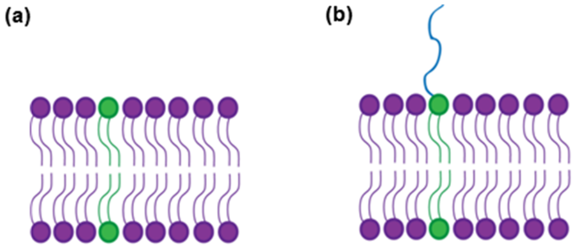

Figure 5.20. Schematic representation of lipid composition of the vesicles used in this section. **(a)** POPC/9-DPPE-GA and **(b)** POPC/9-DPPE-GA/ssDNA. *Note: diagram not drawn to scale.*

Following the same procedure as in section 5.3.2, nanopipettes were exposed to POPC/9-DPPE-GA or POPC/9-DPPE-GA/ssDNA vesicles. Figure 5.21, a shows the current-voltage response obtained for the bare (black) and coated (orange) nanopipette when exposed to POPC/9-DPPE-GA vesicles and Figure 5.21, b shows the current-voltage response before (black) and after exposure to POPC/9-DPPE-GA/ssDNA vesicles (purple).

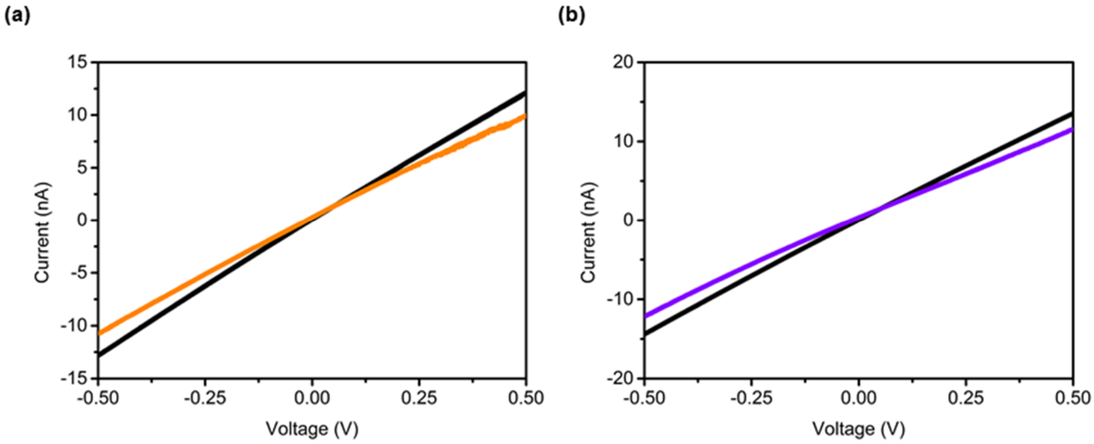

Figure 5.21. CV measurements for a **(a)** bare nanopipette (black, G_{pore} = 24 nS) and after exposure to POPC/DPPE-GA vesicles (orange, G_{pore} = 20 nS) and **(b)** bare nanopipette (black, G_{pore} = 28 nS) and after exposure to POPC/DPPE-GA/ssDNA vesicles (purple, G_{pore} = 23 nS).

In both cases a similar decrease in conductance of 18% (n = 1) and 19% (n = 1) was observed following exposure to POPC/9-DPPE-GA and POPC/9-DPPE-GA/ssDNA vesicles respectively. These decreases in conductance are smaller than the 25 ± 2% conductance decrease seen when coating with POPC vesicles. These values are however, comparable to the control experiment (see section 5.3.2) where on average an 18 ± 4% decrease in conductance was observed solely by changing the 1 M KCl electrolyte concentration by the addition of $CaCl_2$ solution and vesicle hydration medium.

Coating of nanopipettes with either POPC/9-DPPE-GA or POPC/9-DPPE-GA/ssDNA could not at this stage be confirmed due to the limited data available. Assessing the device-to-device variation would help to confirm whether the observed decrease in conductance can be attributed to coating of the nanopipette. In the next section preliminary I(t) measurements were used to address these possible scenarios.

5.3.10 Towards the Coating of Nanopipettes with Capture Probe Decorated Vesicles

I(t) traces for nanopipettes exposed to the control POPC/9-DPPE-GA vesicles showed current blockages at an V_{bias} of -100 mV which were not present in the I(t) traces of the bare nanopipette (Figure 5.22). Using the MATLAB analysis code (see chapter 2) with a 5 σ cut-off, a total of 26 events were detected for the nine s trace shown below.

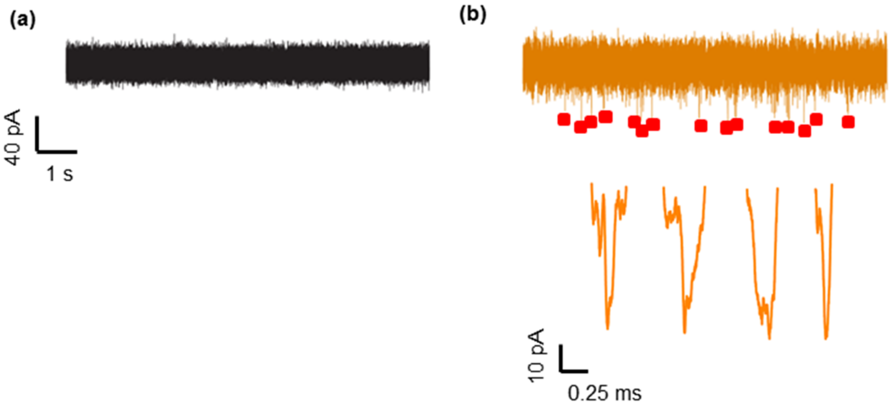

Figure 5.22. Representative I(t) traces with an V_{bias} of -100 mV for a **(a)** bare nanopipette and **(b)** following exposure to POPC/9-DPPE-GA vesicles with typical events shown below. Some of the events detected using the MATLAB code (see chapter 2) are indicated with a red square. I(t) traces were filtered at 20 kHz.

In section 5.3.3, data was presented showing events in the I(t) traces of POPC-coated nanopipettes with an V_{bias} of -100 mV. The scatter plot in Figure 5.23 compares events from the POPC-coated (red triangles) and POPC/9-DPPE-GA exposed nanopipette (orange squares). Although a very small dataset, overall the POPC-coated nanopipette events have a smaller ΔI than those observed with the POPC/9-DPPE-GA exposed nanopipette, while the τ of the two populations appears to be similarly broad.

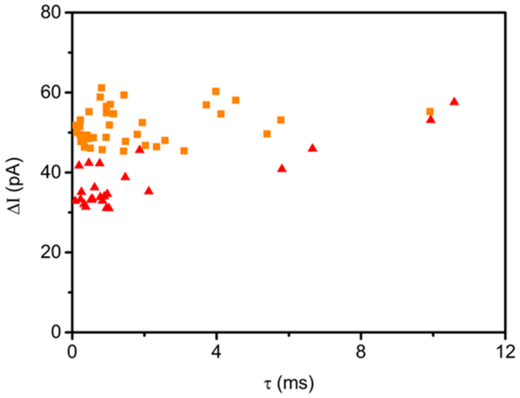

Figure 5.23. Scatter plot of events (ΔI vs. τ) with an V_{bias} of -100 mV, detected using a POPC-coated nanopipette (red triangles, G_{pore} = 38 nS, n = 26) and a nanopipette exposed to POPC/9-DPPE-GA vesicles (orange squares, G_{pore} = 20 nS, n = 39).

It is not clear how the addition of DPPE-GA to POPC vesicles produced this difference in the event ΔI however, it is hypothesised that the lipid species translocating for POPC-coated nanopipettes has a smaller diameter than that for the POPC/9-DPPE-GA exposed nanopipette. A lipid species with a smaller diameter would exclude less electrolyte volume from the pore and hence account for the smaller ΔI.

Similarly when a bare nanopipette was exposed to POPC/9-DPPE-GA/ssDNA vesicles, current blockages emerge in the I(t) trace which were not present for the bare nanopipette (Figure 5.24).

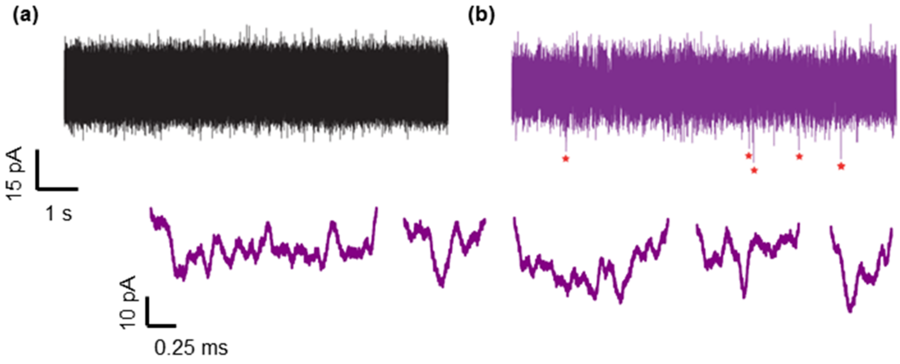

Figure 5.24. Representative I(t) traces with an V_{bias} of -100 mV for a **(a)** bare nanopipette and **(b)** following exposure to POPC/9-DPPE-GA/ssDNA vesicles. Events detected using the MATLAB code (see chapter 2) are indicated with a red square and magnifications of the events are shown below the trace. I(t) trace in (a) were filtered at 20 kHz and in (b) at 10 kHz.

Although, few in number, these events have a smaller ΔI than those seen in the control experiment with POPC/9-DPPE-GA as shown below in Figure 5.25. The events are unlikely to be unreacted 100 nt ssDNA translocations as previous experiments in 1 M KCl (see chapter 4) were unsuccessful in their detection.

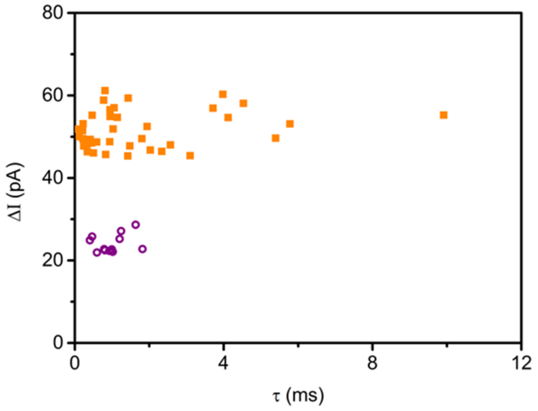

Figure 5.25. Scatter plot of events (ΔI vs. τ) observed for a nanopipette exposed to POPC/9-DPPE-GA vesicles (orange squares, G_{pore} = 38 nS, n = 39) and a nanopipette exposed to POPC/9-DPPE-GA/ssDNA (purple open circles, G_{pore} = 23 nS , n = 13) with an V_{bias} of -100 mV.

These events are tentatively assigned to lipid molecules attached to ssDNA although the exact location of these lipid-DNA complexes is unknown. It is hypothesised that such complexes could be adsorbed to the nanopipette tip in the form of lipid islands or be present in the bulk electrolyte solution. In the next step the nanopipette was exposed to the cssDNA to see if any changes in the I(t) trace would give further insights about the platform.

5.3.11 Towards the Hybridisation of ssDNA to the Capture Probe

The nanopipette set-up was then incubated with the cssDNA sequence for 45 min and a further decrease in conductance was observed (Figure 5.26).

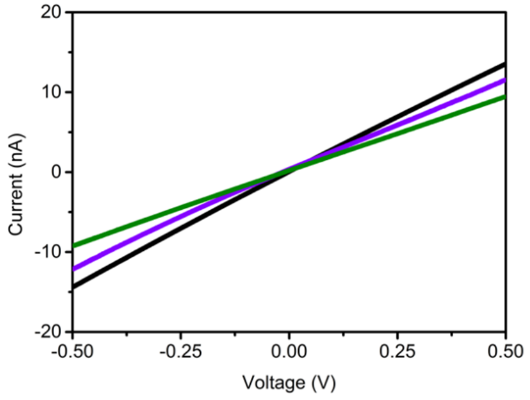

Figure 5.26. CV measurement for a bare nanopipette (black, G_{pore} = 28 nS), after exposure to POPC/DPPE-GA/ssDNA vesicles (purple, G_{pore} = 23 nS) and after incubation with the cssDNA (green, G_{pore} = 19 nS).

This 32% decrease in conductance relative to the bare nanopipette may be due to residual vesicles (or lipid fragments) in the bulk solution coating the nanopipette and is greater than the change in conductance attributed to dilution of the KCl electrolyte (see section 5.3.2).

Figure 5.27, shows a representative I(t) trace recorded following incubation with the cssDNA and supposed coating. A decrease in RMS noise from 53 to 47 pA before and after incubation with the cssDNA is observed perhaps indicative of a more uniform SLB on the nanopipette surface.

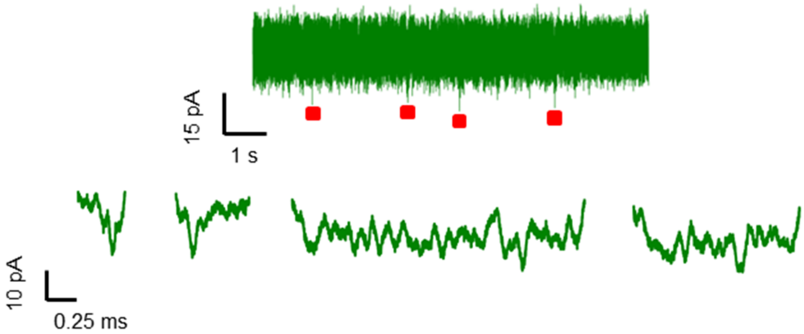

Figure 5.27. Representative I(t) trace with an V_{bias} of -100 mV for the nanopipette exposed to POPC/9-DPPE-GA/ssDNA vesicles and following incubation with the cssDNA. Events detected using the MATLAB code (see chapter 2) are indicated by a red square with magnifications of the events shown below the trace. The I(t) trace was filtered at 10 kHz.

Events detected (green) had a slightly smaller ΔI to those seen after exposure to POPC/9-DPPE-GA (organge). The events also had ΔI that were smaller to those seen before incubation with the cssDNA (purple, Figure 5.28), however the small number of events was not sufficient for statistical analysis.

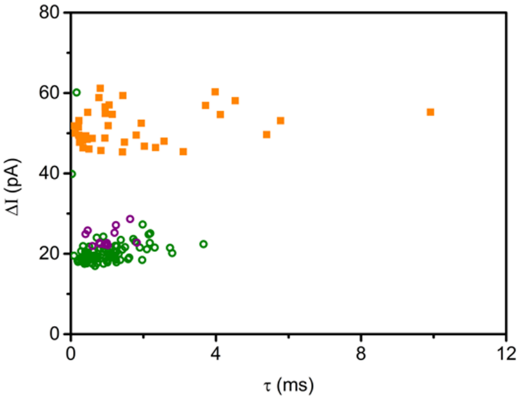

Figure 5.28. Scatter plot of events (ΔI vs. τ) observed for a nanopipette exposed to POPC/9-DPPE-GA vesicles (orange squares, G_{pore} = 38 nS, n = 39), a nanopipette exposed to POPC/9-DPPE-GA/ssDNA (purple open circles, G_{pore} = 23 nS, n = 13) and after incubation with the cssDNA (green open circles, G_{pore} = 19 nS, n = 89) with an V_{bias} of -100 mV.

Nevertheless, it is possible that dsDNA attached to the lipid bilayer (or islands) was indeed detected in the above traces. As with ssDNA the detection of free 100 bp dsDNA is highly unlikely as experiments in 1 M KCl using bare nanopipettes were unsuccessful in their detection (see chapter 4).

It should also be noted that I(t) traces for the nanopipette exposed to POPC/9-DPPE-GA vesicles were recorded with a filter frequency of 20 kHz while the I(t) traces for the nanopipette exposed to POPC/9-DPPE-GA/ssDNA vesicles then incubated with the cssDNA were recorded with a filter frequency of 10 kHz. A filter frequency of 10 and 20 kHz gives a minimum time resolution of ~0.1 and 0.05 ms respectively, with the filter frequency only distorting the ΔI if the event τ is below the minimum time resolution. All events observed for the POPC/9-DPPE-GA and POPC/9-DPPE-GA/ssDNA vesicle exposed nanopipettes had a τ greater than the minimum time resolution set by the filter frequency, while in the case of events seen after incubation with cssDNA, only 2% of events were below the minimum time resolution. Thus, comparison of ΔI despite the different filter frequencies should be valid.

Overall the data presented in this section and sections 5.3.9 and 5.3.10 are very preliminary with further work needed to optimise the coating procedure using this binary lipid mixture. Due to the limited stability of the bilayer, an insufficient number of events were recorded for statistical analysis. A very modest, if any, difference between the ΔI of events observed when the nanopipette was exposed to POPC/9-DPPE-GA/ssDNA vesicles and after incubation with the cssDNA was seen and this difference is very tentatively assigned to ssDNA and dsDNA translocations respectively.

5.4 Conclusion

This chapter presented nanopipettes coated with a POPC SLB using for the first time 1 M KCl electrolyte. For nanopore experiments, 1 M KCl is preferable to lower electrolyte concentrations which decrease the SNR because of its reduced electrolyte conductivity. The preparation of POPC SUV and their subsequent characterisation using DLS has been described. These SUV were then used to coat nanopipette tips and characterised using a combination of CV and I(t) measurements. The I(t) traces showed translocation events that were presumably caused by a breakdown of the SLB or by vesicles in the bulk solution. A device-to-device variation was also noted.

Work then focused on binary lipid mixtures aimed at introducing functionality to the SLB. AFM was used to image the distribution of binary lipid mixtures consisting of POPC with varying mol fractions of DPPE. Using the results from this study, 9 mol% of modified lipid was subsequently used. Preliminary experiments were carried out towards coating nanopipettes with an SLB containing capture probes that would hybridise to cssDNA in the bulk solution. The sequence of the capture probe could potentially be of diagnostic relevance for antibiotic resistance in TB. These experiments tentatively suggest possible detection of ssDNA-lipid and dsDNA-lipid complexes however, given the limited data-set and lack of repeats no firm conclusions can be drawn.

Experimental challenges included the limited stability of the SLB on the nanopipette tip and device-to-device variation. To address these issues, future work should be directed towards optimisation of the coating procedure using additional techniques such as fluorescence microscopy to gain a better understanding of the system. By incorporating a fluorescent lipid, fluorescence microscopy could be used to image the lipid-coated nanopipette tip and depending on the resolution shed light on whether the proposed lipid ‘islands’ exist. Other parameters such as initial starting diameter of the nanopipettes and KCl concentration could be optimised. Moreover, further experiments are needed to be able to distinguish with more certainty an SLB covalently attached to the capture probe and after the formation of dsDNA on the SLB.

5.5 References

(1) Wanunu, M. *Phys. Life Rev.* **2012**, *9*, 125–158.

(2) Fraccari, R. L.; Ciccarella, P.; Bahrami, A.; Carminati, M.; Ferrari, G.; Albrecht, T. *Nanoscale* **2016**, *8*, 7604–7611.

(3) Sze, J. Y. Y.; Kumar, S.; Ivanov, A. P.; Oh, S.; Edel, J. B. *Analyst* **2015**, *140*, 4828–4834.

(4) Steinbock, L. J.; Steinbock, J. F.; Radenovic, A. *Nano Lett.* **2013**, *13*, 1717–1723.

(5) Wanunu, M.; Sutin, J.; McNally, B.; Chow, A.; Meller, A. *Biophys. J.* **2008**, *95*, 4716–4725.

(6) Carlsen, A. T.; Zahid, O. K.; Ruzicka, J.; Taylor, E. W.; Hall, A. R. *ACS Nano* **2014**, *8*, 4754–4760.

(7) Bahrami, A.; Dogan, F.; Japrung, D.; Albrecht, T. *Biochem. Soc. Trans.* **2012**, *40*, 624–628.

(8) Yusko, E. C.; Johnson, J. M.; Majd, S.; Prangkio, P.; Rollings, R. C.; Li, J.; Yang, J.; Mayer, M. *Nat. Nanotechnol.* **2011**, *6*, 253–260.

(9) Hernández-Ainsa, S.; Muus, C.; Bell, N. a W.; Steinbock, L. J.; Thacker, V. V; Keyser, U. F. *Analyst* **2013**, *138*, 104–106.

(10) van Meer, G.; Voelker, D. R.; Feigenson, G. W. *Nat. Rev. Mol. Cell Biol.* **2008**, *9*, 112–124.

(11) Kucerka, N.; Tristram-Nagle, S.; Nagle, J. F. *J. Membr. Biol.* **2005**, *208*, 193–202.

(12) Kucerka, N.; Nieh, M.; Katsaras, J. *Biochim. Biophys. Acta* **2011**, *1808*, 2761–2771.

(13) Stidder, B.; Fragneto, G.; Roser, S. J. *Soft Matter* **2010**, *3*, 214–222.

(14) Singer, S. J.; Nicolson, G. L. *Science* **1972**, *175*, 720–731.

(15) Li, J.; Wang, X.; Zhang, T.; Wang, C.; Huang, Z.; Luo, X.; Deng, Y. *Asian J. Pharm. Sci.* **2014**, *10*, 81–98.

(16) Shearman, G. C.; Ces, O.; Templer, R. H.; Seddon, J. M. *J. Phys.: Condens. Matter* **2006**, *18*, S1105- S1124.

(17) Vries, A. H. De; Mark, A. E.; Marrink, S. J. *J. Phys. Chem. B* **2004**, *108*, 2454–2463.

(18) Somerharju, P.; Virtanen, J. A.; Cheng, K. H.; Hermansson, M. *Biochim. Biophys. Acta, Biomembr.* **2009**, *1788*, 12–23

(19) Chandler, D. *Nature* **2005**, *437*, 640–647.

(20) Dowhan, W. *Annu. Rev. Biochem.* **1997**, *66*, 199–232.

(21) Koynova, R.; Tenchov, B.; MacDonald, R. C. *ACS Biomater. Sci. Eng.* **2015**, *1*, 130–138.

(22) Orsi, M.; Essex, J. W. *Faraday Discuss.* **2013**, *161*, 249–272.

(23) Eze, M. O. *Biochem. Educ.* **1991**, *19*, 204–208.

(24) Kulkarni, C. V. *Nanoscale* **2012**, *4*, 5779–5791.

(25) Alessandrini, A.; Facci, P. *Soft Matter* **2014**, *10*, 7145–7164.

(26) Saiz, L.; Klein, M. L. *J. Chem. Phys.* **2002**, *116*, 3052–3057.

(27) Spuch, C.; Navarro, C. *J. Drug Delivery* **2011**, *2011*, 1–12.

(28) Akbarzadeh, A.; Rezaei-Sadabady, R.; Davaran, S.; Joo, S. W.; Zarghami, N.; Hanifehpour, Y.; Samiei, M.; Kouhi, M.; Nejati-Koshki, K. *Nanoscale Res. Lett.* **2013**, *8*, 1–9.

(29) Ahmed, S. E.; Martins, A. M.; Husseini, G. a. *J. Drug Targeting* **2015**, *23*, 1–27.

(30) Bird, A. *Genes Dev.* **2002**, *16*, 6–21.

(31) Mikeska, T.; Bock, C.; Do, H.; Dobrovic, A. *Expert Rev. Mol. Diagn.* **2012**, *12*, 473–487.

(32) Huynh, L.; Perrot, N.; Beswick, V.; Curmi, P. A.; Sanson, A. *Langmuir* **2014**, *30*, 564–573.

(33) Tattrie, N. H.; J, Bennet, R. J.; Cyr, R. *Can. J. Biochem.* **1968**, *46*, 819–824.

(34) Lorber, B.; Fischer, F.; Bailly, M.; Roy, H.; Kern, D. *Biochem. Mol. Biol. Educ.* **2012**, *40*, 372–382.

(35) Lapinski, M. M.; Castro-Forero, A.; Greiner, A. J.; Ofoli, R. Y.; Blanchard, G. J. *Langmuir* **2007**, *23*, 11677–11683.

(36) Zwang, T. J.; Fletcher, W. R.; Lane, T. J.; Johal, M. S. *Langmuir* **2010**, *26*, 4598–4601.

(37) Lewis, B. A.; Engelman, D. M. *J.Mol. Biol.* **1983**, *166*, 211–217.

(38) Nussio, M. R.; Voelcker, N. H.; Sykes, M. J.; McInnes, S. J. P.; Gibson, C. T.; Lowe, R. D.; Miners, J. O.; Shapter, J. G. *Biointerphases* **2008**, *3*, 96–104.

(39) Maté, S. M.; Vázquez, R. F.; Herlax, V. S.; Daza Millone, M. A.; Fanani, M. L.; Maggio, B.; Vela, M. E.; Bakás, L. S. *Biochim. Biophys. Acta, Biomembr.* **2014**, *1838*, 1832–1841.

(40) Ritter, M.; Schmidt, S.; Jakab, M.; Paulmichl, M.; Henderson, R. *Cell. Physiol. Biochem.* **2013**, *32*, 46–52.

(41) Eaton, P.; West, P. *Atomic Force Microscopy*; Oxford University Press, 2010.

(42) Mulukutla, S.; Shipley, G. *Biochemistry* **1984**, *23*, 2514–2519.

(43) Inoue, T.; Nibu, Y. *Chem. Phys. Lipids* 1999, *100*, 139–150.

(44) Losada-Perez, P.; Mertens, N.; De Medio-Vasconcelos, B.; Slenders, E.; Leys, J.; Peeters, M.; Van Grinsven, B.; Gruber, J.; Glorieux, C.; Pfeiffer, H.; Wagner, P.; Thoen, J. *Adv. Condens. Matter Phys.* **2015**, *2015*, 1–14.

(45) http://www.sigmaaldrich.com/technical-documents/protocols/biology/annealing-oligos.html. Accessed on 1/11/2016.

(46) Hughes, I. G.; Hase, T. P. A. *Measurements and their Uncertainties A Practical Guide to Modern Error Analysis*; Oxford University Press, Oxford 2010.

Chapter 6

Conclusion and Outlook

Synopsis: This chapter presents a summary of the research discussed in this thesis. An overview of the motivations for the work, key findings and challenges are detailed and lastly, a brief discussion on recommendations for future work.

Nanopore-based sensors show potential in the fields of DNA sequencing and medical diagnostics with some progress towards commercialisation already made. In spite of this, drawbacks and challenges still exist, two of which are i) the fast timescale (~μs) of DNA translocations and ii) the inability of nanopores to determine the molecular identity of the translocating species.[1] The aim of this research project was to address these limitations by understanding in greater detail the translocation dynamics of different DNA lengths, L_{DNA} using nanopipettes as a biophysical tool. In addition, the molecular identity of short (~200 bp and below) ssDNA and dsDNA was probed. Finally, previous work in the literature had shown that the 'fluid-wall technology' where solid-state pores (chip-based and nanopipettes) have been coated with a mobile lipid bilayer can be used to have better control over the translocation speed of analytes and pore diameter.[2–4] Moreover, it was envisioned that the sensing performance of a nanopipette could be improved using the fluid-wall technology by incorporating a range of surface-bound capture probes to pre-concentrate the desired target molecule close to the pore. In light of this, a modified fluid lipid bilayer was used to coat nanopipettes in an attempt to detect in-situ hybridisation of ssDNA to its cssDNA.

In this thesis resistive-pulse sensing using nanopipettes together with a range of other techniques and instrumentation including AFM and DLS were used, the details of which are outlined in Chapter 2.

The translocation time, τ as a function of L_{DNA} has a scaling factor, p which has been reported to be ~1.37 – 2.28 for chip-based nanopores operating in 1 M KCl and ~0.86 - 1.01 for nanopipettes in 4 M LiCl.[5–8] In the literature, Ghosal had proposed an analytical model which described the τ of a polyelectrolyte translocating through a pore with a cylindrical geometry.[9,10] However, the model did not fully explain the dependence of the τ on L_{DNA} in our experiments. Chapter 3 described a L_{DNA} dependence study using DNA with lengths between 4 and 48.5 kbp. The τ_{mp} was studied as a function of L_{DNA} using negatively charged nanopipettes and for the first time 1 M KCl electrolyte. In addition, a low-noise, custom-built and high-bandwidth 'Polimi' amplifier was employed to fully resolve DNA translocation events in 1 M KCl. The results presented here found $p = 1.22 \pm 0.01$, which was comparable to studies using chip-based solid-state platforms in 1 M KCl electrolyte but different to that reported for nanopipettes in 4 M LiCl. It was hypothesised that these different values of p, may in part be due to DNA/surface interactions prior to translocation. Analytically this was solved using the Ghosal+ model which took into account friction forces between the DNA and the pore surface prior to DNA translocation through the pore. In this model p could take values between one and two. In the former case DNA/surface interactions are negligible while in the latter case the interactions are an important part of the translocation process. The value p=1.22 ± 0.01 suggested that DNA adsorption to the surface of quartz nanopipettes is indeed an important factor in translocation experiments. Initial experiments were then performed to probe DNA adsorption to the surface of nanopipettes using silane chemistry to coat nanopipettes with APTMS which at pH 8 has a positive charge. It was hypothesised that the positive charge of the nanopipette would increase the τ of translocation events due to increased interaction between the negatively charged DNA prior to translocation and the nanopipette surface. This was found to be the case for the translocation of 4 kbp dsDNA through APTMS coated nanopipettes which showed an increased τ compared to its translocation through unmodified nanopipettes.

In chapter 4 using data from the L_{DNA} study it was predicted that 220 bp dsDNA would be the minimum detectable length using nanopipettes in 1 M KCl and the Polimi amplifier. Good experimental agreement was found with this value as 200 bp dsDNA was successfully detected. The detection of shorter DNA lengths required the use of LiCl electrolyte. In the literature the use of NaCl electrolyte was shown to increase the τ relative to KCl electrolyte,[11,12] with a further increase in τ obtained when using LiCl electrolyte.[11] In particular, however, the detection of a 100 nt sequence and its complement was of interest. The chosen sequence is relevant to the detection of antibiotic resistance in TB. As aforementioned, nanopores are unable to detect the molecular entity of the translocating DNA molecule but by using complementary base pairing between the 100 nt ssDNA and its complement, differentiation of ssDNA and dsDNA current signatures can provide more information to be extracted from nanopore experiments. Using 2 M LiCl electrolyte, the 100 nt sequence was detected although the fast translocation speed proved to be a limitation. However, the ssDNA hybridised to the ccssDNA to form 100 bp dsDNA was successfully detected in 2 and 4 M LiCl.

Lastly in chapter 5, the aim was to coat nanopipettes with a modified mobile lipid bilayer. It was envisioned that the ssDNA of interest could be attached to the lipid bilayer coating the nanopipette thereby acting as a capture probe to pre-concentrate the cssDNA close the pore. Initially, coating of nanopipettes with a mobile lipid bilayer was performed using POPC vesicles. This was followed by coating of the nanopipettes with a binary lipid mixture containing binding sites for the ssDNA of interest. It was expected that different current signatures would allow the differentiation of surface-bound ssDNA and dsDNA translocations through the pore. The preliminary nanopipette coating experiment showed differences in the ΔI of events which were tentatively attributed to ssDNA and dsDNA at the lipid bilayer surface. However, experimental challenges encountered included the limited stability of the lipid bilayer on the nanopipette surface as well as device-to-device variation in noise levels which limited the performance of devices.

Overall, from the research presented in this thesis we have gained a better understanding of the translocation dynamics of DNA molecules in nanopipettes and of the ssDNA and dsDNA sensing capabilities of nanopipettes. While DNA sequencing at the single base pair resolution level using nanopipettes currently seems beyond reach, improved sensing capabilities of nanopipette biosensors could be achieved by building upon some of the capture probe/target interaction systems presented in this thesis.

6.1 References

(1) Wanunu, M. *Phys. Life Rev.* 2012, *9*, 125–158.

(2) Yusko, E. C.; Johnson, J. M.; Majd, S.; Prangkio, P.; Rollings, R. C.; Li, J.; Yang, J.; Mayer, M. *Nat. Nanotechnol.* **2011**, *6*, 253–260.

(3) Hernández-Ainsa, S.; Muus, C.; Bell, N. a W.; Steinbock, L. J.; Thacker, V. V; Keyser, U. F. *Analyst* **2013**, *138*, 104–106.

(4) Albrecht, T. *Nat. Nanotechnol.* **2011**, *6*, 195–196.

(5) Bell, N. A. DNA Origami Nanopores and Single Molecule Transport through Nanocapillaries, University of Cambridge, 2013.

(6) Wanunu, M.; Sutin, J.; McNally, B.; Chow, A.; Meller, A. *Biophys. J.* **2008**, *95*, 4716–4725.

(7) Storm, A. J.; Chen, J. H.; Zandbergen, H. W.; Dekker, C. *Phys. Rev. E: Stat., Nonlinear, Soft Matter Phys.* **2005**, *71*, 1–10.

(8) Storm, A. J.; Storm, C.; Chen, J.; Zandbergen, H.; Joanny, J. F.; Dekker, C. *Nano Lett.* **2005**, *5*, 1193–1197.

(9) Ghosal, S. *Phys. Rev.* **2006**, *74*, 41901.

(10) Ghosal, S. *Phys. Rev. Lett.* **2007**, *98*, 238104.

(11) Kowalczyk, S. W.; Wells, D. B.; Aksimentiev, A.; Dekker, C. *Nano Lett.* **2012**, *12*, 1038–1044.

(12) Uplinger, J.; Thomas, B.; Rollings, R.; Fologea, D.; Mcnabb, D.; Li, J. *Electrophoresis* **2012**, *33*, 3448–3457.

Appendices

Appendix I. Taper Length of Fabricated Nanopipettes

The taper length of nanopipettes pulled with programme 99 was determined using optical micrographs of six nanopipettes. Figure App. 1, shows a typical optical micrograph used to determine l. According to previous work,[13] the diameter, d_b, is where the diameter of the nanopipette is equal to 0.3 mm and the distance between d_b and the nanopipette tip is defined as l. Analysis of images in this way gave $l = 2.7 \pm 0.1$ mm.

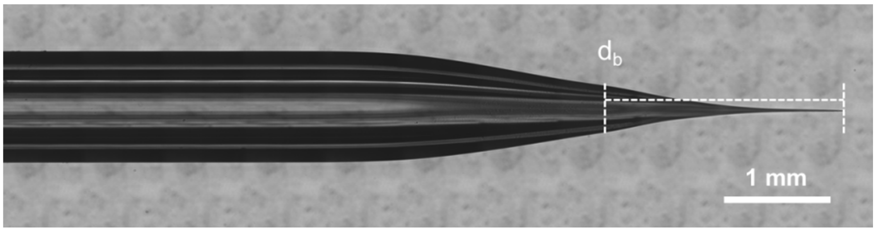

Figure App. 1. Optical micrograph of a nanopipette showing the dimensions of the tip.[t]

---

[t] Image taken by Thomas Mickleburg, a PhD candidate in the Klug group, Imperial College London.

Appendix II. Complete τ_{mp} values for the four L_{DNA} samples.

Table App. 1. τ_{mp} values for the linear population of translocation events.[u]

V_{bias} (mV)	τ_{mp} (ms)			
	48.5 kbp	**10 kbp**	**5.31 kbp**	**4 kbp**
-900	0.869 ± 0.024	0.112	0.051, 0.063	0.047, 0.034
-800	0.901 ± 0.027	0.131	0.070, 0.060	0.043, 0.045
-700	1.064 ± 0.046	0.153, 0.148	0.066, 0.082	0.045 ± 0.005
-600	0.990 ± 0.017	0.176, 0.171	0.083 ± 0.007	0.050 ± 0.005
-500	1.783, 1.390	0.251 ± 0.025	0.113 ± 0.010	0.061 ± 0.007
-400	1.884 ± 0.108	0.286 ± 0.008	0.137 ± 0.009	0.080 ± 0.010
-300	2.822	0.439 ± 0.041	0.104, 0.239	0.174, 0.109
-200		0.524	0.304 ± 0.039	0.153, 0.186

---

[u] For a given V_{bias} where there are three or more ΔI_{mp} values, these have been averaged and the standard error of the mean is quoted. Where there are fewer than three τ_{mp} values at a given V_{bias}, the values are stated.

Appendix III. Complete ΔI_{mp} values for the four L_{DNA} samples

Table App. 2. ΔI_{mp} values for the linear population of translocation events.[v]

V_{bias} (mV)	ΔI_{mp} (ms)			
	48.5 kbp	10 kbp	5.31 kbp	4 kbp
-900	226 ± 40	252	199, 229	246, 209
-800	228 ± 37	215	176, 201	202, 180
-700	161 ± 4	179, 182	155, 180	149 ± 8
-600	126 ± 5	153, 182	150 ± 11	137 ± 8
-500	98, 99	106 ± 4	101 ± 6	104 ± 4
-400	74 ± 2	84 ± 3	82 ± 3	76 ± 5
-300	53	55 ± 2	56, 59	55, 63
-200		41	34 ± 2	32, 35

---

[v] For a given V_{bias} where there are three or more ΔI_{mp} values, these have been averaged and the standard error of the mean is quoted. Where there are fewer than three ΔI_{mp} values at a given V_{bias}, the values are stated.

Appendix IV. Estimating the SNR for the four different L_{DNA}

Table App. 3. Translocation characteristics of long DNA for L_{DNA} between 4 and 48.5 kbp, as a function of V_{bias}. Each cell contains ΔI_{mp} [pA], the filter frequency used [kHz], I_{rms}^{AC} [pA], and the SNR ratio $\Delta I_{mp}/I_{rms}^{AC}$.

V_{bias}	4 kbp	5.31 kbp	10 kbp	48.5 kbp
-200 mV	34 pA 30 kHz 5.3 pA **6.4**	34 pA 30 kHz 5.2 pA **6.6**	41 pA 50 kHz 7.2 pA **5.7**	
-300 mV	59 pA 60 kHz 8.4 pA **7.0**	58 pA 60 kHz 8.1 pA **7.1**	55 pA 50 kHz 8.0 pA **6.8**	53 pA 20 kHz 5.4 pA **9.8**
-400 mV	76 pA 100 kHz 12.1 pA **6.3**	82 pA 100 kHz 13.3 pA **6.2**	84 pA 100 kHz 12.7 pA **6.6**	74 pA 30 kHz 9.1 pA **8.1**
-800 mV	191 pA 200 kHz 25.3 pA **7.5**	188 pA 200 kHz 25.6 pA **7.3**	215 pA 200 kHz 29.3 pA **7.3**	229 pA 100 kHz 19.9 pA **11.5**

Appendix V. Agarose gel electrophoresis confirming purity of 200 bp dsDNA

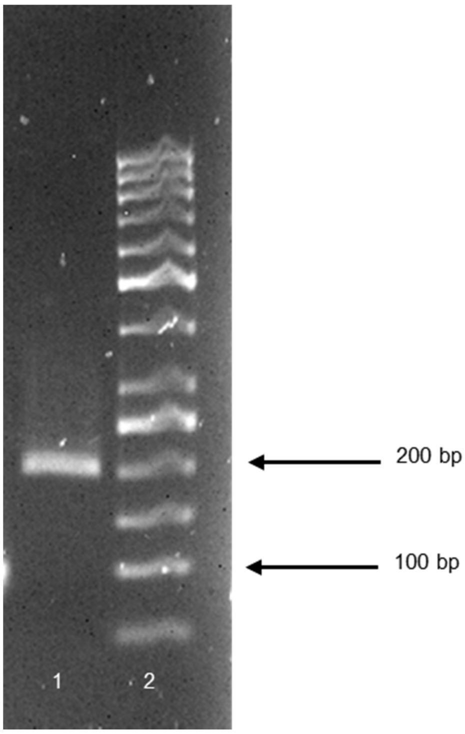

Figure App. 2. Agarose gel electrophoresis (2%, 5 V/cm, 70 min, 1x TBE) image confirming purity of commercial 200 bp dsDNA. Lane 1: 200 bp dsDNA sample and Lane 2: '50 bp ladder' (ThermoFisher).

Appendix VI. Current blockages for POPC-coated nanopipettes

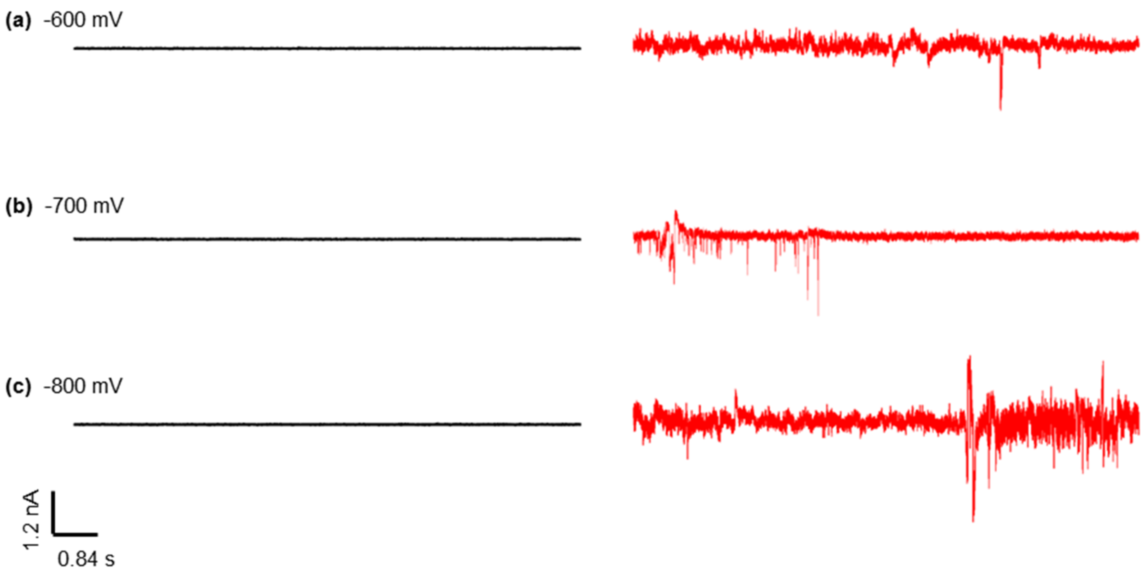

Figure App. 3. I(t) traces for a bare nanopipette (black) and after POPC-coating (red) with an V_{bias} of **(a)** -600, **(b)** -700 and **(c)** -800 mV. Initial G_{pore} = 35 nS. I(t) traces were filtered at 20 kHz.

Appendix VII. Summary of permissions for third party copyright works.

Figure number	Source	Copyright holder	Permission	License number
1.1	Howorka, S.; Siwy, Z. *Chem. Soc. Rev.* **2009**, *38*, 2360–2384.	The Royal Society of Chemistry	Granted	3980931057411
1.2	Deamer, D.; Akeson, M.; Branton, D. *Nat. Biotechnol.* **2016**, *34*, 518–524.	Nature Publishing Group	Granted	3979561143346
1.4	Albrecht, T.; Gibb, T.; Nuttall, P. *Engineered Nanopores for Bioanalytical Applications*; Edel, J.; Albrecht, T., Eds.; Elsevier, 2013.	Elsevier	Granted	3980420856936
2.5	Mingeot-Leclercq, M.-P.; Deleu, M.; Brasseur, R.; Dufrene, Y. F. *Nat. Protoc.* **2008**, *3*, 1654–1659.	Nature Publishing Group	Granted	3979561452537
3.1	Ghosal, S. *Phys. Rev. Lett.* **2007**, *98*, 238104.	American Physical Society	Granted	3979570711373
3.2	Storm, A. J.; Storm, C.; Chen, J.; Zandbergen, H.; Joanny, J. F.; Dekker, C. *Nano Lett.* **2005**, *5*, 1193–1197	American Chemical Society	Granted	See attached (approval 1)
3.3a	Anderson, B. N.; Muthukumar, M.; Meller, A. *ACS Nano* **2013**, *7*, 1408–1414.	American Chemical Society	Granted	See attached (approval 2)
3.3b	Wei, R.; Gatterdam, V.; Wieneke, R.; Tampé, R.; Rant, U. *Nat. Nanotechnol.* **2012**, *7*, 257–263.	Nature Publishing Group	Granted	3980361436164
3.4	Rutkowska, A.; Freedman, K.; Skalkowska, J.; Kim, M. J.; Edel, J. B.; Albrecht, T. *Anal. Chem.* **2015**, *87*, 2337–2344.	American Chemical Society	Granted	See attached (approval 3)
3.5a	Sa, N.; Fu, Y.; Baker, L. A. *Anal. Chem.* **2010**, *82*, 9963–9966.	American Chemical Society	Granted	See attached (approval 4)
3.5b	Fu, Y.; Tokuhisa, H.; Baker, L. A. *Chem. Commun. (Camb).* **2009**, 4877–4879.	Royal Society of Chemistry	Granted	3980380439362

3.9	http://mdc.custhelp.com/euf/assets/content/ Axon%20Guide%203rd%20edition.pdf.	Molecular Devices	Requested	See attached (Molecular Devices request)
4.1	Kowalczyk, S. W.; Wells, D. B.; Aksimentiev, A.; Dekker, C. *Nano Lett.* **2012**, *12* (2), 1038–1044.	American Chemical Society	Granted	See attached (approval 5)
4.2	Uplinger, J.; Thomas, B.; Rollings, R.; Fologea, D.; Mcnabb, D.; Li, J. *Electrophoresis* **2012**, *33* (23), 3448–3457.	John Wiley and Sons	Granted	3980391221459
5.1a	Yusko, E. C.; Johnson, J. M.; Majd, S.; Prangkio, P.; Rollings, R. C.; Li, J.; Yang, J.; Mayer, M. *Nat. Nanotechnol.* **2011**, *6*, 253–260.	Nature Publishing Group	Granted	3980400362732
5.1b	Hernández-Ainsa, S.; Muus, C.; Bell, N. a W.; Steinbock, L. J.; Thacker, V. V; Keyser, U. F. *Analyst* **2013**, *138*, 104–106.	Royal Society of Chemistry	Granted	3980400547834
5.4a	Dowhan, W. *Annu. Rev. Biochem.* **1997**, *66*, 199–232.	Annual Reviews	Granted	See attached (approval 6)
5.4b	Koynova, R.; Tenchov, B.; MacDonald, R. C. *ACS Biomater. Sci. Eng.* **2015**, *1*, 130–138.	American Chemical Society	Granted	See attached (approval 7)

Approval 1

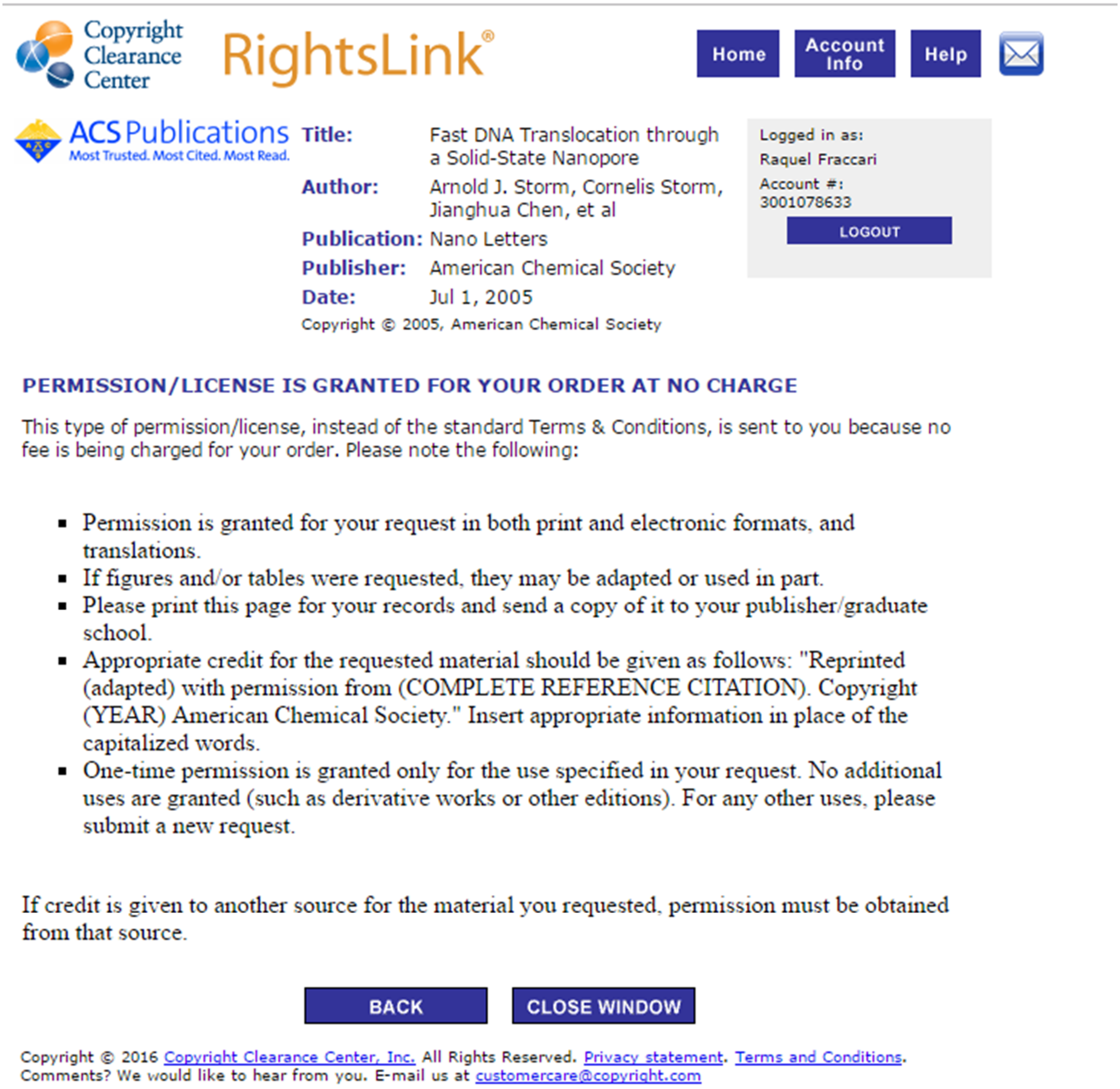

Title: Fast DNA Translocation through a Solid-State Nanopore

Author: Arnold J. Storm, Cornelis Storm, Jianghua Chen, et al

Publication: Nano Letters

Publisher: American Chemical Society

Date: Jul 1, 2005

Logged in as:
Raquel Fraccari
Account #:
3001078633

PERMISSION/LICENSE IS GRANTED FOR YOUR ORDER AT NO CHARGE

This type of permission/license, instead of the standard Terms & Conditions, is sent to you because no fee is being charged for your order. Please note the following:

- Permission is granted for your request in both print and electronic formats, and translations.
- If figures and/or tables were requested, they may be adapted or used in part.
- Please print this page for your records and send a copy of it to your publisher/graduate school.
- Appropriate credit for the requested material should be given as follows: "Reprinted (adapted) with permission from (COMPLETE REFERENCE CITATION). Copyright (YEAR) American Chemical Society." Insert appropriate information in place of the capitalized words.
- One-time permission is granted only for the use specified in your request. No additional uses are granted (such as derivative works or other editions). For any other uses, please submit a new request.

If credit is given to another source for the material you requested, permission must be obtained from that source.

Approval 2

Title: pH Tuning of DNA Translocation Time through Organically Functionalized Nanopores

Author: Brett N. Anderson, Murugappan Muthukumar, Amit Meller

Publication: ACS Nano

Publisher: American Chemical Society

Date: Feb 1, 2013

Copyright © 2013, American Chemical Society

If you're a copyright.com user, you can login to RightsLink using your copyright.com credentials. Already **a RightsLink user** or want to learn more?

PERMISSION/LICENSE IS GRANTED FOR YOUR ORDER AT NO CHARGE

This type of permission/license, instead of the standard Terms & Conditions, is sent to you because no fee is being charged for your order. Please note the following:

- Permission is granted for your request in both print and electronic formats, and translations.
- If figures and/or tables were requested, they may be adapted or used in part.
- Please print this page for your records and send a copy of it to your publisher/graduate school.
- Appropriate credit for the requested material should be given as follows: "Reprinted (adapted) with permission from (COMPLETE REFERENCE CITATION). Copyright (YEAR) American Chemical Society." Insert appropriate information in place of the capitalized words.
- One-time permission is granted only for the use specified in your request. No additional uses are granted (such as derivative works or other editions). For any other uses, please submit a new request.

If credit is given to another source for the material you requested, permission must be obtained from that source.

Approval 3

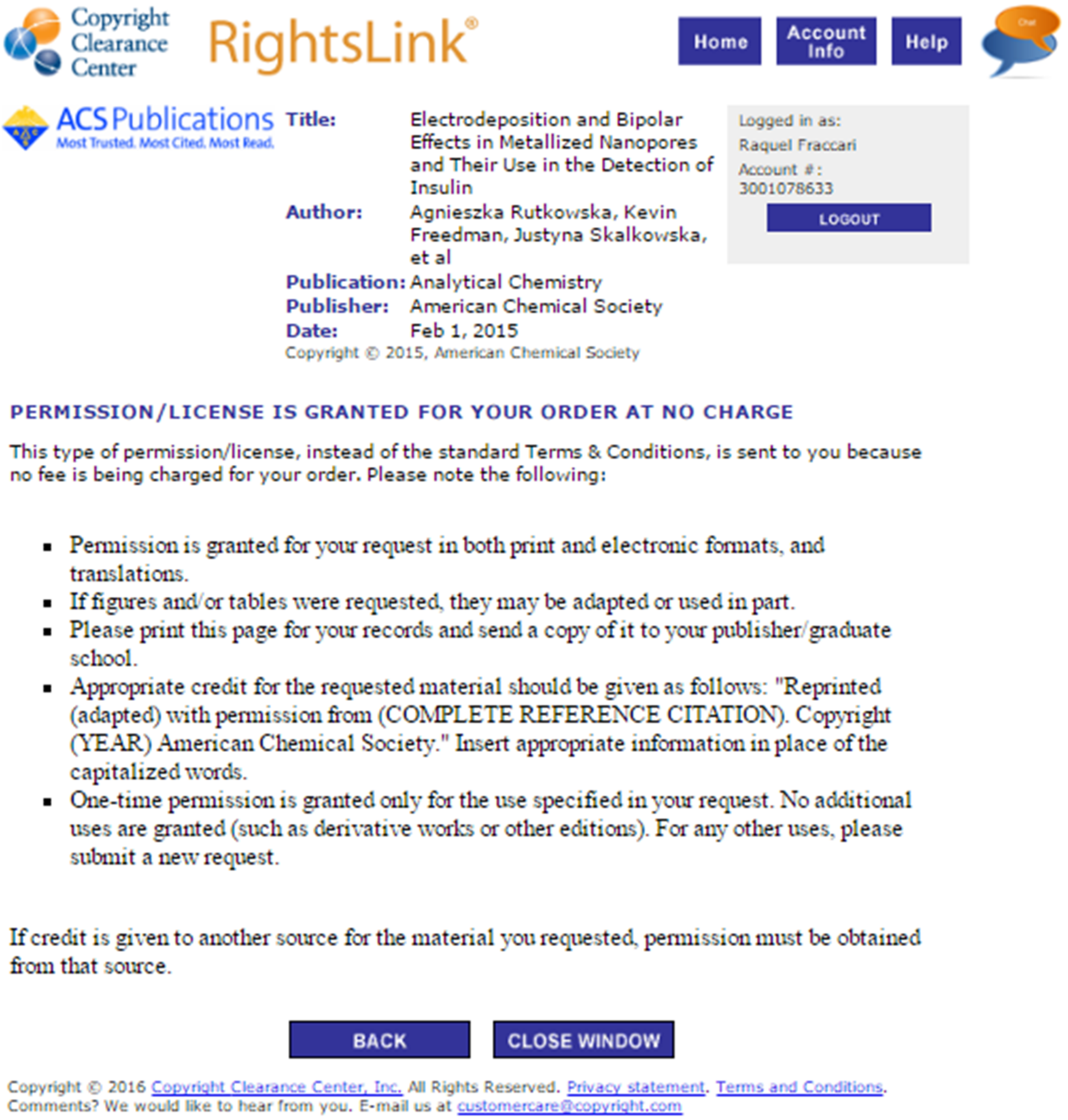

Title: Electrodeposition and Bipolar Effects in Metallized Nanopores and Their Use in the Detection of Insulin
Author: Agnieszka Rutkowska, Kevin Freedman, Justyna Skalkowska, et al
Publication: Analytical Chemistry
Publisher: American Chemical Society
Date: Feb 1, 2015
Copyright © 2015, American Chemical Society

Logged in as:
Raquel Fraccari
Account #:
3001078633

PERMISSION/LICENSE IS GRANTED FOR YOUR ORDER AT NO CHARGE

This type of permission/license, instead of the standard Terms & Conditions, is sent to you because no fee is being charged for your order. Please note the following:

- Permission is granted for your request in both print and electronic formats, and translations.
- If figures and/or tables were requested, they may be adapted or used in part.
- Please print this page for your records and send a copy of it to your publisher/graduate school.
- Appropriate credit for the requested material should be given as follows: "Reprinted (adapted) with permission from (COMPLETE REFERENCE CITATION). Copyright (YEAR) American Chemical Society." Insert appropriate information in place of the capitalized words.
- One-time permission is granted only for the use specified in your request. No additional uses are granted (such as derivative works or other editions). For any other uses, please submit a new request.

If credit is given to another source for the material you requested, permission must be obtained from that source.

Copyright © 2016 Copyright Clearance Center, Inc. All Rights Reserved. Privacy statement. Terms and Conditions.
Comments? We would like to hear from you. E-mail us at customercare@copyright.com

Approval 4

Title: Reversible Cobalt Ion Binding to Imidazole-Modified Nanopipettes
Author: Niya Sa, Yaqin Fu, Lane A. Baker
Publication: Analytical Chemistry
Publisher: American Chemical Society
Date: Dec 1, 2010
Copyright © 2010, American Chemical Society

Logged in as:
Raquel Fraccari
Account #:
3001078633

PERMISSION/LICENSE IS GRANTED FOR YOUR ORDER AT NO CHARGE

This type of permission/license, instead of the standard Terms & Conditions, is sent to you because no fee is being charged for your order. Please note the following:

- Permission is granted for your request in both print and electronic formats, and translations.
- If figures and/or tables were requested, they may be adapted or used in part.
- Please print this page for your records and send a copy of it to your publisher/graduate school.
- Appropriate credit for the requested material should be given as follows: "Reprinted (adapted) with permission from (COMPLETE REFERENCE CITATION). Copyright (YEAR) American Chemical Society." Insert appropriate information in place of the capitalized words.
- One-time permission is granted only for the use specified in your request. No additional uses are granted (such as derivative works or other editions). For any other uses, please submit a new request.

If credit is given to another source for the material you requested, permission must be obtained from that source.

Approval 5

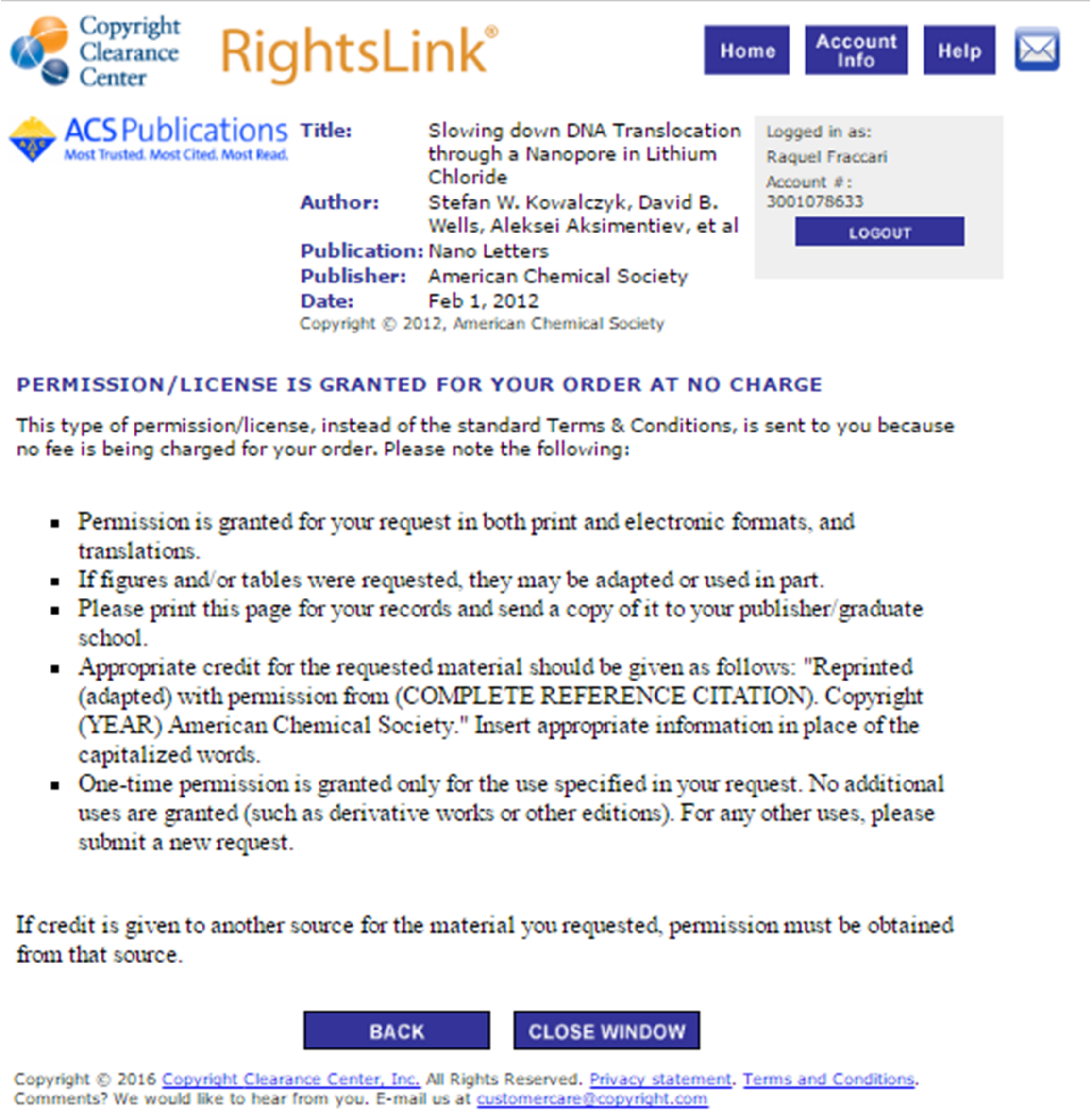

Title: Slowing down DNA Translocation through a Nanopore in Lithium Chloride
Author: Stefan W. Kowalczyk, David B. Wells, Aleksei Aksimentiev, et al
Publication: Nano Letters
Publisher: American Chemical Society
Date: Feb 1, 2012
Copyright © 2012, American Chemical Society

Logged in as:
Raquel Fraccari
Account #:
3001078633

PERMISSION/LICENSE IS GRANTED FOR YOUR ORDER AT NO CHARGE

This type of permission/license, instead of the standard Terms & Conditions, is sent to you because no fee is being charged for your order. Please note the following:

- Permission is granted for your request in both print and electronic formats, and translations.
- If figures and/or tables were requested, they may be adapted or used in part.
- Please print this page for your records and send a copy of it to your publisher/graduate school.
- Appropriate credit for the requested material should be given as follows: "Reprinted (adapted) with permission from (COMPLETE REFERENCE CITATION). Copyright (YEAR) American Chemical Society." Insert appropriate information in place of the capitalized words.
- One-time permission is granted only for the use specified in your request. No additional uses are granted (such as derivative works or other editions). For any other uses, please submit a new request.

If credit is given to another source for the material you requested, permission must be obtained from that source.

Copyright © 2016 Copyright Clearance Center, Inc. All Rights Reserved. Privacy statement. Terms and Conditions.
Comments? We would like to hear from you. E-mail us at customercare@copyright.com

Approval 6

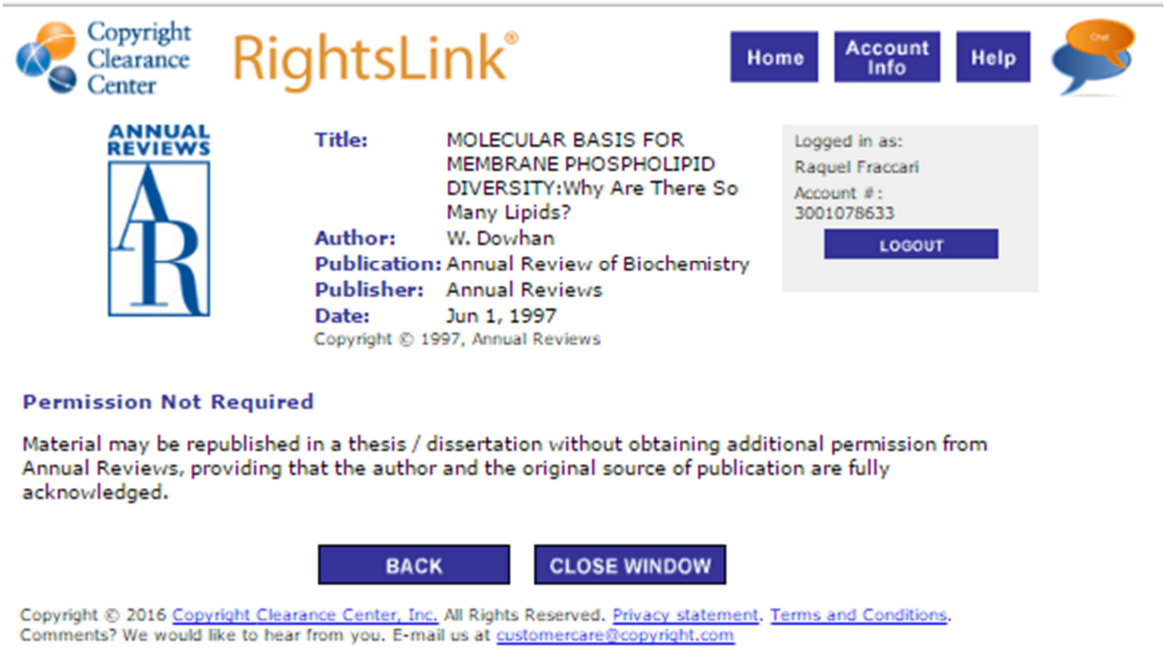

Title: MOLECULAR BASIS FOR MEMBRANE PHOSPHOLIPID DIVERSITY:Why Are There So Many Lipids?
Author: W. Dowhan
Publication: Annual Review of Biochemistry
Publisher: Annual Reviews
Date: Jun 1, 1997
Copyright © 1997, Annual Reviews

Logged in as:
Raquel Fraccari
Account #:
3001078633

Permission Not Required

Material may be republished in a thesis / dissertation without obtaining additional permission from Annual Reviews, providing that the author and the original source of publication are fully acknowledged.

Approval 7

Title: Nonlamellar Phases in Cationic Phospholipids, Relevance to Drug and Gene Delivery
Author: Rumiana Koynova, Boris Tenchov, Robert C. MacDonald
Publication: ACS Biomaterials Science & Engineering
Publisher: American Chemical Society
Date: Mar 1, 2015
Copyright © 2015, American Chemical Society

Logged in as:
Raquel Fraccari
Account #:
3001078633

PERMISSION/LICENSE IS GRANTED FOR YOUR ORDER AT NO CHARGE

This type of permission/license, instead of the standard Terms & Conditions, is sent to you because no fee is being charged for your order. Please note the following:

- Permission is granted for your request in both print and electronic formats, and translations.
- If figures and/or tables were requested, they may be adapted or used in part.
- Please print this page for your records and send a copy of it to your publisher/graduate school.
- Appropriate credit for the requested material should be given as follows: "Reprinted (adapted) with permission from (COMPLETE REFERENCE CITATION). Copyright (YEAR) American Chemical Society." Insert appropriate information in place of the capitalized words.
- One-time permission is granted only for the use specified in your request. No additional uses are granted (such as derivative works or other editions). For any other uses, please submit a new request.

If credit is given to another source for the material you requested, permission must be obtained from that source.

Copyright © 2016 Copyright Clearance Center, Inc. All Rights Reserved. Privacy statement. Terms and Conditions.
Comments? We would like to hear from you. E-mail us at customercare@copyright.com

Molecular Devices Request

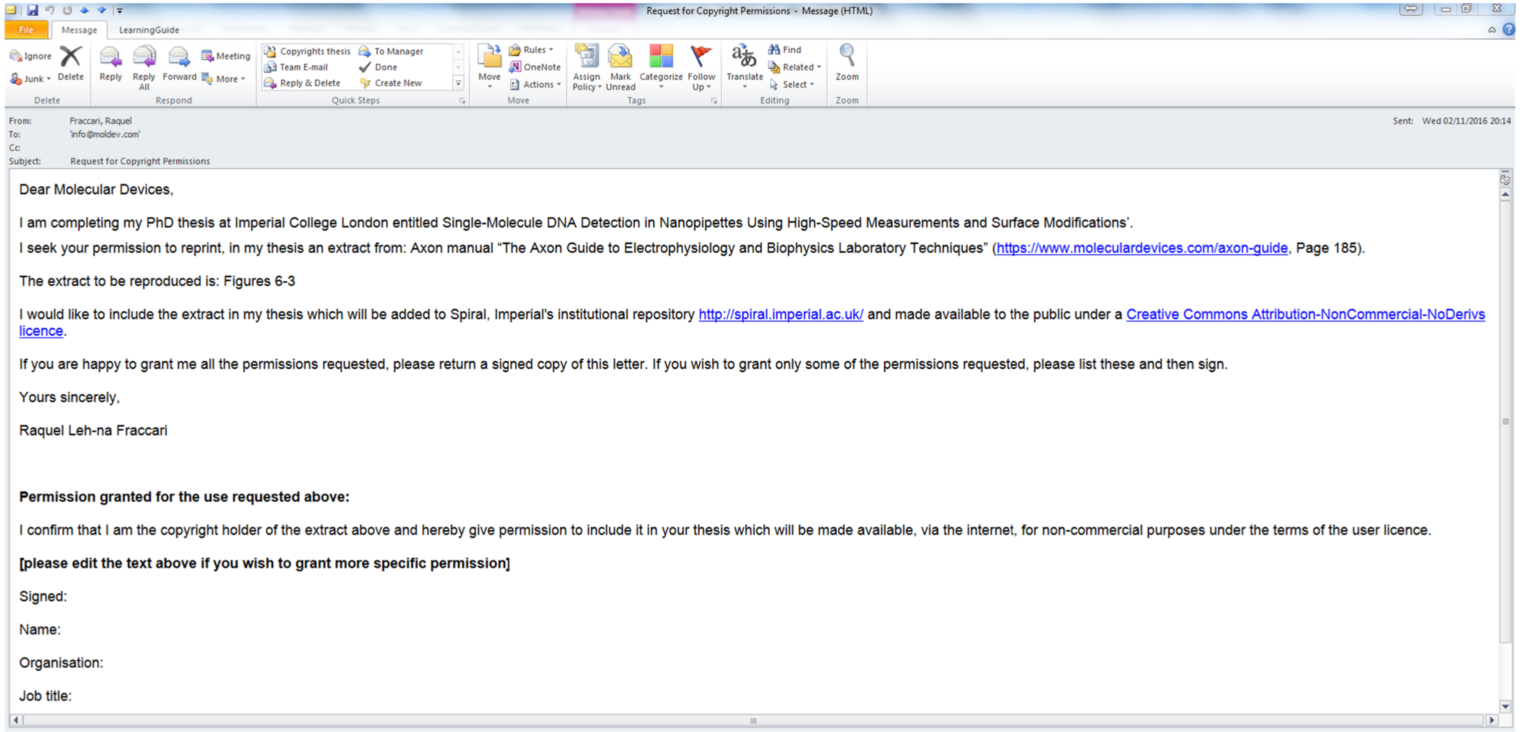

From: Fraccari, Raquel
To: 'info@moldev.com'
Cc:
Subject: Request for Copyright Permissions
Sent: Wed 02/11/2016 20:14

Dear Molecular Devices,

I am completing my PhD thesis at Imperial College London entitled Single-Molecule DNA Detection in Nanopipettes Using High-Speed Measurements and Surface Modifications'.

I seek your permission to reprint, in my thesis an extract from: Axon manual "The Axon Guide to Electrophysiology and Biophysics Laboratory Techniques" (https://www.moleculardevices.com/axon-guide, Page 185).

The extract to be reproduced is: Figures 6-3

I would like to include the extract in my thesis which will be added to Spiral, Imperial's institutional repository http://spiral.imperial.ac.uk/ and made available to the public under a Creative Commons Attribution-NonCommercial-NoDerivs licence.

If you are happy to grant me all the permissions requested, please return a signed copy of this letter. If you wish to grant only some of the permissions requested, please list these and then sign.

Yours sincerely,

Raquel Leh-na Fraccari

Permission granted for the use requested above:

I confirm that I am the copyright holder of the extract above and hereby give permission to include it in your thesis which will be made available, via the internet, for non-commercial purposes under the terms of the user licence.

[please edit the text above if you wish to grant more specific permission]

Signed:

Name:

Organisation:

Job title: